This is to certify that the

dissertation entitled

Characterization of Transient Vibrations In Mechanical Systems: Time-Frequency Localization with Wavelets and STFT.

presented by

Taner Onsay

has been accepted towards fulfillment
of the requirements for

Ph.D. degree in Mechanical Engineering

Alan. G. Haddow
Major professor

Date 03/04/94

CHARACTERIZATION OF TRANSIENT VIBRATIONS IN MECHANICAL SYSTEMS: TIME-FREQUENCY LOCALIZATION WITH WAVELETS AND STFT

By

Taner Önsay

A DISSERTATION

Submitted to
Michigan State University
in partial fulfillment of the requirements
for the degree of

DOCTOR OF PHILOSOPHY

Department of Mechanical Engineering

1994

ABSTRACT

CHARACTERIZATION OF TRANSIENT VIBRATIONS IN MECHANICAL SYSTEMS: TIME-FREQUENCY LOCALIZATION WITH WAVELETS AND STFT

By

Taner Önsay

Linear time-frequency localization techniques are utilized to study transient vibration characteristics of mechanical systems. The advantages, limitations and the conceptual similarities of the short-time Fourier (STFT), Gabor and Wavelet transforms are investigated. Particular attention is given to the application of recently-developed mathematical concepts regarding wavelets, frames and multi-resolution analysis.

In the first part, the effectiveness of the wavelet transform in the analysis of transient wave propagation is explored. The time-scale representations generated by the wavelet transform are utilized to characterize the dynamic behavior of different wavebearing media and the time-evolution of the spectral components of transient waves. The propagation, reflection and scattering of a transient waveform in a dispersive medium are given particular attention due to the similarity in the fundamental properties of the physical phenomena and the analysis tool. As an alternative, a space-wavenumber representation is introduced. The wavelet transform is correlated with the group properties of a dispersed waveform. The self-adjusting window structure of the wavelet transform is exploited during the analysis of different wave-modes in a wave-guide. In applications, the time-evolution of the complex interference patterns in finite systems are investigated. An interesting periodic pulse reconstitution phenomenon is uncovered on a uniform single-span beam.

In the second part, the convolution integral is replaced by an efficient synthesis scheme by using multi-resolution and wavelet frame concepts. The wavelet response function of a linear system is introduced. The transient vibration response of a proportionally-damped wide-band system is constructed by adding together the contributions coming from different resolution levels. The proposed method automatically adjusts the time-frequency resolution at each level and prevents time-domain aliasing problems associated with DFT schemes. In the applications, the transient vibration response of a finite beam is constructed by using a multi-voice Morlet wavelet frame. The effectiveness of the proposed technique is compared with the performance of the classical discrete Fourier transform (DFT) method. The study is concluded with a comprehensive discussion of the use of different wavelet basis, orthonormality and frames.

To my wife Şebnem, for her love and friendship,

and

to my father, for initiating my interest in science.

I a

agement a

and fun-

at MSU.

I w

J. R. L

Engineer

part of the

involvem

experience

I wo

for all the

mental set

ACKNOWLEDGMENTS

I am sincerely gratefull to Dr. A. G. Haddow for his understanding, encouragement and support through out this research project. His friendship, hospitality and fun-loving personality has been a great inspiration during my graduate study at MSU.

I would like to express my appreciation to Professors R. C. Rosenberg and J. R. Lloyd who tried hard to establish a positive atmosphere in the Mechanical Engineering Department for all the graduate students, and provided an important part of the financial support through teaching assistantships during my study. My involvement in the teaching of Vibrations Laboratory sections has been a joyfull experience for me.

I would like to thank our expert mechanics Robert Rose and Leonard Eisele for all their valuable suggestions and assistance during the preparation of experimental setups.

TABLE OF CONTENTS

Table

6.1 Th
sta

6.2. Th
ma
2^{13}

LIST OF TABLES

LIST OF FIGURES

λ_f

ϵ_f

Δ_t

Δ_w

ρ

η

σ_{ij}

τ_{ij}

ϕ

Λ

A

A

A_{ij}

B

B_{ijk}

c

c_f

c_p

f

LIST OF SYMBOLS

ω	circular frequency
ω_c	center frequency of the Morlet wavelet
λ_j	$(j = 1, 2, ...)$, eigenvalues
δ_f	sampling interval in the frequency domain
Δ_t	RMS duration of a signal
Δ_ω	RMS bandwidth of a signal
ρ	material density of the beam
η	material loss factor of the beam
$\phi(t)$	scaling function
$\psi(t)$	wavelet function
φ	angular velocity
$\mathbf{\Lambda}$	Jordan canonical form of system matrix
A	cross sectional area of the beam
$\mathbf{A}$	system matrix
$\mathbf{A}_{0,L}$	matrices for the boundaries at $x = 0, L$
B	complex bending stiffness
B_{3dB}	3dB bandwidth
c	speed of sound in the fluid
c_g	group velocity
c_p	phase velocity
$\mathbf{f}$	vector of external forces

f_c

F_t

F_v

f_w

E

G

H

I

I

k_p

M

M

p

Q

SWT

TFR

TSR

T_{max}

T_n

T_s

V

v

v_j

z

z

f_c	center frequency
$F_0(\omega)$	amplitude of the point force
F_{max}	spectral range of a signal
f_n	natural frequency
E	Young's modulus
$G(\omega)$	high-pass filter
$H(\omega)$	low-pass filter
I	moment of inertia of the plate
$\mathcal{I}$	time-averaged power flow
k_p	propagation constant of the plate
M	bending moment
M	Modal Matrix
p	acoustic pressure
Q	shear force
SWR	space-wavenumber representation
TFR	time-frequency representation
TSR	time-scale representation
T_{max}	total duration of a signal
T_R	period of reconstitution
$\mathbf{T}_x$	field transfer matrix
V	plate transverse velocity
v	state vector
v_j	$(j = 1, ..., 6)$ state variables
x	space coordinate along the length of the beam
z	phase-variable canonical state vector

CHAPTER 1

INTRODUCTION

1.1 Motivation and Objectives

Over the last century, the Fourier transform has demonstrated an unmatched compatibility and efficiency in the analysis of stationary periodic signals. In the meantime, ongoing progress in signal processing and information theory has introduced new time-frequency representation techniques for the analysis of nonstationary transient signals [29,69,116]. In particular, recently there have been both intense research activity and major developments in the mathematical theory of wavelets [14,24,36,43,95]. It is the objective of this thesis to built upon these recent developments and explore their aplicability in mechanical sciences.

The motivation for this study comes from the need to have a better understanding and more accurate prediction of complex transient vibration response of vibro-acoustic systems. The analysis of transient vibration signals may be undertaken for different purposes, such as machine monitoring, fault detection, system identification and active control. A transient vibration or acoustic signal generated by a physical system may carry substantial amount of information about the governing dynamic phenomena. Therefore, during the analysis, the major task is the extraction and interpretation of the relevant information. On the other hand, an accurate prediction of a transient response of a system can help with the design and performance of engineering structures and machinery components. Hence there are two main objectives in this study. The first is the incorporation of the wavelet transform to the analysis of transient wave propagation in dispersive and non-dispersive mediums, and the second is to achieve a more efficient and accurate synthesis scheme for prediction of transient vibration response of linear time-invariant systems by using spectral-partitioning and frame-decomposition concepts.

1.2 Transient Vibration Analysis of Mechanical Systems

For almost two centuries, Fourier analysis has been used as a major mathematical tool in the study of vibro-acoustic systems. Since the eigenfunctions of the derivative operator are complex exponentials ($d(e^{i\omega_n t})/dt = i\omega_n e^{i\omega_n t}$), the solution of the most fundamental differential equations are given as a linear combination of harmonic functions, in terms of sines and cosines. The nonlocal characteristics of the sine-cosine basis makes Fourier transform a one-dimensional analysis tool, such that the information contained in a signal is represented either in time or frequency domains, but not simultanously in both.

In addition to the Fourier transform, the analysis of vibro-acoustic systems has been carried out by employing other statistical measures and transform techniques, such as autocorrelation, cross-correlational, cross-spectrum, cepstrum, coherence, cross-bispectral analysis and Hilbert transform. Although these techniques and the Fourier transform have proved to be very effective tools in the analysis of stationary periodic signals, in essence none of them are designed to give local spectral representations. Therefore, a different analysis tool is needed to study time evolution of the spectrum in nonstationary signals.

Practically, a signal is refered to as nonstationary when the statistical characteristics of the signal depend on the time interval that is being considered. Our daily lives are full of examples of nonstationary transient signals, and there are particular ones that are generated by some vibro-acoustic phenomena. A piece of chalk squeaking on a blackboard, the thunder following a flash of lightning, an automobile passing over bumps, the vibrations of an airplane during touchdown, arrhythmic heart beat of a patient and the sound generated from our speech are all examples of physical processes that generate some form of nonstationary signal. In particular, mechanical systems are very rich sources of transient processes, such as the startup of an engine, meshing between worn gears, a shaft rotating in a damaged bearing, a piston slapping on a cylinder wall, a tool chattering during

a cutting operation, ignition and burning of fuel, onset of cavitation, blade-vortex interactions and impact between loose components. These processes are all capable of generating some form of transient signal that carries information about the characteristics of the governing physical phenomena. The property that is common to all of the above transient vibration phenomena is the time dependent nature of the information transmitted to the outside world.

1.3 Time-Frequency and Time-Scale Representations

In nonstationary signals, the time evolution of the spectrum is an important part of the information carried by the signal. A classical example is a musical score, where the notes on each line (or space) define the local musical spectrum and the type of note represents the duration (count). When notes or chords on each scale are played successively over time then the resulting (synthesized) signal is interpreted by the human ear as a harmonious melody. Similar to a musical score, the entire information transmitted from a vibrating machine component can be broken down into smaller pieces and represented by time-frequency information cells to ease the interpretation of the governing phenomena. As a result, the original one-dimensional signal is transformed into a two-dimensional time-frequency representation (TFR). Alternatively, if the signal is space dependent, then the transformation results in a space-wavenumber representation (SWR).

A time-frequency representation reveals the temporal localization of a signal's spectral components. Different mathematical methods have been developed to generate a TFR from a nonstationary signal. A comprehensive list of the existing TFR techniques can be found in the seperate reviews by Cohen [29] and Hlawatsch and Boudreaux-Bartels [69]. The classification of TFRs is usually made according to linear, quadratic and nonlinear-nonquadratic properties. The group of linear TFRs includes Gabor, STFT and wavelet transforms. Some of the well-known quadratic TFRs are the ambiguity function, Bertrand, Born-Jordan, Choi-Williams, Wigner-Ville and Rihaczek distributions. As an example

of no
tribu
given

tation-
to tra
time-f
sient v
Fourier
shells.
tion W
tures. E
short-co
principle
resolutio
this stud
ble of pr
hand. Wi
that make
and may
comparis
and the s
effective t
[36.51.35.1
dispersive
lar fundam
an effective
in time and

of nonlinear-nonquadratic TFRs, radially-Gaussian and Cohen's nonnegative distributions can be listed. The definitions and the properties of these TFRs are given in [29,69].

In this study, attention is focused on the linear time-frequency representations, and in particular to the application of STFT and wavelet transforms to transient wave propagation phenomena. Some of the linear and quadratic time-frequency representations have been already used in the analysis of transient vibration signals. For example, Hodges *et al.* [70] applied the Short-Time Fourier Transform (STFT) to the analysis of transient vibrations in cylindrical shells. In an analytical study, Wahl and Bolton [131] applied Wigner Distribution (WD) to the identification of dispersive and non-dispersive waves in structures. Both of these time-frequency representation techniques have well-known short-comings. STFT has a time-frequency resolution problem. The uncertainty principle, $\Delta_t \Delta_\omega \geq 1/2$, imposes a trade off between the time and the frequency resolutions [14,23,29,42,60,69,100]. As demonstrated by the examples given in this study, the constant window structure employed by the STFT is not capable of providing sufficient resolution over a wide spectral range. On the other hand, Wigner distribution, due to its quadratic structure, generates cross terms that make the interpretation of the associated physical phenomena quite difficult and may require further processing to yield valuable information [29,69,131]. In comparison to these techniques, the wavelet transform, endowed with the linearity and the self-adjusting window structure, may prove to be a more versatile and effective tool for the analysis of transient vibration signals in certain applications [36,51,95,104,105]. Particularly in the analysis of transient wave propagation in a dispersive medium, the physical phenomena and the analysis tool both have similar fundamental properties. Therefore, the wavelet transform is expected to yield an effective representation for the spectral evolution of the wave components both in time and space coordinates [104].

1.4 Literature on Wavelets, STFT and Gabor Transform

In recent years, considerable developments have been achieved on concepts and theories related to STFT, wavelets, frames and multi-resolution analysis. Since the antecedents of the present linear time-frequency representation techniques date back to the beginning of the 18th century, a complete historical account of the subject is beyond the scope of this study. Therefore, in the following, only some of the selected references will be reviewed to relate the present work to its antecedents. More detailed historical review of the subject and additional references can be found in [14,43,69,94,96,116].

The beginning of the research on harmonic analysis dates back to 1807, when Fourier solved the heat equation by representing a function as a sum of weighted sine-cosine components. Since then, the Fourier transform has developed into a powerfull mathematical tool that is now being used for many different purposes; such as the solution of differential equations, spectral decomposition of signals and analysis of linear time-invariant systems. In the future, in spite of the other developments in the signal processing technology, Fourier analysis will continue to be the basic tool and perhaps applied more widely in the engineering sciences.

In essence, Fourier analysis decomposes a finite energy signal into its sine and cosine components. Therefore, the standard Fourier analysis is not very effective in representation of local information contained in nonstationary signals, such as speech, seismic acceleration or sonar signals. In order to represent the time-evolution of the spectral components, the time-domain and frequency-domain concepts need to be combined into a single framework. In 1946, Gabor [60] introduced a Gaussian weighting window that is translated along the signal while recording the spectrum at succesive time intervals. This process resulted in a two dimensional representation of the signal on the time-frequency plane. The remarkable fact about the Gaussian function is that it provides an optimal localization in the

time-frequency domain. Following Gabor's classical study, the use of other sliding-window functions led the way to the definition of the short-time Fourier transform (STFT). Since Gabor's classical work, STFT has gone through much development and have been applied in many different areas of physical sciences. The details and the properties of STFT can be found in references [2,9,10,61,69,76,103,112]. As stated earlier, the major limitation of the STFT is imposed by the uncertainty principle, $\Delta_t \Delta_\omega \geq 1/2$, which requires a trade-off between the time and frequency resolutions. Therefore, once the window size is selected the resolution is fixed throughout the time-frequency plane.

In comparison to STFT, the self-adjusting window (zooming) property of the wavelet transform brought efficiency into linear time-frequency analysis. The recent excitement in wavelet research was initiated by a geophysical application conducted by Morlet *et al.* [100,101]. As an alternative to Gabor's constant-window decomposition, Morlet suggested the use of constant-Q (quality factor) wavelets in exploring the propagation of a plane wave through a multilayered medium. The success of Morlet's application of wavelets led to more detailed mathematical studies on the subject. Theoretical physicist Grossman associated the wavelet transform to square integrable group representations [64,65]. Since similar ideas and wavelet-like constructions had been already known to mathematicians, it did not take long before a comprehensive mathematical theory was presented by Meyer [94]. The connections between the recent developments on wavelets and the related earlier mathematical studies are reviewed in the references [14,42,94,115,116,124].

The new developments in the wavelet theory caught the attention of the signal processing community and initiated intense research in all the related aspects of the subject. The original wavelet used in Morlet's study did not attract much attention from the signal processing community, since it had a noncompact support and thus made the real-time implementation of the corresponding finite-impulse response (FIR) filter quite difficult. Therefore, Daubechies's [39] construction of the orthonormal basis of compactly supported wavelets was considered a breakthrough and opened the way to a wide field of applications. The

wavelet transform provided the means for looking at a signal at different scales or details. Therefore, wavelets found immediate use in image processing applications and stimulated Mallat's studies [82-85] that established connections between wavelets and multiresolution analysis (MRA).

Meanwhile, there were other important contributions to the theory of wavelets. Battle [11-13] used renormalization group ideas to construct orthonormal wavelets. Frazier and Jawerth [54-58] introduced the ϕ-transform and developed the concept to serve efficiently in signal processing applications. The connection between the spline theory and wavelets is established by Chui [23-27]. Coifman [32-34], Beylkin [17-20] and Wickerhauser [132] developed the theory on atomic decompositions and introduced fast algorithms based on wave packets and best-basis selection routines. These entropy based algorithms were used primarily for compression of acoustic signals and two-dimensional gray scale images. Alpert [3-5] considered the use of wavelets to achieve fast matrix operations and studied the representation of integral operators with wavelets. The concept of frames introduced by Duffin and Schaeffer [48] was tied to the wavelet theory in the studies of Heil and Walnut [68], Daubechies [38, 41-43] and Benedetto [15-16]. The filter bank structure induced by a wavelet and its corresponding scaling function are linked to the quadrature mirror filters by Vetterli and Herley [129].

Unlike the sine-cosine basis used in Fourier transform, the function used to generate a wavelet basis may take a variety of forms, provided that a certain admissibility condition is satisfied as discussed later in section 2.2. Therefore, the question of which wavelet to use comes about frequently in applications. The optimal choice in signal processing applications depends on the regularity and the size of the FIR filter [116,126]. The filter coefficients for compactly supported wavelets are obtained at different regularity conditions by Daubechies [42,43]. The algorithms performing the continuous and the discrete wavelet transforms can be found in the studies conducted by Holschneider [71], Dutilleux [50] Rioul and Duhamel [118] and Shensa [123].

cal

thro

diff

Toda

wave

engi

tech

1.5 M

of the

the re

classi

contin

line (–

space c

The inn

where ov

the inner

The ongoing excitement in wavelet research has been due to the historical collaboration between scientists from different disciplines. The recent breakthrough in wavelet research is the natural outcome of evolution and blending of different concepts and theories that were introduced in diverse fields of science. Today, while mathematicians are trying to discover new interesting features of wavelets, applications of the wavelet theory are being investigated in physical and engineering sciences. In this study, the application of the wavelet theory is extended to the analysis of transient vibrations in mechanical systems.

1.5 Mathematical Preliminaries

In the following, a mathematical background is formed by reviewing some of the preliminary concepts, definitions and notations that are used frequently in the rest of this study. The details of the following definitions can be found in any classical textbook on real and complex analysis, such as [75,119,121].

A finite energy signal or a function $f \in L^2(\mathbf{R})$ is required to be piecewise continuous and square integrable in Lebesque sense. The space $\mathbf{R}$ implies the real line $(-\infty, \infty)$. The space $\mathbf{Z}$ consists of all the positive and negative integers. The space of all square-summable sequences $\{c_n\}$ are denoted by $\ell^2(\mathbf{Z})$.

The norm associated with the Hilbert space $L^2(\mathbf{R})$ is defined as

$$\|f\|_{L^2} = \left[\int_{-\infty}^{\infty} |f(t)|^2 \, dt \right]^{1/2} \tag{1.1}$$

The inner product of two functions $f, h \in L^2(\mathbf{R})$ is defined as

$$\langle f, h \rangle = \int_{-\infty}^{\infty} f(t) \, \overline{h(t)} \, dt \tag{1.2}$$

where overbar denotes complex conjugation. The relation between the norm and the inner product is given by $\|f\|^2 = \langle f, f \rangle$.

H_1 –

for f_1

where f

ture. th

correpor

capital

the imp

basis i

where

Evaluating t

If a bounded linear operator F maps one Hilbert space to another, $F : H_1 \longrightarrow H_2$, then the adjoint operator F^* is defined as $F^* : H_2 \longrightarrow H_1$ such that

$$\langle f_1, F^* f_2 \rangle = \langle F f_1, f_2 \rangle \tag{1.3}$$

for $f_1 \in H_1$ and $f_2 \in H_2$. If $F^* = F$ then F is called self adjoint.

The Fourier transform and its inverse are defined as

$$\begin{aligned} \widehat{f}(\omega) &= \frac{1}{\sqrt{2\pi}} \int_{-\infty}^{\infty} f(t)\, e^{-i\omega t}\, dt\,, \\ f(t) &= \frac{1}{\sqrt{2\pi}} \int_{-\infty}^{\infty} \widehat{f}(\omega)\, e^{i\omega t}\, d\omega \end{aligned} \tag{1.4}$$

where f and $\widehat{f}$ are assumed to be absolutely integrable. In engineering literature, the Fourier transform $\widehat{f}$ is denoted sometimes by the capital letter of the correponding function, such as F. In this study, both notations, the hat and the capital letter, will be used interchangeably without causing confusion. Some of the important properties of the Fourier transform are listed in Appendix A.

A family of functions $\psi_{mn} \in L^2(\mathbf{R})$, with $m, n \in \mathbf{Z}$, forms an orthonormal basis in $L^2(\mathbf{R})$, provided that

$$\langle \psi_{mn}, \psi_{jk} \rangle = \delta_{mn} \delta_{jk}, \qquad j, k, m, n \in \mathbf{Z} \tag{1.5}$$

where the Kronecker delta is defined by $\delta_{mn} = 1$ if $m = n$ and $\delta_{mn} = 0$ otherwise.

For a finite sequence $x(n)$, $n = 0, ..., (N-1)$, the z-transform is defined by

$$X(z) = \sum_{n=0}^{N-1} x(n)\, z^{-n}\,. \tag{1.6}$$

Evaluating the z-transform on the unit circle, $z = e^{i\omega}$, gives

$$X(e^{i\omega}) = \sum_{n=0}^{N-1} x(n)\, e^{-i\omega n}\,. \tag{1.7}$$

Then, the discrete Fourier transform (DFT) is defined by dividing the frequency range $[0, 2\pi]$ into N intervals

$$X(k) = \sum_{n=0}^{N-1} x(n)\, e^{-ink(2\pi/N)}\,, \qquad k = 0, 1, ..., (N-1)\,. \tag{1.8}$$

The preceding equation forms the basis for the construction of FFT algorithms used in applications.

1.6 Organization of the Dissertation

Following the preceding general introduction and the survey of literature, the second chapter establishes a background on the fundamental properties of linear time-frequency representation (TFR) techniques. Particular attention is given to the recent developments in the wavelet theory that are pertinent to this research. A summary of the basic mathematical concepts and definitions is followed by a detailed discussion of the algorithms used during the implementations. The basic features of the STFT and the wavelet transform are demonstrated on synthetic signals.

In Chapters 3 and 4, the STFT and wavelet transforms are utilized during the analysis of transient waves propagating in dispersive and nondispersive mediums. As an example of a dispersive medium, the bending vibrations of a beam is considered. The TFRs of the transient vibration response are analyzed to characterize the dispersion, reflection and the cut-off phenomena. The closed form analytical solution of an infinite beam is used to introduce a space-wavenumber representation (SWR). The use of a wavelet transform leads to the discovery of an interesting pulse reconstitution phenomenon on a free-free beam. As an example of a nondispersive medium, acoustic wave propagation in an open-ended pipe is considered and the signature of the echos are analyzed by using TFRs.

Chapters 5 and 6 are devoted to the development of a synthesis scheme for the prediction of the transient vibration response. Chapter 5 presents the

fundamental concepts and relationships governing the wavelet frame expansion of the convolution integral. The analytical construction leads to the introduction of wavelet response functions. Then, in Chapter 6, the developed synthesis scheme is used to predict the transient response of a beam. It is shown that the time-domain aliasing problems associated with an FFT construction scheme are eliminated by this wavelet frame synthesis technique.

In Chapter 7, some of the secondary issues that are raised during the main text are discussed in detail. The bandwidth of the Morlet filter is changed to study the effect on the resolution of the wavelet transforms. The implementation of different wavelet basis is investigated by considering a reference signal. The study is concluded with a comprehensive discussion of the use of the wavelet transform in other applications in mechanical sciences.

ical c

TFR

focus

some

sic pr

benc

2.1 In

variati

domai

Deper

quadra

the sh

to time

T

basis use

a fixed-w

frequency

ated by the

wavelet tra

CHAPTER 2

LINEAR TIME-FREQUENCY REPRESENTATIONS

The objective of this chapter is to introduce some of the basic mathematical concepts, definitions and properties of linear time-frequency representations (TFRs). Due to its relatively new appearance in mechanical sciences, attention is focused on the wavelet transform. In order to give a self-contained presentation, some of the fundamental concepts and algorithms are explained in detail. The basic properties of the STFT and wavelet transform are demonstrated by considering benchmark synthetic signals.

2.1 Introduction

Time-frequency representations characterize local spectral and temporal variations in a signal. The transformation of a signal into the time-frequency domain is performed by applying a specific mathematical operation on the signal. Depending on the properties of this operation, the transformation may be linear, quadratic or nonlinear [29,69,116]. Within the group of linear transformations, the short-time Fourier transform (STFT) and the wavelet transform (WT) lead to time-frequency and time-scale representations, respectively.

The properties of a linear transformation depend on the structure of the basis used during the decomposition. The STFT and Gabor transforms employ a fixed-window sine-cosine basis, which imposes certain restrictions on the time-frequency resolutions. Whereas, the basis used in the wavelet transform is generated by the dilations and translations of a basic wavelet function. As a result, the wavelet transform has a very desirable self-adjusting window structure and a large

lass

f th

.2 S

.2.1

ı ent

v th a

i ner

w ere

tr nsfor

w l-loca

th time

of he F

we l-suit

In

of pectra

is l nown

by sing a

spe trum

tati n of t

of th e sign

class of admissible basis functions. The mathematical definitions and properties of these linear transform techniques are explained further in the following.

2.2 STFT, Gabor and Wavelet Transforms

2.2.1 Mathematical Background

From a mathematical perspective, the linear integral transforms that are mentioned above can be viewed as an inner product of a signal or a function f with a specific set of functions. For example, in the case of Fourier transform, the inner product representation becomes

$$(\mathcal{F}\, f)(\omega) = \langle f,\, h\rangle \;=\; \int_{-\infty}^{\infty} f(t)\,\overline{h(t)}\,dt \qquad h(t) = e^{i\omega t} \tag{2.1}$$

where the overbar represents complex conjugation. In Fourier transform, the transformation kernel $h(t)$ is constructed from sine-cosine functions, which are well-localized in frequency but widely spread in time. The information regarding the time dependendence of the spectral components becomes buried in the phase of the Fourier transform. Therefore, it is fair to say that Fourier transform is not well-suited for the analysis of time-local spectrum.

In the analysis of nonstationary signals, a classical approach to localization of spectral evolutions is the use of a sliding-window spectrum of the signal, which is known as the Short-Time Fourier Transform (STFT). The STFT is performed by using a short-length window function. As the window is shifted in time, a new spectrum is defined at each position, thus generating a time-frequency representation of the signal. Again, the transformation can be viewed as an inner product of the signal f with a windowed sine-cosine basis as follows:

$$(\mathcal{G}_b\, f)(\omega) = \langle f,\, h_b\rangle \;=\; \int_{-\infty}^{\infty} f(t)\,\overline{h_b(t)}\,dt \qquad h_b(t) = g(t-b)\,e^{i\omega t} \tag{2.2}$$

where b defines the translation of the window function $g(t)$. Since generally the window $g(t)$ is compactly supported or well-localized in time, its application on the sine-cosine functions generates a basis that has the desired localization properties. The selection of the window function is based on the anticipated time and frequency localization characteristics. Some of the commonly used STFT window functions are listed in Appendix B. The efficiency of the localization in the time-frequency plane is influenced by the width of the window function. However, as discussed later in this study, the window size can not be selected arbitrarily, but needs to satisfy the uncertainty inequality. The examples given later in this chapter may help to clarify some of the preceding concepts.

As a special case of the STFT, Gabor [60] has shown that the use of a Gaussian window will result in optimal time-frequency localization. Thus, the Gabor transform is defined as

$$\begin{aligned} (\mathcal{G}_b^\alpha f)(\omega) &= \langle f,\, h_b^\alpha \rangle \;=\; \int_{-\infty}^{\infty} f(t)\, \overline{h_b^\alpha(t)} dt \;, \\ h_b^\alpha(t) &= g_\alpha(t-b)\, e^{i\omega t}, \qquad\qquad g_\alpha(t) = \frac{1}{2\sqrt{\pi\alpha}}\, e^{-t^2/4\alpha} \;. \end{aligned} \tag{2.3}$$

The basic properties of the STFT applies equally to the Gabor transform. Therefore, in this study, the Gabor transform will be also refered to as an STFT.

In the case of wavelet transform, although a similar inner product operation is still employed in the definition, the form of the basis functions differs significantly. The continuous wavelet transform (CWT) of a signal $f \in L^2(\mathbf{R})$ with respect to a family of wavelets is defined as [14,23,36,43,94]

$$\begin{aligned} (\mathcal{W} f)(a,b) &= \langle f,\, h_{a,b} \rangle \;=\; \int_{-\infty}^{\infty} f(t)\, \overline{h_{a,b}(t)}\, dt \;, \\ h_{a,b}(t) &= |a|^{-\frac{1}{2}}\, h\left(\frac{t-b}{a}\right) \;, \qquad\qquad a, b \in \mathbf{R},\; a \neq 0 \;. \end{aligned} \tag{2.4}$$

The family of functions $h_{a,b}$ is generated from a single function h by performing dilation and translation operations, which are controlled by the parameters a and

b, respectively. The original function h is referred to as the "*basic wavelet*" or the "*mother wavelet*". The mother wavelet has to satisfy an admissibility condition that ensures the existance of an inverse wavelet transform. The admissibility condition is stated as

$$\int_{-\infty}^{\infty} |\omega|^{-1} \left|\widehat{h}(\omega)\right|^2 d\omega < \infty \tag{2.5}$$

where $\widehat{h} = (\mathcal{F}\, h)$ is the Fourier transform of the mother wavelet. The admissibility condition requires $\widehat{h}(0) = 0$, which implies

$$\int_{-\infty}^{\infty} h(t)dt = 0\,. \tag{2.6}$$

Therefore, the mother wavelet is expected to have some oscillations about the zero mean. Distinct families of wavelets can be generated by selecting different admissible $h(t)$ functions.

In applications, a sublattice is constructed by discretizing the dilation and translation parameters a and b. First, the constants a_0 and b_0 are assigned to the dilation and translation step sizes. Then, applying the definitions

$$a = a_0^m \qquad \text{and} \qquad b = nb_0a_0^m \tag{2.7}$$

with $m, n \in \mathbf{Z}$ to the relation given in equation (2.4) results in a discrete set of wavelets

$$h_{mn}(t) = a_0^{-m/2}\, h(a_0^{-m}t - nb_0)\,. \tag{2.8}$$

Since the translation parameter b is designed to depend on the dilation index, the time-frequency resolution of the wavelet is adjusted automatically at different scales. The width of the time-frequency window becomes smaller at higher scales and elongates at lower frequencies. This self-adjusting window property is the major difference between the wavelet transform and STFT.

For example, considering $n = 0$, larger values of m generate oscillating functions h_{m0} which are spread out in time. The examples shown in Figure 2.1

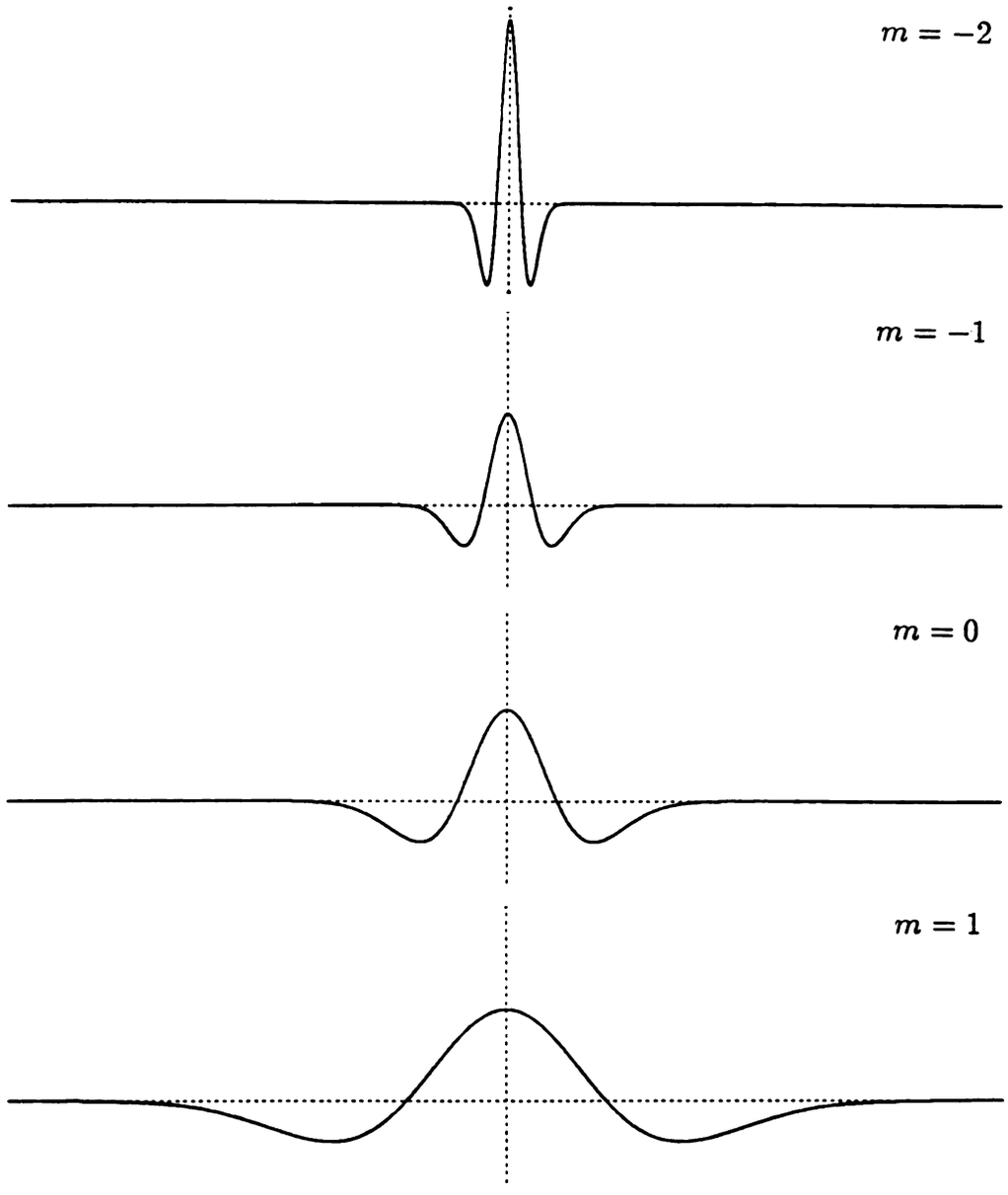

Figure 2.1 The Mexican hat wavelet and its dilations in the time domain.

Figur 2.2

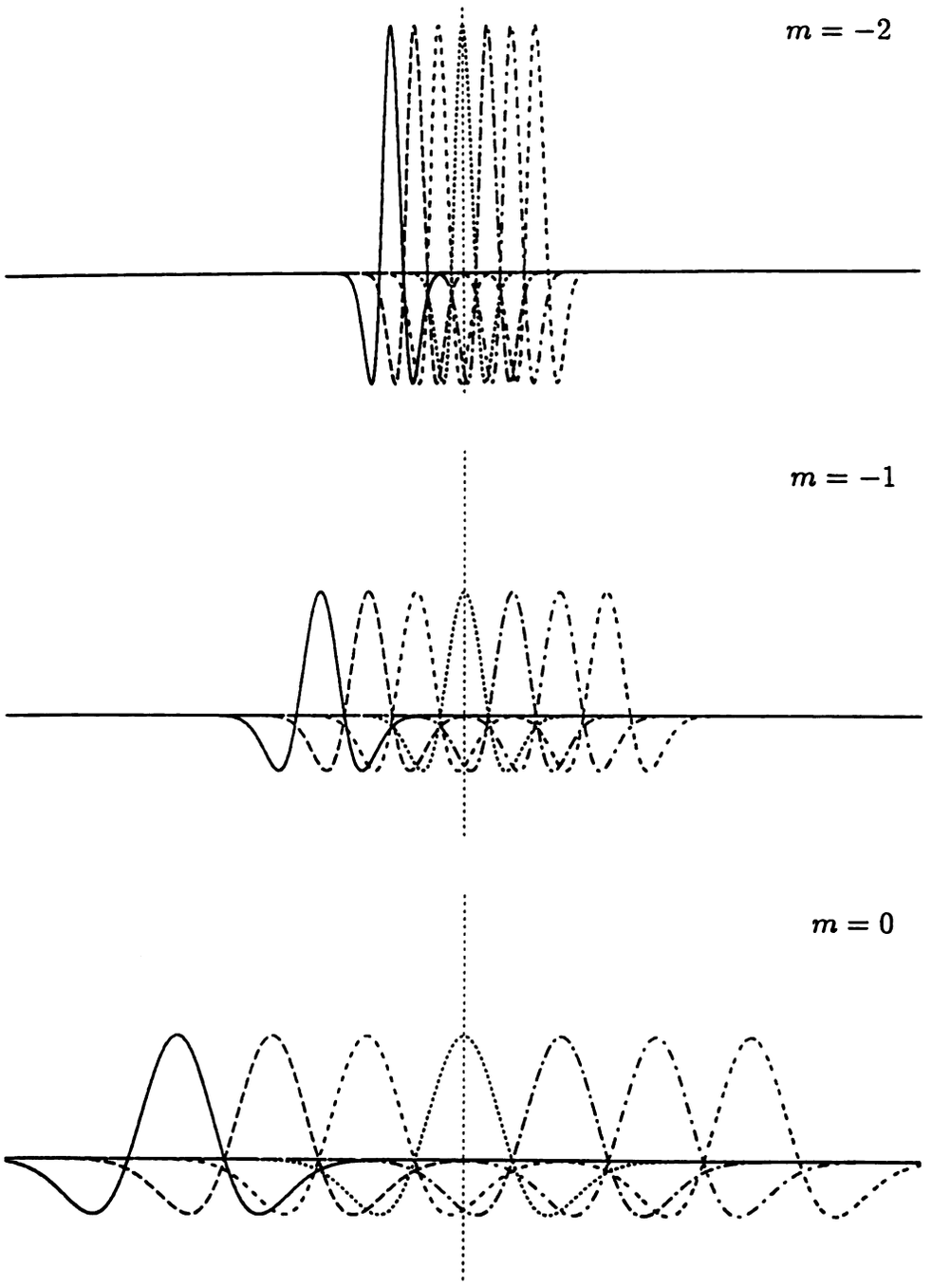

Figure 2.2 The translation of the Mexican hat wavelet at different scales. The translations are from left to right $n = -6, -4, -2, 0, 2, 4, 6$.

are generated by using the Mexican hat wavelet, which is defined later in section 2.3.2.1. Since at low frequencies it would take longer time to see a change in the information content of the signal, the redundancy during the sampling of the signal is automatically avoided by the larger translation step size of the wavelet, as demonstrated in Figure 2.2. Whereas, for large negative values of m, a shrunken version of the mother wavelet gives a higher resolution, which is more appropriate for representation of high frequency variations in a signal. This self-adjusting resolution (zooming) property of the wavelet transform is analogous to the operational principles of a microscope or a telescope. The detail of the information at different levels of magnification or scale is analyzed with an adequate resolution. The benefit of the zooming property is that the wavelet transform has a relatively more efficient coverage of the time-frequency plane.

2.2.2 Time-Frequency Space Coverage

The main difference between the STFT and the Wavelet transform is in their coverage of the time-frequency plane. As sketched in Figure 2.3, STFT maintains a constant window size throughout the transformation plane, whereas the window size is automatically adjusted in the wavelet transform. For higher frequencies the time-width is contracted and for lower frequencies it is dilated. This zooming property of the wavelet transform is utilized in many different signal processing applications.

By looking at the time-frequency coverage of the STFT, it is natural to wonder if the size of the basic window element can be made smaller to achieve better localization characteristics. Unfortunately, the answer is negative. The uncertainty principle sets a lower bound on the time-frequency window size of the STFT, which is discussed in the following.

2.2.3 Time-Frequency Resolution and the Uncertainty Principle

Consider a finite energy signal $f \in L^2(\mathbf{R})$ and its Fourier transform $\widehat{f}$. Then, in the time domain, the center and radius of the signal are defined, respec-

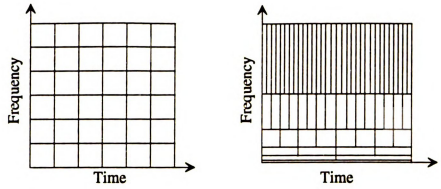

a) STFT b) Wavelet Transform

Figure 2.3 Time-frequency space coverage of the STFT and Wavelet transform.

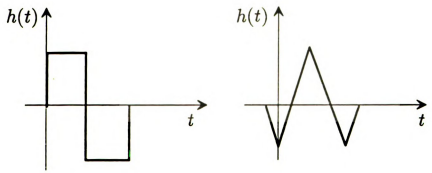

a) Haar Wavelet b) Spline Wavelet

Figure 2.4 Two classical examples on wavelet functions.

tively, as [23,60,69]

$$t_c = \frac{1}{\|f\|_{L^2}^2} \int_{-\infty}^{\infty} t\,|f(t)|^2\,dt$$
$$\Delta_f = \frac{1}{\|f\|_{L^2}} \left\{ \int_{-\infty}^{\infty} (t - t_c)^2 |f(t)|^2\,dt \right\}^{1/2} \tag{2.9}$$

Similarly, in the frequency domain, the corresponding center and radius becomes

$$\omega_c = \frac{1}{\|\widehat{f}\|_{L^2}^2} \int_{-\infty}^{\infty} \omega^2\,|\widehat{f}(\omega)|^2\,d\omega$$
$$\Delta_{\widehat{f}} = \frac{1}{\|\widehat{f}\|_{L^2}} \left\{ \int_{-\infty}^{\infty} (\omega - \omega_c)^2 |\widehat{f}(\omega)|^2\,d\omega \right\}^{1/2} \tag{2.10}$$

In the engineering literature, $2\Delta_f$ and $2\Delta_{\widehat{f}}$ are referred to as the RMS duration and the RMS bandwidth of the signal, repectively.

Based on the preceding definitions, the uncertainty principle states that

$$\Delta_f\,\Delta_{\widehat{f}} \geq \frac{1}{2} \tag{2.11}$$

The proof for this inequality is provided in Appendix C. The fundamental concept behind the uncertainty principle is that a function f cannot have arbitrarily small duration Δ_f and bandwidth $\Delta_{\widehat{f}}$ about the centers in time t_c and frequency ω_c, respectively. The uncertainty principle imposes a limit on the choice of the window size.

The uncertainty inequality becomes an equality only for the modulated Gausian function;

$$f(t) = \frac{1}{2\sqrt{\pi\alpha}}\, e^{-i\omega t}\, e^{-t^2/(4\alpha)} \tag{2.12}$$

which results in an optimal localization in the time-frequency plane.

2.3 Wavelet Families; Definitions and Properties

As mentioned earlier, any function that satisfies the admissibility condition can be used as a mother wavelet. Some of the important properties that are considered during the selection of a wavelet are the compactness (support), orthogonality, regularity (smoothness) and the spectral decay characteristics. The following examples are intended to give a taste of different wavelet families. The list is in no way exhaustive, and one can find many other examples listed in the literature [7,11,14,23,36,43,69,94,95,100,122].

2.3.1 Haar and Spline Wavelets

Although the Haar function has been known since 1910, its relation to wavelet theory and multi-resolution analysis has been brought to attention very recently. The Haar wavelet is defined as

$$h(t) = \begin{cases} 1, & 0 \le t < \frac{1}{2}, \\ 1, & \frac{1}{2} \le t < 1, \\ 0, & \text{otherwise.} \end{cases} \tag{2.13}$$

A sketch of the Haar wavelet is given in Figure 2.4a. Inspite of its simple construction, the Haar wavelet does not have a desirable time-frequency localization behavior, since $\widehat{h}(\omega) \propto |\omega|^{-1}$ as $\omega \longrightarrow \infty$. Therefore, the Haar function has been used generally for academical purposes to demonstrate the construction of an orthonormal wavelet basis in $L^2(\mathbf{R})$.

Another simple example is obtained by using the linear spline hat function,

$$\phi(t) = \begin{cases} t, & 0 \le t \le 1, \\ 2-t, & 1 \le t \le 2, \\ 0, & \text{otherwise.} \end{cases} \tag{2.14}$$

which is known as the scaling function and satisfies the dilation equation $\phi(t) = \sum c_k \phi(2t-k)$ with $c_k = 1/2, 1, 1/2$. Then, the equation $h(t) = \sum (-1)^k c_{1-k} \phi(2t-k)$ defines the first-order spline wavelet as

$$h(t) = -\frac{1}{2}\phi(2t+1) + \phi(2t) - \frac{1}{2}\phi(2t-1) \tag{2.15}$$

which is sketched in Figure 2.4b. One can increase the order of the spline function to achieve a higher number of continuous derivatives. These linear spline orthonormal wavelet bases were studied by Battle and Lemarie [11,43].

2.3.2 Derivatives of the Gaussian Function

The derivatives of the Gaussian function constitute another family of wavelets. The Gaussian function and its Fourier transform are defined as

$$g(t) = e^{(-t^2/2)} \qquad \stackrel{\mathcal{F}}{\longleftrightarrow} \qquad \widehat{g}(\omega) = e^{(-\omega^2/2)} \,. \tag{2.16}$$

Following the definition of the derivative operator, $D^n = d^n/dt^n$, $(n = 1, 2, ...)$, the first eight derivatives of the Gaussian function are obtained as follows:

$$\begin{aligned}
D^1 g(t) &= -t\, e^{(-t^2/2)} \\
D^2 g(t) &= (t^2 - 1)\, e^{(-t^2/2)} \\
D^3 g(t) &= -(t^2 - 3)\, t\, e^{(-t^2/2)} \\
D^4 g(t) &= (t^4 - 6t^2 + 3)\, e^{(-t^2/2)} \\
D^5 g(t) &= -(t^4 - 10t^2 + 15)\, t\, e^{(-t^2/2)} \\
D^6 g(t) &= (t^6 - 15t^4 + 45t^2 - 15)\, e^{(-t^2/2)} \\
D^7 g(t) &= -(t^6 - 21t^4 + 105t^2 - 105)\, t\, e^{(-t^2/2)} \\
D^8 g(t) &= (t^8 - 28t^6 + 210t^4 - 420t^2 + 105)\, e^{(-t^2/2)}
\end{aligned} \tag{2.17}$$

These functions are plotted in Figure 2.5. Note that the odd and even ordered derivatives generate odd and even functions, respectively. The functions become more oscillatory, as the order of the derivative is increased. For $n > 2$, the shape of the functions becomes very similar to the modulated Gaussian function $\exp(-ict - t^2/2)$, which is discussed in more detail later in this chapter.

The preceding derivatives of the Gaussian function are used to define a family of wavelets, given as

$$h(t) = C_n\, D^n g(t) \qquad \stackrel{\mathcal{F}}{\longleftrightarrow} \qquad \widehat{h}(\omega) = C_n\, (i\omega)^n\, \widehat{g}(\omega) \tag{2.18}$$

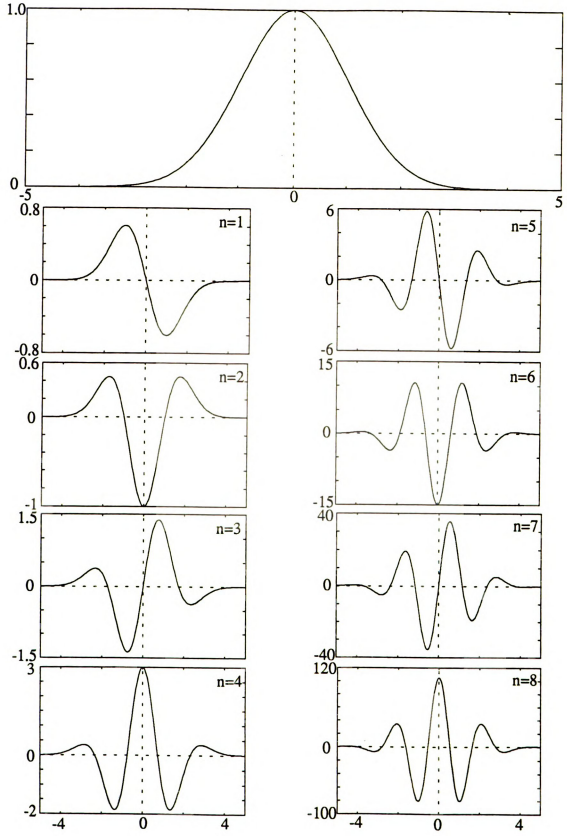

Figure 2.5 The Gaussian function and its derivatives, $D^n g = d^n g/dt^n$.

where $g(t)$ and $\widehat{g}(\omega)$ are defined in equation (2.16). The normalization constant C_n is obtained by applying the L^2-norm $\|\psi\|_{L^2} = 1$.

In order to derive a general relation for the normalization constant C_n, first we consider the equality between L^2-norms of the wavelet in the time and frequency domains

$$\|h\|_{L^2} = \left[\int |h(t)|^2\, dt\right]^{1/2} = \left[\int |\widehat{h}(\omega)|^2\, d\omega\right]^{1/2} = \|\widehat{h}\|_{L^2}\,.$$

Then, the evaluation of the second integral is performed as follows:

$$\begin{aligned}\int \left|C_n\,(i\omega)^n\, e^{(-\omega^2/2)}\right|^2 d\omega &= 2C_n^2 \int_0^\infty \omega^{2n}\, e^{-\omega^2}\, d\omega \\ &= C_n^2\, \frac{(2n-1)!!}{2^n}\,\sqrt{\pi}\,.\end{aligned}$$

Equating the norm on the right-hand side to unity and solving for the normalization constant gives

$$C_n = \pi^{-1/4}\left[\frac{2^{2n-1}\,(n-1)!}{(2n-1)!}\right]^{1/2}, \qquad n = 1, 2, \ldots\,. \tag{2.19}$$

The preceding result together with equation (2.18) define a general formula for the wavelets generated from the derivatives of the Gaussian. In the following examples, two particular cases are singled out from the above list and studied in more detail.

2.3.2.1 Example 1: Mexican Hat Wavelet

Following a sign change in the second derivative of the Gaussian, the Mexican hat wavelet and its Fourier transform are defined as [42]

$$h(t) = \frac{2}{\sqrt{3\sqrt{\pi}}}\,(1-t^2)\,e^{(-t^2/2)} \qquad \overset{\mathcal{F}}{\longleftrightarrow} \qquad \widehat{h}(\omega) = \frac{2}{\sqrt{3\sqrt{\pi}}}\,\omega^2\, e^{(-\omega^2/2)} \tag{2.20}$$

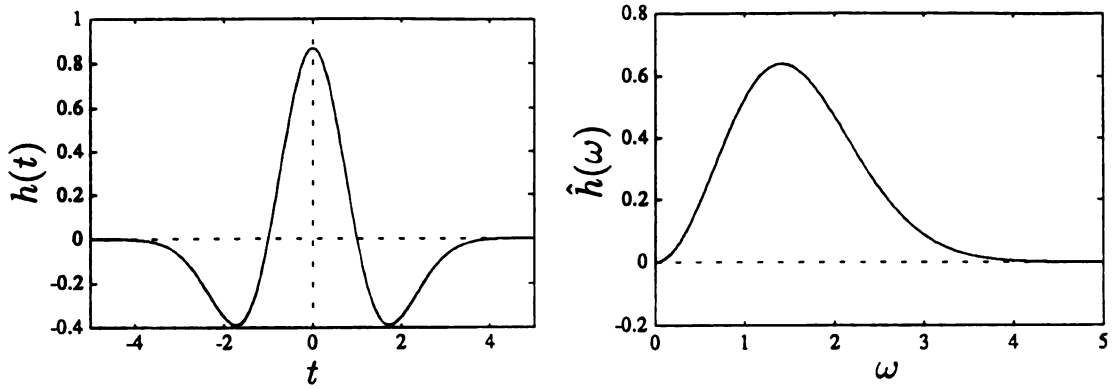

Figure 2.6 The Mexican hat wavelet and its Fourier transform.

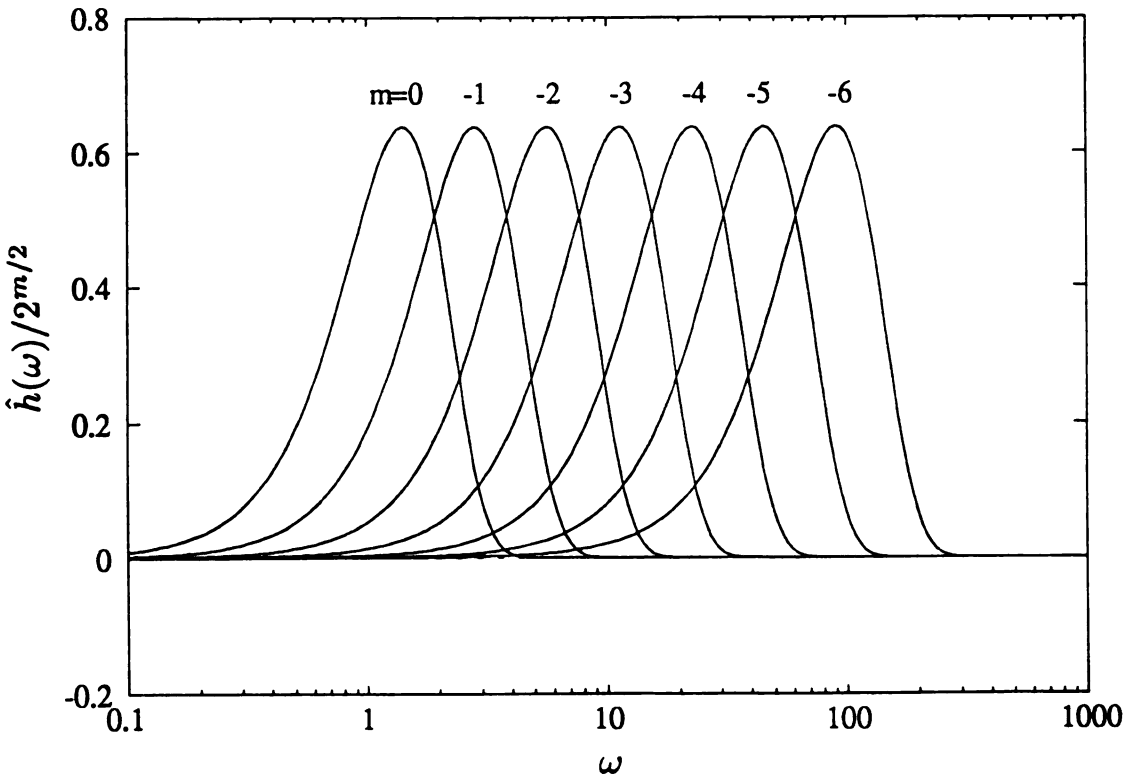

Figure 2.7 The filter bank structure induced by the Mexican hat wavelet.

where the normalization constant is determined by substituting $n = 2$ in equation (2.18). A sketch of the Mexican hat wavelet is given in Figure 2.6. From this mother wavelet, a family of wavelets h_{mn} are generated by using $a_0 = 2$ and $b_0 = 1$ in equations (2.7) and (2.8), which results in a dyadic grid with $a = 2^m$ and $b = n2^m$. The wavelets corresponding to this dyadic grid are defined by

$$h_{mn}(t) = \frac{2}{2^{m/2}\sqrt{3\sqrt{\pi}}} \left[1 - \left(\frac{t}{2^m} - n\right)^2\right] \exp\left[-\frac{1}{2}\left(\frac{t}{2^m} - n\right)^2\right], \qquad (2.21)$$

and their Fourier transforms become

$$\widehat{h}_{mn}(\omega) = 2\,\pi^{-\frac{1}{4}}\,(2^m/3)^{\frac{1}{2}}\,(\omega 2^m)^2\,e^{[-(\omega 2^m)^2/2]}\,e^{-in2^m\omega}\,. \qquad (2.22)$$

This set of discrete wavelet functions generate a bandpass filter bank structure, as shown in Figure 2.7. Since the bandwidth, $2\Delta_{\widehat{h}}$, of the wavelet bandpass filter is proportional to the center frequency ω_c, the quality factor $Q = \omega_c/2\Delta_{\widehat{h}}$, remains constant at each level of dilation. As a result, the wavelet transform is also known as a "constant-Q" analysis.

The four samples $\psi_{-2,0}, \psi_{-1,0}, \psi_{0,0}$ and $\psi_{1,0}$ from the above family of wavelets were plotted earlier in Figure 2.1. Note that, as the dilation index m gets larger, the wavelets spread out. Whereas, large negative m values generate shrunken versions of the mother wavelet which are used in representing high frequency components of a signal. Each distinct scale, or m value, generates a different resolution in translation. As shown in Figure 2.2, within a given interval, the wavelet $\psi_{-2,0}$ takes twice as many steps as its dilated version $\psi_{-1,0}$. This logarithmic adjustment of the translational resolution with respect to the dilation index results in a very effective "zooming" property of the wavelet.

2.3.2.2 Example 2: D8G Wavelet

Similar to the Mexican hat wavelet, the eighth derivative of the Gaussian is used to define the D8G wavelet as follows:

$$h(t) = \pi^{-1/4}\left(\frac{2^{15}\,7!}{15!}\right)^{1/2}(t^8 - 28t^6 + 210t^4 - 420t^2 + 105)\,e^{(-t^2/2)} \qquad (2.23)$$

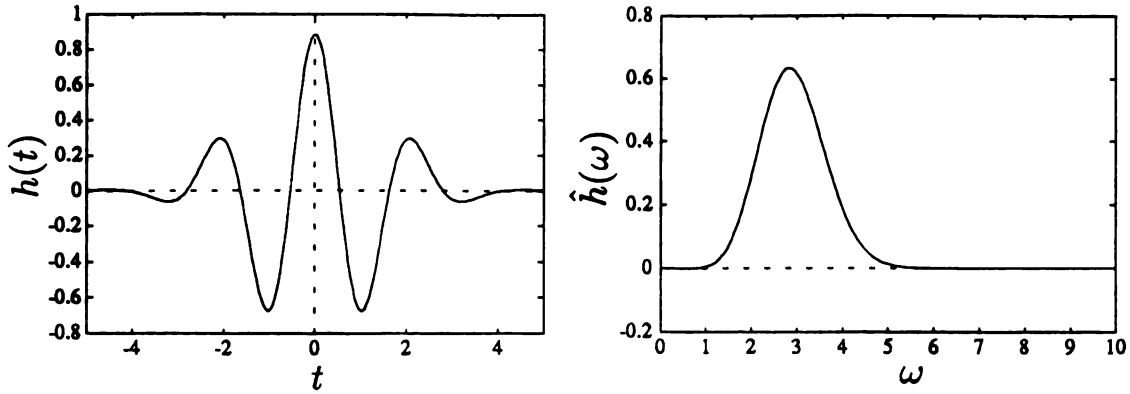

Figure 2.8 The D8G wavelet and its Fourier transform.

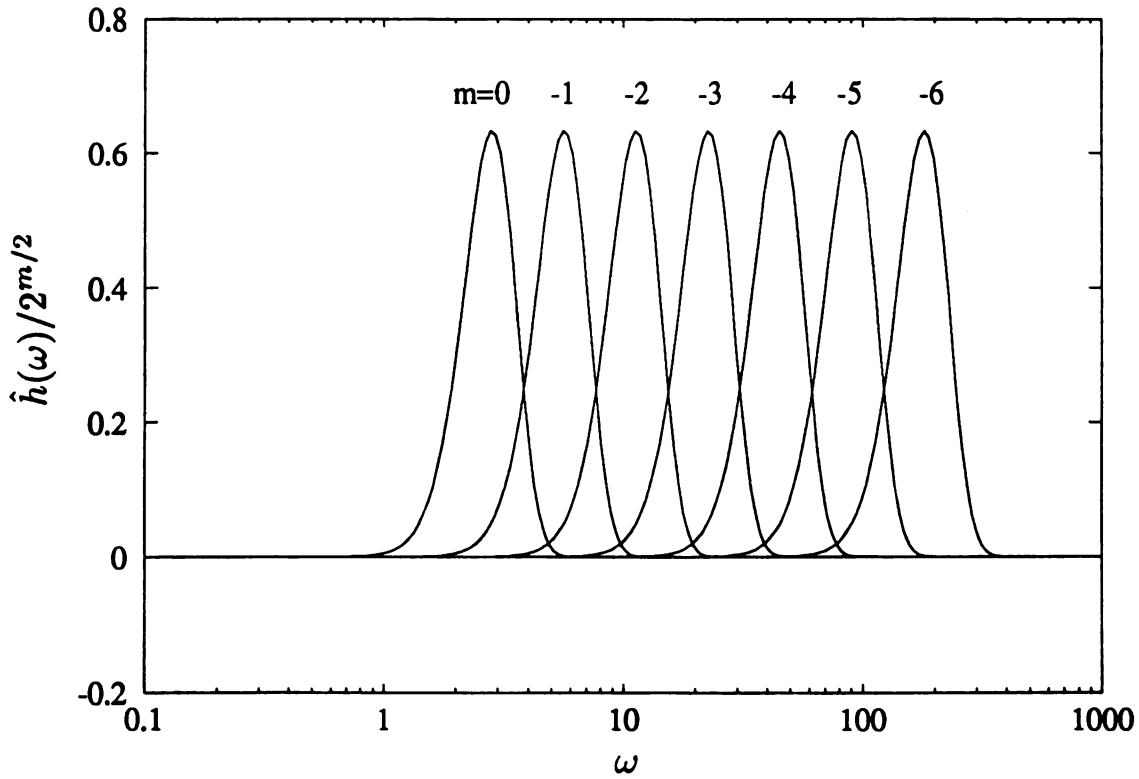

Figure 2.9 The filter bank structure induced by the D8G wavelet.

where again the normalization constant is determined by using $\|h\|_{L^2} = 1$. The Fourier transform of the D8G wavelet is obtained as

$$\widehat{h}(\omega) = \pi^{-1/4} \left(\frac{2^{15}\, 7!}{15!} \right)^{1/2} \omega^8 \, e^{(-\omega^2/2)} \, . \tag{2.24}$$

A plot of the D8G wavelet is provided in Figure 2.8. Since in comparison to the Mexican hat wavelet, the D8G contains more oscillations, the quality factor is relatively higher and the bandpass filter bank structure shown in Figure 2.9 demonstrates that feature.

2.3.2.3 Example 3: Complex DG Wavelets

In some applications, a complex wavelet with real and imaginary parts that are in quadrature is found to be very usefull. Since the order of the derivative causes alternating odd-even functions for the Gaussian wavelets, two successive derivatives can be combined to define a new complex wavelet given as

$$h(t) = C_n D^n g(t) + i C_{n+1} D^{n+1} g(t) \, . \tag{2.25}$$

As a result, the wavelet transform will also have real and imaginary parts. The advantage of such an odd-even real and imaginary parts is that the phase of the transform would display dicontinuities in the signal. This complex family of functions looks very similar to the modulated Gaussian wavelets discussed in the following.

2.3.3 Modulated Gaussian (Morlet) Wavelet

The modulated Gaussian wavelet became popular after Morlet [100,101] made extensive use of it in geophysical studies. The definition of the Morlet wavelet and its Fourier transform are given as follows:

$$\begin{aligned} h(t) &= \pi^{-1/4} \left(e^{-i\omega_c t} - e^{-\omega_c^2/2} \right) e^{-t^2/2} \\ \xleftrightarrow{\mathcal{F}} \quad \widehat{h}(\omega) &= \pi^{-1/4} \left[e^{-(\omega-\omega_c)^2/2} - e^{-\omega_c^2/2}\, e^{-\omega^2/2} \right] . \end{aligned} \tag{2.26}$$

The Fourier transform has a symmetric Gaussian distribution about the center frequency ω_c. As implied by equation (2.26), the center frequency ω_c defines the number of oscillations in the time domain as well as the bandwidth of the wavelet filter in the frequency domain. Depending on the application, different values are used for ω_c. One of the choices depends on the time-domain criteria of having a ratio of 1:2 between the highest peak and the neighbouring one [43] and results in $\omega_c = \pi\,[2/\ln 2]^{1/2} = 5.3364$, which is approximated in practice as $\omega_c = 5$.

Since in equation (2.26), the contribution coming from the second term is quite small, for relatively large values of ω_c, the simplified form of the Morlet wavelet and its Fourier transform become

$$h(t) = \pi^{-1/4}\, e^{-i\omega_c t}\, e^{-t^2/2} \qquad \stackrel{\mathcal{F}}{\longleftrightarrow} \qquad \widehat{h}(\omega) = \pi^{-1/4}\, e^{-(\omega_c-\omega)^2/2}\,. \tag{2.27}$$

The real and the imaginary parts of the Morlet wavelet and its Fourier transform are given in Figure 2.10. The filter bank structure generated by the Morlet wavelet is plotted in Figure 2.11.

In applications, the implementation of the Morlet wavelet can be performed by considering the Euler's formula $e^{i\theta} = \cos(\theta) + i\sin(\theta)$. Thus, the complex Morlet wavelet can be split into two seperate real wavelets as

$$h(t) = h_1(t) + i\,h_2(t) \tag{2.28}$$

where

$$h_1(t) = \pi^{-1/4}\,\cos(ct)\,e^{-t^2/2}, \qquad\qquad h_2(t) = -\pi^{-1/4}\,\sin(ct)\,e^{-t^2/2}\,.$$

As a result, the wavelet transform has real and imaginary parts, which is usually represented in magnitude and phase format.

2.3.4 Battle-Lemarié Wavelets

The Battle-Lemarie [11-13] cubic spline wavelets are known as very smooth wavelets and therefore they are called the "queen of wavelets". Battle-Lemarie

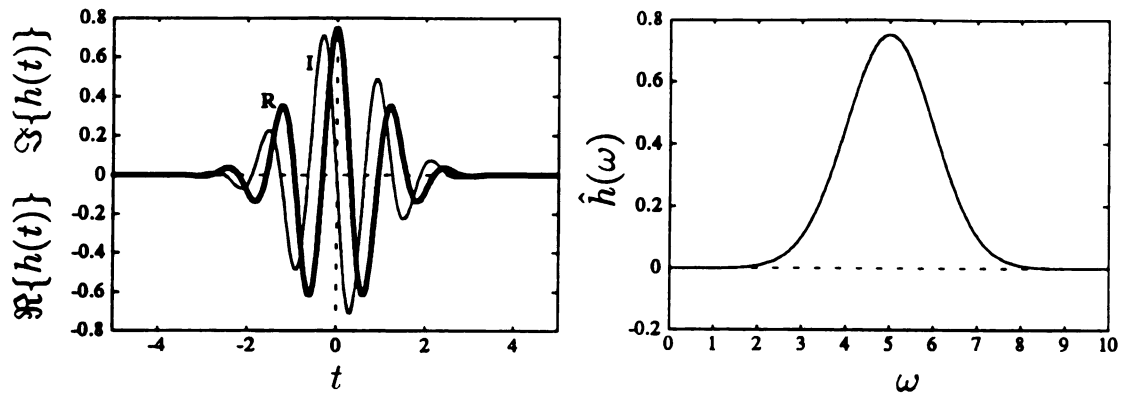

Figure 2.10 The Morlet wavelet; a) real and imaginary parts and b) its spectrum.

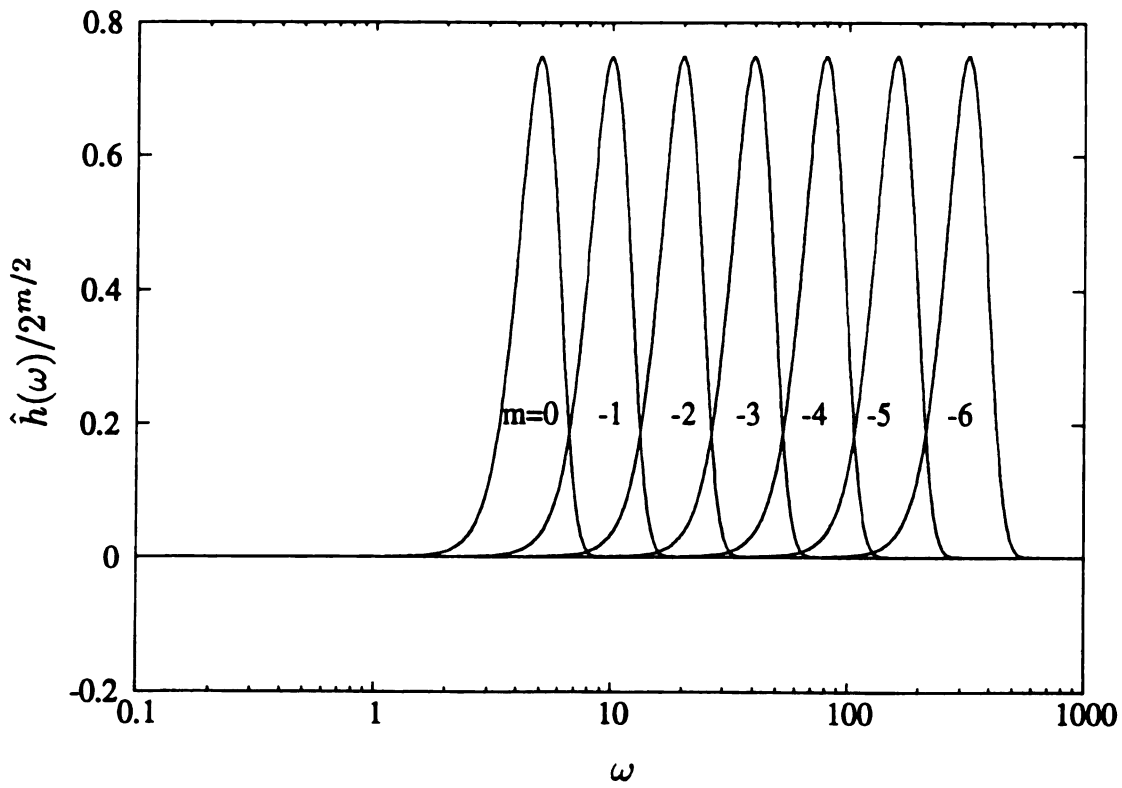

Figure 2.11 The filter bank structure induced by the Morlet wavelet.

wavelets have infinite support and exponential decay. The following example, for the Battle-Lemarie wavelet family, is utilized later in the final chapter of this study.

In real-time signal processing applications, the wavelets are implemented as quadrature mirror filters [129], which are composed of a pair of low-pass and high-pass filters. For the Battle-Lemarie wavelet, the low-pass filter is defined in the frequency domain as

$$H(\omega) = \left[2(1-u)^4 \frac{315 - 420u + 126u^2 - 4u^3}{315 - 420v + 126v^2 - 4v^3}\right]^{1/2} \tag{2.29}$$

where $u = \sin^2(\omega/2)$ and $v = \sin^2(\omega)$. A common choice for the corresponding high-pass filter is $G(\omega) = e^{-i\omega}\overline{H(\omega + \pi)}$. In the signal processing literature [129], these two filters $H(\omega)$ and $G(\omega)$ are known as quadrature mirror filters. Based on these quadrature mirror filters, the corresponding wavelet is defined as

$$\widehat{\psi}(2\omega) = G(\omega)\,\widehat{\phi}(\omega) \tag{2.30}$$

where

$$\widehat{\phi}(\omega) = (2\pi)^{-1/2} \prod_{j=1}^{\infty} H(\omega/2^j) \tag{2.31}$$

is known as the scaling function [43]. A plot of the scaling function, the Battle-Lemarie wavelet, and the corresponding spectra are given in Figure 2.12. The wavelet has oscillations about the origin that decay slowly as $|t| \longrightarrow \infty$. The bandpass filter has an exponentially decaying magnitude, which may be quite desirable in some applications.

2.3.5 Daubechies's Compactly Supported Orthonormal Wavelets

In addition to the preceding classical definitions of wavelets, Daubechies constructed compactly supported wavelets which are favored in signal processing applications involving FIR filters. While the details of the mathematical theory

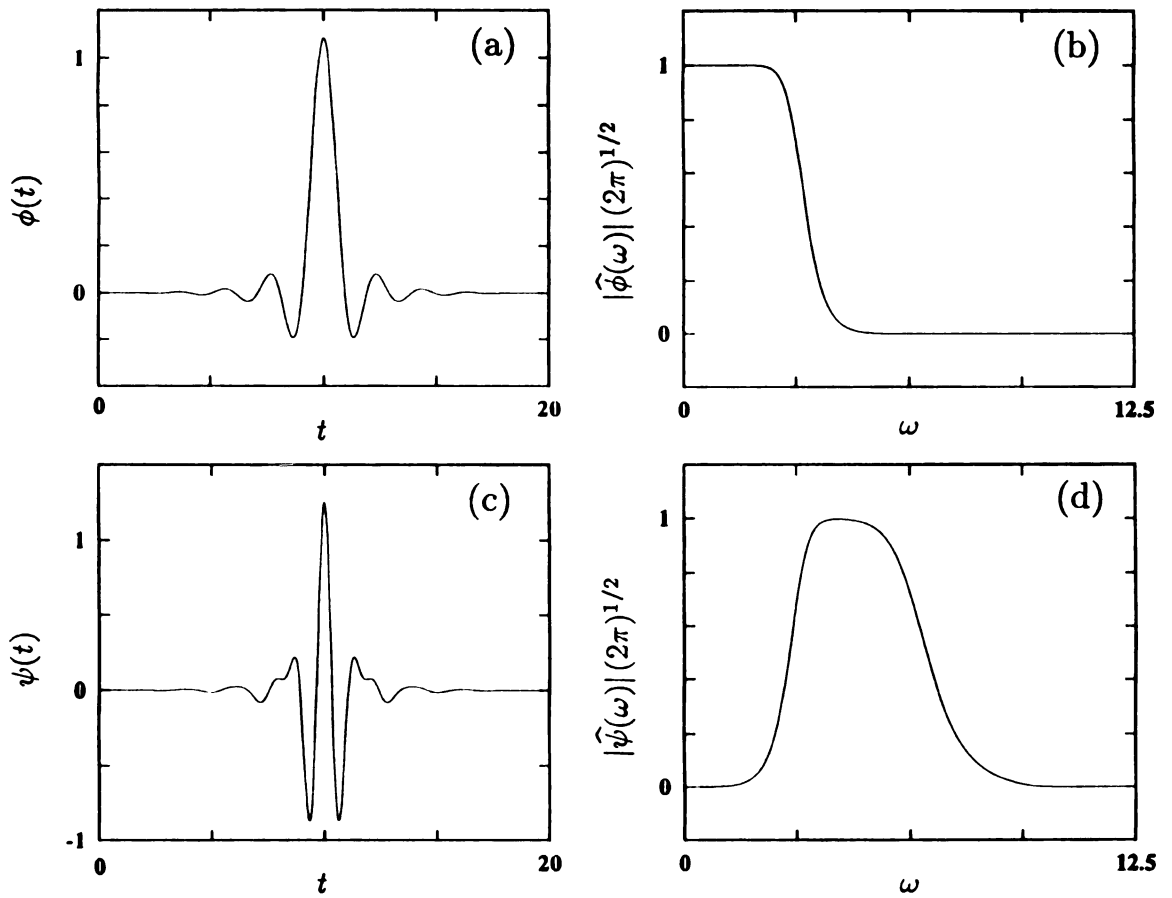

Figure 2.12 The Battle-Lemarie wavelet; a) the scaling function, b) the spectrum of the scaling function, c) the wavelet and d) the spectrum of the wavelet.

behind Daubechies's orthonormal wavelets can be found in her original work [38-43], some of the main concepts and definitions are summarized in Appendix D.

Daubechies's [39] proved that the step sizes $a_0 = 2$ and $b_0 = 1$ lead to the construction of a special family of wavelets with compact support, which also form an orthonormal basis for the Hilbert space $L^2(\mathbf{R})$. As an example of Daubechies's compactly supported orthonormal wavelets, the D10 case is considered in the following. This wavelet has 20 non-vanishing coefficients, h_n, for the low-pass filter H, which are calculated in [43]. The relations given earlier in equation (2.30-2.31) define the spectrum of the wavelet and the scaling function. In Figure 2.13, the D10 wavelet and the scaling function are plotted. The support of the wavelet is defined as $(-10, 10)$, or $(0, 20)$ as shown in Figure 2.13. Although the spectral representations of the Lemarie and D10 wavelets, given in Figures 2.12 and 2.13, look similar, their time domain plots are quite different due to the distinction in their phases. More importantly, the D10 wavelet has a finite support. The performance of both of these wavelets in the analysis of physical signals are compared later in the final chapter.

2.3.6 Multiresolution Analysis

Mathematically, the orthonormal wavelets are closely related to the multiresolution analysis (MRA). The concepts that are introduced in the context of MRA are used in the second part of this study to construct the transient vibration response of a linear time-invariant system. The following brief review is intended to bridge the gap between the wavelets and the MRA concepts to form a background for later constructions. More details of the definitions and theory of MRA can be found in Mallat's work [82-85] and the follow-up is given in Daubechies's studies [38-43].

In multiresolution analysis, a function $f \in L^2(\mathbf{R})$ is represented as a limit of successive approximations. The Hilbert space $L^2(\mathbf{R})$ is decomposed systematically

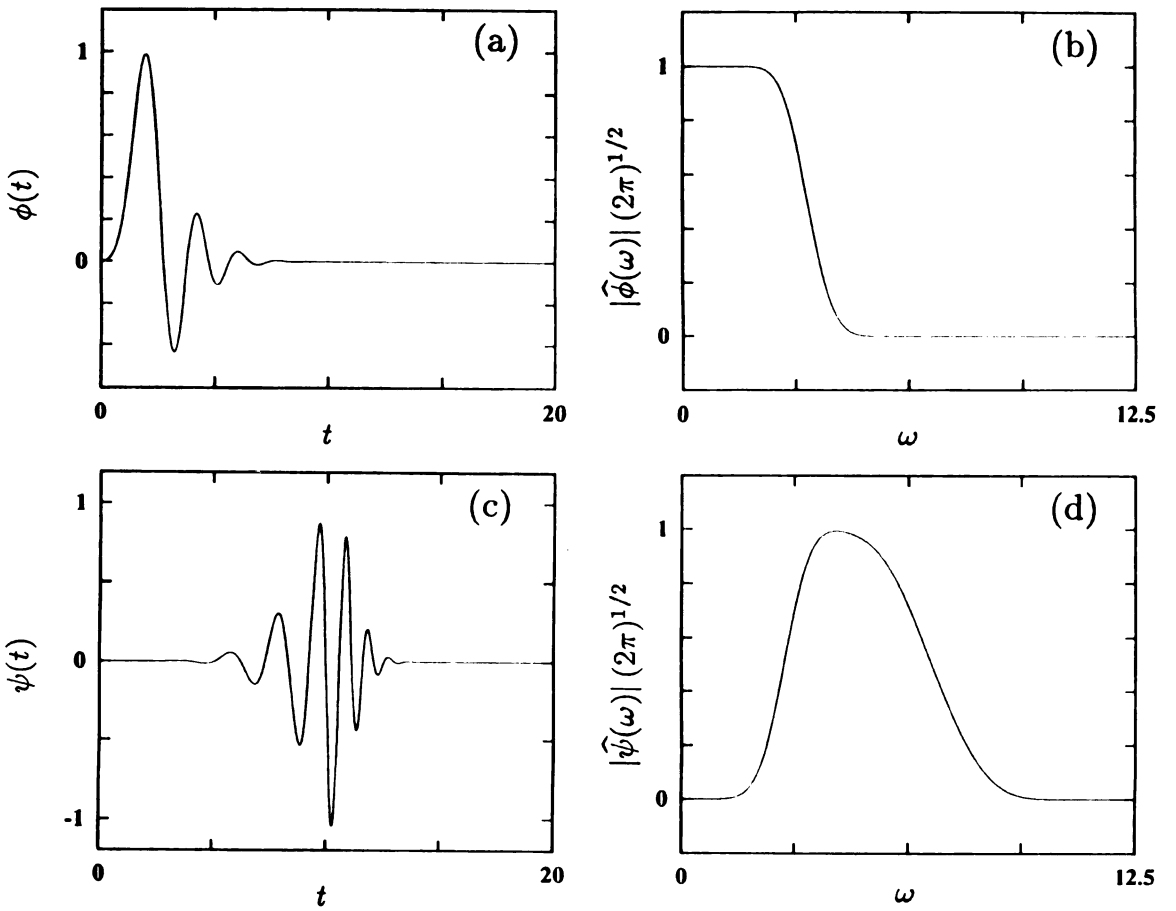

Figure 2.13 Daubechies's compactly supported wavelet; a) the scaling function, b) the spectrum of the scaling function, c) D10 wavelet and d) the spectrum of the wavelet.

into a ladder of closed subspaces $\mathbf{V}_m$, which satisfy the following conditions [82,84]:

$$\begin{aligned}
&1) \quad \ldots \subset \mathbf{V}_2 \subset \mathbf{V}_1 \subset \mathbf{V}_0 \subset \mathbf{V}_{-1} \subset \mathbf{V}_{-2} \subset \ldots \\
&2) \quad \bigcap_{m\in\mathbf{Z}} \mathbf{V}_m = \{0\}, \qquad \overline{\bigcup_{m\in\mathbf{Z}} \mathbf{V}_m} = L^2(\mathbf{R}) \\
&3) \quad f \in \mathbf{V}_m \Leftrightarrow f(2\cdot) \in \mathbf{V}_{m-1} \Leftrightarrow f(2^m\cdot) \in \mathbf{V}_0 \\
&4) \quad f \in \mathbf{V}_m \Rightarrow f(\cdot - 2^{-m}n) \in \mathbf{V}_m \qquad \forall n \in \mathbf{Z}
\end{aligned} \tag{2.32}$$

Condition (3) implies that the subspaces $\mathbf{V}_m$ are scaled versions of $\mathbf{V}_0$, which is an important aspect of the multiresolution analysis. The orthogonal projection $P_m f$ of a function f onto the subspace $\mathbf{V}_m$ corresponds to an approximation with resolution 2^m, and $\mathbf{V}_m \to L^2(\mathbf{R})$ as $m \to -\infty$.

Corresponding to each $\mathbf{V}_m \subset \mathbf{V}_{m-1}$, there exists an orthogonal complement $\mathbf{W}_m \subset \mathbf{V}_{m-1}$, such that

$$\mathbf{V}_{m-1} = \mathbf{V}_m \bigoplus \mathbf{W}_m, \tag{2.33}$$

where the circled-plus sign represents a direct sum. In comparison to nested subspaces $\mathbf{V}_m$, the subspaces $\mathbf{W}_m$ satisfy

$$\mathbf{W}_m \cap \mathbf{W}_k = \{0\} \qquad \text{and} \qquad \mathbf{W}_m \perp \mathbf{W}_k\,, \qquad \forall m \neq k\,. \tag{2.34}$$

Therefore, the Hilbert space $L^2(\mathbf{R})$ can be represented by the direct sum

$$L^2(\mathbf{R}) = \bigoplus_{m\in\mathbf{Z}} \mathbf{W}_m. \tag{2.35}$$

If a ladder of subspaces satisfy the preceding requirements of the multiresolution analysis, then there exists an orthonormal wavelet basis for $L^2(\mathbf{R})$

$$\{\psi_{mn};\ m,n \in \mathbf{Z}\} \qquad \text{with} \qquad \psi_{mn}(x) = 2^{-m/2}\psi(2^{-m}x - n)\,, \tag{2.36}$$

such that, for all $f \in L^2(\mathbf{R})$

$$P_{m-1} f = P_m f + \sum_{n \in Z} \langle f, \psi_{mn} \rangle \, \psi_{mn} \, . \tag{2.37}$$

Again, P_m is the orthogonal projection onto $\mathbf{V}_m$. On each fixed scale m, the wavelets $\{\psi_{m,n}(x);\ n \in \mathbf{Z}\}$ form an orthonormal basis of $\mathbf{W}_m$. Furthermore, there exists a companion to ψ, called the scaling function $\phi \in \mathbf{V}_0$, such that for a fixed scale m the set

$$\{\phi_{m,n};\ n \in \mathbf{Z}\} \qquad \text{with} \qquad \phi_{m,n}(x) = 2^{-m/2} \phi(2^{-m} x - n) \tag{2.38}$$

form an orthonormal basis of $\mathbf{V}_m$. The following example may help to clarify the preceding mathematical concepts.

Example: Haar Basis

A classical example for an orthonormal wavelet basis and the multiresolution analysis is the Haar wavelet. The details of the Haar multiresolution analysis is given in Appendix E.

As an application of the Haar multiresolution analysis, consider the Gaussian function

$$f(x) = \frac{2}{\sqrt{\pi}} \exp(-x^2) \, .$$

The projection of this Gaussian function onto the Haar multiresolution subspaces is performed as follows:

$$\begin{aligned} P_m f &= \frac{2}{2^m \sqrt{\pi}} \sum_n \int_{2^m n}^{2^m (n+1)} \exp(-x^2) \, dx \\ &= \frac{2}{2^m \sqrt{\pi}} \sum_n \int_{2^m n}^{\infty} \exp(-x^2) \, dx - \frac{2}{2^m \sqrt{\pi}} \sum_n \int_{2^m (n+1)}^{\infty} \exp(-x^2) \, dx \\ &= \frac{1}{2^m} \sum_n \Big[\operatorname{erf}\big(2^m (n+1)\big) - \operatorname{erf}\big(2^m n\big) \Big] \end{aligned}$$

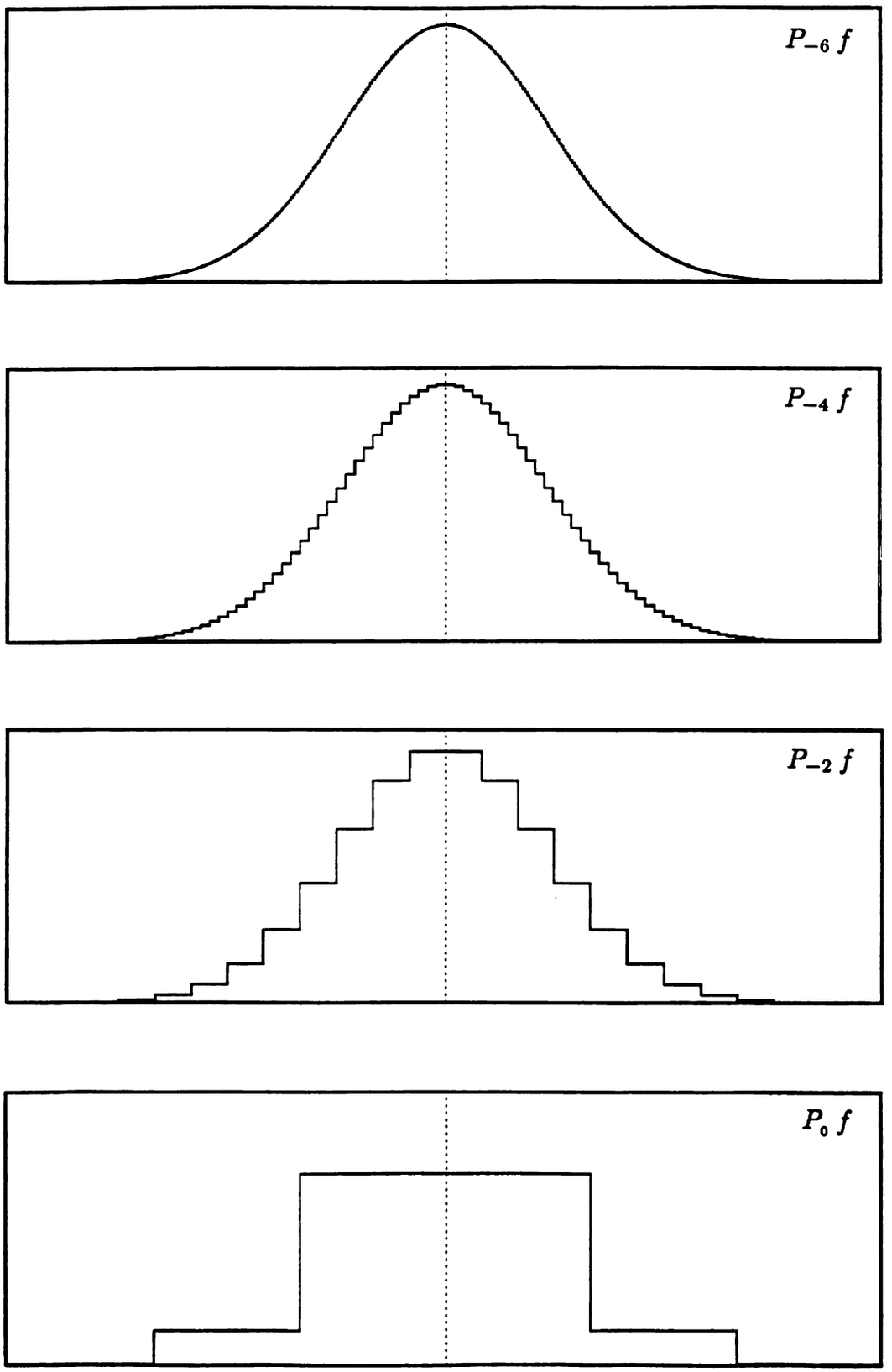

Figure 2.14 Projections of the Gaussian function onto multiresolution subspaces.

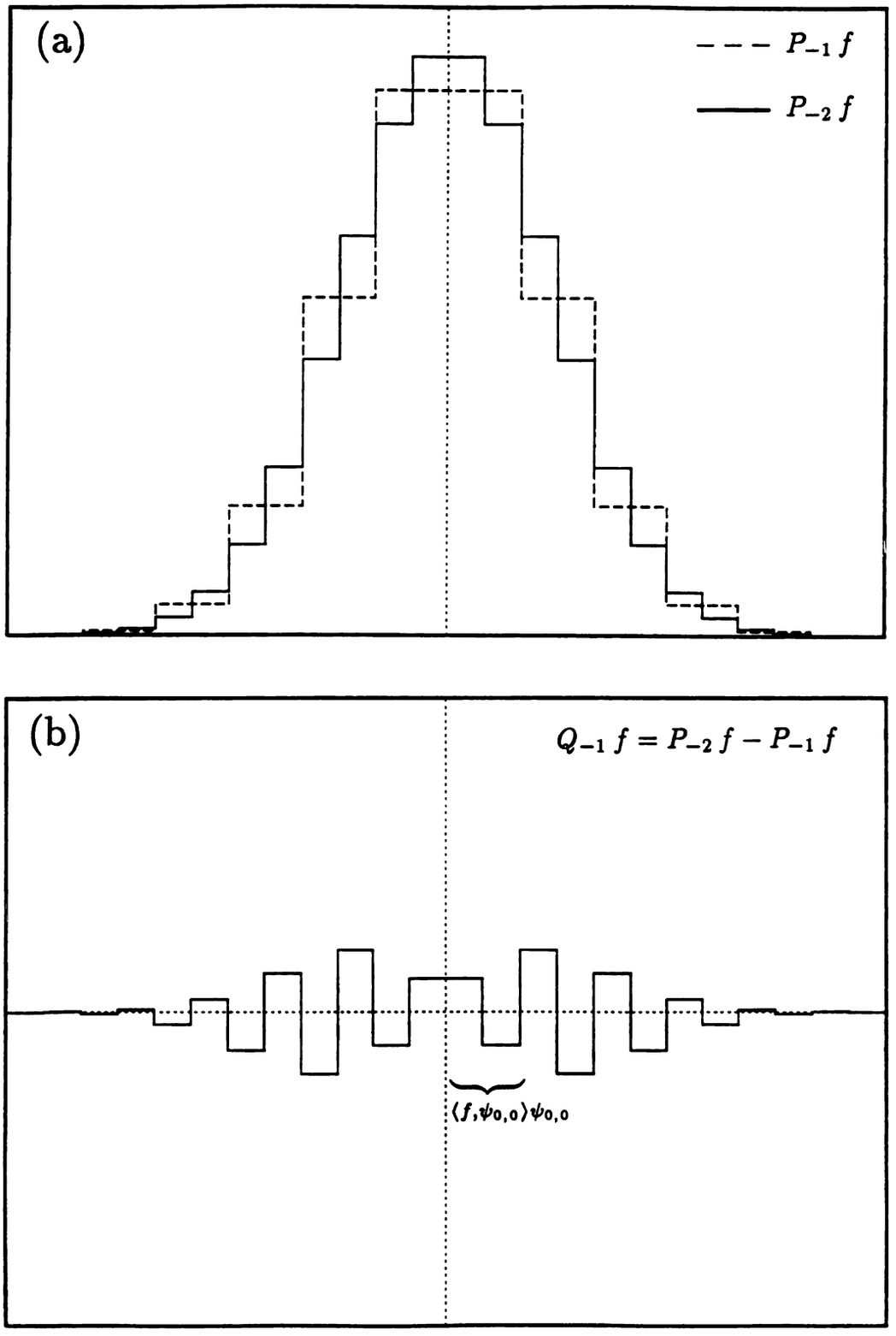

Figure 2.15 a) Representation of the Gaussian function in $\mathbf{V}_{-1}$ and $\mathbf{V}_{-2}$ subspaces.
b) Projection of the Gaussian function onto $\mathbf{W}_{-1}$ subspace.

where erf is the error function. Four different projections are given in Figure 2.14. For a given (m, n) pair, the error function is evaluated by using a fifth-order polynomial approximation. Note that, in Figure 2.14, as m gets large negative values, the projection of f simulates the Gaussian function more closely. Two of the projection are overlayed on Figure 2.15a. The difference between the two projections is plotted in Figure 2.15b, which gives the sum of the integer-translates of the Haar wavelet multiplied by the wavelet coefficients or the inner products, which is also implied by the equations (2.37) and (E.8).

2.4 Implementation of the Wavelet Transform

Since the recent progress on wavelet theory began, there has been various suggestions for the implementation of the wavelet transform for different purposes. Algorithme á trous was introduced by Holschneider *et al.* [71], and later applied to real time analysis of sound from musical instruments by Dutilleux [50]. The tree-algorithm of Mallat and Meyer [82,94,96] was based on orthonormal wavelet basis and designed originally to perform multiresolution decomposition of images. A detailed review of the existing algorithms, their properties and relationship to each other can be found in the studies by Shensa [123] and Rioul and Duhamel [118]. In principle, all the algorithms perform some form of filtering operation on the signal while carrying out an interpolation and decimation on each stage. In the following, some of the basic properties of the well-known algorithms are reviewed briefly.

2.4.1 Existing Algorithms

Algorithme á trous (algorithm with holes) does not require orthogonal wavelets and can be implemented on multi-voice schemes [50]. The basic principle of the algorithm is based on the sampling of the mother wavelet in the time domain. Then, at every stage, its dilated version is generated before the discrete convolution of the filter with the signal is performed. A sketch of the operational

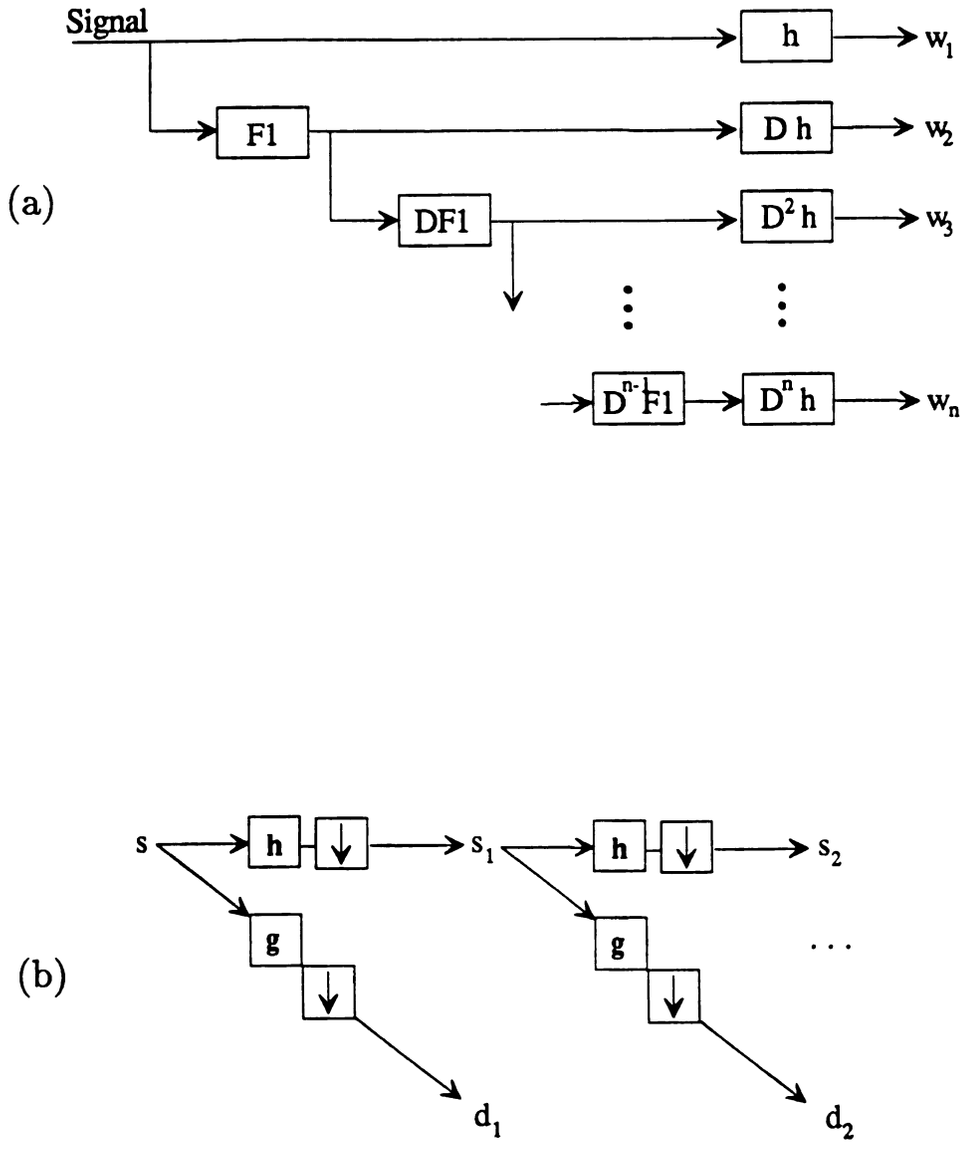

Figure 2.16 The sketch of two algorithms for implementation of wavelet transform; a) algorithme á trous, and b) multiresolution algorithm.

structure of the algorithm is given in Figure 2.16a. In this sketch, the dilation operation which places zeros in between every sample is marked by D, the preintegrator is defined by $F1 = 1 + TDF$, the unit sample delay operator is expressed by T, the sampled wavelet by h and the wavelet coefficients by $\mathbf{w_n}$ [50]. The way the algorithm works is that, an output is generated for every sample of the input. Therefore, the resulting TFR is very dense and highly redundant. Infact, the size of the input array grows with the number of filtering stages. The redundancy is sometimes usefull, since dense representation may ease the visualization of spectral evolutions on the time-scale plane. On the other hand, the algorithm can be adjusted to skip certain number of samples, at every stage of the filtering operation, generating a less dense TFR.

The tree algorithm of Mallat and Meyer is based on orthonormal wavelet basis. A sketch of the tree algorithm is given in Figure 2.16b. In this figure, the box with a downward arrow stands for the decimation operation. The filter h is a low-pass filter and the filter g is the corresponding high-pass filter. These two filters are related to each other and their definition involves certain constraints which are detailed in Mallat and Meyer's seperate works [82,84,94,96]. The dual filter structure has been known in signal processing literature as quadrature mirror filtering [129].

In addition to these two classical algorithms, Beylkin *et al.* [17] introduced a fast wavelet transform algorithm that was specifically designed for fast numerical application of dense matrices and integral operators. The algorithm is based on Coifman's [32-34] entropy-based best-adapted wavelet packets. As Strang [124] has stated in his review paper, all good wavelet algorithms are based on recursion. As shown in Figure 2.16b, the recursion takes place only on the upper branch of the tree-algorithm. A more efficient implementation for the orthonormal wavelet decomposition and synthesis can be achieved by extending the recursion to both branches [58].

In this study, the implementation of the wavelet transform is carried out by using an FFT based discrete wavelet transform algorithm. The main operational

features of the algorthme á trous are combined with the FFT based bandpass filtering scheme to perform non-real time transformations. In the following, the basic principles of the discrete wavelet transform are layed out.

2.4.2 Discrete Wavelet Transform

Continuous wavelet transform (CWT) of a signal $s \in L^2(\mathbf{R})$ with respect to a family of wavelets was defined earlier in equation (2.4). In signal processing applications, the discrete version of the wavelet transform is applied on a signal $s(nT_s)$ which is sampled in time with the sampling frequency $f_s = 1/T_s$. The discrete version of the CWT is defined as

$$(\mathcal{W}\, s)(a, nT_s) = T_s \frac{1}{\sqrt{a}} \sum_k s(kT_s)\, \overline{h\left(\frac{(k-n)T_s}{a}\right)}\,. \tag{2.39}$$

It is a common practice to simplify the preceding equation by selecting $T_s = 1$ and defining

$$h_a(n) = \frac{1}{\sqrt{a}} \overline{h\,(-n/a)}\,, \tag{2.40}$$

where the subscript a denotes a particular wavelet bandpass filter. Then, the standard form of the DWT becomes

$$(\mathcal{W}_a\, s)(n) = \sum_k s(k)\, h_a(n-k)\,. \tag{2.41}$$

In signal processing terminology, this final form represents a discrete convolution of a signal sequence with a noncausal band-pass filter. In the following, the subscript "a" is dropped to simplify the notation.

In a practical setting, unless the wavelet has a finite support, one would generally need to truncate an infinite sequence at a finite number of samples M. The truncated wavelet sequence is represented by $h_t(n)$, $n = -M/2, \cdots\cdots, M/2$, which has a z-transform defined as

$$H_t(z) = \sum_{k=-M/2}^{M/2} h_t(n)\, z^{-n}\,. \tag{2.42}$$

For the implementation of the convolution operation, we need to define a causal filter. This is obtained by shifting the wavelet sequence by $M/2$ samples in positive direction;

$$h_{tc}(n) = h_t(n - M/2), \qquad n = 0, \cdots, M-1 \tag{2.43}$$

which in the z-domain corresponds to

$$H_{tc}(z) = H_t\, z^{-M/2} = \sum_{n=0}^{M-1} h_t(n)\, z^{-(n+M/2)} .$$

In this final form, the wavelet has become a Finite Impulse Response (FIR) filter. The convolution of the FIR filter with the signal generates an output of the form:

$$Y_{tc}(z) = S(z)\, H_{tc}(z) . \tag{2.44}$$

Then, the corresponding response in the ℓ^2-domain becomes

$$y_{tc}(n) = \sum_{k=0}^{M-1} h_{tc}(k)\, s(n-k) . \tag{2.45}$$

However, from the mathematical point of view this result is a little short of what we were really looking for, that is the convolution of the signal with a noncausal wavelet filter. This objective can be achieved by performing a simple shift operation in time, which would convert the causal output to a noncausal one. Therefore, we consider z-domain representation of the convolution given in equation (2.44) and multiply both sides by $z^{M/2}$ to obtain

$$\begin{aligned} z^{M/2}\, Y_{tc}(z) &= S(z)\, H_{tc}(z)\, z^{M/2} \\ &= S(z)\, H_t(z) = Y_t . \end{aligned}$$

In the ℓ^2-domain, the preceding relation becomes

$$y_t(n) = y_{tc}(n + M/2), \qquad n = 0, \cdots, M-1 . \tag{2.46}$$

Therefore, during the implementation of the wavelet transform first the output from the causal filter is determined and then the desired noncausal output is obtained by shifting the signal. If the sampling period $T_s \neq 1$ needs to be taken into account, the indices n and k are replaced by nT_s and kT_s in the above formulations.

2.4.3 Filter Bank Implementation by Using FFT

During the implementation of the wavelet transform, the relation given in equation (2.44) forms the basic operation of the algorithm. The relation between the z-transform and the Fourier transform implies that the response of a particular filter is just a simple multiplication of the Fourier transforms of the signal and the wavelet impulse response function. Therefore, for every scale of the wavelet transform, the band-pass filter is defined and implemented by using the above procedure. Later, the output is inverse Fourier transformed by using an FFT algorithm. Alternatively, the output can be interleaved by any number of samples to adjust the resolution. The only difficulty with the present approach is the length of the filter and the signal. For example, in a Morlet wavelet transform with $\omega_c = 5$, an FFT size of 2^{15} gives aproximately 10 octave range before aliasing starts to take effect in higher octaves. In order to process long-length signals, the overlap-add method is employed during the filtering operation. The details of the method can be found in any textbook on signal processing, such as [108,111].

Unless otherwise indicated, the wavelet transforms used in the rest of this study are performed by using the Morlet wavelet, given in equation (2.27). The center frequency is fixed as $\omega_c = 5$. The effect of different choices of the center frequency is discussed later in the final chapter.

2.5 STFT and Wavelet Transform of Synthetic Signals

In the following examples, four different synthetic signals are considered to demonstrate some of the properties of the Gabor (STFT) and wavelet transforms. The characteristic time-frequency representations resulting from these bench-mark

signals will be helpfull during the interpretation of the transforms obtained from measured physical signals, which are considered later in this study.

The implementation of the discrete Gabor (STFT) transform is performed by using an FFT algorithm. During the implementation of the STFT, the window type, size and the translation step are varied. The wavelet transform is implemented by using the Morlet wavelet in an FFT based bandpass filtering algorithm, as discussed earlier. In the display of the wavelet transforms, the "scale(octave)" parameter differs from the dilation index only by a sign, $octave = -m$.

2.5.1 Unit Sample Pulse

During the initial phases of the implementation and evaluation of the wavelet transform, a signal consisting of a unit magnitude sample-pulse $\delta(n - M/2)$ has been found to be very useful. As shown at the top of Figure 2.17, the signal consists of a unit amplitude sample pulse located at the center of a time series that has zeros assigned to the rest of the M samples.

The time-scale representation resulting from the wavelet transform can be displayed in different graphical formats. For the pulse signal, the magnitude of the wavelet transform is shown in three different formats in Figures 2.17 and 2.18a. The contours in Figure 2.17a have a $40\,dB$ range with $2\,dB$ rise per contour. The color scale used throughout this study is defined in the Appendix I. A comparison of Figures 2.17b and 2.18a may help in understanding some of the features of the color-coded plots generated from measured physical signals in later sections.

The discrete convolution of the filter (wavelet) impulse response function with this unit pulse signal generates an output that characterizes the spectral content of the filter bank structure induced by the wavelet transform. Since a pulse signal is ultimately localized in time, its Fourier representation requires equal contributions from all spectral components. Whereas in the wavelet transform, as shown in Figure 2.17, the contracted versions of the mother wavelet have much larger contributions in the representation of the pulse.

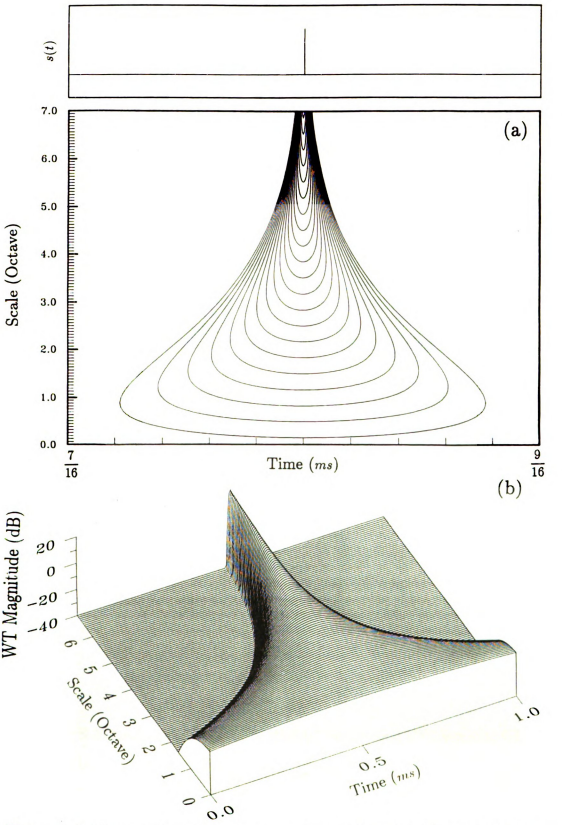

Figure 2.17 The wavelet transform of a unit sample pulse. The magnitude is displayed as a) a zoomed topological plot and b) a fishnet plot.

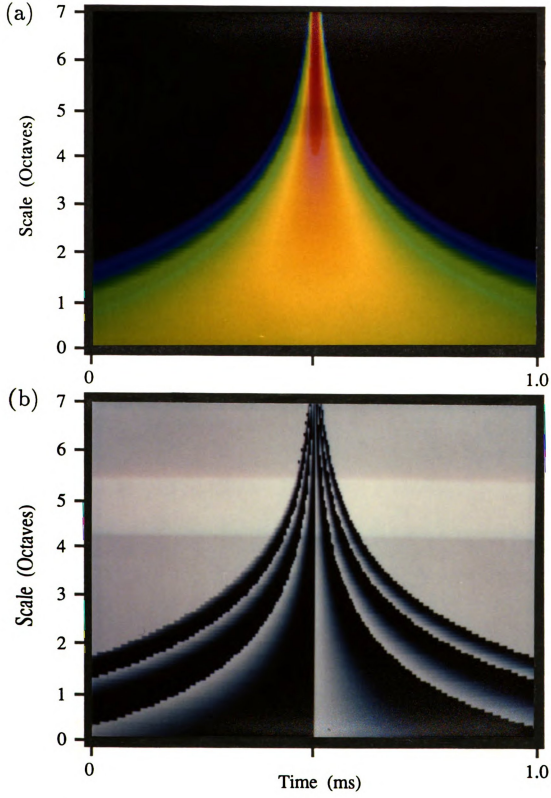

Figure 2.18 Color coded plot for the wavelet transform of a unit sample pulse; a) the magnitude and b) the phase.

The phase of the wavelet transform also plays an important role and carries a part of the information. In Figure 2.18b, the phase of the transform is displayed by using a linear gray scale that runs from white to black within 0 to 2π range. Thus, each black to white transition implies the completion of one cycle in the corresponding wavelet basis. These cyclic linear phase changes are observed to occur more frequently at higher scales. The logarithmic contraction of the wavelet basis is evident from the conical shape of the phase distribution. The constant phase line running vertically through all scales at the center of Figure 2.18b indicates the location of the sharp change in the signal.

In the analysis of vibration signals, a pulse may represent a sharp change in the observed variable, such as the acceleration signal following an impact on a structure. In the following chapter, the preceding features observed from the wavelet transform of the pulse signal are utilized to study impact induced transient vibrations of a beam.

2.5.2 Two Sines and a Pulse

The Fourier transform, due to its sine-cosine basis, is known to perform very effectively on signals containing sinusoidal components. However, when local perturbations in a signal occur, it effects all spectral components. As discussed earlier, in a sliding-window spectrum (STFT), the uncertainty principle imposes a trade off between time and frequency resolutions. Therefore, as demonstrated in the following, the size of the window function has an influence on the outcome of the transformation.

In this example, the signal consists of two sine components, with frequencies at $f_1 = 44\,Hz$ and $f_2 = 15 \cdot f_1$, and a pulse superimposed at the center of the time record, as shown at the top of Figure 2.19. The magnitude of the wavelet transform plotted in Figure 2.19 shows two wide horizontal bands corresponding to the sine components and a conic-vertical strip at the center that penetrates through these bands. The other half-conical distributions on either side of the time record are due to start-up and termination transients that are generated by the wavelet filter bank. Note that the magnitude of the conic-vertical strip

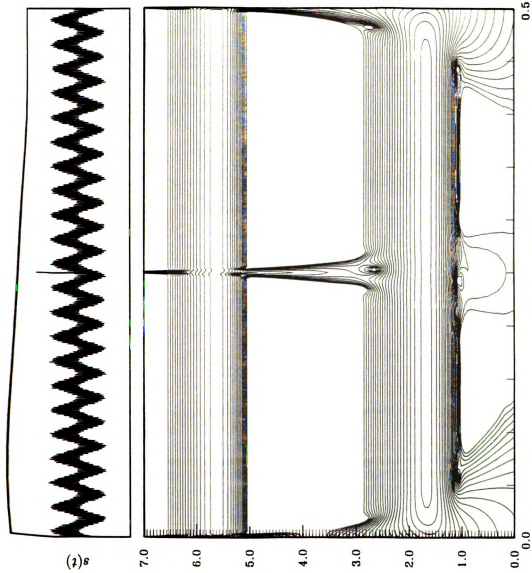

Figure 2.19 The wavelet transform of a signal composed of two sinusoids and a pulse. The contours have 40 *dB* range with 2 *dB* rise per contour.

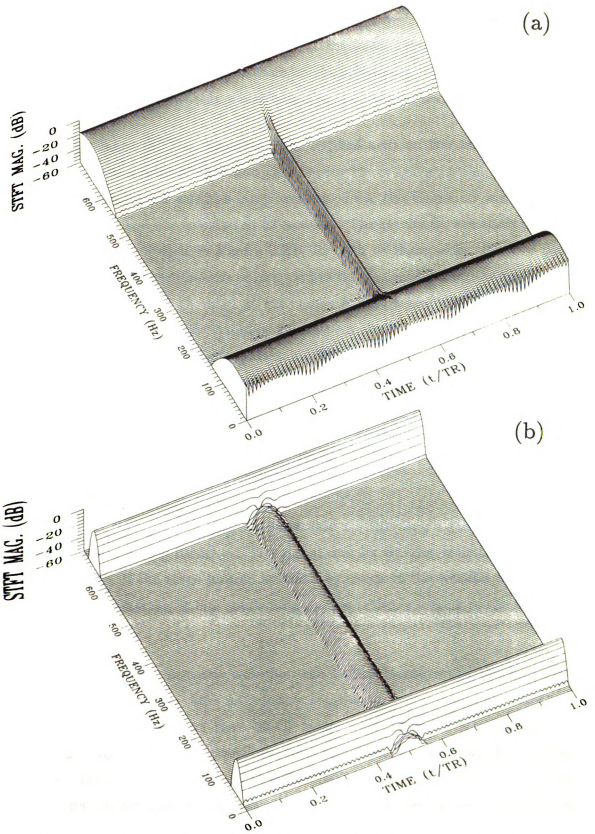

Figure 2.20 The magnitude of the STFT for the signal shown in Figure 2.19. The Gaussian window length is a) 256 and b) 1024 samples.

increases and its width gets smaller at the higher octave levels, which gives a clear indication of the location and magnitude of the pulse. However, the same is not true for the time-frequency localization of the sinusoidal components, since they are represented over relatively wider bands in the wavelet transforms.

The Gabor (STFT) transform was applied next on the same signal. The signal contained a total of 4096 samples. During the transformation, two different lengths, 256 and 1024 samples long, were used for the Gaussian window. The translation step size was selected as 32 samples. The results for the short and long window cases are plotted in Figure 2.20. In both of these plots, the two peaks running parallel to the time axis correspond to the sinusoidal components, and the ridge penetrating through them at the center is associated with the pulse. The transform based on the short window length provides relatively better time localization of the pulse, but poor frequency localization of the sinusoidal components. The opposite is true for the choice of the longer time window. As discussed earlier and demonstrated clearly in this example, the constant window structure of the STFT requires a trade-off between time and frequency resolutions.

2.5.3 Gaussian Enveloped Log-Sweep

In this example, the signal is generated by sampling a gaussian-enveloped logarithmic sine-sweep function. The signal and its wavelet transform are given in Figure 2.21. If the ridge formed by the magnitude of the wavelet transform is traced, it forms a straight line confirming the logarithmic scaling of the frequency axis.

Similar to the previous example, the Gabor transform of the signal was performed by using two different window lengths, and the results are plotted in Figure 2.22. The contours have $60\,dB$ range with $3\,dB$ rise per contour. As shown in Figure 2.22a, the transform resulting from the short window displays relatively better time-localization at higher frequencies. Increasing the size of the transformation window, in Figure 2.22b, results in a better frequency localization at lower frequencies, but as a trade off, gives away from the time-localization characteristics.

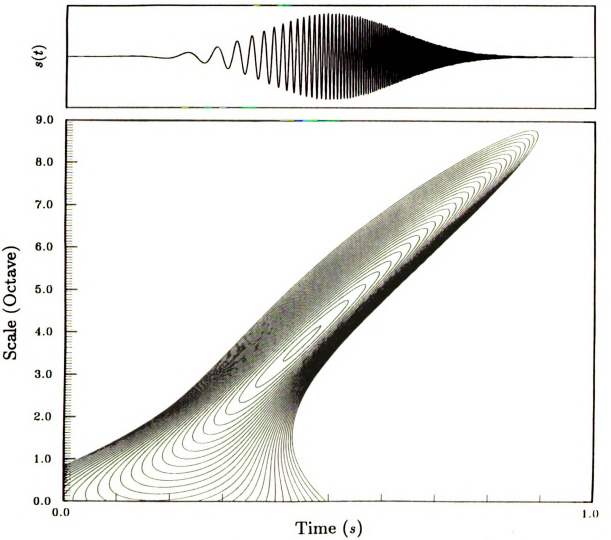

Figure 2.21 A Gaussian enveloped logarithmic sine-sweep signal and its wavelet transform. The contours have $60\,dB$ range with $2\,dB$ rise per contour.

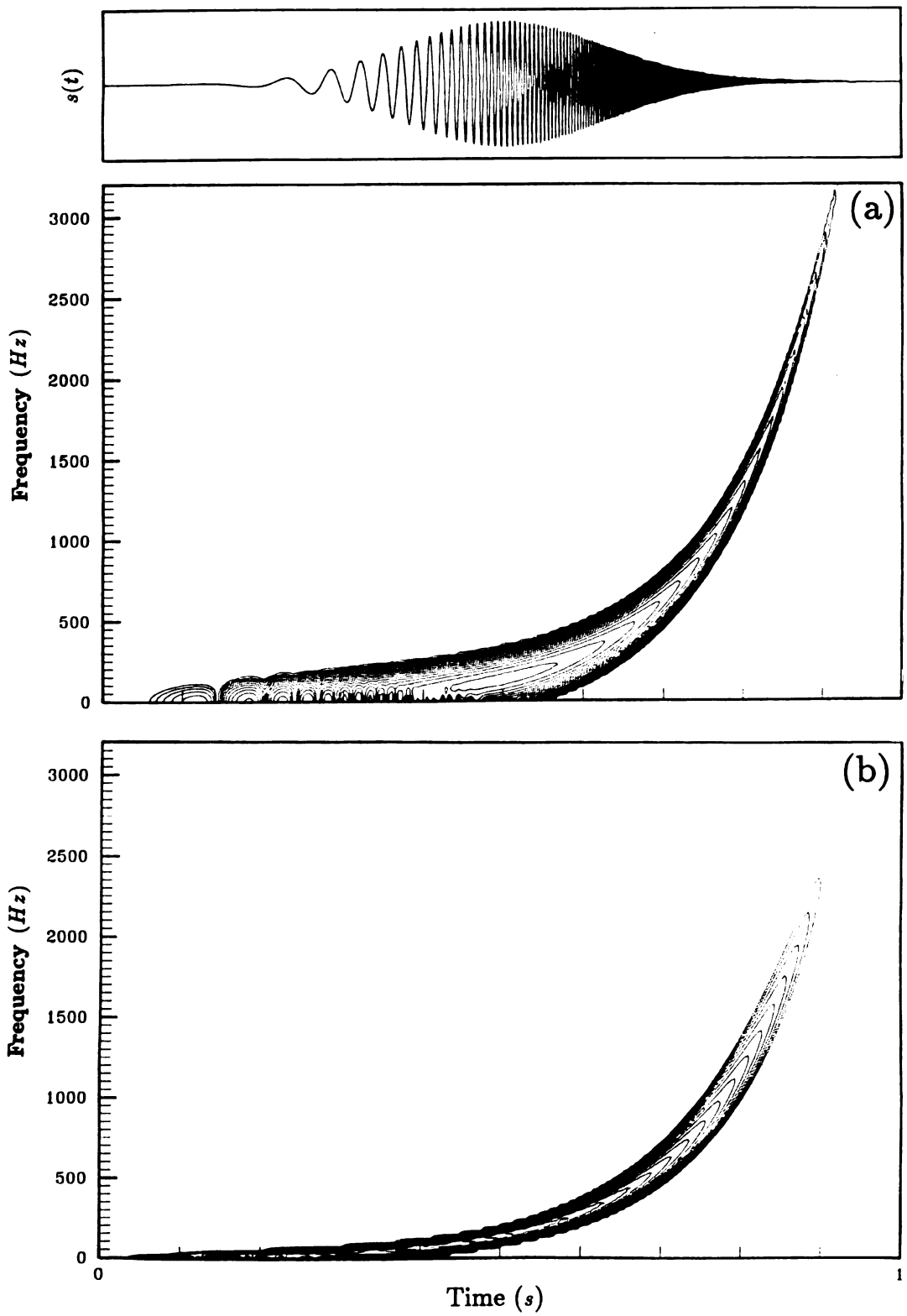

Figure 2.22 The STFT of the signal shown in Figure 2.21. The Gaussian window length is a) 256 and b) 1024 samples.

The benefit of using a time-frequency representation is demonstrated clearly in this example. The time-evolution of the spectral components were displayed effectively both in wavelet and Gabor transforms. As shown in later applications, similar time-evolving spectral behaviors are encountered in the dynamic response of some physical systems.

2.5.4 Exponentially Decaying Sinusoidal Signal

The transient vibration response of dynamic systems generally involve some kind of sinusoidal function decaying exponentially in time. If the system is excited by a short-duration transient force, the response may look similar to the signal shown in Figure 2.23. The wavelet transform of the signal displays two different characteristics of the signal simultaneously. The initial start-up transient of the signal is represented by the conic-vertical strip, which is very similar in shape to the wavelet transform given in Figure 2.17a. The exponentially decaying response is well-localized in the time-scale plane with the peak magnitude representing the center of the signal's envelope. The nose extending to the right characterizes an exponentially decaying sinusoid. In vibro-acoustic systems, similar behaviors are associated with non-dispersive transient vibrations of structures, as demonstrated in the following chapter.

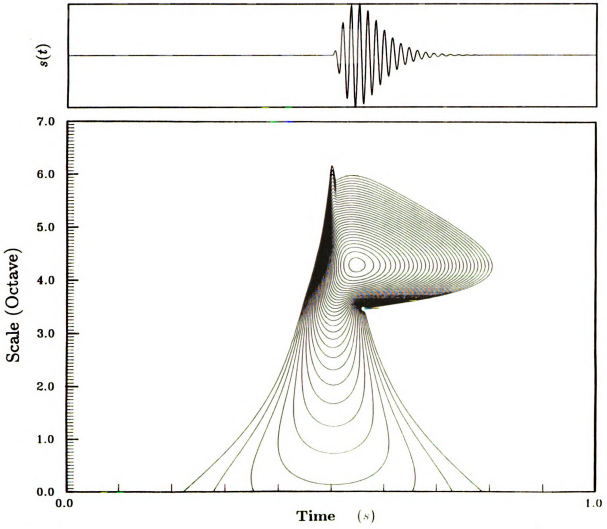

Figure 2.23 The wavelet transform of an exponentially decaying transient sinusoidal signal. The contours have $60\,dB$ range with $2\,dB$ rise per contour.

CHAPTER 3

WAVELET TRANSFORM ANALYSIS OF TRANSIENT WAVE PROPAGATION

In this part of the study, the effectiveness of the wavelet transform in the analysis of transient wave propagation is investigated. The characteristics of different wavebearing media are explored by using time-scale representations resulting from the wavelet transform of measured acceleration and acoustic signals. The dispersion of a transient waveform is given particular attention, since the physical phenomenon and the analysis tool (wavelet transform) both have similar fundamental properties. As an alternative, a space-wavenumber representation is introduced by considering the wavelet transform of the space-dependent vibration response of a beam. The relationship between the time-scale representation and the group velocity of a transient waveform is emphasized. The self-adjusting window structure of the wavelet transform is exploited during the analysis of different wave-modes in a wave-guide. The propagation and the dispersion of the higher wave-modes and the associated cut-off phenomenon are identified from the time-scale representations. Physical examples are utilized to compare the advantages and limitations of the wavelet and Gabor transforms.

3.1 Introduction

It is well-known that, in a dispersive medium, an arbitrary waveform evolves in time and space if the phase speed depends on the frequency. Since each progressive wave component propagates with a different phase speed, the initial shape of a transient waveform is distorted in time. Similarly, a wavelet basis is generated by dilating and translating an original waveform in space or in time. An outstanding property of the wavelet transform is the built-in self-adjusting (zooming)

window structure that helps to resolve high and low-frequency transient phenomena effectively. This zooming property of the wavelet transform can be utilized to identify the distinct spectral charateristics of a transient waveform propagating in a dispersive medium.

Before going into the details of the wavelet transform analysis of transient waves, it is appropriate to begin our discussion with a brief background on the propagation of waves in dispersive and nondispersive mediums.

3.2 Waves in Dispersive and Nondispersive Media

In a wave-bearing medium, the propagation of a simple harmonic progressive wave, $\exp(ikx - i\omega t)$, is characterized by the relationship that exists between the wavenumber k and the frequency ω. If the dispersion relation is linear, such as in an acoustic medium ($k = \omega/c$), then an arbitrary waveform would maintain its original shape during its propagation. However, there are many physical systems for which the relationship between the wavenumber and the frequency is expressed by nonlinear functional forms. [37,67,97,113]. For such cases, the phase speed of waves is dependent on the frequency of vibrations. Consequently, different progressive wave components making up the original shape of an arbitrary waveform travel at different speeds, and results in the dispersion of the waveform. Classical examples of wave dispersion are the gravity waves in deep-waters and the decomposition of white light into its spectral colors. As an example of propagation in a nondispersive medium, the wave motion along the length of a string or in an acoustic medium can be considered. Other examples of dispersive media are discussed in Rayleigh's [113] and Havelock's [67] studies.

For flexural waves, a beam or a plate becomes a dispersive medium. For example, when a transient waveform is induced on a uniform beam, the flexural wave components propagate at different speeds and thus cause dispersion. When such dispersion phenomena takes affect, the phase and group velocities of a waveform are used to determine the characteristics of the wave-bearing medium.

3.2.1 Phase and Group Velocities

The propagation characteristics for a group of waves were mentioned first by Hamilton (1839) in his published short abstracts. The analytical treatment and the classical definition of the group velocity are attributed to Stokes (1876). The detailed treatment of phase and group velocities were originated from Lord Rayleigh's [113] classical work. Many of the modern treatments of the wave propagation concepts are based on Rayleigh's interesting formulations and definitions. In a later work, Havelock made extensive use of the wave-group concepts and studied many different problems that were related to propagation of disturbances in dispersive media. Among the more recent collections in the literature, detailed discussion of wave groups can be found in the studies conducted by Brillouin [22], Achenbach [1] and Miklowitz [97]. The following summary on phase and group velocity concepts are intended to form a background for later discussions.

The concept of wave-group is introduced by considering a simple harmonic progressive wave component propagating in a one-dimensional medium, which is defined by [22]

$$y(x,t) = A\,\cos(kx - \omega t) = A\,\cos\left[k(x - c_p t)\right] \tag{3.1}$$

where $c_p = \omega/k$ is the phase velocity of the wave. A simple wave group can be constructed by adding two such harmonic wave components together [97];

$$y(x,t) = A\,\cos\left[k(x - c_p t)\right] + A\,\cos\left\{(k + \Delta_k)\left[x - (c_p + \Delta_c)t\right]\right\}. \tag{3.2}$$

In this wave group, the wavenumber and the phase velocity are assumed to differ slightly between the two components. The preceding equation can be reorganized into a more managable form by first expanding the trigonometric functions, and then taking the limits of the incremental differences. When the higher order terms are neglected the first-order representation gives

$$y(x,t) \simeq 2A\,\cos\left[(dk/2)(x - c_g t)\right]\,\cos\left[k(x - c_p t)\right] \tag{3.3}$$

where the group velocity is defined by

$$c_g = c_p + k\frac{dc_p}{dk} . \tag{3.4}$$

The envelope of the wave-group moves with the velocity c_g, while the wave carried under the envelope propagates with the velocity c_p. Therefore, as pointed out by Rayleigh [113], for an observer travelling with the envelope, if $c_p \neq c_g$, then the carrier waves will look as if they are propagating from one end of the group, passing the observer and propagating toward the other end.

The preceding analysis can be generalized to include an arbitrary waveform composed of a finite number of simple harmonic progressive wave components. In this more general case, the velocity of the group is defined as [67,113]

$$c_g = \frac{d(kc_p)}{dk} = \frac{d\omega}{dk} \tag{3.5}$$

The group velocity also represents the speed at which energy is propagated in a wave-bearing medium. Achenbach [1] derived equation (3.5) for the speed of propagation of energy by considering the general definition of the Lagrangian density for a linear elastic, homogenous, isotropic body.

It is interesting to note that Brillouin [22] refers to the wave packets as "wavelets", which in the context used, refers to the physical wave motion and has no relation to the present mathematical theory on wavelets. Never-the-less, the envelope of a carrier wave in the wave group analysis looks very similar to the windowing function used in STFT. Furthermore, since wave groups are local phenomena, a local analysis, such as the wavelet transform, should be very effective in generating time-frequency and space-wavenumber representations. In the following, a sample from each type of media is considered in order to investigate the application of the wavelet transform to the analysis of transient wave propagation.

3.3 Dispersive Medium: Bending Waves on a Beam

Within the group of dispersive media, the propagation of flexural waves along a beam is known as a classical example, which can be studied in detail both analytically and experimentally. However, since the bending vibrations of a beam is governed by a fourth-order PDE, evanescent waves are generated near impedance discontinuities or external disturbances, which need to be considered in addition to the positive- and negative-going waves. Therefore, a closed form solution to the response of a beam can be found only for very special initial conditions.

In the following, the analytical formulation for the vibration response of an infinite beam is presented by considering a specific set of initial conditions. The results obtained from the numerical simulation are used to predict the vibration characteristics of a physical setup. In the experimental measurements, a semi-infinite beam is simulated by using an unechoic termination at the end of a long beam. The measured vibration signals are analyzed by using the STFT and the wavelet transforms.

3.3.1 Bending Waves on an Infinite Beam: An Analytical Study

Considering the flexural vibrations of a uniform beam at broadband low-frequencies, the equation governing the transverse displacements is derived as

$$EI\frac{\partial^4 y(x,t)}{\partial x^4} + \rho A\frac{\partial^2 y(x,t)}{\partial t^2} = 0 \tag{3.6}$$

where the effects of shear deformations and rotary inertia have been neglected. Note that, the contribution of such effects becomes significant (above 10%) only when $\lambda < 6h$, where λ is the bending wavelength and h is the thickness of the beam.

The simple harmonic progressive wave solution $y(x,t) = \exp(ikx - i\omega t)$ of the governing equation results in the dispersion relationship

$$k^4 - \frac{\rho A\omega^2}{EI} = 0\,. \tag{3.7}$$

The dispersion relation not only governs the possible wave types, but it is also used to define the phase and group velocities [37];

$$c_p = \frac{\omega}{k} = \sqrt{\omega}\left(\frac{EI}{\rho A}\right)^{1/4}, \qquad c_g = \frac{d\omega}{dk} = 2c_p\,. \tag{3.8}$$

Since the phase velocity is directly proportional to the half power of the frequency, the high frequency wave components are expected to propagate with a faster wave speed. Therefore, the initial shape of an arbitrary waveform, which in general is composed of many different Fourier components, will be distorted as the waves propagate along the beam. This would result in the dispersion of the transient waveform and cause the spectral distribution to evolve in time and space.

If the beam is subjected to certain initial conditions, then a different solution procedure needs to be followed. As mentioned earlier, closed form analytical solutions are tractable only for very special initial conditions. One such special case was studied by Boussinesq (1885) for the initial conditions defined as

$$y(x,t)\Big|_{t=0} = f(x) \qquad \text{and} \qquad \frac{\partial y(x,t)}{\partial t}\Big|_{t=0} = \kappa\,\frac{d^2 g(x)}{dx^2} \tag{3.9}$$

where $\kappa^2 = EI/(\rho A)$. By using the Fourier transform, the solution for the free vibration response of an infinite beam subject to the preceding initial conditions is obtained as [92]

$$\begin{aligned} y(x,t) = \frac{1}{\sqrt{2\pi}}\Bigg[& \int_{-\infty}^{\infty} f(x - 2u\sqrt{\kappa t})\,(\cos u^2 + \sin u^2)\,du \\ & - \int_{-\infty}^{\infty} g(x - 2u\sqrt{\kappa t})\,(\cos u^2 - \sin u^2)\,du\Bigg]\,. \end{aligned} \tag{3.10}$$

This integral solution can be evaluated further for a specific choice of functions defining the initial conditions, such as

$$f(x) = \frac{y_0}{2\sqrt{\pi\alpha}}\,e^{-x^2/4\alpha} \qquad \text{and} \qquad g(x) = \frac{v_0}{2\sqrt{\pi\alpha}}\,e^{-x^2/4\alpha} \tag{3.11}$$

where y_0 and v_0 are the amplitudes of the initial displacement and initial velocity of the beam. Substituting these functions, $f(x)$ and $g(x)$, back into equation (3.6) and then evaluating the integrals give

$$y(x,t) = \frac{1}{\sqrt{2\pi}} \beta^{-1/4} e^{(-x^2\alpha/\beta)} \left[y_0 \cos(\theta) + v_0 \sin(\theta) \right], \qquad (3.12)$$

where

$$\theta(x,t) = x^2 \kappa t/\beta - \frac{1}{2} \tan^{-1}(\kappa t/\alpha), \qquad \beta(t) = 4(\kappa^2 t^2 + \alpha^2).$$

The corresponding velocity and the acceleration response of the beam can be obtained by differentiating the dispacement response $y(x,t)$ with respect to time.

The preceding closed-form solution is utilized to analyze the propagation of bending waves on an infinite beam. In the numerical simulations, the properties and the cross-sectional dimensions of the beam were matched to the physical setup used in later experiments. The system consisted of a steel beam having a cross sectional area 50.8 by 6.35 mm. The time-response of the beam was calculated at two different field points; one at $x = 0$ and the other at $x = 2.858$ m. The response of the system was obtained by considering an impulsive excitation applied at the origin, which was simulated by using the initial velocity distribution given in equation (3.11) and by letting the initial dispacement $y_0 = 0$.

The vibration response of the beam at the two field points are plotted in Figure 3.1. For clarity, the time axis is shifted artificially by 2 ms, and the actual starting point for calculated response (the positive-time) is indicated by arrows. The wave motion is initiated by the sharp impulsive acceleration observed at the origin, as shown in Figure 3.1a. Since the simple harmonic wave components making up this initial pulse are travelling at different phase speeds, the dispersion process spreads the wave components apart. Therefore each component arrives to the later field point at different times, as observed in Figure 3.1b. The corresponding velocity and displacement of the beam are given in Figures 3.1c and 3.1d.

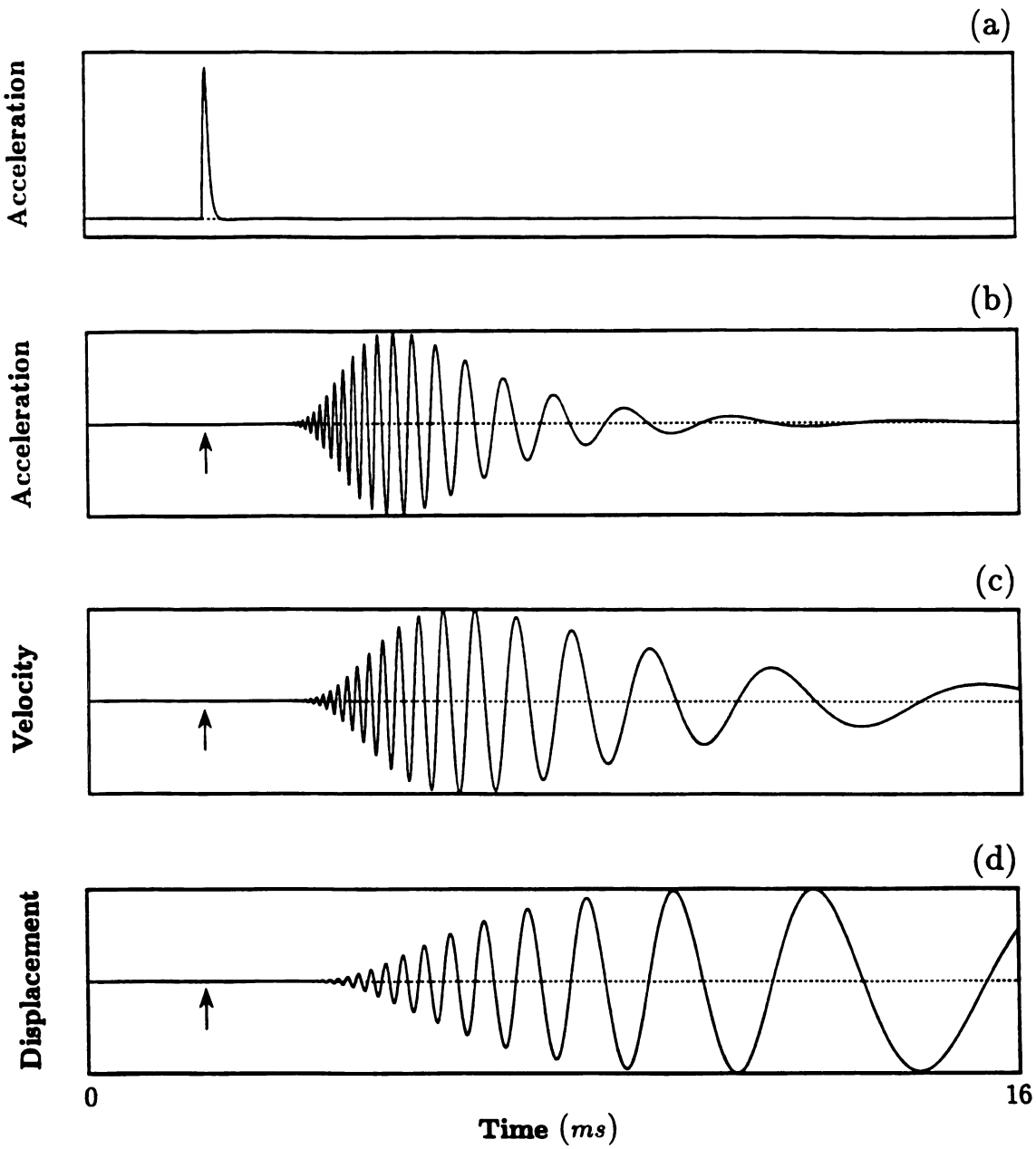

Figure 3.1 The vibration response of an infinite beam following an impulsive excitation; a) acceleration at $x = 0$, b) acceleration at $x = 2.858\ m$, c) velocity at $x = 2.858\ m$, and d) displacement at $x = 2.858\ m$.

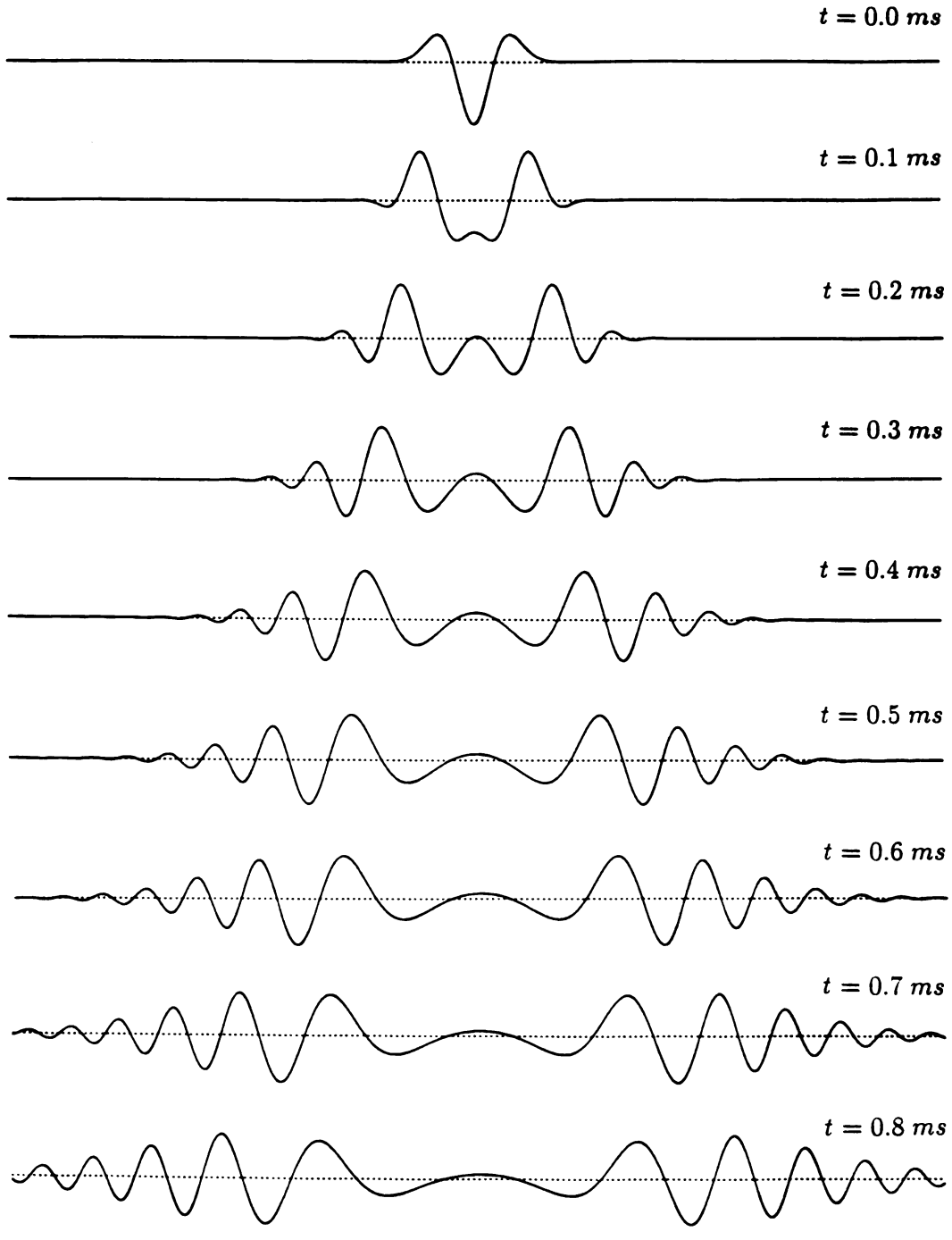

Figure 3.2 The spatial distribution of the velocity response of the beam at successive time intervals.

The envelope is observed to stretch out in time as moved from the acceleration to displacement response of the beam.

In order to clarify the dispersion phenomena, the spatial distribution of the velocity response is plotted in Figure 3.2 at successive time intervals. It is interesting to note that, substitution of $g(x)$ from equation (3.11) into equation (3.9) generates the second derivative of the Gaussian function which was treated in detail in section 2.3 as the Mexican Hat wavelet. In other words, the velocity distribution induced by the impulsive excitation of the beam is approximated by the negative of the Mexican hat wavelet function, which is plotted in Figure 3.2 at $t = 0.0\ ms$. At later instances, the shape of the original pulse is immediately lost as the wave components start to propagate in negative and positive directions. As time progresses, it is observed from Figure 3.2 that the short-wavelength (high-frequency) components are travelling ahead of the group while the long-wavelength (low-frequency) components are trailing behind them. As a result, an observer sitting at a later field point will record a sequence of wave components arriving at different times, with the high-frequency components leading the group.

When the components making up an original transient waveform are spread over a wide spectral range, the resulting evolution of the spectrum becomes a natural candidate for the wavelet transform analysis. The reason is that the self-adjusting window structure of the wavelet transform results in a time-scale representation that displays the growth of the spectral components with varying resolutions. Therefore, as demonstrated in the following examples, the wavelet transform is an effective tool and a perfect match for the analysis of transient waves propagating in a dispersive medium.

The wavelet transform of the acceleration signal at the two field points are plotted in Figures 3.3 and 3.4. These contour plots have a range $20\,dB$ with $1\,dB$ rise per contour. The time-scale representation given in Figure 3.3 looks very similar to the wavelet transform of the unit sample pulse given in Figures 2.16 and 2.17. The curved ridge of the wavelet transform observed in Figure 3.4 is a

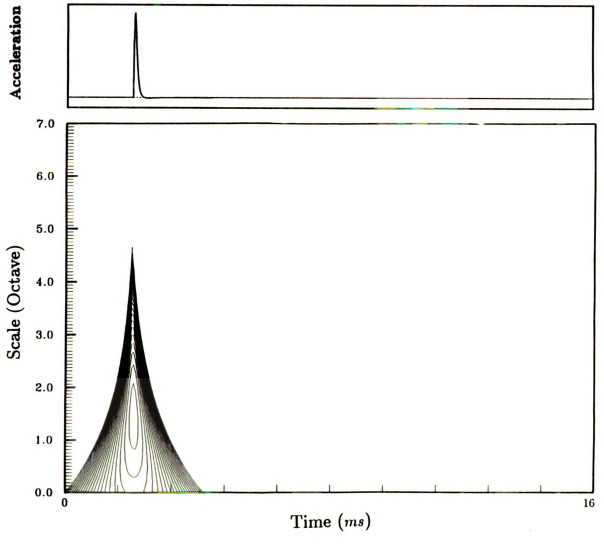

Figure 3.3 The wavelet transform of the acceleration response at $x = 0$. (Analytical).

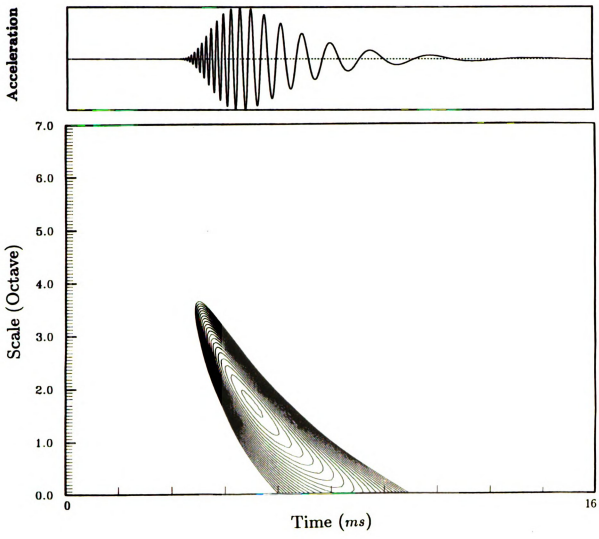

Figure 3.4 The wavelet transform of the acceleration response at $x = 2.858\,m$. (Analytical).

characteristic of the dispersion phenomena. A more detailed discussion of similar time-frequency representations is given following the experimental results.

The wavelet transform not only generates time-frequency representations, but it can also be used to characterize the dynamic behavior of a system in the space-wavenumber domain. For the present problem, the spatial distribution of the acceleration response is obtained at two different times and plotted at the top of Figures 3.5 and 3.6. Note that, in these figures, the scale represents the wavenumber. A comparison of the space-wavenumber representations given in Figures 3.5 and 3.6 reveals that the high-wavenumber components are leading the wave group while low-wavenumber components are trailing behind them. Since according to the dispersion relationship, given in equation (3.7), the wavenumber is proportional to the half power of the frequency, a large wavenumber is associated with a high frequency. Therefore, the curved ridges observed in Figures 3.4 and 3.6 complement each other in a nice way.

In the following experimental analysis, the preceding analytical results are confirmed and further details of the dispersion phenomena are discussed.

3.3.2 Bending Waves on a Semi-Infinite Beam: Experimental Analysis

A semi-infinite uniform beam was used in the experimental study of propagation and dispersion of bending waves. The excitation of the beam at the free-end is expected to generate a response that is comparable to the response of an infinite beam discussed earlier. The mathematical model implies that, in a semi-infinite beam, any disturbance initiated at the free end would propagate away for ever. In a physical system, this infinite propagation condition is simulated on a finite beam by using an unechoic termination. For bending vibrations, burying one end of a long beam into a fine-grained dry sand, as sketched in Figure 3.7, gives a quite satisfactory result in terms of simulating an unechoic termination.

The experimental setup, sketched in Figure 3.7, consisted of a slender steel beam with one end buried in a sand box. The beam was 50.8 by 6.35 mm in cross-section and 3.658 m in total length. Two miniature accelerometers were

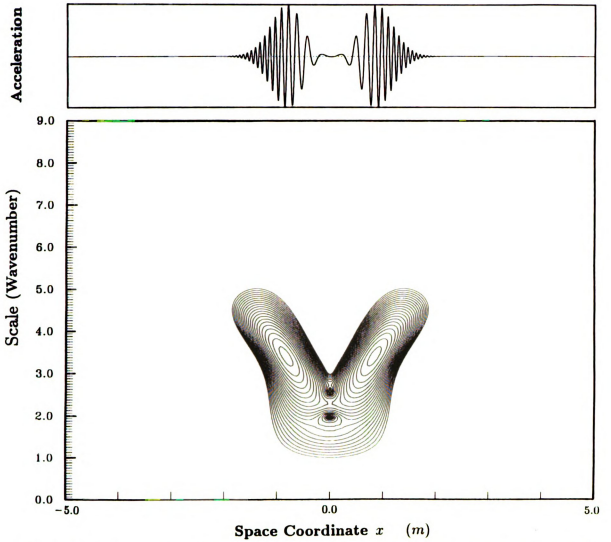

Figure 3.5 The space-wavenumber distribution for the acceleration response of the beam at time $t = 1\ ms$.

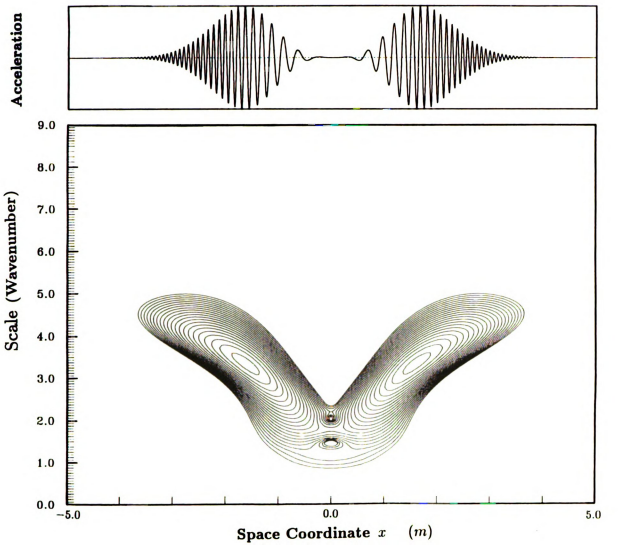

Figure 3.6 The space-wavenumber distribution for the acceleration response of the beam at time $t = 2\ ms$.

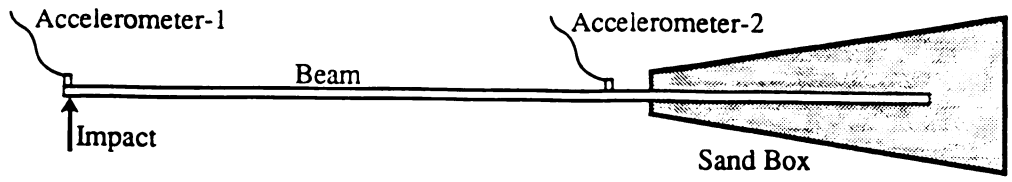

Figure 3.7 The experimental setup used for the simulation of a semi-infinite beam.

mounted firmly on the beam, one at the free end and the other further down the beam near the sand box, at a distance 2.858 m from the free end. An impulsive force was applied to the beam by using two different impacters. First, a tuned impact hammer having a myler tip was employed; and later, a small glass ball was used. The acceleration data from the two accelerometers was recorded and later analyzed by using a computer code performing the wavelet transform.

In the experiments, a hammer blow was applied to the beam at the tip of the free end in a direction parallel to the horizontal plane. The initial instances of the signal measured from the accelerometer, mounted just across the impact point, is displayed at the top of Figure 3.8. Note that, the reflection from the sand covered end of the beam is observed to be negligible, thus confirming the effectiveness of the unechoic termination. The wavelet transform of this initial acceleration signal given in Figure 3.8 is repeated as a color-coded magnitude plot in Figure 3.10a. The contours in Figure 3.8 have $20\,dB$ range with $1\,dB$ rise per contour. The center frequencies of the Morlet wavelet filters, in Figures 3.8-3.10, correspond to $f_c^m = 2^m \cdot 400\ Hz$, with $m = 0, ..., 7$. Since the acceleration signal generated by the initial impact is very similar to the impulsive excitation used in

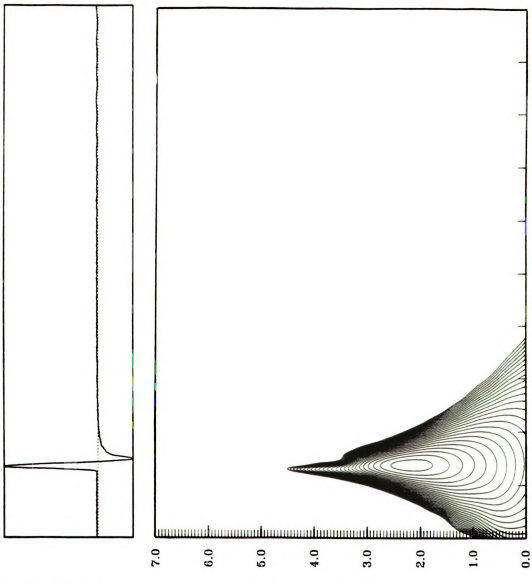

Figure 3.8 The wavelet transform of the signal measured from the accelerometer-1.

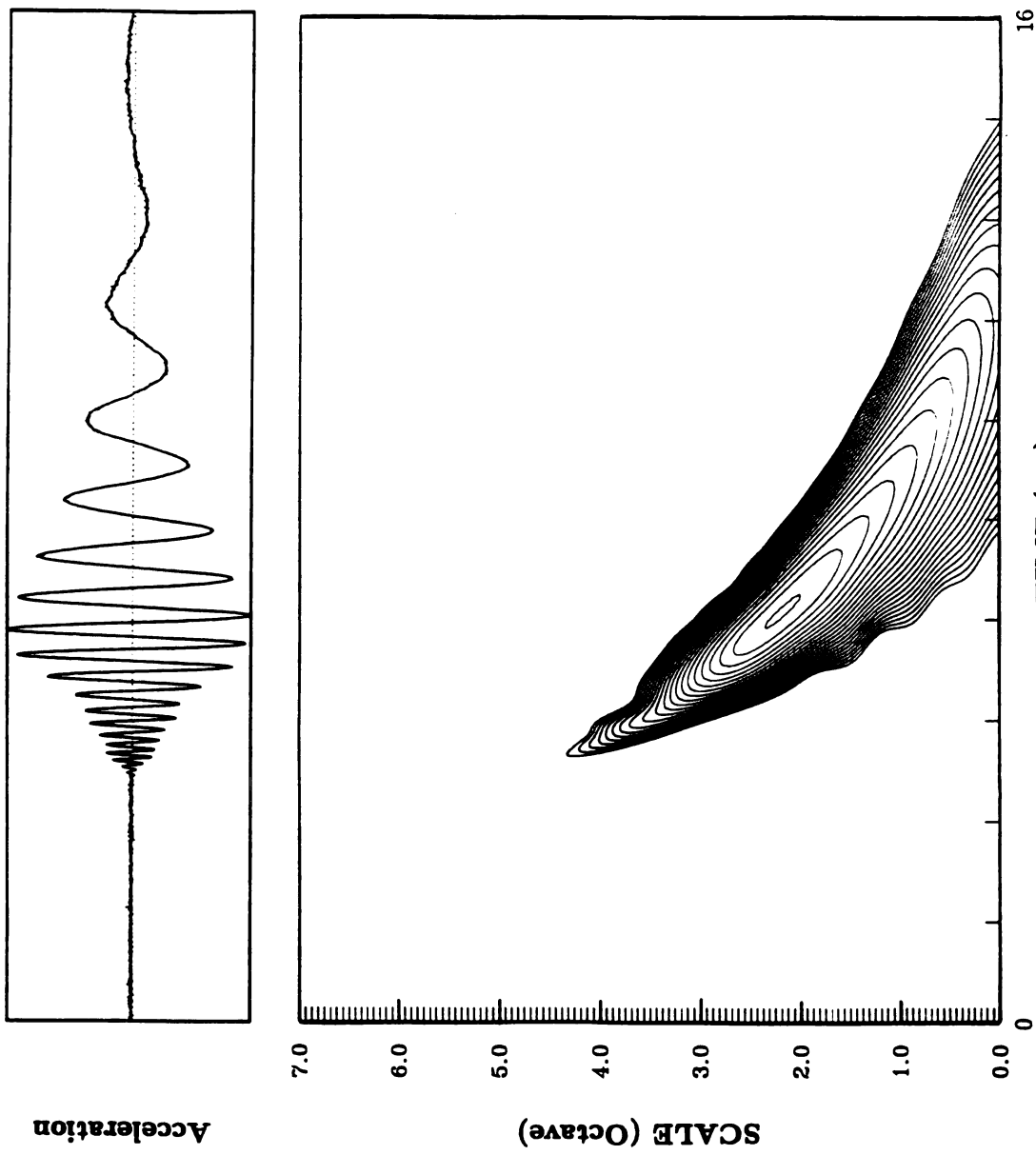

Figure 3.9 The wavelet transform of the signal measured from the accelerometer-2.

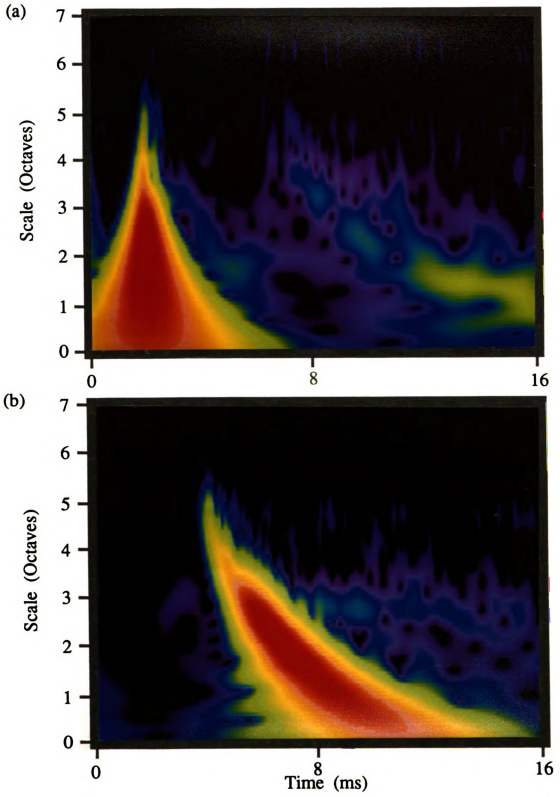

Figure 3.10 Color-coded plots for the wavelet transform of the signals measured from a) accelerometer-1 and b) accelerometer-2.

the analytical model, the wavelet transforms shown in Figures 3.3 and 3.8 have very similar features.

Following the initial impact, each individual progressive wave component constituting the initial waveform propagates with a different phase velocity. Therefore, the waveform is dispersed as the waves forming the original pulse propagate toward the second observation point. The acceleration response of the beam at the second observation point, given in Figure 3.9, shows that the high frequency progressive wave components are leading the wave group, while the low frequency components are trailing behind them. The wavelet transform of the acceleration signal, given in Figures 3.9 and 3.10b, displays clearly the evolution of the spectral components during the dispersion phenomena. The contours in Figure 3.9 have $20\,dB$ range with $1\,dB$ rise per contour. The similarity between the analytical time-frequency representation given in Figures 3.4 and the experimental one given in Figure 3.9 is quite remarkable. The curved shape of the graph observed in Figure 3.10b confirms the inverse relationship $T \propto 1/\sqrt{\omega}$ between the arrival time T and the frequency ω. In order to have a correct interpretation of such time-scale representations, the information exposed by the wavelet transform needs to be clarified in the context of wave dispersion.

So far in this study, the discussion of the dispersion phenomena was based on the simple harmonic progressive wave decomposition of the original transient waveform. However, in order to interpret a wavelet transform, the building block needs to be changed to the "progressive wavelet components". A progressive wavelet component is nothing more than a group of simple harmonic wave components added together. For example, the Fourier transform of the mother wavelet given in Figure 2.10(b) can be interpreted as a continuous group of simple harmonic progressive wave components that has a Gaussian distribution about a center frequency. Thus, each wavelet component is characterized by an associated group of waves that have a particular propagation speed given by equation (3.8). The center frequency of a wavelet component determines the group velocity and thus the arrival times in Figure 3.10(b). For example, in Figure 3.10 the center

frequency, $3200Hz$, corresponding to the third octave results in a group velocity of $866.8\ m/s$. Considering the distance travelled, from the free end up to the second observation point, this group velocity yields an arrival time of $3.3\ ms$; which is in good agreement with $3.5\ ms$ measured from the wavelet transform results given in Figures 3.10a and 3.10b.

3.3.3 Wave-Guide Behavior of a Beam

In order to extend the use of the wavelet transform, the wave-guide behavior of the semi-infinite beam was investigated experimentally. The myler tipped impact hammer used in the preceding experiments was capable of exciting only the broadband mid-frequencies of the steel beam. In the second set of experiments conducted on the same setup, higher frequencies were excited by using a small glass ball as an impacter. The glass ball was hung from a string and then swung from an initially displaced position to hit the free end of the beam at a point half-way across its height. The impact of the glass ball excited the high-frequency bending modes across the height of the specimen. Therefore, in addition to the fundamental bending wave mode propagating along the beam, now the propagation of the first plate-mode was also recognized in the results. Consequently, the beam started to behave more like a wave-guide.

The time traces of the two accelerometer signals recorded after the initial impact are plotted at the top of Figures 3.11 and 3.12. The corresponding wavelet transforms given in these figures are repeated as color-coded plots in Figure 3.13. The contours in Figures 3.11 and 3.12 have $20\,dB$ range with $1\,dB$ rise per contour. The center frequencies of the Morlet bandpass wavelet filters correspond to $f_c^m = 2^m \cdot 400\ Hz$, with $m = 0, ..., 7$. These time-scale representations reveal that the impact of the glass ball has excited the fundamental flexural mode across the height of the beam. By considering the free edges across the height, the fundamental resonance is predicted as $12890\ Hz$; which is comparable to the value $12930\ Hz$ measured form the physical system. Therefore in Figure 3.13a, the resonance of the first plate-mode is extending along the fifth octave, which has a center frequency of $12800\ Hz$. Due to dissipation, the magnitude of the standing

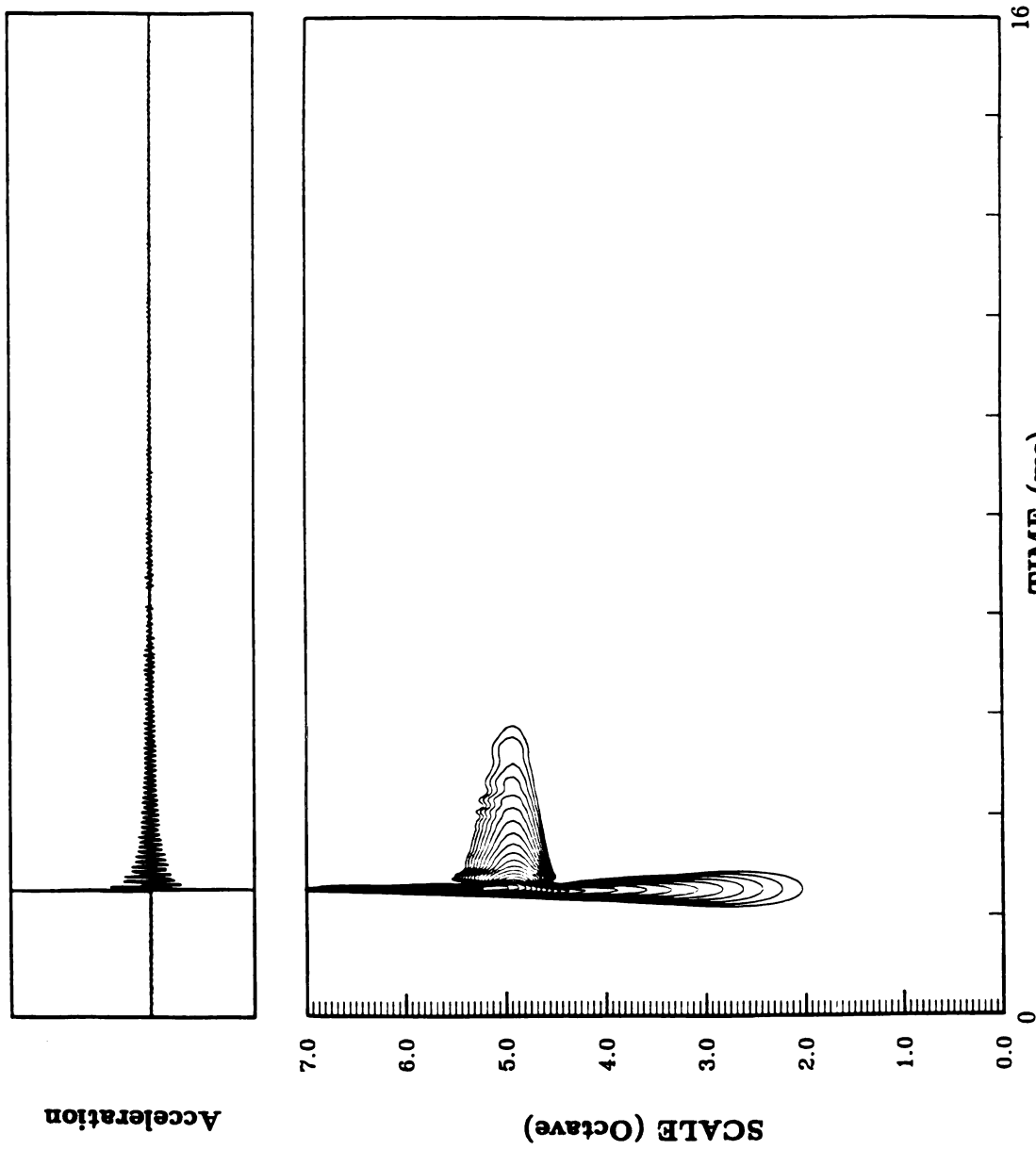

Figure 3.11 The wavelet transform of the signal measured from accelerometer-1.

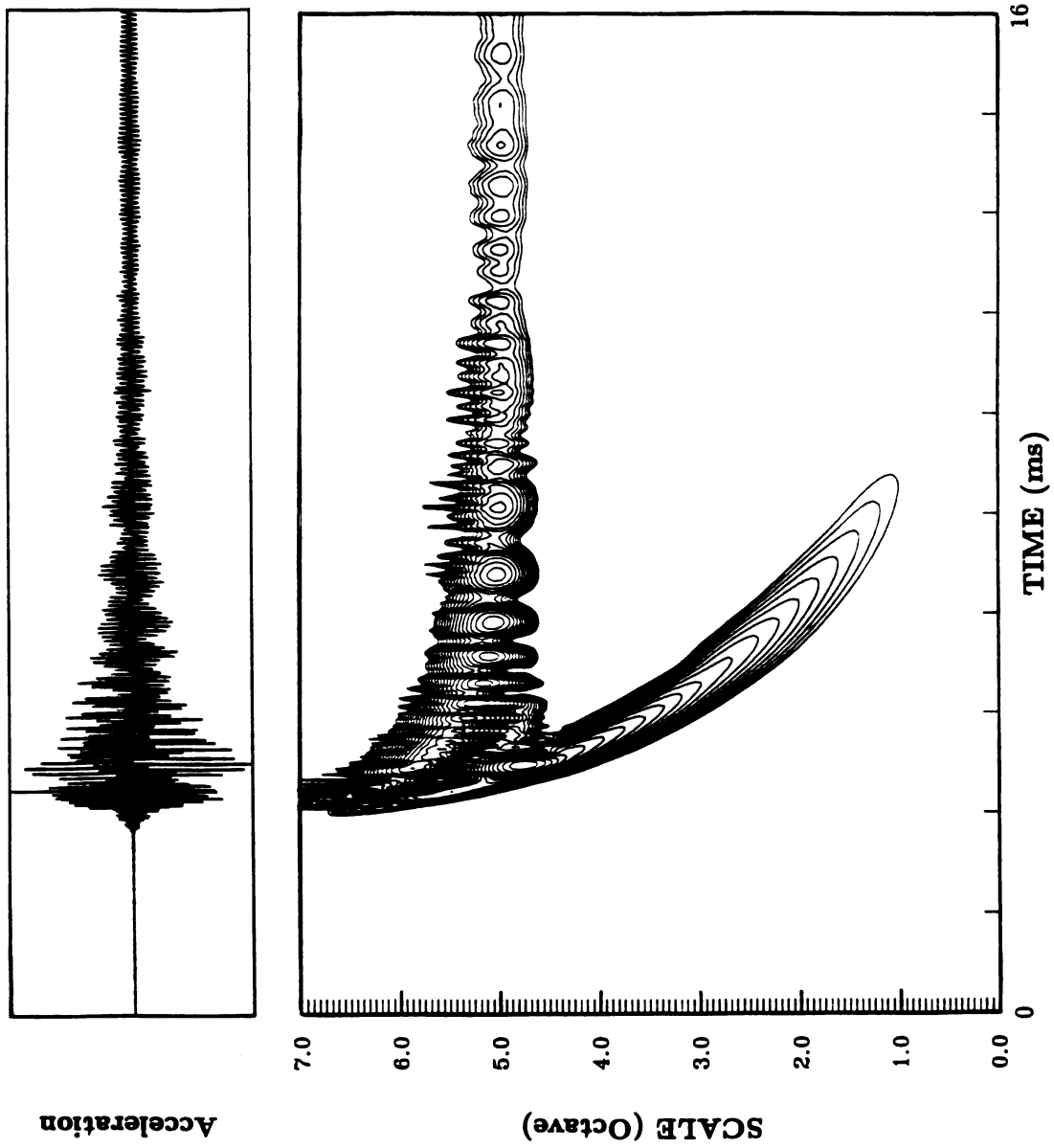

Figure 3.12 The wavelet transform of the signal measured from accelerometer-2.

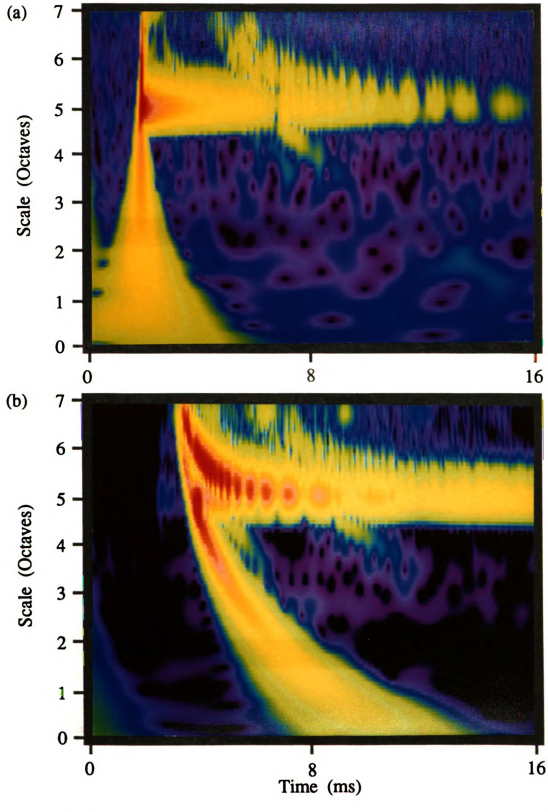

Figure 3.13 Color-coded plots for the wavelet transform of the signals measured from a) accelerometer-1 and b) accelerometer-2.

wave that is set across the height of the beam decays in time following the initial impact. Considering the wave-guide properties of the beam, it is concluded that this higher plate-mode can propagate along the beam only for frequencies higher than the cut-off, 12930 Hz. In Figure 3.13b, the dispersion of the primary bending wave-mode is now accompanied by a secondary dispersion phenomena that extends from higher frequencies down to the cut-off frequency where it decays off. Although the dispersion of the fundamental bending wave-mode is carried all the way down to the lower scales, the dispersion of the plate-mode is contained above the cut-off frequency; since this latter mode can not propagate along the beam at lower frequencies.

The large frequency range of the spectral evolutions observed in this example gives us a good opportunity to compare the two different time frequency representations resulting from the STFT and the wavelet transforms. Therefore, in Figures 3.14-3.16, the acceleration signals obtained from the two field points are re-analyzed by using the STFT. During the application of the STFT to the signals, a Gaussian window was used. The window length is chosen as 512 samples and the translation step size is assigned 16 samples. The contours in Figures 3.14 and 3.15 have 20 dB range with 1 dB rise per contour. Comparison of the wavelet transforms given in Figures 3.11-3.13 with the STFT results given in Figures 3.14-3.16 shows that the general characteristics of the dispersion and cutoff phenomena are represented succesfully by both of the transform techniques. However, the wavelet transform demonstrates a better performance in localization of physical characteristics in the time-frequency plane. For example, in Figure 3.11, the beginning of the initial pulse is localized precisely by the wavelet transform, whereas STFT gives a relatively much wider band in Figure 3.14. Also, the wavelet transform given in Figure 3.12 presents a much more detailed representation for the transient wave motion, which, in comparison, is smeared out in Figure 3.15 due to the constant window structure of the STFT.

The second accelerometer output recorded in this example is used as a reference signal later in Chapter 7 to compare the performance of other wavelet functions.

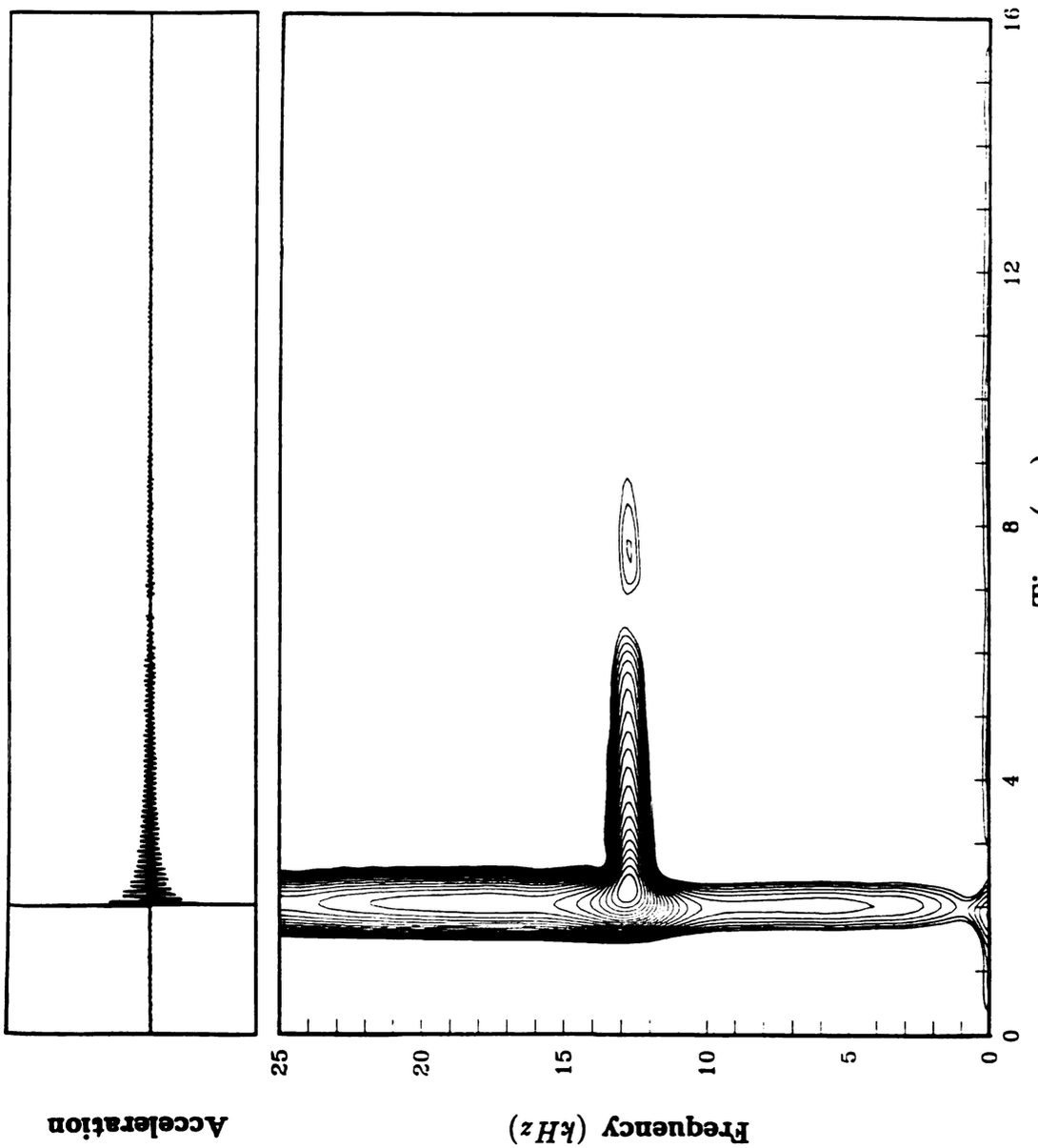

Figure 3.14 The STFT of the signal measured from accelerometer-1.

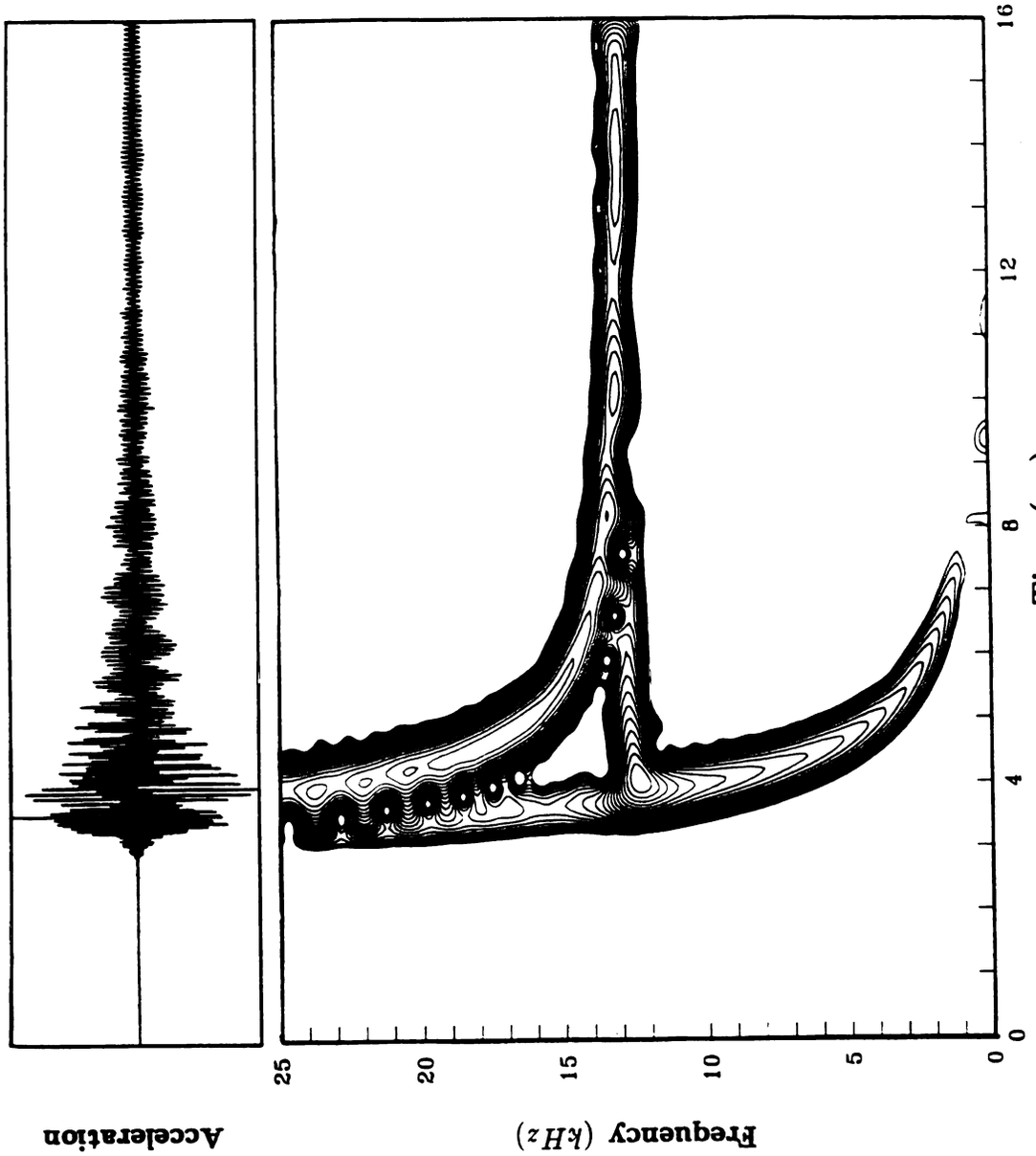

Figure 3.15 The STFT of the signal measured from accelerometer-2.

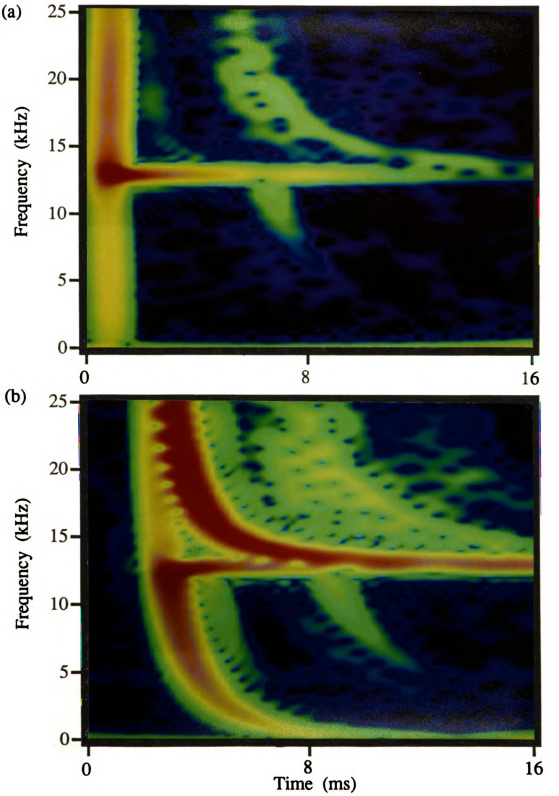

Figure 3.16 Color-coded plots for the STFT of the signals measured from a) accelerometer-1 and b) accelerometer-2.

3.4 Nondispersive Medium: Acoustic Waves in a Pipe

In the case of a nondispersive system, the analysis of transient wave motion becomes relatively more tracktable and leads to easy-to-interpret time-frequency representations. In the following example, the propagation of an acoustic waveform in a long air-filled pipe is analyzed by using STFT and wavelet transforms.

3.4.1 Dispersion Relation for the Acoustic Medium

The equation governing the propagation of an acoustic disturbance is obtained from the Navier-Stokes equations which represent the continuity of fluid mass-flow and the fluid momentum-density. The first-order equation governing an acoustic motion is given by

$$\frac{\partial^2 p(x,t)}{\partial t^2} = c^2 \frac{\partial^2 p(x,t)}{\partial x^2} \tag{3.13}$$

where c is the speed of sound in the medium. The preceding second order PDE is known as the wave equation. The details for the solution of the wave equation, under different initial conditions and boundary impedances, can be found in classical textbooks, such as [92,102,113]. Therefore, here we consider only the simple harmonic progressive wave solution $y(x,t) = \exp(ikx - i\omega t)$ of the governing equation to obtain the dispersion relationship

$$c = \omega/k \tag{3.14}$$

In this case, the definitions of the phase and group velocities given in equations (3.1) and (3.5) imply that $c_p = c_g = c$. Since the phase and group velocities are independent of the frequency of the wave components, the initial shape of a waveform is maintained throughout time and space. In general, the dissipation in the medium is expected to attenuate the amplitude of the acoustic waves without effecting its shape. This shape-preserving characteristic of a nondispersive medium is demonstrated in the following example on a physical setup.

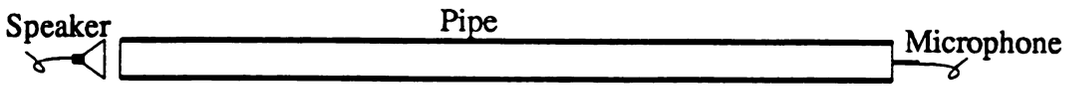

Figure 3.17 A sketch of the setup used for the acoustic pipe experiment.

3.4.2 Experimental Analysis of Acoustic Wave Motion

In this example, the nondispersive wave-bearing medium consists of a long pipe with both ends open to atmospheric air, as sketched in Figure 3.17. A uniform aluminum pipe with 64 mm inner diameter and 2.41 m length was used in the experiments. A measuring microphone was placed at one end of the pipe. The acoustic waveform was generated by using a 75 mm diameter speaker which was placed at a distance 5 cm away from the end of the pipe. This seperation between the speaker and the pipe minimized the interference which otherwise would distort the waveform during its reflections from the boundary. A function generator was used to initiate the pulse. The measured acoustic pressure is plotted at the top of Figure 3.18. Form this time trace, it is oberved that the shape of the pulse is maintained despite the reflections from the free boundaries. The time interval between each arrival of the pulse at the microphone is calculated as $T = 2L/c = 14.05\ ms$. This prediction compares well with the measured value $T = 14.10\ ms$, which corresponds to the time intervals between the center of the peaks in the wavelet transform given in Figure 3.18. The contours in Figure 3.18 have 40 dB range with 2 dB rise per contour. The center frequencies of the Morlet wavelet filters are given by $f_c^m = 2^m \cdot 200\ Hz$, with $m = 0, ..., 7$. The time-scale representation shown in Figure 3.18 demonstrates that the original signature of the waveform is repeated in each cycle as the waveform propagates in the pipe.

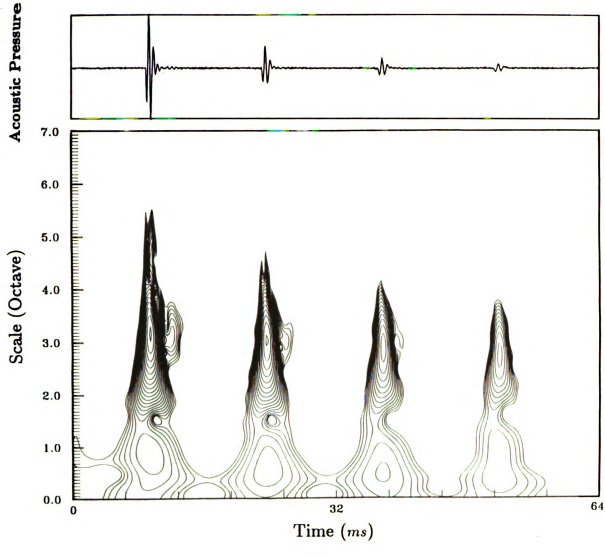

Figure 3.18 The wavelet transform of the acoustic pressure signal.

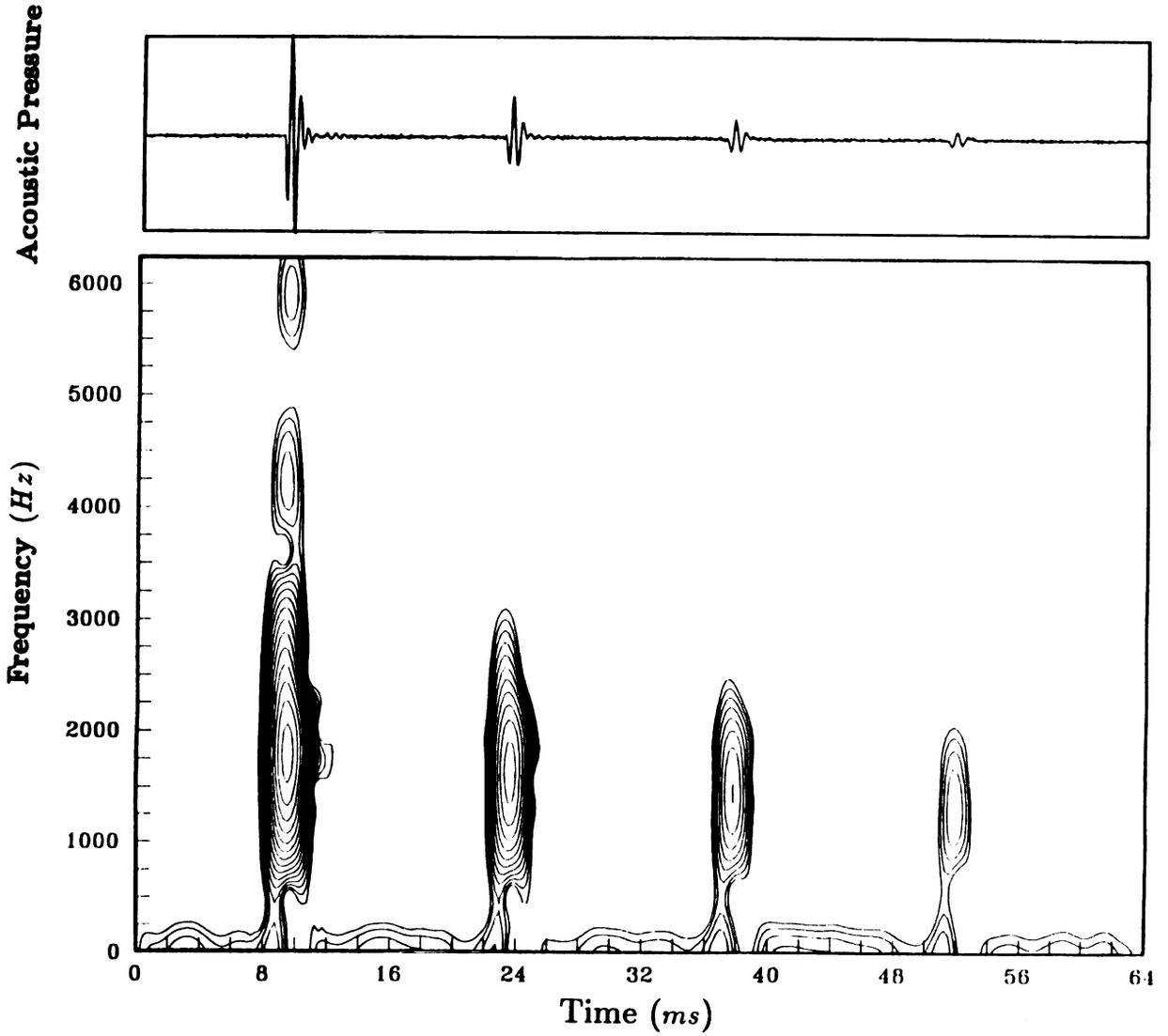

Figure 3.19 The STFT of the acoustic pressure signal.

As time progresses, the amplitude of the waveform becomes attenuated, but its shape is preserved.

In order to give a comparison, the STFT of the same acoustic pressure signal was performed and the result is plotted in Figure 3.19. The STFT was performed by using a Gaussian window. In Figure 3.19, the contours have $40\,dB$ range with $2\,dB$ rise per contour. The window length is chosen as 512 samples, and the translation step size is assigned 16 samples. As observed from Figure 3.19, some of the basic features of the acoustic wave motion is also captured by the STFT with a reasonable localization. However, the time-frequency representation given in Figure 3.19 lacks the low frequency detail and the sharp time localization characteristics demonstrated by the wavelet transform in Figure 3.18.

3.5 Discussion and Conclusions

In summary, the preceding examples gave a clear demonstration of the advantages of using a time-frequency representation for the analysis of transient wave motion. In particular, transient wave propagation in a dispersive medium is found to be a perfect example for the effective use of the self-adjusting window and variable resolution properties of the wavelet transform. The wavelet transform is capable of displaying the details of the spectral evolutions over a wide range of frequencies. In essense, the wavelet transform is expected to work equally well in other physical phenomena that have similar wide-band scaling and time-evolving characteristics.

The preceding examples demonstrated that the time-scale representations (TSR) generated by the wavelet transform reveal distinctive signatures of transient waveforms and help to identify the wavebearing characteristics of the medium. The arrival times observed from the wavelet transform are associated with the group velocities of the wavelet components. In the analysis of wave-guides, the wavelet transform is shown to be an effective tool in seperating the evolution of different wave-modes and in analyzing the cut-off phenomenon. In a nondispersive medium, time-frequency analysis helps to localize echos from the boundaries. The

local spectral content of the reflected waves are used to identify the dynamic characteristics of the boundaries and the propagator itself.

As an alternative, space-wavenumber representation (SWR) is introduced for a one-dimensional system. The display of SWRs succesively in time gives a clear picture of the spatial-evolution of the wave components. Since it is quite difficult to perform a high-resolution simultaneous measurement of space-dependent response of a physical system, SWRs are expected to be of more use in the analysis of analytical signals.

In the following chapter, the degree of difficulty involved in the analysis of dispersion phenomenon is increased by including other complicating effects, such as multiple reflections of waves from the boundaries.

CHAPTER 4

WAVE PROPAGATION IN FINITE STRUCTURES: TRANSFER MATRICES AND WAVELET TRANSFORM

In the following, the self-adjusting (zooming) window structure of the wavelet transform is utilized to analyze complex transient wave-interference patterns generated by the reflections in a finite dispersive medium. The flexural vibration of a beam is used as an example to study the propagation, reflection and dispersion of a transient waveform. In order to analyze different beam configurations easily, the general frequency response function of a single-span beam is formulated by using impedance boundary conditions in a transfer matrix method. For a free-free beam, the results obtained from the numerical analysis are confirmed by experimental measurements. The wavelet transform of the acceleration signals resulted in symmetric grid-patterns in the time-scale domain, and led to the discovery of an interesting pulse reconstitution phenomenon.

4.1 Introduction

In an unbounded continuous medium, if there are no impedance discontinuities in the field, the propagation characteristics of a transient waveform will depend only on the properties of the wavebearing medium. However, in a physical structure, the dispersion phenomenon is usually accompanied by additional effects, such as reflection and scattering of the wave components which are caused by impedance discontinuities, boundaries and external disturbances. In such cases, the interaction of the incident and reflected wave components may result in complex wave interference patterns which are difficult to analyze by using one-dimensional spectral methods. In the analysis of such complex transient wave motion, the use of time-frequency or space-wavenumber representations may

provide an effective means for studying time and space evolution of the spectral components contained in the transient response. The transient vibration response of a system can be obtained either by experimental measurements or by numerical simulations of an analytical model.

One of the effective ways of determining the transient vibration response of a linear time-invariant system is based on the use of the frequency response function together with the excitation in a convolution integral. In the analysis of linear one-dimensional systems, the frequency response function can be determined by using a transfer matrix method. Here, the word "dimension" refers to the number of independent space coordinates. In literature [80,86-91,106,107,110], the effectiveness of the transfer matrix approach has been already established during the analysis of different one-dimensional systems. Particularly, the use of wave-mode representations in the transfer matrices has made the approach analytically more tracktable and numerically more efficient [107].

In the following, the transfer matrix approach is employed to formulate the frequency response function (FRF) of a point-excited single-span beam that has general impedance boundary conditions. The formulated FRF is utilized to construct the transient vibration response of different beam configurations. Later, the results are analyzed by using the wavelet transform and compared with experimental findings.

4.2 Transfer Matrices: General Method of Analysis

When a one-dimensional vibro-acoustic system performs single-frequency time-harmonic vibrations, it is often possible to seperate the time and space dependence. In such problems, the spatial distribution of the vibration amplitude is governed in general by a set of ordinary differential equations (ODEs). These governing ODEs can be transformed into a general state-space form [106,107]

$$\frac{d\mathbf{v}}{dx} = \mathbf{A}\,\mathbf{v} + \mathbf{f} \tag{4.1}$$

where $\mathbf{v}, \mathbf{f} \in \mathbf{C}^n$ and $\mathbf{A}$ is a complex matrix. The elements of $\mathbf{v}$, $\mathbf{f}$ and $\mathbf{A}$ represent system variables, external forces and system parameters, respectively. The most crucial step in the development of transfer matrices is the construction of the modal matrix $\mathbf{M}$ which follows from the eigenvalues and eigenvectors of the system matrix $\mathbf{A}$. The modal matrix is used to transform equation (4.1) into an uncoupled phase variable canonical form

$$\frac{d\mathbf{z}}{dx} = \mathbf{\Lambda}\,\mathbf{z} + \mathbf{M}^{-1}\,\mathbf{f} \tag{4.2}$$

where the elements of the diagonal matrix $\mathbf{\Lambda}$ represent the eigenvalues of $\mathbf{A}$. The preceding uncoupled form allows the solution of the system response as

$$\mathbf{z}(x) = \mathbf{T}_{(x-x_0)}\,\mathbf{z}(x_0) + \int_{x_0}^{x} \mathbf{T}_{(x-\xi)}\,\mathbf{M}^{-1}\,\mathbf{f}(\xi)\,d\xi \tag{4.3}$$

The matrix exponent $\mathbf{T}_{(x-x_0)} = e^{\mathbf{\Lambda}(x-x_0)}$ is known as the field transfer matrix of the system. Using $\mathbf{z} = \mathbf{M}^{-1}\mathbf{v}$, the system response is transformed from the canonical form back into the physical state variable representation

$$\mathbf{v}(x) = \mathbf{M}\,\mathbf{T}_{(x-x_0)}\,\mathbf{M}^{-1}\,\mathbf{v}(x_0) + \int_{x_0}^{x} \mathbf{M}\,\mathbf{T}_{(x-\xi)}\,\mathbf{M}^{-1}\,\mathbf{f}(\xi)\,d\xi \tag{4.4}$$

The effectiveness of the transfer matrix method is not only due to the compactness and ease of deriving the solutions, but also comes from the interpretation of the results in both physical and canonical state variable representations. It is known [106,107,134] that the elements of the canonical state vector $\mathbf{z}$, represent the complex amplitudes of the wave-modes which are present in the system. The canonical form of the solution given in equation (4.3) implies that the complex wave amplitudes are transfered from a station at x_0 to a latter station at x by applying the field transfer matrix and by adding the contributions from the external disturbances. During this operation, the diagonal form of the field transfer matrix renders the approach analytically more tractable and computationally less

involved. In addition, by equating the complex eigenvalue λ to ik in the characteristic equation, $\det|\lambda\mathbf{I} - \mathbf{A}| = 0$, one can obtain a dispersion relation for the wave-bearing medium [106].

An outstanding feature of the transfer matrix method is that the inclusion of boundaries and different constraints does not increase the size of the matrices. Such physical complexities are handled very efficiently in a compact form by performing simple matrix algebra, which is demonstrated later in the applications. After the inclusion of all the constraints, one always ends up with a fundamental relation of the form [106]

$$\mathbf{B}\,\mathbf{z} = \mathbf{b} \tag{4.5}$$

where $\mathbf{z}$ is the reference state that is being solved. The physical characteristics of the system and the external disturbances are represented by $\mathbf{B}$ and $\mathbf{b}$, respectively. The solution of $\mathbf{z}$ requires the inverse of the matrix $\mathbf{B}$, which will exist only if $\det(\mathbf{B}) \neq 0$. This condition is satisfied for most physical systems, since there is always some kind of mechanism that dissipates energy. Consequently, as the frequency ω is varied no true resonances (singularities) are encountered, and the amplitude of the response stays finite.

The transfer matrix approach defined above is employed in Appendix F to formulate the general bending vibration response of a flexible beam. The transfer matrices, derived in Appendix F, are applied in the following to formulate the vibration response of a single-span beam.

4.3 Vibration Response of a Single-Span Beam

A single-span uniform beam is considered to have arbitrary boundary conditions represented by mechanical impedances, as sketched in Figure 4.1. The response of the beam to a concentrated force F_0 acting at $x = \alpha_f L$ is obtained in terms of the transfer matrices; starting from the left-hand side, the relationship between the states $\mathbf{z}(x)$ and $\mathbf{z}(0)$ can be expressed as

$$\mathbf{z}(0) = \mathbf{T}_{(-x)}\,\mathbf{z}(x) \tag{4.6}$$

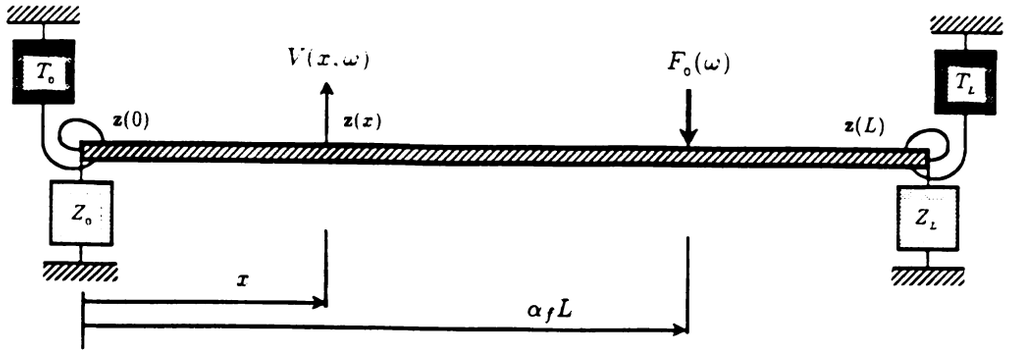

Figure 4.1 A single-span beam with general translational and rotational impedance boundary conditions and a point force.

Similarly, the relationship between the states $\mathbf{z}(x)$ and $\mathbf{z}(L)$ is obtained from equation (F.10) as

$$\mathbf{z}(L) = \mathbf{T}_{(L-x)}\,\mathbf{z}(x) + \mathbf{T}_{(L-\alpha_f L)}\,\mathbf{C}^{-1}\,\mathbf{K}^{-1}\,\mathbf{f}_0 \tag{4.7}$$

where, for the present problem, $\mathbf{f}_0 = \left[\begin{array}{cccc} 0 & 0 & 0 & -i\omega F_0(\omega)/B \end{array}\right]^{\mathrm{T}}$.

The boundary conditions, given in equation (F.28), require that

$$\begin{bmatrix} 1 & 0 & \ell_{11} & \ell_{12} \\ 0 & 1 & \ell_{21} & \ell_{22} \end{bmatrix} \mathbf{z}(0) = 0, \qquad \begin{bmatrix} r_{11} & r_{12} & 1 & 0 \\ r_{21} & r_{22} & 0 & 1 \end{bmatrix} \mathbf{z}(L) = 0 \tag{4.8}$$

where ℓ_{ij} and r_{ij} are the corresponding elements of the reflection matrices, $\mathbf{R}_0$ and $\mathbf{R}_L$, defined in equation (F.26).

The four matrix relations, given in equations (4.6-4.8), are sufficient to determine the velocity response of the system. In order to solve for the reference state of the flexural vibrations, $\mathbf{z}(x)$, the state vectors at the boundaries, $\mathbf{z}(0)$ and $\mathbf{z}(L)$, are eliminated by substituting equations (4.6) and (4.7) into equation (4.8).

Then, the resulting two matrix equations are combined into a single partioned-matrix relation as

$$\underbrace{\begin{bmatrix} \mathbf{A}_0\,\mathbf{T}_{(-x)} \\ \hline \mathbf{A}_L\,\mathbf{T}_{(L-x)} \end{bmatrix}}_{\mathbf{B}} \mathbf{z}(x) = \underbrace{\begin{bmatrix} \mathbf{0} \\ \hline -\mathbf{A}_L\,\mathbf{T}_{(L-\alpha_f L)}\,\mathbf{C}^{-1}\,\mathbf{K}^{-1}\,\mathbf{f}_0 \end{bmatrix}}_{\mathbf{b}} \tag{4.9}$$

which is in the general form defined in equation (4.5). In the preceding equation,

$$\mathbf{B} = \begin{bmatrix} e^{-ik_p x} & 0 & \ell_{11}e^{ik_p x} & \ell_{12}e^{-k_p x} \\ 0 & e^{k_p x} & \ell_{21}e^{ik_p x} & \ell_{22}e^{-k_p x} \\ r_{11}e^{ik_p(L-x)} & r_{12}e^{-k_p(L-x)} & e^{-ik_p(L-x)} & 0 \\ r_{21}e^{ik_p(L-x)} & r_{22}e^{-k_p(L-x)} & 0 & e^{k_p(L-x)} \end{bmatrix} \tag{4.10}$$

$$\mathbf{b} = \begin{bmatrix} 0 & 0 & \gamma_3 & \gamma_4 \end{bmatrix}^{\mathrm{T}} \tag{4.11}$$

where, by assigning $\lambda = k_p L$, the elements of the vector $\mathbf{b}$ are defined as

$$\gamma_3 = \frac{i\omega F_0(\omega)}{4 B k_p^3}\left[i r_{11}\, e^{i\lambda(1-\alpha_f)} - r_{12}\, e^{-\lambda(1-\alpha_f)} - i\, e^{-i\lambda(1-\alpha_f)} \right]$$

$$\gamma_4 = \frac{i\omega F_0(\omega)}{4 B k_p^3}\left[i r_{21}\, e^{i\lambda(1-\alpha_f)} - r_{22}\, e^{-\lambda(1-\alpha_f)} + e^{\lambda(1-\alpha_f)} \right]$$

The eigenfrequencies of an undamped system are determined from its charateristic equation, by solving $\det(\mathbf{B}) \equiv \Delta = 0$, where

$$\Delta = \ell_s\, r_s\, e^{-(1-i)\lambda} - \ell_{22}\, r_{22}\, e^{-(1+i)\lambda} - \ell_{11}\, r_{11}\, e^{(1+i)\lambda} + e^{(1-i)\lambda} - (\ell_{21}\, r_{12} + \ell_{12}\, r_{21}) \tag{4.12}$$

In the preceding equation, $\ell_s = (\ell_{11}\,\ell_{22} - \ell_{12}\,\ell_{21})$ and $r_s = (r_{11}\,r_{22} - r_{12}r_{21})$. It is clear that for an undamped system, the characteristic equation gives real roots, λ_i. However, if damping is present, the roots will have both real and imaginary parts. In a physical system, the presence of any form of energy dissipation, such as

an impedi

premultip

of the sy

variables.

back tran

points alc

given earl

Th

transfer m

transfer m

$$H_{zf}(\omega) = \frac{1}{\Delta}$$

where r_b =

for the reg

is the same

and $x = L$

equation (

Sim

when the b

characteris

$$(r_{11} r_{22} -$$

As a specif

$r_{11} = r_{22} =$

an impedance boundary, guarantees the existence of $\mathbf{B}^{-1}$. Under such conditions, premultiplying the right-hand-side of equation (4.9) with $\mathbf{B}^{-1}$ gives the response of the system in terms of the phase-variable canonical form $\mathbf{z}(x)$. The physical variables, such as the velocity amplitude $V(x,\omega)$, can be recovered by using the back transformation given in equation (F.16). The velocity amplitudes of other points along the beam can be determined by using the state transfer relationships given earlier.

The dynamic charateristics of the system can be expressed in terms of the transfer mobility of the system, which is defined as $H_{xf}(\omega) = V(x,\omega)/F_0(\omega)$. The transfer mobility of the system between the points x and $x_f = \alpha_f L$ is obtained as

$$\begin{aligned} H_{xf}(\omega) = \frac{1}{\Delta}\big[& - \ell_{11}\,\gamma_3\, e^{k_p(L+ix)} - \ell_{12}\,\gamma_4\, e^{-ik_p(L-x)} + \ell_{a}\, r_c\, e^{-k_p(L-ix)} - \ell_{a}\, r_b\, e^{k_p(iL-x)} \\ & - \ell_{21}\,\gamma_3\, e^{k_p(L-x)} - \ell_{22}\,\gamma_4\, e^{-k_p(x+iL)} + \gamma_3\, e^{k_p(L-ix)} + \gamma_4\, e^{k_p(x-iL)} \\ & - \ell_{22}\, r_c\, e^{-k_p(L+ix)} - \ell_{12}\, r_b\, e^{ik_p(L-x)} + \ell_{21}\, r_c\, e^{k_p(x-L)} + \ell_{11}\, r_b\, e^{k_p(x+iL)}\big] \end{aligned} \tag{4.13}$$

where $r_b = r_{21}\,\gamma_3 - r_{11}\,\gamma_4$, $r_c = r_{22}\,\gamma_3 - r_{12}\,\gamma_4$ and $x \le \alpha_f L$. The transfer mobility for the region $x > \alpha_f L$ can be readily obtained in a similar manner. The result is the same as that obtained by interchanging the boundary impedances at $x = 0$ and $x = L$, i.e. r_{ij} with ℓ_{ij}, and substituting $(L - x)$ for x, $(1 - \alpha_f)$ for α_f in equation (4.13).

Simplification of equation (4.13) leads to the standard results. For example, when the boundary impedances at $x = 0$ and $x = L$ are made equal, $\ell_{ij} = r_{ij}$, the characteristic equation reduces to

$$(r_{11}\, r_{22} - r_{12}\, r_{21})^2\, e^{-(1-i)\lambda} - r_{22}^2\, e^{-(1+i)\lambda} - r_{11}^2\, e^{(1+i)\lambda} + e^{(1-i)\lambda} - 2 r_{12}\, r_{21} = 0 \tag{4.14}$$

As a specific example, if we consider a pinned-pinned beam, the coefficients become $r_{11} = r_{22} = 1$ and $r_{12} = r_{21} = 0$, which when substituted into equation (4.14) gives

the characteristic equation as $\sin(kl) = 0$, as expected. Other more complex boundary conditions can be analyzed easily by using the above relations in a numerical algorithm.

In the analysis of a single span beam, the general solution for the drive-point mobility, given in equation (4.13), can be used to investigate a wide variety of configurations with different boundary conditions. In the following, a few of the ideal boundary conditions are considered to study the transient wave propagation in a single-span beam.

4.4 Transient Response of a Free-Free Beam: Analytical Study

In literature [45,67,92,97,102,113], transient wave propagation in a finite dispersive medium is known as a challenging analytical problem, since closed form solutions are not tractable for most of the practical systems. Therefore in applications, the propagation of transient waves are studied by employing either numerical or experimental techniques. In the following, the wavelet transform is applied to the analysis of impact induced transient vibrations of a uniform beam for different boundary conditions. The analytical results obtained for a free-free beam are later compared with experimental measurements.

The transient vibration response of a single-span beam at an excitation point can be predicted by using the definition of the drive-point mobility $H_{xf}(\omega) = V(x,\omega)/F_0(\omega)$, stated earlier before equation (4.41). For a given point force $F_0(\omega)$, the velocity response $V(x,\omega)$ is determined in the complex frequency domain. In general, a closed-form solution for the time-domain velocity response $v(x,t)$ is difficult to obtain from $V(x,\omega)$ by using the inverse continuous Fourier transform. Usually, numerical techniques are employed during the calculation of the inverse Fourier transform. The Discrete Fourier Transform (DFT) is one of the methods used commonly in practice, and requires uniform sampling of the response function in the frequency domain. There are well-known pitfalls and limitations related

wi
di
st

di
tic
a
co
ne
ex
ere
an

tio
$\tilde{Z}_L$
the
bea
by
ure
The
with
enc

4.5

an in
ing a
doma
havio

with the application of the DFT, such as the time-domain aliasing problem. These difficulties and alternate solution procedures are discussed seperately later in this study.

In the following numerical simulations, the time-domain response is predicted by using an FFT algorithm. The size of the FFT used during the computations was $N = 2^{15}$, which over a frequency range of $f_{max} = 6.25\ kHz$ resulted in a uniform sampling interval $\delta_f = 0.78125\ Hz$. The spectrum of the force $F_0(\omega)$ is considered to have a Gaussian distribution about the origin and decays by 20 dB near 6 kHz. The spectrum of the force is designed to simulate the sharp impulsive excitation used in the experiments that are discussed later. The beam is considered to be made of aluminum with dimensions 38.1 by 6.35 mm in cross-section and 1.402 m in length.

Since both boundaries of the beam are considered to be free, the translational and rotational impedances on each boundary should be $\widetilde{Z}_0 = \widetilde{T}_0 = 0$ and $\widetilde{Z}_L = \widetilde{T}_L = 0$. The excitation and the observation points are collocated at one of the free ends of the beam. The predicted time domain acceleration response of the beam is plotted at the top of Figure 4.2. The time-scale representation generated by the wavelet transform demonstrates an interesting interference pattern in Figure 4.2. The contours in Figure 4.2 have 20 dB range with 2 dB rise per contour. The center frequencies of the Morlet wavelet filters correspond to $f_c^m = 2^m \cdot 40\ Hz$, with $m = 0, ..., 7$. The details of the physical phenomena governing this interference pattern is discussed in the following experimental analysis.

4.5 Transient Response of a Free-Free Beam: Experimental Analysis

The preceding analytical results showed that, following the application of an impulsive load on a finite beam, the interference of bending waves propagating along the beam may generate an interesting signature in the time-frequency domain. The following experimental results confirm this predicted dynamic behavior and shed light on the physical principles behind the unusual interference

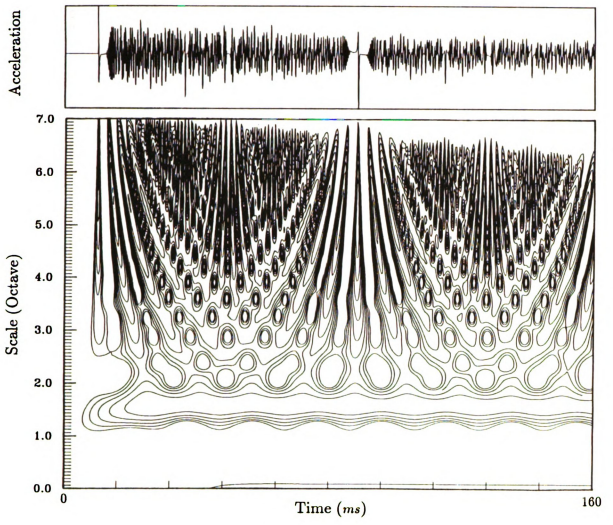

Figure 4.2 The predicted acceleration response of a free-free beam and its wavelet transform.

patterns.
terial pro
different.

4.5.1 Ex

In
was recon
held in a
from each
ends. Ag
free end a
signal is p
instances
following
which the
Upon ref
toward th
the initia
point, wh
reflection
results in
represent
details of

Th
contour a
wavelet t
contours
the Morle
primary
form to t
2.17. Aga

patterns. Two different beam configurations were tested. In each case, the material properties, the length and the cross-sectional dimensions of the beam were different.

4.5.1 Experiments on a Steel Beam

In the first set of experiments, the specimen used in the preceding chapter was reconfigured as a free-free beam with a length $L = 3.658\ m$. The beam was held in a horizontal position by hanging it at two points, at a distance $L/10$ away from each boundary. A miniature accelerometer was mounted at one of the free ends. Again, by using the myler-tipped hammer, the beam was impacted at the free end at a point just across from the accelerometer. The recorded acceleration signal is plotted in Figure 4.3a. In order to display some of the details, the initial instances of the time trace is enlarged in Figure 4.3b. These time traces show that, following the initial occurrence of the pulse, a quiet period of time exists, during which the bending waves travel along the beam toward the other free boundary. Upon reflecting from the other boundary, each wave component propagates back toward the observation point. Since high frequency components that are present in the initial pulse travel at a faster phase speed, they arrive first at the observation point, which is clearly displayed in Figure 4.3b. As time progresses, multiple reflections of waves from the boundaries together with the dispersion phenomena results in a complicated transient interference pattern. In a way, a time-frequency representation helps to unfold this complex interference pattern and expose the details of the time evolution of the spectral components.

The wavelet transform of the signal is given in Figures 4.4-4.6 by using both contour and color-coded plots. In Figures 4.5 and 4.6b, the first quarter of this wavelet transform is enlarged to show more details of the initial instances. The contours have $20\,dB$ range with $1\,dB$ rise per contour. The center frequencies of the Morlet wavelet filters correspond to $f_c^m = 2^m \cdot 20\ Hz$, with $m = 0, ..., 7$. The primary vertical band corresponds to the initial impulse, which is very similar in form to the transform of a unit sample pulse, given earlier in Figures 2.16 and 2.17. Again, following a quiet moment, the first curved band represents the initial

(a)

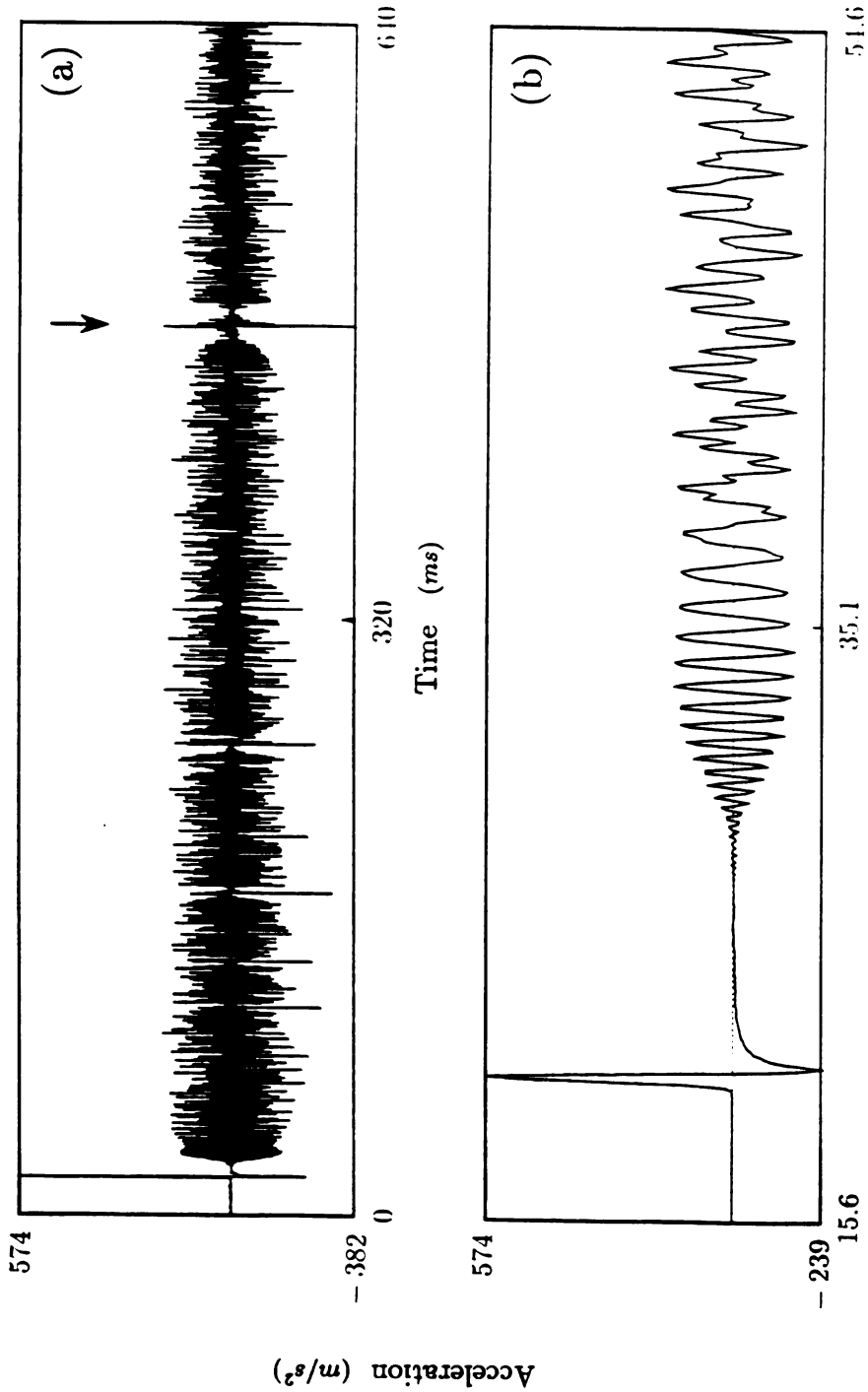

Figure 4.3 a) The acceleration signal measured from the steel beam with free boundaries. b) An enlarged view of the initial instances.

eleration

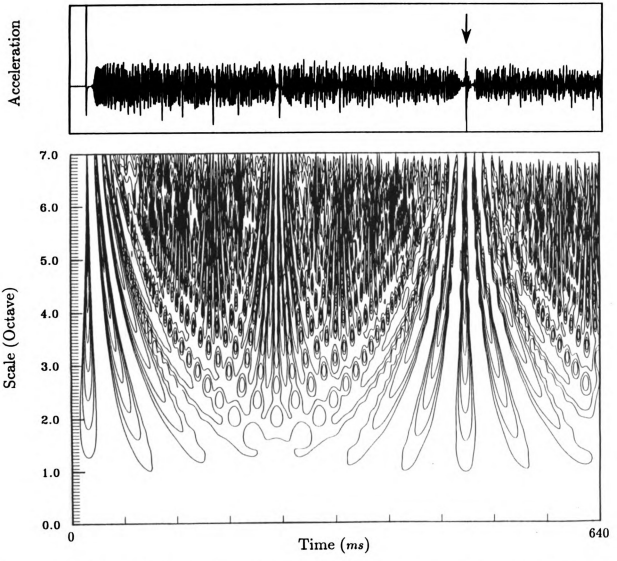

Figure 4.4 The wavelet transform of the acceleration signal measured from the steel beam.

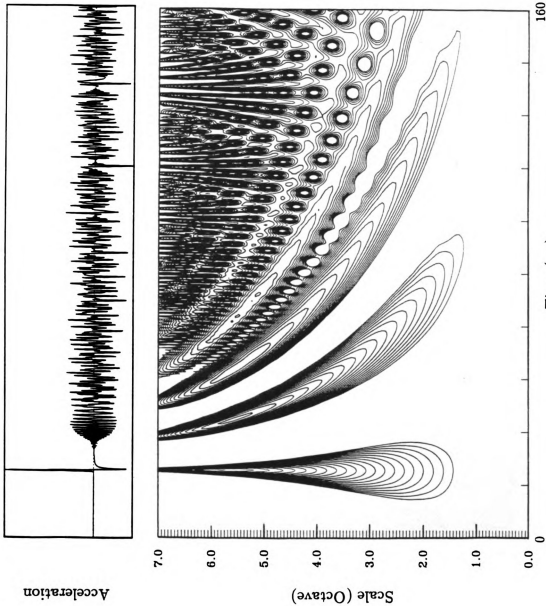

Figure 4.5 The initial instances of the wavelet transform given in Figure 4.4.

(a)

Scale (Octaves)

7
6
5
4
3
2
1
0

(b)

Scale (Octaves)

7
6
5
4
3
2
1
0

Figure

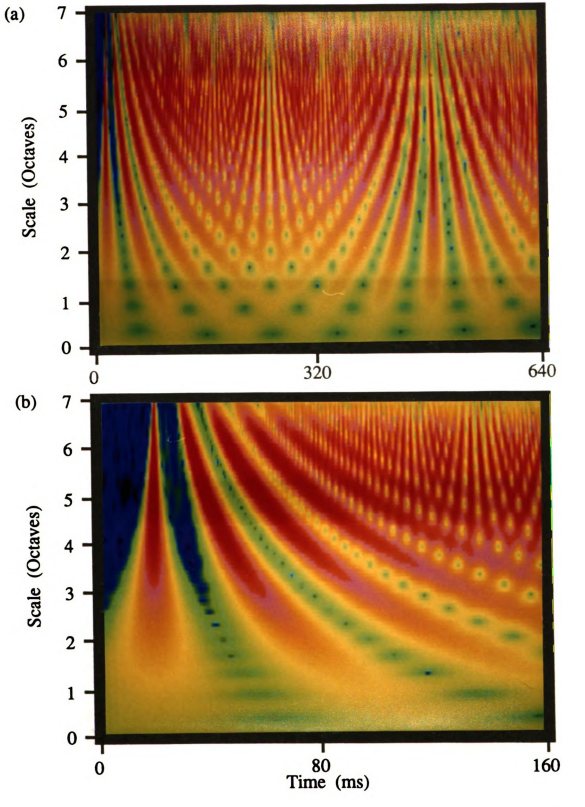

Figure 4.6 Color-coded plots for the wavelet transform of the acceleration signal measured from the steel beam.

arrival of
wave com
the other
the diper
point at
and resul
at a give
compone
This beh
$t \approx 38$ m
the high
second l
dispersio
by the t

T
ingly im
around
selves w
remarka
propaga
The acc
this pul
interest
period

which i
ysis of
equatio
sured a
the syst
present

arrival of the wave components. Following the original impact, each individual wave component completes a round-trip by first propagating, then reflecting from the other boundary, and finally propagating back to the initial point. Due to the dipersion phenomena, each wavelet component approaches to the observation point at a different time $T \propto 1/\sqrt{\omega}$. This same process repeats itself over time and results in a succession of such bent curves in Figures 4.5 and 4.6b. Therefore, at a given time, such as 80 ms in Figure 4.6b, there may be more than one wavelet component in the signal with each being associated with a different loop-count. This behavior is also observed from the time trace shown in Figure 4.3b. At about $t \approx 38$ ms, while the low frequency component is completing its first round-trip, the high frequency component having a faster phase speed has already finished its second loop. As the time progresses, these multiple reflections together with the dispersion of the waves generate an extraordinary interference pattern as displayed by the time-scale representation given in Figure 4.6a.

The interference pattern shows a symmetry property that reveals a seemingly impossible pulse reconstitution phenomenon. After a period of time, at around 500 ms in Figures 4.4 and 4.6a, all spectral components reallign themselves with their original relative phases, and reconstruct the original pulse. This remarkable reconstruction phenomenon occurs after the wave components have propagated in a dispersive medium and reflected many times from the boundaries. The acceleration time trace, plotted in Figure 4.3a, also gives a clear exposition of this pulse reconstitution phenomenon, as indicated by the small arrow. Another interesting fact about this phenomenon is that it repeats itself with a constant period given by

$$T_R = L^2/(\pi\sqrt{Eh^2/12\rho}) \tag{4.44}$$

which is obtained by using the method of images and by performing a group analysis of the propagating bending waves [67,97]. For the steel beam, the preceding equation gives $T_R = 456.9$ ms, which is confirmed by the experimental value measured as 455.5 ms. As might be expected, the material damping that is present in the system causes a slight misallignment of the wave components. However, in the present lightly-damped system, the spatial attenuation of the wave components

does not
suremen
of the wa
the main

4.5.2 Ex

In
ments w
different
the syste
the bear
mountin
from the
top of F
original
4.8. In F
center fr
with m =
to the p
stitution
value 7S

In
initial p
to the fi
respecti
almost
rence of
distribu
scales.
signatur
many ot

does not obscure the periodic repetition of the pulse-reformation. Further measurements conducted for longer periods of time have shown that the magnitude of the wavelet transform decays slowly starting from higher frequencies. However, the main grid structure observed in Figure 4.6a is repeated.

4.5.2 Experiments on an Aluminum Beam

In order to raise confidence in the preceding findings, a second set of experiments were conducted on an aluminum beam that had similar free boundaries, but different dimensions. This second example forms the experimental counterpart of the system simulated numerically earlier in section 4.3. Again, the dimensions of the beam were 38.1 mm by 6.35 mm in cross-section and 1.402 m in length. The mounting conditions, instrumentation and the testing procedure were repeated from the previous experiment. The measured acceleration data is plotted at the top of Figure 4.7, where again the arrow points to the first reconstruction of the original pulse. The wavelet transform of this signal is given in Figures 4.7 and 4.8. In Figure 4.7, the contours have $20\,dB$ range with $2\,dB$ rise per contour. The center frequencies of the Morlet wavelet filters correspond to $f_c^m = 2^m \cdot 40\ Hz$, with $m = 0, ..., 7$. The general features observed from these figures are very similar to the preceding steel beam case. For this aluminum beam, the period of reconstitution is calculated from equation (4.44) as 78.5 ms, which is confirmed by the value 78.3 ms measured from the experimental results.

In order to have a closer look at the pulse reformation phenomenon, the initial part of the wavelet transform and the part of the signal corresponding to the first reconstruction are enlarged in Figures 4.9-4.10 and Figure 4.11-4.12, respectively. The signature of the original pulse, observed in Figures 4.9-10, is almost exactly repeated later in time as shown in Figures 4.11-4.12. The occurrence of the pulse is detected easily by recognizing the conical shape of the phase distribution and the constant phase line running vertically downward though all scales. Note that in Figure 4.10b the constant phase line has a distinctive wavy signature near the base line. In addition to the reconstruction of this signature, many other distinctive features of the phase distribution are repeated in Figure

ation

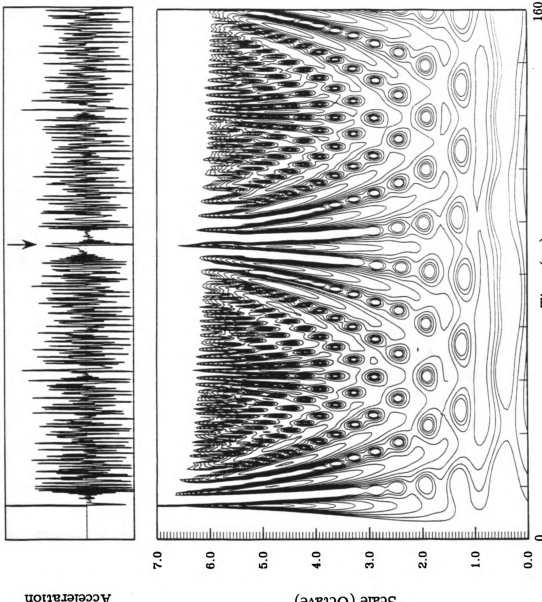

Figure 4.7 The wavelet transform of the acceleration signal measured from the aluminum beam.

Scale (Octaves)

7
6
5
4
3
2
1
0

Fig

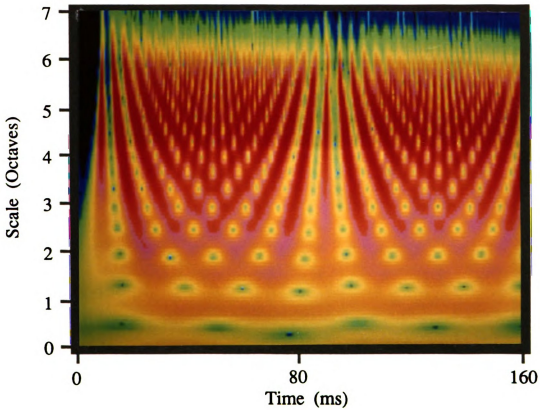

Figure 4.8 Color-coded plot for the wavelet transform of the acceleration signal measured from the aluminum beam.

celeration

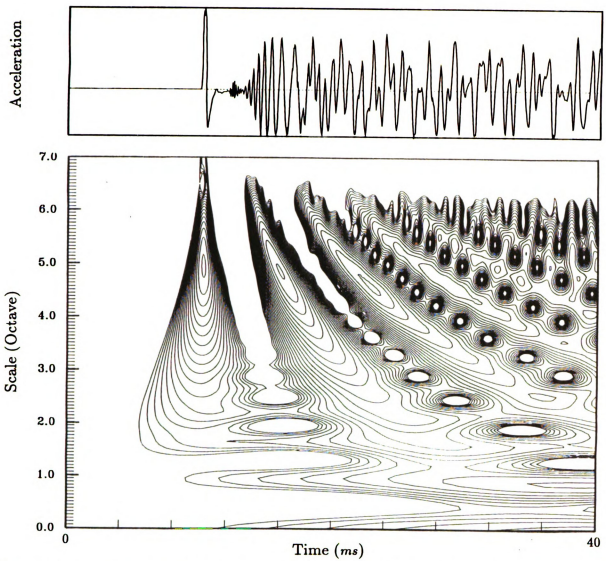

Figure 4.9 An enlarged view of the initial instances of the wavelet transform given in Figure 4.7.

(a)

Scale (Octaves)

(b)

Scale (Octaves)

Fig

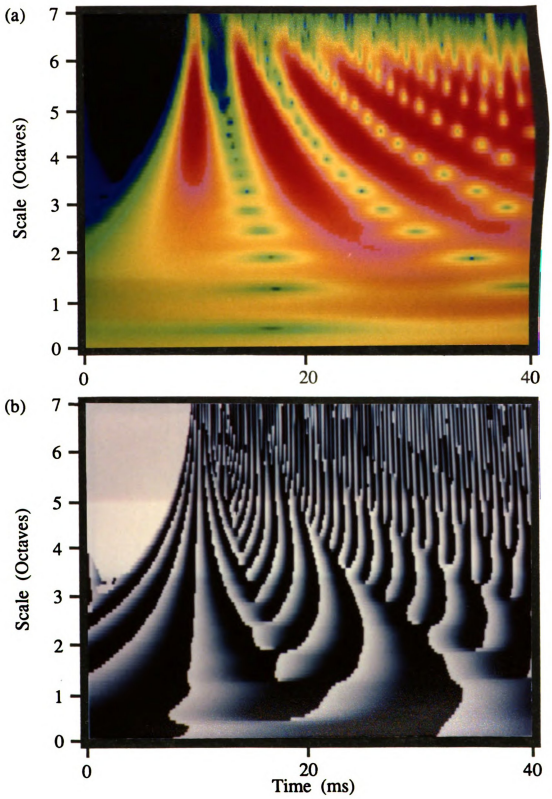

Figure 4.10 Color-coded plot for the details of the initial instances of the wavelet transform given in Figure 4.8; a) magnitude and b) phase.

ieration

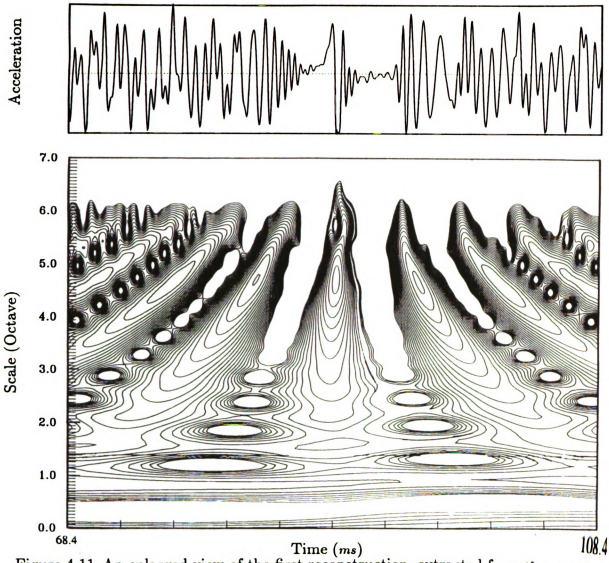

Figure 4.11 An enlarged view of the first reconstruction, extracted from the wavelet transform given in Figure 4.7.

(a)

Scale (Octaves)

(b)

Scale (Octaves)

Figu

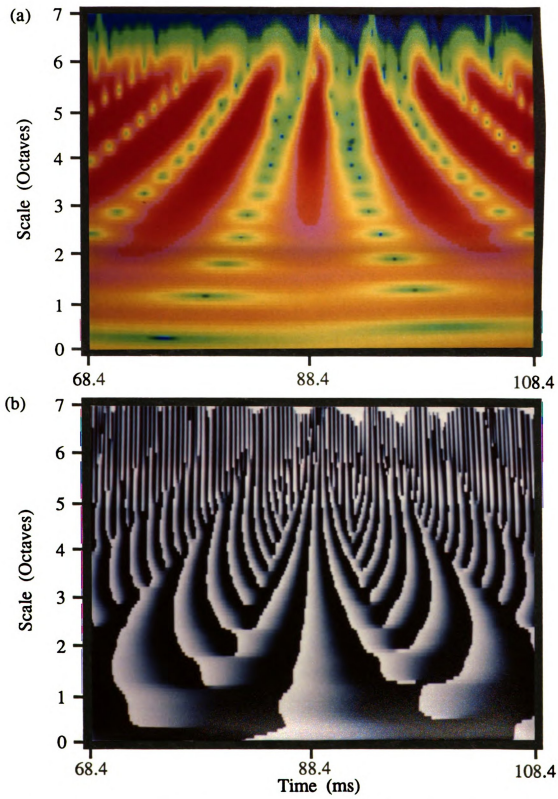

Figure 4.12 Color-coded plot for the details of the first pulse-reconstruction segment of the wavelet transform given in Figure 4.8; a) magnitude and b) phase.

4.12(b).
themsel

4.6 Mo

earlier
method
since a
matrice
simulat
configu
interfer
follow,
listed i

4.6.1 P

the tra
values
observe
are coll
domain
The cer
with m
transfor
symmet
halved,
for the
interfer

4.12(b), which further proves that the spectral components are indeed realligning themselves during the pulse reformation phenomenon.

4.6 More Examples with Different Configurations

For a single-span beam, a general frequency response function was derived earlier by considering mechanical impedances of boundaries in a transfer matrix method. The impedance formulation of the boundaries is a very effective approach, since a large group of beam configurations can be analyzed by using the same matrices. In the following, some other well-known ideal boundary conditions are simulated to demonstrate the transient vibration characteristics of different beam configurations. The objective is to study the similarity of the impact induced wave interference patterns in different beam configurations. In all of the examples that follow, the beam properties and simulation parameters are kept the same as those listed in section 4.3.

4.6.1 Pinned-Pinned Beam

In order to introduce ideally pinned supports at both ends of the beam, the translational impedances at the boundaries $\widetilde{Z}_0 = \widetilde{Z}_L$ are assigned very large values and the rotational impedance are set to zero, $\widetilde{T}_0 = \widetilde{T}_L = 0$. In order to observe the reconstitution phenomenon, the excitation and the observation points are collocated at the center of the beam. In Figure 4.13, the predicted time domain acceleration response of the beam and its wavelet transform are plotted. The center frequencies of the Morlet wavelet filters correspond to $f_c^m = 2^m \cdot 40\ Hz$, with $m = 0, ..., 7$. The time-scale representation (TSR) resulting from the wavelet transform looks quite similar to the free-free beam response, repeating a typical symmetric grid pattern. Since the distance the waves travel following each count is halved, $L/2$ instead of L, the reconstitution time is a quarter of its value calculated for the free-free beam, $T_R = 78.5/4 = 19.6\ ms$. The physical interpretation of the interference pattern follows from the free-free case.

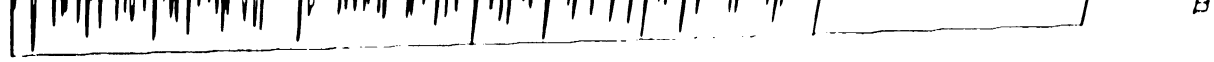

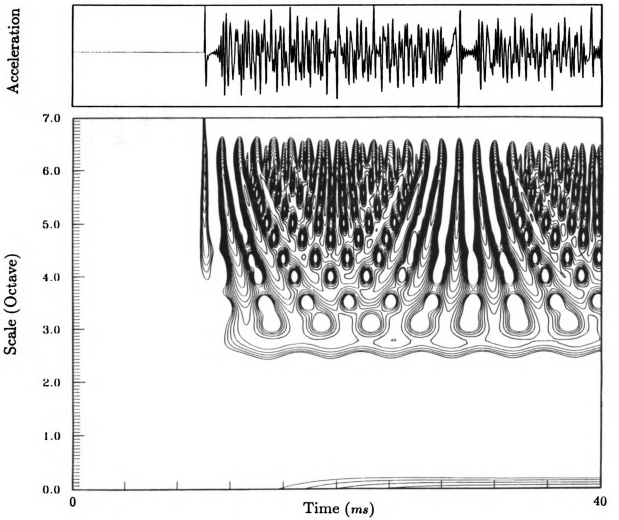

Figure 4.13 The predicted acceleration response of a pinned-pinned beam, and its wavelet transform.

4.6.2

very
$\tilde{T}_L$, a
with
and
frequ
$m =$
in ea
on th
energ
decay
obser
comp
other
struc

4.6.3

a two
end-t
ends
proce
earlie
of the
pin c
is all
collo

wave
cies c

4.6.2 Clamped-Clamped Beam

In an ideally clamped boundary, both of the mechanical impedances become very high. Therefore, in this case, all the boundary impedances, $\widetilde{Z}_0 = \widetilde{Z}_L = \widetilde{T}_0 = \widetilde{T}_L$, are assigned a common large value. Again, the observation point is collocated with the external force at the center of the beam. The predicted vibration response and the corresponding wavelet transform are given in Figure 4.14. The center frequencies of the Morlet wavelet filters correspond to $f_c^m = 2^m \cdot 40\ Hz$, with $m = 0, ..., 7$. The TFR shown in Figure 4.14 is similar to the results observed in earlier cases. Infact, the transient wave interference pattern depends little on the boundary conditions, provided that the boundary reflects the incoming energy or the reflection coefficient is unity. Since, the evanescent components decay off within a few wavelengths from a boundary, the interference pattern observed at high frequencies is totally due to positive- and negative-going wave components. If the boundary is transmitting part of the incident power to some other wavebearing medium, then the scattered wave components will break the structure of the interference patterns, as demontrated in the following example.

4.6.3 Pin-Connected Two Beams

The aluminum beam used in the preceding examples is duplicated, and thus a two-span configuration is obtained by laying two identical beams horizontally end-to-end and considering an ideal pin-connection between them. The other two ends of the beams are allowed to vibrate freely. There is a simple numerical procedure to extend the transfer matrix formulation of a single-span beam given earlier to such multi-span configurations; the frequency response function for one of the beams can be used as the boundary impedance for the other. Since an ideal pin connection is free to rotate, the torsional impedance at the pin connection is allowed to vanish. In this example, the observation and excitation points are collocated at either one of the free ends of the beams.

The predicted response of the combined system and its corresponding wavelet transform are given in Figure 4.15. The Morlet wavelet center frequencies correspond to $f_c^m = 2^m \cdot 40\ Hz$, with $m = 0, ..., 7$. At the initial instances,

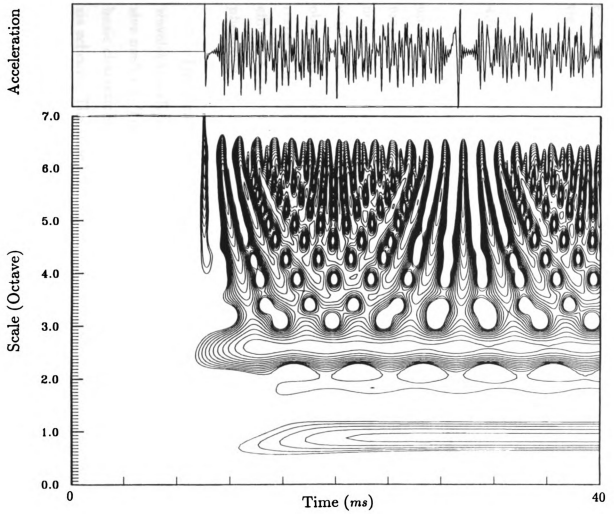

Figure 4.14 The predicted acceleration response of a clamped-clamped beam, and its wavelet transform.

the wa
mediat
a miss
multip
the tim
examp
to char
time.

4.6 Di

under
may be
nonuni
exist.
observ
respec
efficac
pheno

wavel
sive n
basic
sis sc
demo
ing t
wind
wide
inter
retu

the wave interference pattern looks similar to earlier examples, but starting immediately with the third loop-count an interesting cancellation happens causing a missed curve in the TSR. In later moments, the combination of dispersion, multiple-reflections and scattering causes the grid pattern to be smeared out in the time-frequency plane. Therefore, the interference patterns observed in earlier examples are not repeated, the symmetry is lost, and no distinctive signature seems to characterize the transient vibrations of the system during the later instances of time.

4.6 Discussion and Conclusions

In practice, the pulse reformation phenomenon is expected to exist only under very special circumstances. The conditions for its occurrence are such that it may be difficult to observe this phenomenon in practical systems where dissipation, nonuniformities, non-ideal boundaries and asymetric configurations are likely to exist. Even on a single-span beam it was observed only when the excitation and observation points were collocated at the boundaries or at the center. In that respect, the results presented above were intended mainly to demonstrate the efficacy of the wavelet transform in uncovering complex transient wave propagation phenomena.

The preceding results and discussions demonstrated the effectiveness of the wavelet transform in the analysis of transient waves propagating in a finite dispersive medium. The similarity in the general structure of the wavelet basis and the basic characteristics of the physical phenomena brought about a powerful analysis scheme. The time-scale representations resulting from the wavelet transform demonstrated a very efficient way of exposing the evolution of the spectrum during the dispersion and reflection of an impulsive waveform. The self-adjusting window structure of the wavelet transform provided adequate resolutions over a wide spectral range and thus, resulted in an efficient localization of the complex interference patterns in the time-scale domain. The TSRs clearly displayed the return of each wave component after each round-trip; its propagation along the

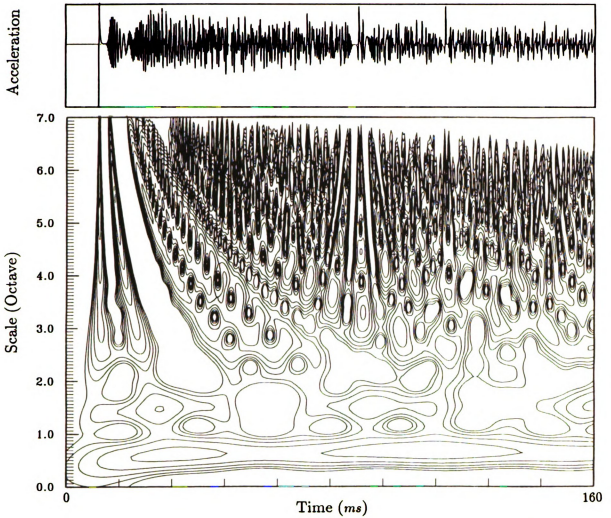

Figure 4.15 The predicted acceleration response of pin-connected beams, and its wavelet transform.

beam, r

vation p

its wav

wavefor

limitati

effective

plex sp

constar

harmo

chapte

to mo

struc

stimu

of a

beam, reflection from the boundary, and then its propagation back to the observation point. In addition, the decomposition of a transient vibration signal into its wavelet components resulted in a wave-group representation of the dispersed waveform.

The physical examples demonstrated the basic advantages and some of the limitations of the wavelet transform analysis. The wavelet transform performs effectively for vibration signals that have wide-band frequency content with complex spectral evolutions in time. However, in the analysis of standing waves, the constant-Q characteristics of the wavelet transform makes it difficult to distinguish harmonic contributions coming from individual modes.

Finally, it should be stressed that the analysis scheme demonstrated in this chapter by using relatively simple mechanical structures is perfectly applicable to more complex systems that may have different dispersive characteristics and structural configurations. Indeed, it is hoped that the results presented here will stimulate the use of the time-frequency representation techniques in a wide field of applications.

wavel
tion o
transi
tem b
by an
wavel
issues
discu
consi
integ

5.1 I

pulse
nami
tance
analy
vibro
mula
but i

CHAPTER 5

WAVELET FRAME EXPANSIONS AND WAVELET RESPONSE FUNCTIONS

The main goal of this chapter is to lay the framework for the theory of wavelet response functions by arguing for their practical use in the characterization of linear system dynamics. Particular attention is given to the synthesis of the transient time-domain response of a proportionally-damped wide-band linear system by using its frequency response function. The convolution integral is replaced by an efficient synthesis scheme which is developed by using multi-resolution and wavelet frame concepts. In order to give a self-contained presentation, some of the issues regarding time-domain aliasing and the concept of wavelet frames will be discussed. Later, the definition of the wavelet response function is introduced by considering the wavelet series expansion of the forcing function in the convolution integral.

5.1 Introduction

In the analysis of linear time-invariant (LTI) systems, frequency and impulse response functions are utilized frequently during the characterization of dynamic behaviors. Since frequency response functions (FRFs), such as a receptance, impedance or an accelerance, are readily available in today's multi-channel analyzers and softwares, they are employed commonly in experimental analysis of vibro-acoustic systems. Therefore, in analytical studies, the frequency-domain formulation of a system's response not only facilitates the mathematical derivations, but it also generates results that are easily compared to physical measurements.

In com
sient re
linear s
the tra
frequer
Fourier

by mea
excitat
that th
nusoida
domain
distribu
many c
acterist

5.2 Pr

tions, s

5.2.1 C

tation i

where
of an L

In comparison to FRFs, impulse response functions are used to represent the transient response characteristics of linear systems. The impulse response function of a linear system acts as the kernel of the convolution integral, where the latter defines the transient response of the system to an arbitrary excitation. In the complex frequency domain, the convolution integral becomes a simple multiplication of the Fourier transforms, which is related to the definition of an FRF.

Basically, a frequency or an impulse response function can be determined by measuring the dynamic response of a system to a sinusoidal or an impulsive excitation. The major difference between these classical excitation functions is that they have opposite time-frequency localization characteristics. An ideal sinusoidal excitation extends throughout time and is well-localized in the frequency domain, whereas an impulsive excitation is well-localized in time but has a widely distributed spectrum. Between these two extreme excitation types, one can find many different functions, such as wavelets, that have desirable localization characteristics both in time and frequency domains.

5.2 Preliminary Concepts and Background

In order to form a background to the succeeding mathematical constructions, some of the major concepts and definitions are discussed in the following.

5.2.1 Convolution Integral

The response of a linear time-invariant (LTI) system to an arbitrary excitation is given by the convolution integral

$$y(t) = \int_{-\infty}^{\infty} f(\tau)\, h(t-\tau)\, d\tau \tag{5.1}$$

where $f(t)$ and $h(t)$ represent the excitation and the impulse response function of an LTI system, respectively. In order to replace the convolution integral by

a simpler algebraic operation, the Fourier transform of the preceding equation is performed;

$$\int_{-\infty}^{\infty} y(t)\, e^{-i\omega t}\, dt = \int_{-\infty}^{\infty} \left[\int_{-\infty}^{\infty} f(\tau)\, h(t-\tau)\, d\tau \right] e^{-i\omega t}\, dt$$

$$= \int_{-\infty}^{\infty} f(\tau)\, e^{-i\omega\tau}\, d\tau \int_{-\infty}^{\infty} h(t)\, e^{-i\omega t}\, dt$$

which is simplified as

$$Y(\omega) = H(\omega)\, F(\omega), \tag{5.2}$$

with $Y(\omega)$, $F(\omega)$, and $H(\omega)$ representing the Fourier transforms of $y(t)$, $f(t)$, and $h(t)$, respectively. The interchange of the integrals is allowed by the Fubini's theorem. Equation (5.2) implies that the convolution of two functions in the time-domain is equivalent to the multiplication of their Fourier transforms in the complex frequency domain. The simplicity of this algebraic operation is the main reason for the use of the Fourier transform in evaluation of the convolution integral to obtain the response of an LTI system.

The frequency response function, $H(\omega)$, is usually analytically tractable from a dynamic model of the system, or else it can be determined experimentally. Therefore, if the Fourier transform of the input $F(\omega)$ is known, the time domain representation of the system response can be obtained by evaluating the inverse Fourier transform of the frequency-domain response

$$y(t) = \frac{1}{\sqrt{2\pi}} \int_{-\infty}^{\infty} Y(\omega)\, e^{i\omega t}\, d\omega\ . \tag{5.3}$$

In practice, the evaluation of the preceding integral causes serious difficulties, and closed-form analytical solutions are known to exist only for very special cases.

A more practical and commonly used alternate approach is based on the discretization of the frequency-domain response $Y(\omega)$. Then, the corresponding discrete-time system response is obtained by applying the inverse discrete Fourier

transform (DFT) to the sequence of samples. For narrow-band systems, this DFT approach may generate acceptable results with reasonable computational load. However, in lightly-damped wide-band LTI systems, time-domain aliasing creates additional difficulties and imposes restrictions on the number of samples and the sampled frequency range.

5.2.2. Signal Bandwidth and Duration; Time-Domain Aliasing

In the applications, generally the continuous spectrum $Y(\omega)$ is sampled uniformly over a finite number of frequencies. During this discretization process, the sampling interval and the number of samples need to be chosen carefully to prevent time-domain aliasing of the synthesized signal.

During the forward transform, frequency-domain aliasing is prevented by choosing the sampling frequency $F_s \geq 2F_{max}$, where F_{max} represents the spectral range of the transformed signal. Similarly, during the inverse Fourier transform, time-domain aliasing is averted by choosing the sampling duration $T_s \geq 2T_{max}$, where T_{max} represents the total duration of the reconstructed signal [108,111]. Duality of the forward and inverse Fourier transform concepts is apparent from the preceding statements. In practical applications involving the forward transform, the spectral range of the signal is estimated aprior to the transformation. The estimate is based on physical considerations and also on the objectives imposed by the particular application.

In practice, it is well-known that a signal which is highly localized in time, such as an impact acceleration signal, has a Fourier transform which is wide spread throughout the spectrum. On the other hand, a sharp peak in a spectral representation is associated with a signal that has a very long duration in time. Therefore, during the application of an FFT synthesis scheme to the reconstruction of a transient vibration response, a narrow bandwith resonance peak in the frequency response function corresponds to a long duration signal in the time-domain. In comparison, high-frequency structural vibrations generally have wide bandwidths

that generates short duration transient signals. Consequently, the relationship between the bandwidth and the time-duration of a transient vibration signal needs to be known to choose proper sampling parameters.

In vibro-acoustic systems, the reveberation time is used frequently as a convenient measure for the duration of a transient response. The definition of the reveberation time and the related concepts are summarized in Appendix H. The reveberation time is given as $T_R = 2.2/B_{3dB}$, where B_{3dB} is the half-power bandwidth. Other definitions of bandwith that are in common use are listed in Appendix G. The relationship between the bandwidth of the system and the duration of its impulse response is stated as

$$T_{max} = \frac{2.2}{B_{3dB}} . \tag{5.4}$$

Again in Appendix H, the half-power bandwidth is shown to be directly proportional to the loss factor η and the natural frequency f_n of the system:

$$B_{3dB} = \eta f_n . \tag{5.5}$$

The preceding expression for the half-power bandwidth is quite general, and it is also valid for vibrations of multi-modal systems in bending, torsion and in longitudinal motions [37]. Note that, if the loss factor is held constant, the bandwidth increases with the natural frequency. This point is fundamental in enabling us to exploit the properties of wavelets, as discussed later in this study.

The combination of the preceding relations provides an upper bound for the interval between frequency samples

$$\delta_f = \frac{1}{T_s} \leq \frac{1}{2T_{max}} = \frac{B_{3dB}}{4.4} \tag{5.6}$$

which needs to be satisfied for an unalliased time-domain construction. For lighly-damped systems, equations (5.4) and (5.5) imply long signal durations, and therefore, require very frequent sampling within a given frequency range. For a multi-modal system, the frequency response function is generally spread over a wide

spectral range and therefore render the efficiency of such sampling schemes questionable. The problem is nothing more than the well-known time frequency resolution problem associated with the Fourier transform.

A solution to the preceding problem is the partitioning of the spectrum into different resolution frequency bands. For example, the Shannon wavelet basis that is generated from the sinc function, $\sin(\pi t)/\pi t$, can be used to divide the spectrum into disjoint partitions [14,23,116], as shown in Figure 5.1a. If we consider the continuous set of all positive frequencies $\omega \in \mathbf{R}^+ = (0, \infty)$, the dyadic division implies [23,58]

$$\mathbf{R}^+ = \bigcup_{m=-\infty}^{\infty} (2^m \Delta_{\widehat{\psi}}, 2^{m+1} \Delta_{\widehat{\psi}}]$$

where the rms-bandwidth is defined by $B_{rms} = 2\Delta_{\widehat{\psi}}$, with the latter being the radius. Certainly, the Shannon wavelets, with their infinite support and slow decay characteristics, would not be the most practical choice. In that respect, the concept of frames comes to the rescue and relaxes the choice of the wavelet basis at the expense of overlapping the spectral bands as shown in Figure 5.1b. In the following sections, the variable resolution property of the wavelet frame expansions are exploited during the decomposition of the convolution integral.

5.3 Frames and Wavelet Response Functions

In the synthesis of transient response, the time-frequency resolution problem induced by the Fourier transform can be averted by dividing the frequency spectrum into variable resolution bands. The multi-scale and variable-resolution (zooming) properties of the wavelet transform provide the desired structure for accurate reconstruction of the time-domain response. A combination of the wavelet and the frame concepts are employed to replace the convolution integral with a set of multi-resolution components. The transient response of the system is formed by adding the contributions coming from different resolution levels. In order to form the background for later discussions, the frame concepts are reviewed briefly in the following.

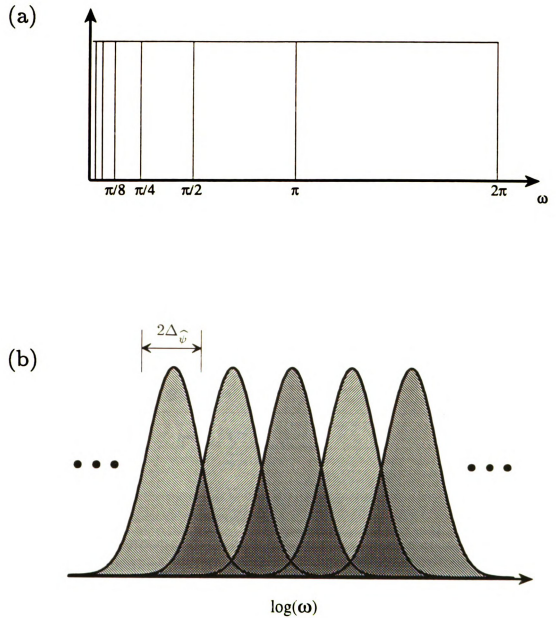

Figure 5.1 Partitioning of the spectrum; a) disjoint support of the Shannon wavelet basis and b) the overlapped coverage by a typical wavelet frame.

5.3.

later

[42.4

fram

The

to a

The

$c \in \ell$

The

gener

boun

wher

5.3.1. The Frame Concepts

The frame concepts were first introduced by Duffin and Schaeffer [48] and later by Young [135], Heil and Walnut [68] and treated in detail by Daubechies [42,43] and Benedetto [15,16] within the context of the wavelet theory.

In a Hilbert space $\mathbf{H}$, a family of functions $\{\psi_{mn};\ m,n \in \mathbf{Z}\}$ constitutes a frame if there exists bounds $A > 0$ and $B < \infty$ such that, for every $f \in \mathbf{H}$

$$A\|f\|^2 \leq \sum_{m,n} |\langle f, \psi_{mn}\rangle|^2 \leq B\|f\|^2 \,. \tag{5.7}$$

The frame operator is defined as $T : \mathbf{H} \longrightarrow \ell^2(\mathbf{Z})$ such that any $f \in \mathbf{H}$ is mapped to a $c_{mn} \in \ell^2(\mathbf{Z})$ as follows:

$$(Tf)_{mn} = \langle f, \psi_{mn}\rangle \;=\; c_{mn} \,.$$

The associated adjoint operator is given by $T^* : \ell^2(\mathbf{Z}) \longrightarrow \mathbf{H}$, such that for any $c \in \ell^2(\mathbf{Z})$, this operator generates

$$\begin{aligned} T^*c &= \sum_{m,n} c_{mn}\tilde{\psi}_{mn} \\ &= \sum_{m,n} \langle f, \psi_{mn}\rangle\, \tilde{\psi}_{mn} = f \,. \end{aligned} \tag{5.8}$$

The family of functions $\{\tilde{\psi}_{mn} : m,n \in \mathbf{Z}\}$ constitutes a dual frame, which is generated from ψ_{mn} as shown in the following. From the preceding definitions the bounds on the operators are derived as

$$A\,I \leq T^*T \leq B\,I$$

$$B^{-1}\,I \leq (T^*T)^{-1} \leq A^{-1}\,I$$

where I is the identity operator. Therefore, the dual frame is defined by

$$\tilde{\psi}_{mn} = (T^*T)^{-1}\psi_{mn} \,, \qquad\qquad m,n \in \mathbf{Z} \,. \tag{5.9}$$

Then, for any $f, g \in \mathbf{H}$ we have

$$\langle f, g \rangle = \sum_{m,n} \langle f, \psi_{mn} \rangle \, \langle \tilde{\psi}_{mn}, g \rangle \ ,$$

which implies the frame expansion

$$f = \sum_{m,n} \langle f, \psi_{mn} \rangle \, \tilde{\psi}_{mn} = \sum_{m,n} \langle f, \tilde{\psi}_{mn} \rangle \, \psi_{mn} \ . \tag{5.10}$$

The preceding definitions apply to all different forms of frames that may be defined in a Hilbert space $\mathbf{H}$. In general, the frames are classified by their frame bounds, as discussed in the following.

The ratio B/A represents the redundancy of the frame. Frames having B/A close to one are called "snug frames", which are used to generate approximate reconstructions [42,43]

$$f_{appr} = \frac{2}{A+B} \sum_{m,n} \langle f, \psi_{mn} \rangle \, \psi_{mn} \ . \tag{5.11}$$

In this case the tilde sign is dropped, which implies that the analyzing wavelet frame is used during both the analysis and the reconstruction stages. If the two frame bounds are equal, $A = B$, then it is called a "tight frame", and the above relationships imply

$$\sum_{m,n} |\langle f, \psi_{mn} \rangle|^2 = A \|f\|^2 \ , \tag{5.12}$$

which gives

$$f = A^{-1} \sum_{m,n} \langle f, \psi_{mn} \rangle \, \psi_{mn} \ . \tag{5.13}$$

This last formula looks very similar to the expansion of any $f \in L^2(\mathbf{R})$ in terms of an orthonormal basis. However, even the tight frames do not form an orthonormal

basi

orth

by u

resul

fram

5.3.2

resolu

the sa

follow

where

the di

form

Simila

basis. As a natural extension, a tight frame with $A = B = 1$ generates an orthonormal basis, which can be used in the series expansion

$$f = \sum_{m,n} \langle f, \psi_{mn} \rangle \, \psi_{mn} \, . \tag{5.14}$$

During the applications considered in the next chapter, a frame is generated by usign the Morlet wavelet with four voices per octave. This particular choice results in a very snug frame as discussed later. In the following, the preceding frame concepts are extended to the wavelet frame expansions.

5.3.2 Wavelet Frame Expansions

Earlier in Chapter 2 the discrete form of the wavelet families and multi-resolution concepts were discussed. In order to generate some usefull relationships, the same discretization process will be carried out in two stages as shown in the following.

Let us begin by considering the family of wavelet functions

$$\psi^{a,b}(t) = \frac{1}{\sqrt{|a|}} \psi \left(\frac{t-b}{a} \right) \tag{5.15}$$

where $a, b \in \mathbf{R}$ and $a \neq 0$. As a first step in the two-stage discretization process, the dilation parameter is assigned $a = 2^m$ with $m \in \mathbf{Z}$. Then, the semi-discrete form of the wavelet family is represented by

$$\psi_m^b(t) = 2^{-m/2} \, \psi \left(\frac{t-b}{2^m} \right) , \qquad m \in \mathbf{Z} \, . \tag{5.16}$$

Similarly, the translation parameter is discretized by using $b = n2^m$, which gives

$$\psi_{mn}(t) = 2^{-m/2} \, \psi(2^{-m} t - n) \, , \qquad m, n \in \mathbf{Z} \, . \tag{5.17}$$

The semi-discrete form, which has continuous translation property, can be decomposed into elementary discrete wavelet components

$$\psi_m^b(t) = \sum_{n=-\infty}^{\infty} \langle \psi_m^b, \tilde{\psi}_{mn} \rangle \, \psi_{mn}(t) \,, \qquad m, n \in \mathbf{Z} \,. \tag{5.18}$$

which will be usefull in the following wavelet frame expansions.

The preceding discrete wavelet components are combined with the earlier frame concepts to decompose a function $f \in L^2(\mathbf{R})$ into multi-resolution components. In order to obtain some usefull structures, the decomposition will be carried out in two steps. First, the frequency localization will be performed by representing the function as a series of detail functions, and later each detail function will be resolved into time-local wavelet components.

The semi-discrete form of the wavelets, given in equation (5.16), are utilized to decompose a function $f \in L^2(\mathbf{R})$ as [23]

$$f(t) = \sum_{m=-\infty}^{\infty} f_m^{\psi}(t) \,, \tag{5.19}$$

where

$$f_m^{\psi}(t) = \int_{-\infty}^{\infty} \langle f, \tilde{\psi}_m^b \rangle \, \psi_m^b(t) \, db \,, \qquad m \in \mathbf{Z} \,. \tag{5.20}$$

is the projection of f onto the mth resolution subspace and therefore, it represents the detail contained in the original function at the mth resolution level. Therefore it is proper to call f_m^{ψ} the "detail function".

In order to achieve time localization at each resolution level, the wavelet expansion of ψ_m^b given in equation (5.18) is substituted back into the preceding

exp

This

wher

As a

pansi

many

cedir

funct

$\hat{\psi}_{mn}$(

the P

the d

expression, and then the summation and integration are interchanged as follows:

$$
\begin{aligned}
f_m^{\psi}(t) &= \int_{-\infty}^{\infty} \langle f, \widetilde{\psi}_m^b \rangle \left[\sum_{n=-\infty}^{\infty} \langle \psi_m^b, \widetilde{\psi}_{mn} \rangle \, \psi_{mn}(t) \right] db \\
&= \sum_{n=-\infty}^{\infty} \left[\int_{-\infty}^{\infty} \langle f, \widetilde{\psi}_m^b \rangle \, \langle \psi_m^b, \widetilde{\psi}_{mn} \rangle \, db \right] \psi_{mn}(t) \\
&= \sum_{n=-\infty}^{\infty} \langle f, \widetilde{\psi}_{mn} \rangle \, \psi_{mn}(t) \, .
\end{aligned}
$$

This result implies

$$
f_m^{\psi}(t) = \sum_{n=-\infty}^{\infty} F_{mn} \psi_{mn}(t) \, , \tag{5.21}
$$

where the wavelet coefficients F_{mn} are defined by

$$
F_{mn} = \langle f, \widetilde{\psi}_{mn} \rangle = \int_{-\infty}^{\infty} f(t) \, \overline{\widetilde{\psi}_{mn}(t)} \, dt \, , \qquad m, n \in \mathbf{Z} \, . \tag{5.22}
$$

As a result of the preceding two-level localization process, the wavelet series expansion of f, defined in equation (5.19), becomes

$$
f(t) = \sum_{m=-\infty}^{\infty} \sum_{n=-\infty}^{\infty} F_{mn} \, \psi_{mn}(t) \, . \tag{5.23}
$$

Since the whole wavelet concept is based on recursion relations, there are many simplifications that one can consider during the implementation of the preceding concepts. For example, the Fourier transform of the elementary wavelet functions is obtained recursively from the Fourier transform of the mother wavelet, $\widehat{\psi}_{mn}(\omega) = 2^{m/2} \, e^{-in2^m\omega} \, \widehat{\psi}(2^m\omega)$, by using the shifting and scaling properties of the Fourier transform, given in Appendix A. Therefore, the Fourier transform of the detail function defined in equation (5.21) becomes

$$
\begin{aligned}
\widehat{f}_m^{\psi}(\omega) &= \sum_{n=-\infty}^{\infty} F_{mn} \, \widehat{\psi}_{mn}(\omega) \\
&= 2^{m/2} \, \widehat{\psi}(2^m\omega) \, F_m(\omega) \, .
\end{aligned} \tag{5.24}
$$

where

The p
explo
For e
lution
weigh
trans

5.3.3

volut

If the
convo
Subs
the c
assu

Thi

where the modulated wavelet coefficients F_m are defined as

$$F_m(\omega) = \sum_{n=-\infty}^{\infty} F_{mn}\, e^{-in2^m\omega} \,. \tag{5.25}$$

The preceding series expansion in terms of elementary wavelet components can be exploited in physical applications concerning transient response of linear systems. For example, equation (5.21) implies that the detail of a signal at the mth resolution level is equivalent to the sum of the integer translates of wavelet functions weighted by the wavelet coefficients. This multi-resolution property of wavelet transform is utilized in the following decomposition of the convolution integral.

5.3.3 Wavelet Response Functions

The response of an LTI system to an arbitrary input is given by the convolution integral

$$y(t) = \int_{-\infty}^{\infty} f(\tau)\, h(t-\tau)\, d\tau \,. \tag{5.26}$$

If the input to the system is classified as a finite energy signal, $f \in L^2(\mathbf{R})$, then the convolution integral can be resolved into a discrete latice of elementary wavelets. Substituting the wavelet series expansion of the input $f(t) = \sum_m f_m^{\psi}(t)$ back into the convolution integral and interchanging the summation and integration, by assuming $\sum \|f_m^{\psi}\|^2 < \infty$, yields

$$\begin{aligned} y(t) &= \int_{-\infty}^{\infty} \left[\sum_{m=-\infty}^{\infty} f_m^{\psi}(\tau) \right] h(t-\tau)\, d\tau \\ &= \sum_{m=-\infty}^{\infty} \left[\int_{-\infty}^{\infty} f_m^{\psi}(\tau)\, h(t-\tau)\, d\tau \right] . \end{aligned}$$

This result can be reorganized as

$$y(t) = \sum_{m=-\infty}^{\infty} y_m^{\psi}(t) \,, \tag{5.27}$$

by de

Equa
into n
from

the n

where
conta

which

Note
the c
respo
call
func

of t
syst

by defining

$$y_m^{\psi}(t) = \int_{-\infty}^{\infty} f_m^{\psi}(\tau)\, h(t-\tau)\, d\tau\,, \qquad m \in \mathbf{Z}\,. \tag{5.28}$$

Equations (5.27) and (5.28) suggest the decomposition of the convolution integral into multi-resolution components. As sketched in Figure 5.2b, the response y_m from each level of resolution carries a distinct detail of the overall system response.

In the frequency domain, the Fourier transform of the system response, at the mth resolution level is obtained from equation (5.28) as

$$\begin{aligned} \widehat{y}_m^{\psi}(\omega) &= \widehat{f}_m^{\psi}(\omega)\,\widehat{h}(\omega) \\ &= 2^{m/2}\,\widehat{\psi}(2^m\omega)\,F_m(\omega)\,\widehat{h}(\omega) \\ &= F_m(\omega)\,\widehat{h}_m^{\psi}(\omega)\,. \end{aligned} \tag{5.29}$$

where the relation given in equation (5.24) is utilized. The preceding equation contains a new function defined as

$$\widehat{h}_m^{\psi}(\omega) = 2^{m/2}\,\widehat{\psi}(2^m\omega)\,\widehat{h}(\omega)\,, \qquad m \in \mathbf{Z}\,,$$

which in the time domain implies

$$h_m^{\psi}(t) = \int_{-\infty}^{\infty} \psi_m(\tau)\, h(t-\tau)\, d\tau\,, \qquad m \in \mathbf{Z}\,. \tag{5.30}$$

Note that $\psi_m = \psi_{m0}$ is the dilated version of the mother wavelet localized around the origin. The preceding equation implies the convolution of the system impulse response function with an elementary wavelet function. Therefore, it is natural to call h_m^{ψ} a "*wavelet response function*". The superscript ψ is a reminder that these functions are determined following a particular choice of the mother wavelet.

In summary, the original convolution integral is replaced by the convolution of the impulse response with the elementary input signals. The output of the system is formed by adding contributions coming from each resolution level, as

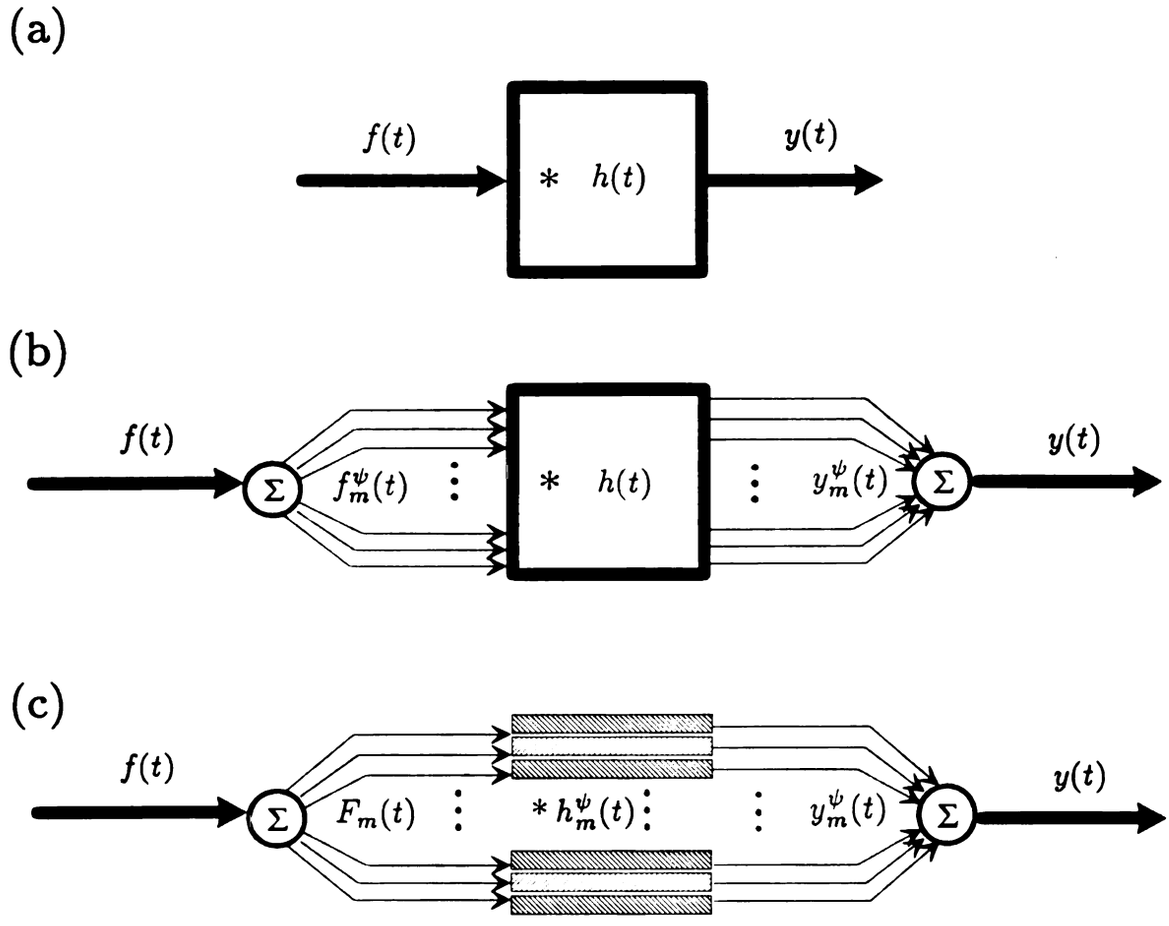

Figure 5.2 The block-diagram representation of the convolution operation for an LTI system; a) standard representation, b) wavelet frame expansion of the input, and c) implementation based on wavelet response functions.

sketc

respo

is a r

"Imp

5.4 A

an al

input

input

into

w

sketched in Figure 5.2c. Besides their mathematical implications, the wavelet response functions also have an associated physical meaning. This new definition is a natural extension of the well-known concept such as "Frequency Response", "Impulse Response" and "Indicial Response" functions of a linear system.

5.4 An Alternate Construction

The natural extansion that follows from the preceding discussion is to find an alternate representation for the convolution integral by decomposing both the input f and the impulse reponse function h. Therefore, the series expansion of the input $f(t) = \sum_m f_m^\psi(t)$ and the impulse response $h(t) = \sum_j h_j^\psi(t)$ are substituted into the convolution integral;

$$\begin{aligned} y(t) &= \int_{-\infty}^{\infty} \left[\sum_{m=-\infty}^{\infty} f_m^\psi(\tau) \right] \left[\sum_{j=-\infty}^{\infty} h_j^\psi(t-\tau) \right] d\tau \\ &= \sum_{m=-\infty}^{\infty} \sum_{j=-\infty}^{\infty} y_{m;j}^\psi(t) \,, \end{aligned} \tag{5.31}$$

where

$$y_{m;j}^\psi(t) = \int_{-\infty}^{\infty} f_m^\psi(\tau)\, h_j^\psi(t-\tau)\, d\tau \,, \qquad m,k \in \mathbf{Z} \,. \tag{5.32}$$

The Fourier transform of the preceding expression gives

$$\widehat{y}_{m;j}^\psi(\omega) = \widehat{f}_m^\psi(\omega)\, \widehat{h}_j^\psi(\omega) \,. \tag{5.33}$$

From equation (5.24) we have

$$\begin{aligned} \widehat{f}_m^\psi(\omega) &= 2^{m/2}\, \widehat{\psi}(2^m\omega)\, F_m(\omega) \\ \widehat{h}_j^\psi(\omega) &= 2^{j/2}\, \widehat{\psi}(2^j\omega)\, H_j(\omega) \end{aligned} \tag{5.34}$$

wher

stitut

Ther

if m

the f

that

to-o

dom

5.5

addi

prop

of t

from

the

impl

5.5.

wav

Four

this

where the original definition is extended for the impulse response function h. Substituting the preceding relationships back into (5.33) gives

$$\widehat{y}^{\psi}_{m;j}(\omega) = 2^{(m+j)/2}\,\widehat{\psi}(2^{j}\omega)\,\widehat{\psi}(2^{m}\omega)\,F_{m}(\omega)\,H_{j}(\omega)\,. \tag{5.35}$$

Therefore, the contribution coming from the mth resolution level is significant only if m and j are close to each other. If the wavelet has sharp decay characteristics in the frequency domain, excitation in one frequency band remains localized around that particular band. This argument agrees with our understanding of the one-to-one input-output relationship that governs the linear systems in the frequency domain.

5.5 Implementation of the Wavelet Response Functions

Equation (5.27) implies that the overall system response is formed by the addition of all contributions from different resolution levels. Therefore, it is appropriate to perform the inverse Fourier transform on each individual component of the response, $\widehat{y}^{\psi}_{m}(\omega)$, and later superimpose all the time reponses contributed from different detail levels. The advantage gained during this operation is that the sampling interval used at each resolution level can be adjusted during the implementation of the DFT.

5.5.1 Bandpass Filtering with Wavelets

Since each one of the wavelet components acts as a bandpass filter, the wavelet response functions can be determined accurately by using the inverse Fourier transforms. Consider $\widehat{y}^{\psi}_{m}(\omega)$ to be localized within $\omega_1 \leq \omega \leq \omega_2$. First, this function is shifted to the origin by an amount $\omega_c = (\omega_1 + \omega_2)/2$ and then the

inver

Then

Note
frequ
beari

phys
discu

5.6 I

wave
spect
prop
rectl
phen
in a
trans
mult
toge
term

inverse Fourier transform is performed

$$
\begin{aligned}
y_m^{*\psi}(t) &= \frac{1}{\sqrt{2\pi}} \int_{-\infty}^{\infty} \widehat{y}_m^{\psi}(\omega + \omega_c)\, e^{i\omega t}\, d\omega \\
&= e^{i\omega_c t}\, \frac{1}{\sqrt{2\pi}} \int_{-\infty}^{\infty} \widehat{y}_m^{\psi}(\omega)\, e^{i\omega t}\, d\omega \\
&= e^{i\omega_c t}\, y_m^{\psi}(t)
\end{aligned}
$$

Then, the response is obtained from

$$
y_m^{\psi}(t) = e^{-i\omega_c t}\, y_m^{*\psi}(t) \tag{5.36}
$$

Note that, the spectral range for $\widehat{y}_m^{*\psi}(\omega)$ is defined as $-\omega_1 \leq \omega \leq \omega_2$. The frequency ω_c acts as a carrier with $y_m^{\psi}(t)$ being imposed on it as an information bearing signal.

The above concepts and relations are applied in the following chapter to physical problems. The efficiency of the wavelet frame reconstruction scheme is discussed by using examples.

5.6 Discussion and Conclusions

As it was discovered earlier during the analysis of wave dispersion, the wavelet decomposition and reconstruction performs effectively on signals having spectral evolutions that are spread over a wide band of frequencies. In the case of proportional-bandwidth systems, the duration of a transient response depends directly on the frequency of vibrations. High-frequency (wide-bandwidth) transient phenomena results in short signal durations and therefore requires more samples in a given time frame. The opposite is true for low-frequency (narrow-bandwidth) transient vibrations. During the construction of transient vibration response for a multi-modal system, both high- and low-frequency components need to be added together to form the overall system response. Consequently, the short- and long-term dynamic behaviors of the system need to be generated at different resolutions,

and th

frame

to cor

the re

are fu

wavel

functi

There

meani

systen

the a

and this point is the fundamental reason for the advantage of the proposed wavelet frame synthesis scheme.

The partitioning of the spectral range by using wavelet frames allows us to consider the output from different resolution levels and automatically adjusts the resolution and the time-duration at different levels of detail. Since wavelets are functions that are localized both in time and frequency, the definition of the wavelet response function fills in the gap between impulse and frequency response functions, which are sharply localized either in time or frequency but not in both. Therefore, it may be argued that wavelet forcing functions are physically more meaningful and may find further use in the experimental analysis of vibro-acoustic systems.

The implementation of the proposed synthesis scheme is clarified during the applications considered in the following chapter.

sis
res
exa
the
cita
the
tran
tion
tern
mult
obta

6.1

spac
deco
has
rela
way
both

wave

CHAPTER 6

APPLICATIONS OF WAVELET FRAME EXPANSIONS AND WAVELET RESPONSE FUNCTIONS

In the following applications, the effectiveness of the wavelet frame synthesis scheme is investigated by considering the construction of the transient vibration response of a finite beam. First, some simple decomposition and reconstruction examples are considered to form a background on wavelet frame expansions. Later, the time history for the acceleration response of a free-free beam to an impact excitation is obtained by employing two different methods. In the classical method, the frequency response of the system is uniformly sampled and then inverse Fourier transformed. The time-domain aliasing problem associated with a DFT construction scheme is demonstrated by considering a lightly-damped system. As an alternative, wavelet frame expansion is used to partition the spectral range into multi-resolution frequency bands, where the response from each resolution level is obtained by using a proper sampling interval.

6.1 Introduction

The mathematical theory and applications of orthonormal basis for Hilbert spaces has been under development for more than a century. In recent studies, the decomposition of signals and functions in non-orthonormal basis, such as frames, has started to receive more attention [15,16,38,42,43,48,68,135]. In particular, the relationship between the frames and wavelets developed recently has opened the way to new analysis and synthesis schemes that benefit from the advantages of both concepts.

The synthesis scheme introduced in the preceding chapter was based on wavelet frame expansions. In the following, multi-voice Morlet wavelet frames are

defined, which are later used to decompose and reconstruct benchmark signals and transient response of a beam.

6.2 Wavelet Frame Expansions

There are many different wavelets that can be used to generate a frame in $L^2(\mathbf{R})$. Due to its smoothness and mathematical simplicity the Morlet wavelet is chosen for the following applications. Since a multi-voice construction is needed to form a usefull frame from the Morlet wavelet, the following presentation begins with a discussion of this issue. Later, the decomposition and reconstruction features of the wavelet frame are studied by giving examples.

6.2.1 Multi-Voice Morlet Wavelet Frames

In the applications, a frame generated by a family of wavelets can be quite usefull during decomposition and reconstruction of functions and signals. The redundancy introduced by a snug, or even better a tight frame, can be exploited during applications [42]. Certainly, different wavelets generate frames with distintive properties. The characteristics of different wavelet frames are investigated in Daubechies's studies [42,43]. In the following, some of her results are used directly without repeating long derivations and proofs.

The Morlet wavelet, used earlier for analysis purposes, has considerable potential for generating effective wavelet frame expansions. In particular, the multi-voice schemes that generate snug frames are very suitable for wavelet frame expansion of functions and signals. In a multi-voice construction, the number of filter-banks that partition the frequency range in a dyadic grid are increased by introducing fractional dilations (or voices) of the mother wavelet. A new family of wavelets is generated from the mother wavelet by each fractional dilation;

$$\psi^j(t) = 2^{-j/N}\,\psi(2^{-j/N}\,t) \qquad j = 0, 1, \ldots, N-1 \tag{6.1}$$

whe

wav

as

whe

wav

whe

(6.2

by t

fram

$B =$

resul

rest

6.2.

chec

func

The

cien

where N is the number of voices in each octave. Then, the definition of the Morlet wavelet given in equation (2.27) implies that the new wavelets should be defined as

$$\psi^j(t) = 2^{-j/N}\,\pi^{-1/4}\,\exp\left[-i\omega_c 2^{-j/N} t\right]\,\exp\left[-2^{-2j/N}\,\frac{t^2}{2}\right]$$

where again $j = 0, 1, \ldots, N-1$. On a discrete lattice, the preceding multi-voice wavelet representation yields

$$\psi^j_{mn}(t) = \frac{2^{-(m/2+j/N)}}{\pi^{1/4}}\,\exp\left[-i\,\omega_c\,2^{-j/N}(2^{-m}t - n)\right]\,\exp\left[-2^{-2j/N}\,\frac{(2^{-m}t-n)^2}{2}\right] \tag{6.2}$$

where $m, n \in \mathbf{Z}$ and $j = 0, 1, \ldots, N-1$. Depending on the choice of N, equation (6.2) leads to the construction of different wavelet frames with each characterized by the corresponding frame bounds. Daubechies has shown that a Morlet wavelet frame constructed by using four voices has the frame bounds $A = 6.918$ and $B = 6.923$, which yield a redundancy ratio $B/A = 1.0008$. Therefore, $N = 4$ results in a very snug frame. This four-voice Morlet wavelet frame is used in the rest of this chapter to decompose and reconstruct functions and signals.

6.2.2 Reconstruction of the Dirac Delta Function

A dirac delta function (distribution) can be used as a simple means of checking the reconstruction properties of Morlet wavelet frames. The dirac delta function is defined as

$$\delta(t - t_0) = \begin{cases} 0, & t \neq t_0 \\ \int_{-\infty}^{\infty} \delta(t - t_0)\,dt = 1 \end{cases}$$

The wavelet frame decomposition of the delta function generates wavelet coefficients which are obtained as

$$F^j_{mn} = \langle \delta, \psi^j_{mn} \rangle = \int_{-\infty}^{\infty} \delta(t - t_0)\,\overline{\psi^j_{mn}(t)}\,dt = \overline{\psi^j_{mn}(t_0)}\,.$$

In or

assig

are d

Follo

(5.1

Alt

in a

effe

wa

nu

in

in

wa

ho

re

oc

di

6

a

t

In order to simplify the computations, the location of the dirac delta pulse is assigned to the origin $t_0 = 0$. Then, from equation (6.2) the wavelet coefficients are derived as

$$F_{mn}^{j} = \frac{2^{-(m/2+j/N)}}{\pi^{1/4}} \exp\left[i\omega_c 2^{-j/N} n\right] \exp\left[-2^{-2j/N} \frac{n^2}{2}\right] ,$$

$$m, n \in \mathbf{Z}, \quad j = 0, 1, \ldots, N-1 .$$

Following such a decomposition, the wavelet frame expansion given in equation (5.11) implies that the original delta function can be approximated closely by

$$\delta_{appr}(t) \simeq \frac{2}{A+B} \sum_{j,m,n} F_{mn}^{j} \psi_{mn}^{j}(t) . \tag{6.3}$$

Although such an expansion theoretically requires m to take all integer values in $\mathbf{Z}$, in applications m has to be limited to a finite interval. In order to demonstrate the effectiveness of such a truncation, equation (6.3) is simulated with the preceding wavelet coefficients by using the four-voice Morlet frame. In Figure 6.1, the total number of octaves used during the decomposition-reconstruction process is varied in each of the cases (a) through (d). Inclusion of contributions from higher octaves in Figure 6.1a results in a finer resolution and gives better cancellation of the waviness on either side of the pulse. As observed from this example, no matter how sharp the signal might be, the total number of octaves for a satisfactory resonstruction of the original signal can be expected to be in the order of 20 octaves. For smoother signals, one can use even smaller number of octaves as discussed in the following examples.

6.2.3 Reconstruction of Synthetic Signals

In general, for a given signal the wavelet coefficients are not tractable analytically, but needs to be calculated numerically. Therefore, the discrete wavelet transform algorithm that was introduced earlier in section 2.4 is reconfigured to

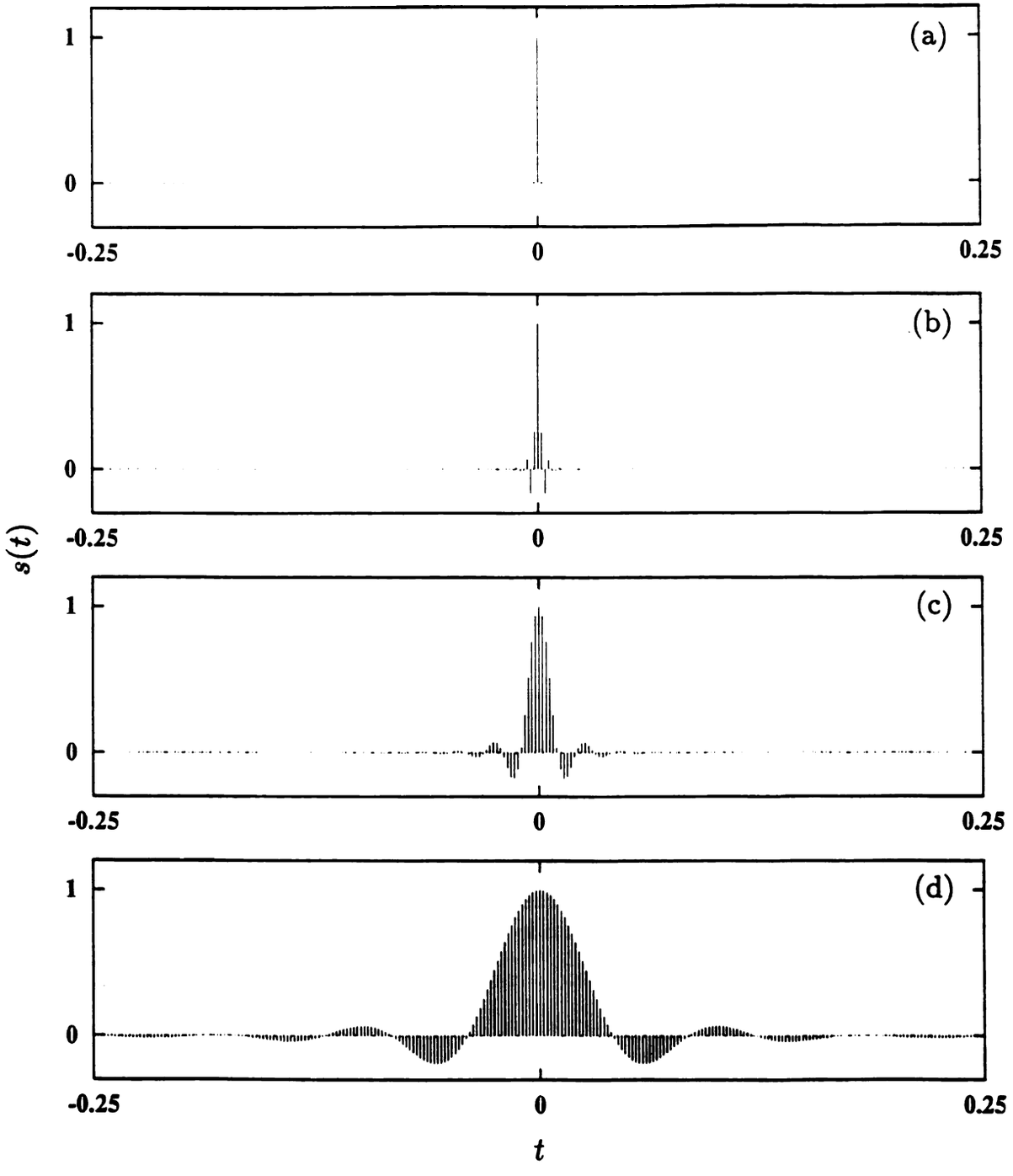

Figure 6.1 The reconstruction of a dirac delta function by using wavelet frame expansions. The total number of octaves used during the reconstruction are a) 19, b) 15, c) 11 and d) 7.

output wavelet frame coefficients for a given signal. The four-voice Morlet wavelet frame expansion scheme used in the preceding example is applied to some well-known synthetic signals. In each of the following examples, a total of nine octaves are used during the decomposition and reconstruction operations. In Figure 6.2, the original and the resconstructed signals are compared to each other. The results show that the nine octave range gives quite accurate reconstructions for smoothly varying signals. However, sharp discontinuties require contribution from higher scales for better reconstruction.

In order to evaluate the potential of the frame reconstruction scheme, the preceding decomposition-reconstruction algorithm was applied on a measured acceleration signal. The acceleration signal measured earlier in section 4.4 is used here as an example. The physics of the governing transient wave propagation phenomena was studied earlier in section 4.4. The original acceleration signal, plotted in Figure 6.3a, was first decomposed into the Morlet wavelet frame representation, and later reconstructed by using nine octaves. The reconstructed acceleration signal is plotted in Figure 6.3b. A comparison of the original and the reconstructed signals shows that the wavelet frame expansion succesfully recovers the main temporal and spectral characteristics of the acceleration signal. The nine octave range, that was used during the resonstruction process, filters out very low- and high-frequency components of the original signal.

The decomposition and reconstruction properties of the wavelet frame expansions considered in the preceding examples helped us gain confidence and insight in the procedure. So far, both the starting point and the end result were chosen as the time-domain representation of a signal. However, in many engineering applications, the frequency domain is the most suitable starting point for the formulation of a system's response. In the following, the utilization of wavelet frame expansions to obtain transient vibration response of linear systems is investigated. In order to clarify the benefits of using wavelet response functions in such a synthesis scheme, first the limitations of a commonly used discrete Fourier transform (DFT) approach are discussed by considering an example.

(د) x

(ه) x

(و) x

(ز) x

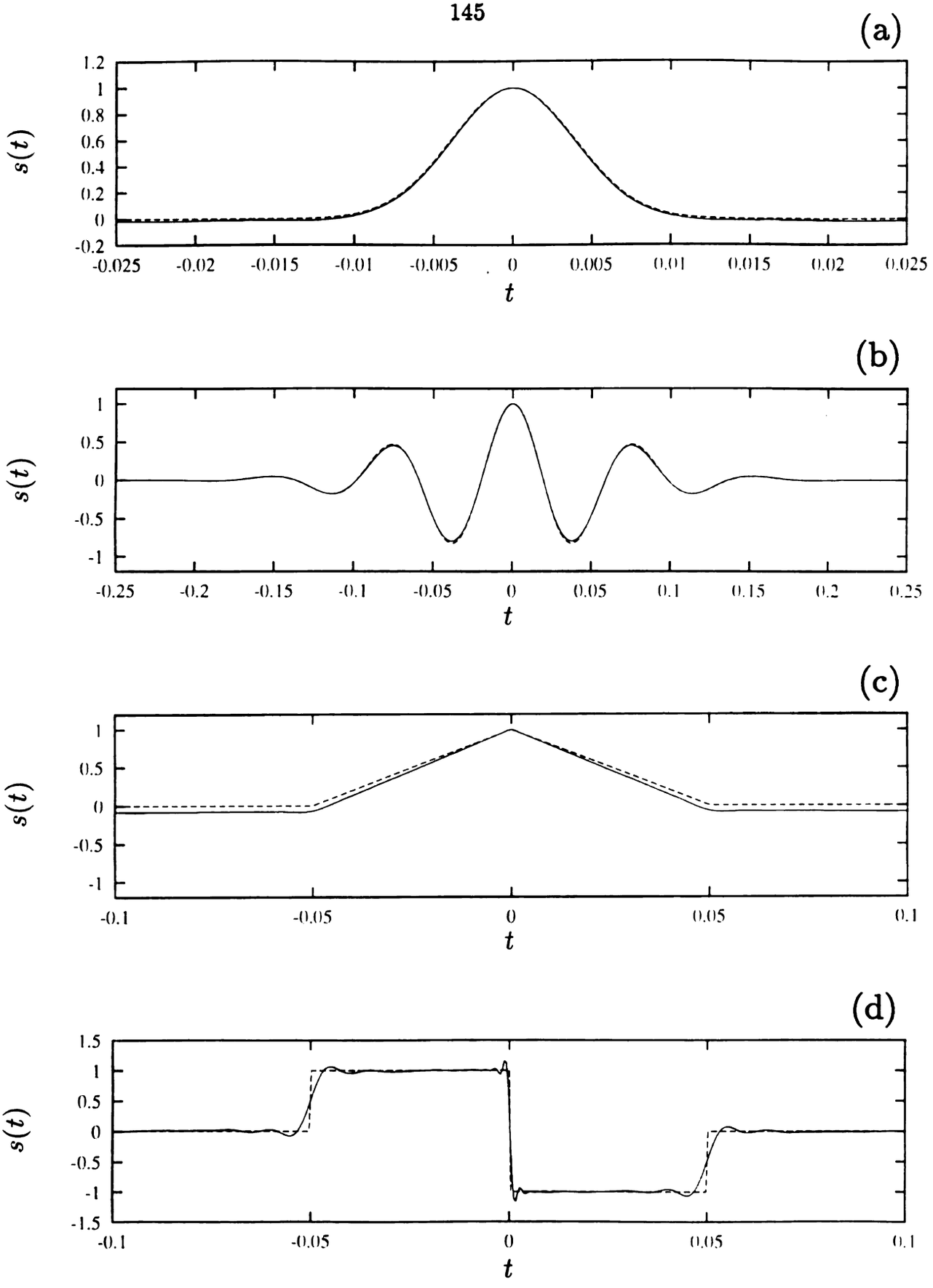

Figure 6.2 Examples on decomposition and reconstruction of synthetic signals. The wavelet frame contains nine octaves and four voices. --- Original signal, — Reconstructed signal.

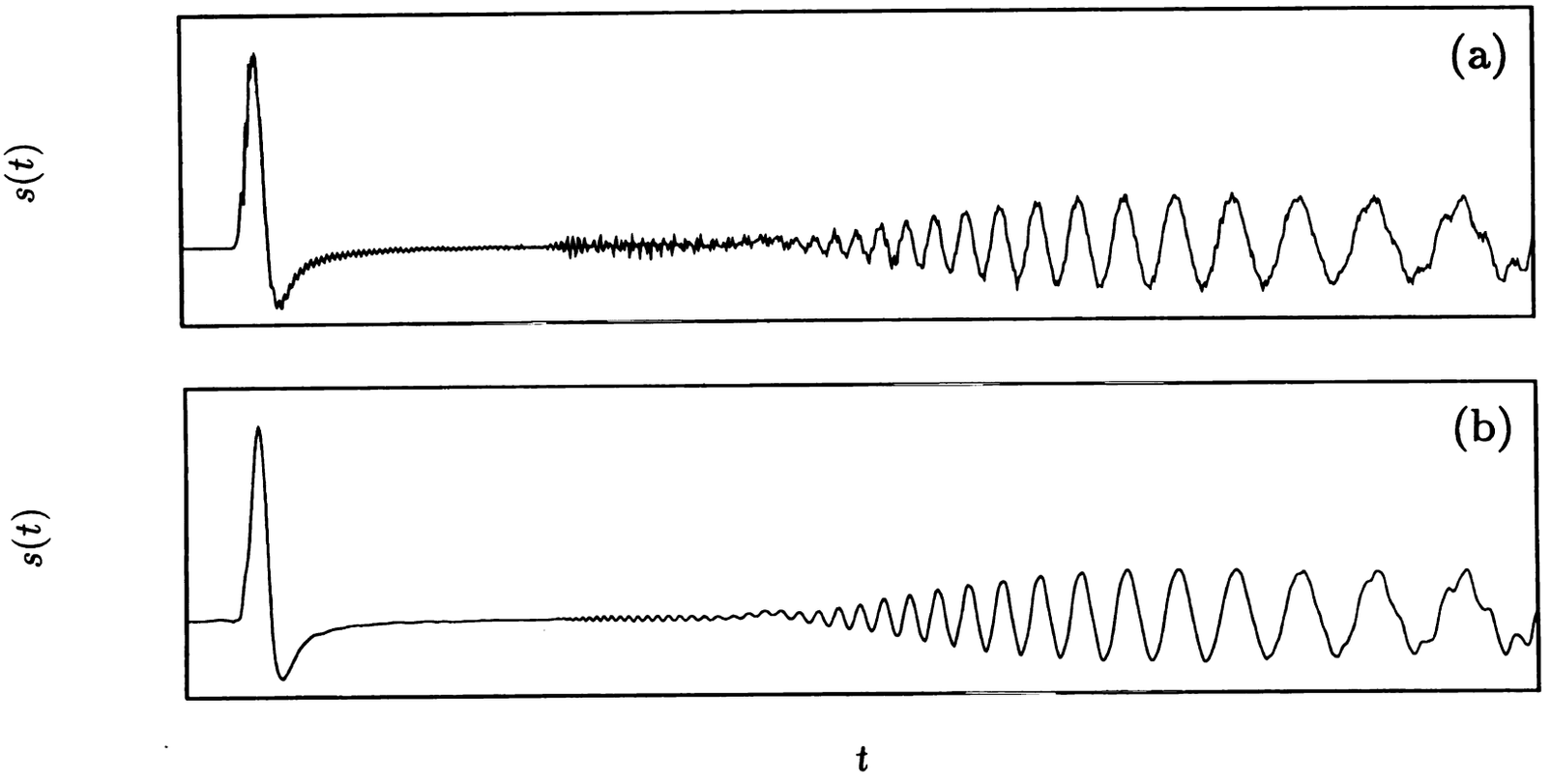

Figure 6.3 The reconstruction of a measured acceleration signal. The wavelet frame contains nine octaves and four voices. a) Original signal, b) Reconstructed signal.

6.3

6.3 Transient Response of a Beam: FFT Synthesis

In the following, the discrete Fourier transform is used to synthesize the transient vibration response of a uniform beam that has free boundaries. The specimen is considered to have the same material and geometric properties as the aluminum beam used in section 4.4.2. The drive-point accelerance of the beam is obtained by using the transfer matrix method, given by equation (4.13). The magnitude of the accelerance is given in Figure 6.4a. An average loss factor of $\mu = 0.001$ is used to characterize the material damping in the aluminum beam. The system is considered to be excited by a Gaussian pulse, which has a spectral distribution as shown in Figure 6.4b, with the magnitude decaying off near $6\,kHz$. In experiments, a similar spectrum for the excitation was observed from the measurements conducted with a myler-tipped hammer during its impact on the beam. According to equation (5.2), the response of the system is given by $Y(\omega) = H(\omega)\,F(\omega)$. Therefore, the action of the force may be thought of as though it is low-pass filtering the impulse response of the system.

In order to apply the inverse discrete Fourier transform, the frequency response $Y(\omega)$ is sampled in the frequency domain. The bandwidths and the upper bounds for the sampling interval are calculated by using the relations given in equations (5.5) and (5.6). The results are tabulated in Table 6.1. Since the first mode has the smallest bandwidth, the sampling criteria is determined by using the corresponding frequency interval, which is $\delta_f \leq 0.0033$. The spectral range is chosen to include $0\,Hz$ to $F_{max} = 12800\,Hz$. Consequently, in order to prevent time domain aliasing, the size of the FFT needs to satify $N \geq 7\,757\,576$, which is unacceptably large for all practical purposes. If the frequency interval is fixed, the use of smaller number of FFT points will increase the interval between frequency samples. Therefore, the contribution coming from the modes at the lower end of the spectrum (which have smaller bandwidths and large T_s) will cause aliasing during reconstruction of the system's time response.

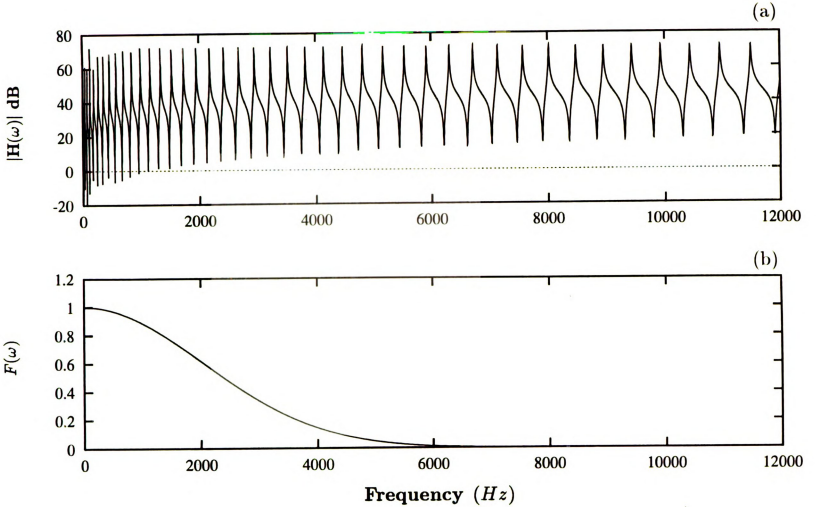

Figure 6.4 a) The magnitude of the drive-point accelerance for the aluminum beam.
b) The spectrum of the impulsive force.

Table 6.1 The natural frequencies, the associated bandwidths and the suggested sampling intervals.

Mode #	$f\,(Hz)$	$B_{3dB}\,(Hz)$	$\delta_f \leq$
1	14.43	0.0144	0.0033
2	39.77	0.0398	0.0090
3	77.97	0.0780	0.0177
4	128.89	0.1289	0.0293
5	192.55	0.1926	0.0438
6	268.94	0.2689	0.0611
7	358.05	0.3581	0.0814
8	459.90	0.4599	0.1045

The effect of the sampling interval on the constructed system response is investigated by considering different FFT sizes in the present problem. In Figure 6.5, the vibration response of the beam is obtained by sampling the frequency response at four different sampling intervals. The detail at the initial instances of time, following the impulsive force, is shown in Figure 6.6. As observed clearly from Figures 6.5a and 6.6a, the sampling interval $6.25\,Hz$ causes unacceptably heavy aliasing in the time domain and hardly displays any information relevant to the physics of the wave propagation and dispersion. As the sampling interval becomes smaller, proceeding downward in Figures 6.5 and 6.6, the effect of aliasing slowly weakens down. However, as demonstrated by the above calculations, even the case $N = 2^{15}$, given in Figure 6.5d, still carries the effects of aliasing coming from low-ordered modes. Consequently, as long as the synthesized response contains aliased modal contributions, these results can qualify only as rough approximations.

The preceding example demonstrated the time-frequency resolution problem associated with the Fourier transform. As peaks get sharper in the frequency

Acceleration (m/s^2)

Fig.

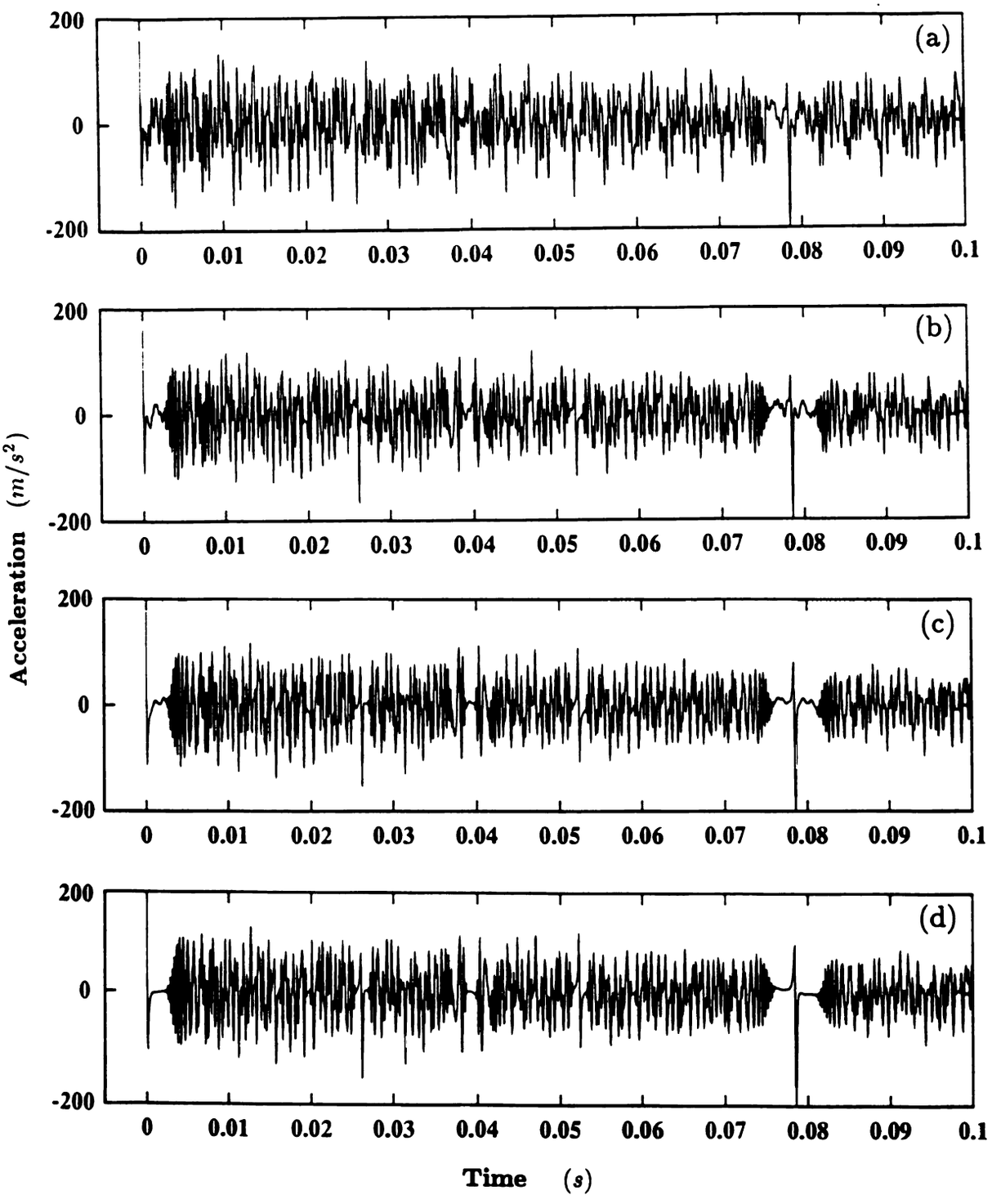

Figure 6.5 The transient vibration response of the free-free beam synthesized from its frequency response function by using uniform sampling and inverse discrete Fourier transform. The sampling intervals and the corresponding FFT sizes are a) $\delta_f = 6.25\ Hz$, $N = 2^{12}$, b) $\delta_f = 3.125\ Hz$, $N = 2^{13}$, c) $\delta_f = 1.5625\ Hz$, $N = 2^{14}$, and d) $\delta_f = 0.78125\ Hz$, $N = 2^{15}$.


Acceleration (m/s^2)

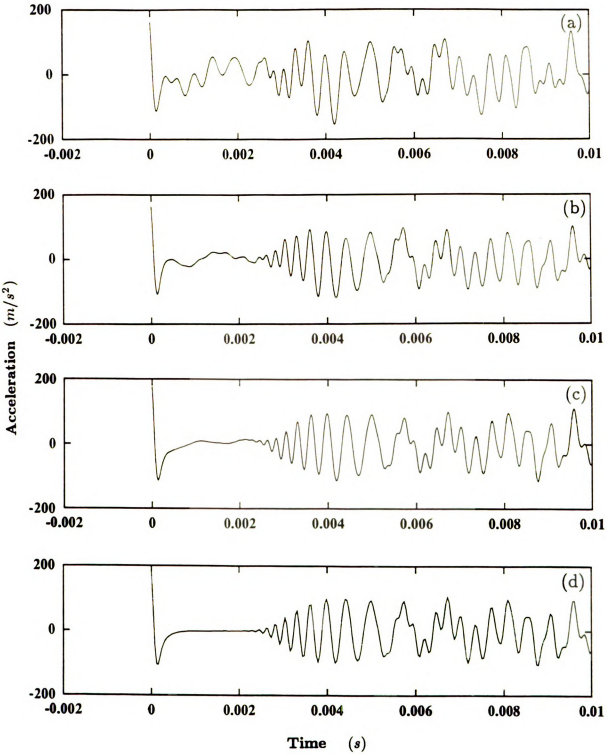

Figure 6.6 The initial instances of the system response, corresponding to the cases shown in Figure 6.5.

dom
The
bec
crea
spe
diff
res

6.4

syn
fra
coe
fra
fun
fra
fun
are

per
the
the
mo
wa
is
the
co
for
Ta
vir

domain, it takes longer for the transient response to decay in the time domain. Therefore, the effectiveness of using uniform sampling in the frequency domain becomes questionable, since the bandwidth of the frequency response function increases proportionally with frequency. It would certainly be more efficient if the spectrum could be divided into multi-resolution bands with each band assigned a different sampling interval. The wavelet frame expansion provides such a multi-resolution construction, as shown in the following.

6.4 Transient Response of a Beam: Wavelet Frame Synthesis

In the preceding chapter, the convolution integral was replaced with a new synthesis scheme. In the following applications, the implementation of the wavelet frame synthesis is carried out in three stages. In the first stage, the wavelet frame coefficients of the excitation signal is determined. A four-voice Morlet wavelet frame is used throughout this analysis. In the second stage, wavelet response functions of the system are calculated. In the final stage, the modulated wavelet frame coefficients are found and multiplied with the associated wavelet response function. Then, the response contributions coming from different resolution levels are added together to form the vibration response of the system.

The response of the system is synthesized by using 9 octaves and 4 voices per octave, which makes a total of 36 resolution components. In order to optimize the performance of the reconstruction, the nine octave range was offset to span the octave range $m = 4, \ldots, 12$, the decision being based on the distribution of the modal frequencies of the beam. The number of samples in each frequency interval was fixed at 2^{13} samples. Therefore, on each octave-band the spectral resolution is automatically adjusted, becoming smaller at lower-frequency bands. Some of these features are summarized in Table 6.2. Note that, the frequency resolution corresponding to 4th octave, $\delta_f = 0.004\,Hz$, is very close to the value required for the un-aliased synthesis of the first modal contribution, which was stated in Table 6.1 as $\delta_f \leq 0.0033$. Therefore, as far as aliasing is concerned, the results are virtually unaffected.

Table 6.2. The center frequency for each octave band, the associated maximum frequency and the sampling interval required for 2^{13} samples.

m (Octave)	$f_{center}\ (Hz)$	$F_{max}\ (Hz)$	$\delta_f\ (Hz)$
0	0.8493	2.1232	0.00026
1	1.6986	4.2466	0.00052
2	3.3973	8.4931	0.00010
3	6.7945	16.986	0.00207
4	13.589	33.973	0.00415
5	27.178	67.945	0.00829
6	54.356	135.89	0.01659
7	108.71	271.78	0.03318
8	217.42	543.56	0.06635
9	434.85	1087.1	0.13270
10	869.70	2174.2	0.26540
11	1739.4	4348.5	0.53080
12	3478.8	8697.0	1.06160

6.4.1 Unit Sample Pulse Excitation

The acceleration response of the aluminum beam following an initial impulsive force is obtained by using the wavelet frame expansions, and the result is shown in Figure 6.7a. Following the initial excitation, the acceleration response decays slowly in time while showing off the pulse-reformation phenomenon four times in Figure 6.7a. The duration until the first occurance of the pulse-reformation phenomena are given in more detail in Figure 6.7b. Further details for the initial instances of the system response and the pulse-reformation are provided in

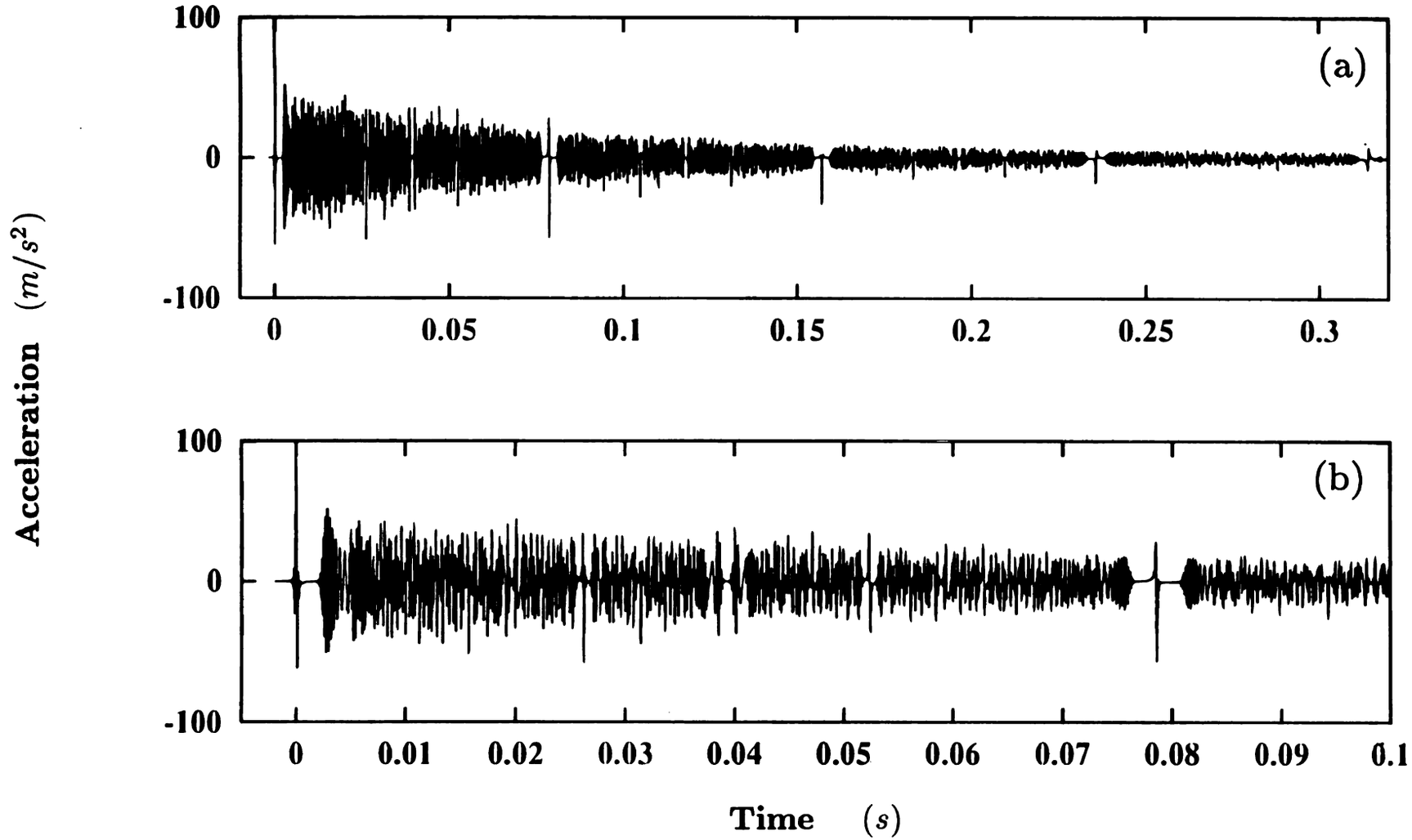

Figure 6.7 a) The acceleration of the free-free beam in response to an impulsive excitation. The response is synthesized by using a Morlet wavelet frame defined by nine octaves and four voices. b) The details of the first pulse-reformation process.

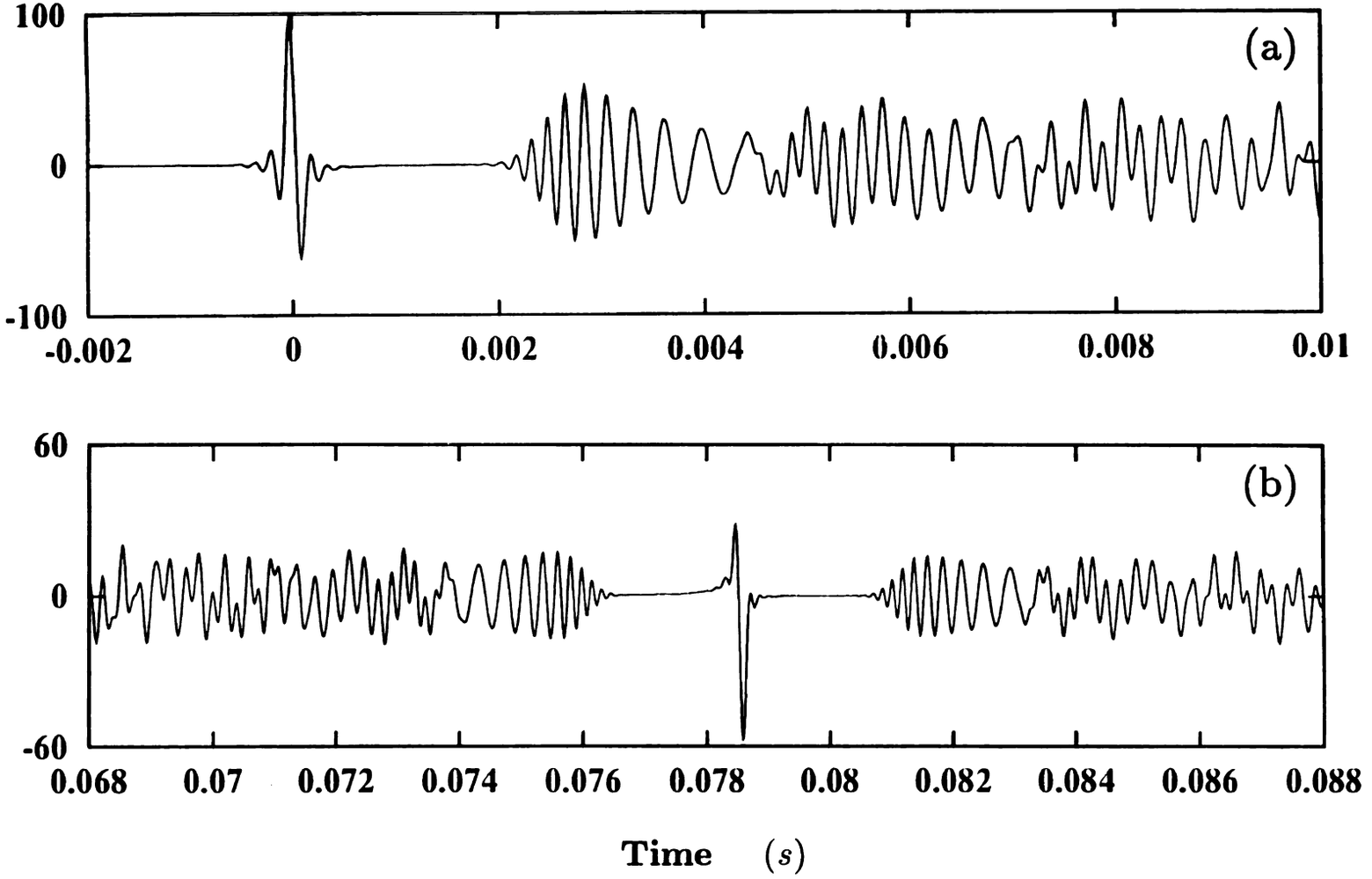

Figure 6.8 An expanded view of the original and the reconstructed pulses. a) Original pulse, b) Reconstructed pulse.

Fig
78.5
the
rese
repr
on
to a
ran
the
osc
init
tio
res
the
res
no
co
to
pr
is
δ_f
hig
du
6.3
tir
tir
wa
th
in

Figure 6.8. The pulse-reformation phenomenon is observed to occur at around 78.5 ms, following the initial pulse. As discussed earlier in relation to Figure 6.1, the decomposition of a unit sample pulse over nine-octaves gives an oscillatory representation during the reconstruction. As demonstrated earlier in Figure 6.1, the representation of a delta function over nine octaves results in a function oscillating on both sides of a sharp peak. Therefore it is fair to say that the system responds to an excitation that has a wide-band spectral representation defined in $0-9\ kHz$ range. Infact, the affect of this forcing function is observed from the response for the initial instances of time in Figure 6.8a, where the initial vibrations mimic the oscillatory behavior of the excitation. The flat zero response region following the initial pulse, and also before and after the reconstructed pulse, give a clear indication of the quality of the synthesized system response. The reason is that a zero response over an extended period of time requires perfect cancellations between the response contributions coming from different resolutions. In comparison, the results given in Figure 6.6 demonstrated that the aliased signal components did not allow this cancellation to occur completely.

The effectiveness of the present approach is clarified by considering the contribution to the response of the system from each resolution level. In reference to Figure 5.2, the response components $y_m^{\psi}(t)$ are studied independently. For the present problem, the response of the system contributed from five different octaves is presented in Figure 6.9. Since the frequency resolution is altered at each octave, δ_f increases with m, and thus the time duration of the signal becomes shorter at higher frequency bands. The striking feature is that this adjustment of the time duration works to prevent aliasing at all resolution levels. As observed from Figure 6.9, each response component decays off within the first half of the corresponding time window length. As a result, both the long-time (low-frequency) and short-time (high-frequency) behavior of the system are obtained simultaneously. In a way, the wavelet frame synthesis works like a microscope, displaying the details of the system dynamics at different levels of magnification with adequate resolutions.

This way of viewing the contents of a signal can give us further insight into the pulse reconstruction phenomenon discussed earlier. In the following, the

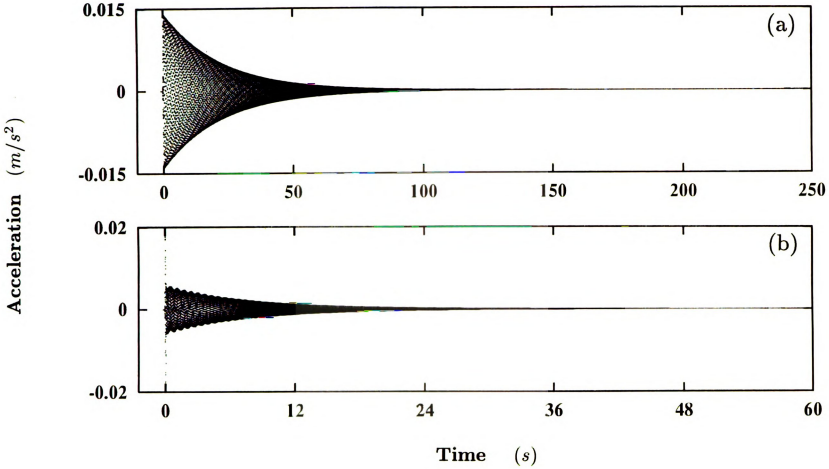

Figure 6.9 The envelope of the acceleration response of the system contributed from different octave resolutions, $y_m^{\psi}(t)$. The octave numbers are a) $m = 4$, b) $m = 6$, c) $m = 8$, d) $m = 10$ and e) $m = 12$.

0.25

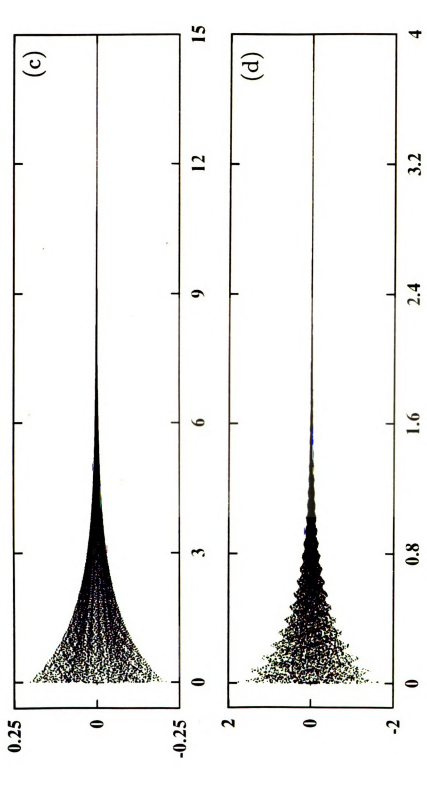

Figure 6.9 (Continued).

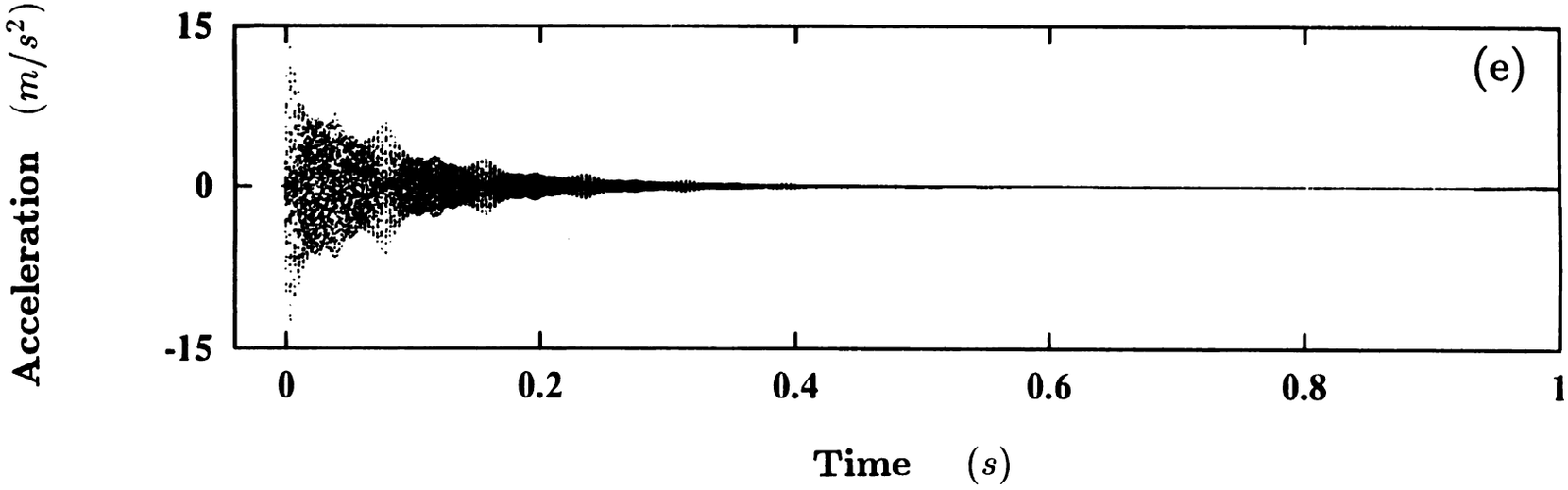

Figure 6.9 (Continued).

response of the system contributed from each resolution level is used to give a better explanation for the pulse-reformation phenomenon. Note that, the response given in Figure 6.7a was constructed by summing all the contributions coming from different resolution levels at a given time, $y(t) = \sum y_m^{\psi}(t)$. In Figure 6.10, the system's response is displayed at three successive octave resolution levels. It is obvious that the projection of the unit sample pulse to each resolution subspace results in a different wave pattern in the system's response contributions. It is the summation of such wave groups that results in the initial pulse shown in Figure 6.8a. In all three cases shown in Figure 6.10, the initial wave group is observed to continue to disperse and go through multiple reflection until $t = 78.5ms$ (pointed by the arrows). Remarkably, at each resolution level the wavegroup reformes into its original shape at around $t = 78.5\ ms$, the only difference being slightly lower magnitudes due to dissipation. Consequently, the summation of such wave groups at $t = 78.5\ ms$ results in an another pulse looking very similar to the original one, as shown in Figure 6.8b. The initial and the reconstructed waveform observed in Figure 6.10c, is expanded for better comparison in Figure 6.11. After many reflections from the boundaries and continued dispersion throughout its propagation, the original waveform is very closely duplicated with only a slight reduction in the magnitude due to material damping.

6.4.1 Gaussian Pulse Excitation

The unit sample pulse used in the preceding example is not a physically realistic forcing function due to its sharpness. As a result of using a limited number of octaves, the decomposition of the unit sample pulse was lacking high frequency information and thus in Figure 6.8 small amplitude oscillations were observed about $t = 0$. A more realistic function that can be used to simulate an impulsive excitation is the Gaussian pulse. The acceleration response of the beam due to a Gaussian pulse excitation is obtained by employing the preceding wavelet frame expansion scheme. The results, which are given in Figure 6.12, portray features similar to Figure 6.7, but now the contribution coming from the higher frequency bands is reduced. The detail of the initial and reconstructed pulses are given in Figure 6.13. The smoothness of the Gaussian pulse has prevented the

Acceleration (m/s^2)

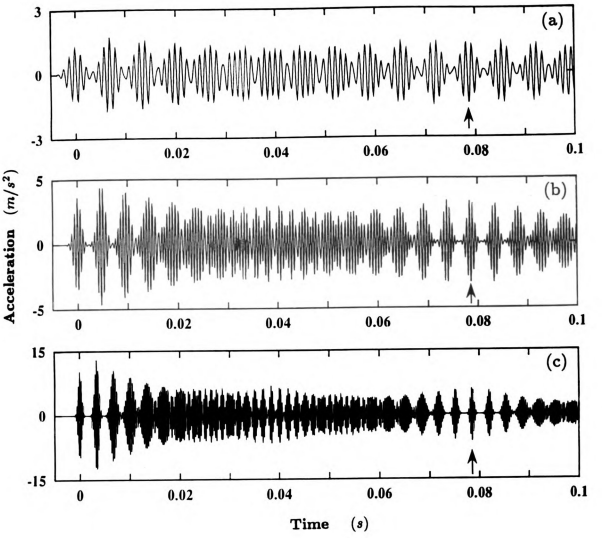

Figure 6.10 The reconstruction of the initial wave group at three different octave resolutions. The reconstruction time is $T_s = 78.5\ ms$. The octave numbers are a) $m = 10$, b) $m = 11$ and c) $m = 12$.

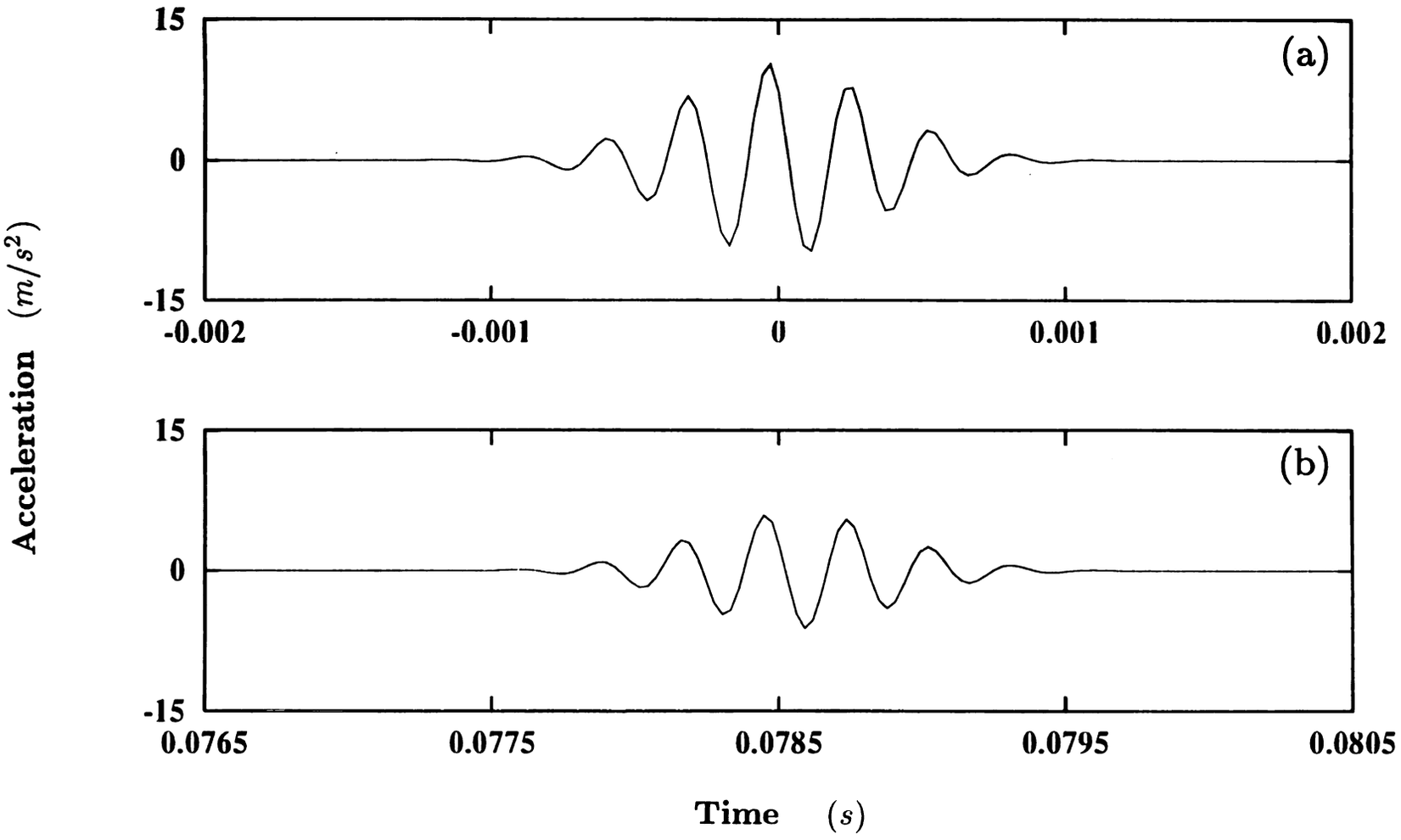

Figure 6.11 The reconstruction of the original wave group at the 12th octave resolution. a) Original wave group, b) Reconstructed wave group.

small oscillations on either side of the original and reconstructed pulses which were observed earlier in Figure 6.8. These results look very similar to the acceleration signals measured in experiments discussed in Chapter 4.

6.5 Discussions and Conclusions

A comparison of the results obtained from the uniformly-sampled discrete Fourier transform method (Figure 6.5d) and those obtained from a wavelet frame expansion (Figure 6.12b) shows an overall similarity in the constructed time domain signals. In particular, the details of the initial instances given in Figures 6.6d and 6.13a are quite similar. Small differences are due to the aliasing that is present in the former case.

In general, the self-adjusting sampling property of the wavelet frame synthesis scheme results in a more efficient construction, since the details of the signal are generated at different resolutions. A distinct advantage of the wavelet frame reconstruction scheme is that the effect of the excitation on the system's response can be viewed at different scales. The resolution at each scale level is matched with the detail of the reconstructed component of the response. Consequently, the short- and long-time duration contributions to the overall system response are obtained simultaneously. However, in comparison to a direct FFT inversion scheme, the wavelet frame expansion method is generally more difficult to implement. The advantage of the proposed synthesis scheme becomes more pronounced as the range of frequencies contained in the signal becomes larger.

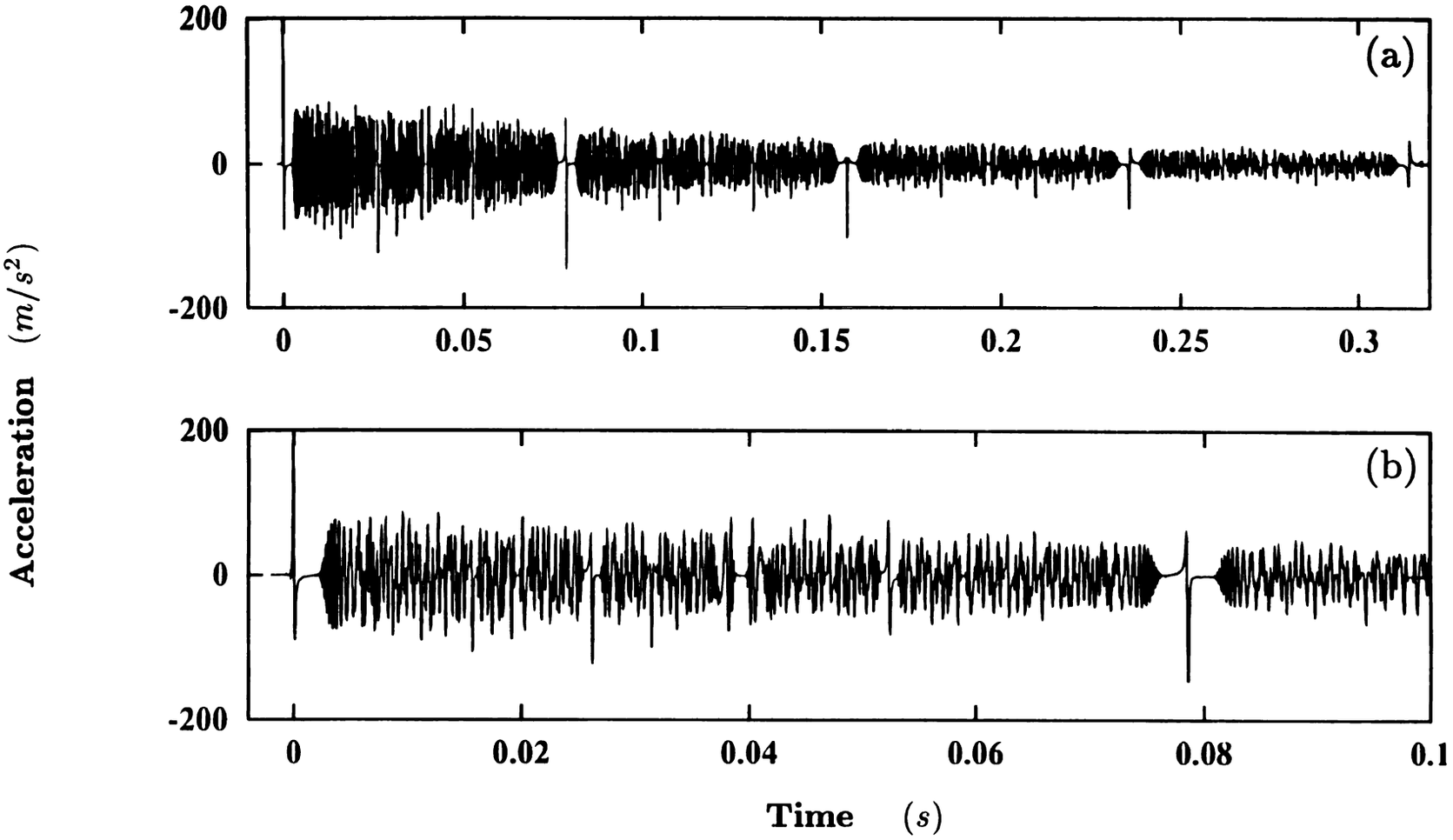

Figure 6.12 a) The acceleration of the free-free beam in response to a Gaussian pulse excitation. The response is synthesized by using a Morlet wavelet frame

(a)
200

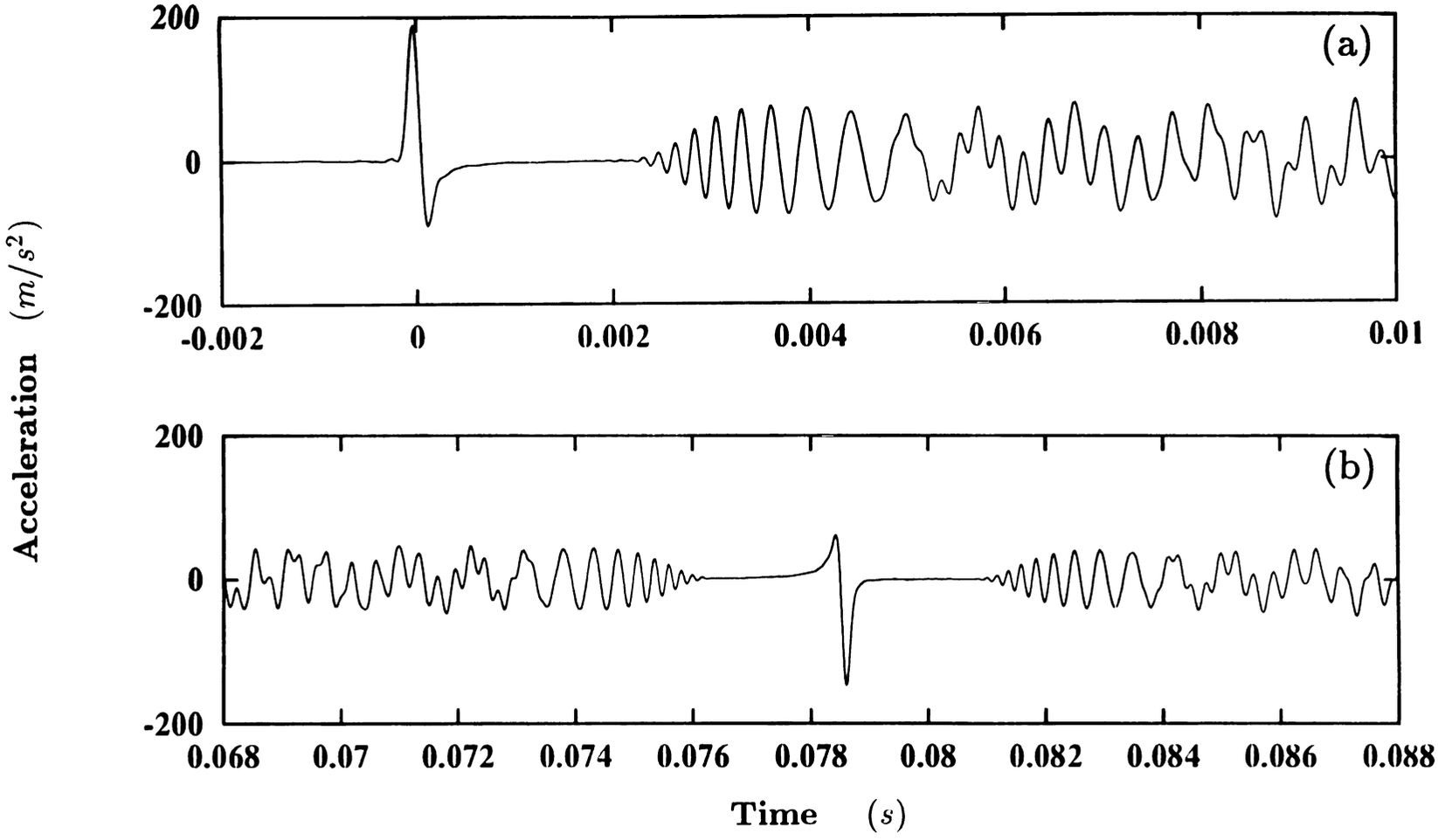

Figure 6.13 A detailed view of the original and the reconstructed pulses. a) Original pulse, b) Reconstructed pulse.

CHAPTER 7

DISCUSSION AND CONCLUSIONS

In this concluding part of the study, some of the secondary issues raised during the preceding chapters are considered in more detail. For example, since wavelet transform can operate with different wavelets, the performance of alternate choices are investigated. The use of different bandwidths in Morlet wavelet filters are also discussed, and the effect on the resolution of the transforms is studied by considering a reference signal. The distinction between wavelet frames and orthonormal basis is discussed in the context of reconstruction of transient signals. The chapter is concluded with a discussion on other possible applications of wavelets in mechanical systems, a summary of the properties of wavelets, and a presentation of the specific contributions of this research.

7.1 Alternate Choices for Wavelets

During the application of the wavelet theory, one of the difficult decisions that needs to be made is the choice of the mother wavelet. Since the beginning of the recent uptrend in the wavelet research, many different families of wavelets have been suggested for use in applications, as listed in the literature [14,24,36,43,94,116,122]. With the current trend, it is expected that different types will be discovered in the near future. In applications, the properties that are considered during the selection of a wavelet basis are listed as; the orthogonality of the basis (vs. frames), support range (finite or infinite), symmetry, regularity (smoothness), real or complex types, size of the quadrature mirror filters, existence of the side bands in the spectrum, decay characteristics in both time and frequency domains and the ease of implementation. In a particular application, it may be sufficient to consider only a few of these properties and disregard the

others. For example, in signal compression applications, the selection of a particular type of wavelet depends very much on the characteristics of the signal that is being analyzed. One solution to this difficult selection problem is suggested by Coifman [32-34], where an entropy-based algorithm is designed to operate on a wide class of wavelets.

In the analysis of mechanical systems, the physical interpretation of the transform becomes as important as the other factors. One needs to understand the physical meaning of the basic building blocks themselves before decomposing a measured signal into its corresponding components. For example, earlier in section 3.3.3, the group velocity and the propagation of vibrational energy were nicely related to the time-scale representations generated by the Morlet wavelet transform. Both the dispersion and the cutoff phenomenon were clearly identified from the wavelet transform of the acceleration signal, which was measured from a semi-infinite beam following the impact of a hammer on the free end. This particular acceleration signal was analyzed first by using the Morlet wavelet transform with $\omega_c = 5$, and later, by employing STFT with two different window sizes. The signal and resulting TFRs were plotted in Figures 3.11-3.13. Since this particular acceleration signal contains two different dynamic phenomena that have spectral components evolving simultaneously in time, it is used in the following as a reference signal to study the performance of different wavelet families.

7.1.1 Morlet Wavelet with Different Center Frequencies

In some applications, wavelet filters with narrower bandwidths are found to give more effective displays of the spectral evolution of a nonstationary signal [36]. So far in this study, a particular form of the Morlet wavelet was used having a center frequency $\omega_c = 5$. The definition of the Morlet wavelet, given in section 2.3.4, implies that the bandwidth of the wavelet filter is defined by the center frequency, ω_c, of the mother wavelet. Therefore, if ω_c is increased, the bandpass filter bank structure induced by the Morlet wavelet will become narrower and shifted toward higher frequencies. In order to demonstrate the effect of increasing the center frequency on the TFRs, the reference acceleration signal is transformed

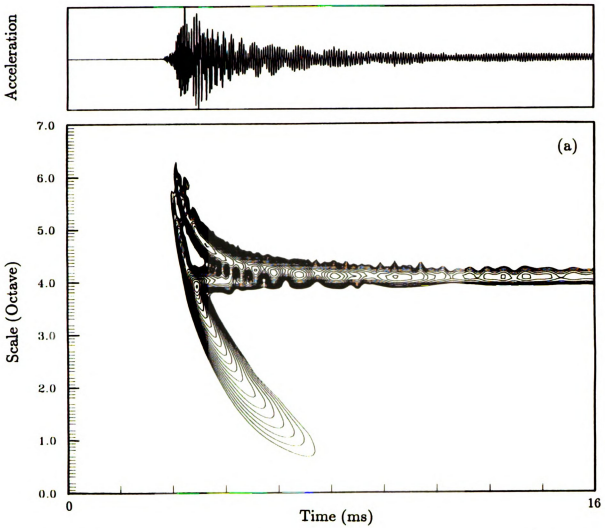

Figure 7.1 The wavelet transform of the reference acceleration signal by using Morlet wavelet. The center frequency a) $\omega_c = 10$ and b) $\omega_c = 20$.

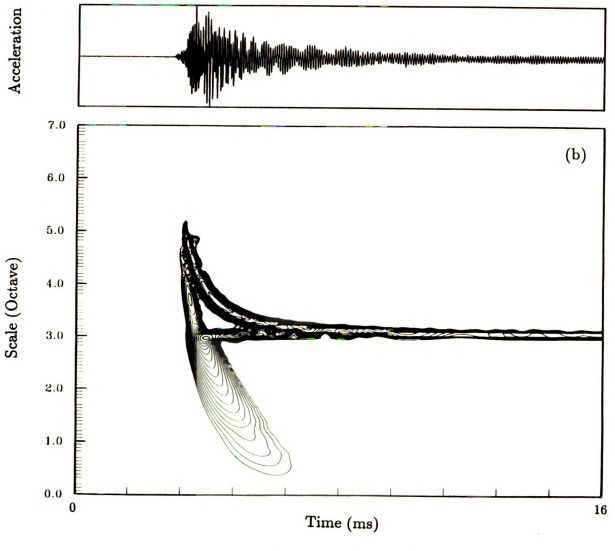

Figure 7.1 (Continued).

by using two different ω_c values in the Morlet wavelet. In Figure 7.1, the TFRs corresponding to $\omega_c = 10$ and $\omega_c = 20$ are displayed. A comparison between the earlier transform result (based on $\omega_c = 5$) given in Figure 3.12 and the present TFRs, reveals that better spectral localization can be achieved by adjusting ω_c. For instance, the two physical phenomena, the dispersion of the fundamental flexural wave motion and the cutoff of the first plate-mode, are seperated clearly in Figure 7.1a. However, as the bandwidth becomes narrower with increasing ω_c, the quality of the time localization starts to deteriorate in the wavelet transforms. Based on other examples considered in this study, it can be concluded that, for a typical transient vibration analysis application, the center frequency will vary between 5 and 20. The final choice will be dictated by the particular application.

7.1.2 Mexican Hat and Battle-Lemarie Wavelets

The Mexican hat and the Battle-Lemarie wavelets were introduced in section 2.3, and their graphs were plotted in Figures 2.7 and 2.12, respectively. Unlike the Morlet wavelet, these wavelets are both real, and therefore they generate real transforms. Again, the same acceleration signal is transformed by using Mexican hat and Battle-Lemarie wavelets. The magnitudes of the transforms are plotted in Figures 7.2 and 7.3. The general signature of the TFR given in Figure 7.1 is observed also in both of these wavelet transforms. However, the details of the TFR displayed in Figures 7.2 and 7.3 are more complicated and some of the features are not easily associated with any particular physical phenomenon. In particular, at higher scales it is difficult to distinguish between the ridges corresponding to the two different dynamic behaviors; the dispersion of the fundamental flexural wave motion and the cutoff phenomenon.

7.1.3 Daubechies's Compactly Supported Orthonormal Wavelet

The compactly supported orthonormal wavelets were introduced specifically for image and signal compression applications. In comparison to infinite-support slowly-decaying wavelets, Daubechies's wavelets are expected to give superior performance in real-time FIR filter bank implementations. However, in the analysis

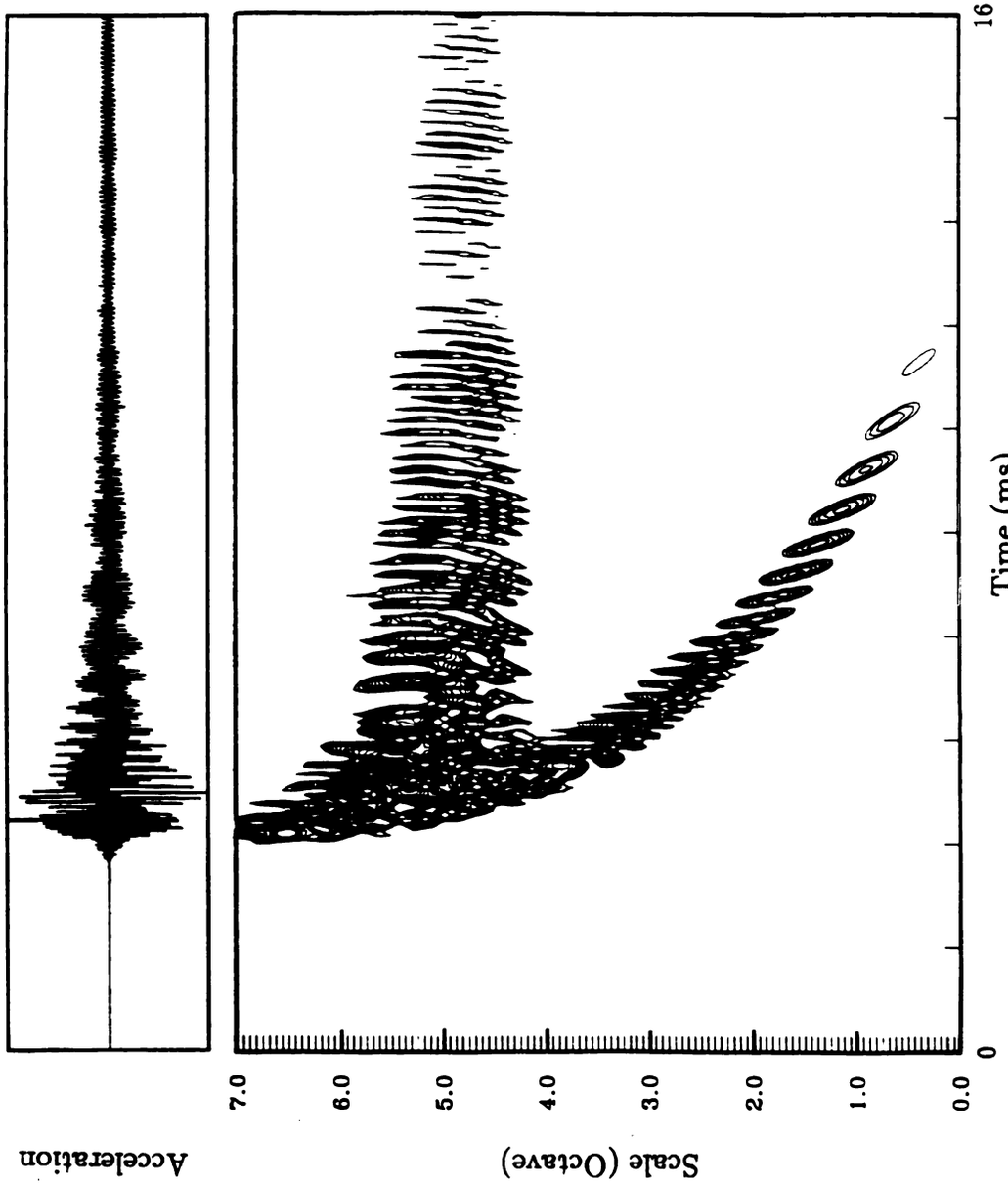

Figure 7.2 The wavelet transform of the reference acceleration signal by using Mexican Hat wavelet.

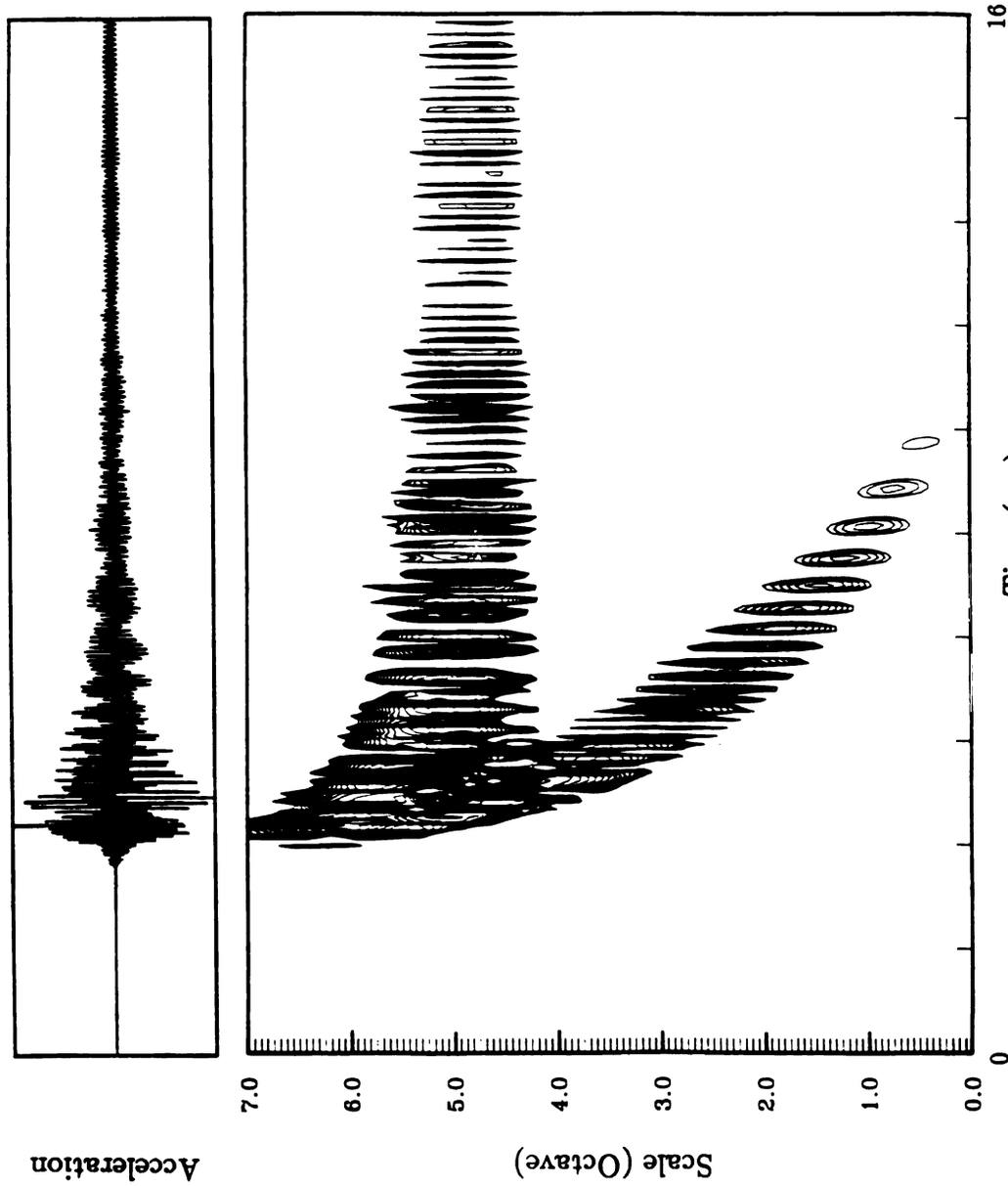

Figure 7.3 The wavelet transform of the reference acceleration signal by using Battle-Lemarie wavelet.

of signals measured from physical systems, the interpretation of the transforms based on Daubeshies's wavelets may become quite difficult if not impossible.

As an example of Daubechies's [43] compactly supported orthonormal wavelets, the D10 wavelet was considered earlier in section 2.3.6. A graphical representation of the D10 wavelet was given in Figure 2.13. Note that, the D10 wavelet is also real and therefore will generate real transforms. The application of the D10 wavelet to the reference acceleration signal resulted in a TFR as shown in Figure 7.4a. It is interesting to note that if the D10 wavelet shown in Figure 2.13c is time-reversed, the result would look similar to a dispersing wave group, as discussed earlier in section 3.3. Such a time-reversed D10 wavelet was also tested, and the resulting TFR is presented in Figure 7.4b. Since both the D10 wavelet and its time-reversed versions are real valued, the TFRs capture only the general signature of the physical processes. As in the preceding examples, it is difficult to associate every detail provided by the transforms with a particular physical phenomenon.

Certainly, the above wavelets may perform better in other applications, such as signal compression and multi-resolution analysis of images. For the applications considered in this study, the complex wavelet introduced by Morlet has performed substantialy better than the others. The time-frequency localization and symmetry properties of the Morlet wavelet matched very well with the analyzed physical phenomena. It may be argued that any wavelet that has real and imaginary parts that are in quadrature, such as the one introduced in equation (2.25), may perform as well as the Morlet wavelet. Infact, the wavelet defined by equation (2.25), derivatives of Gaussian function, looks very similar to the Morlet wavelet, and therefore it is expected that they may be equally effective in the analysis of nonstationary vibration signals.

Elevation

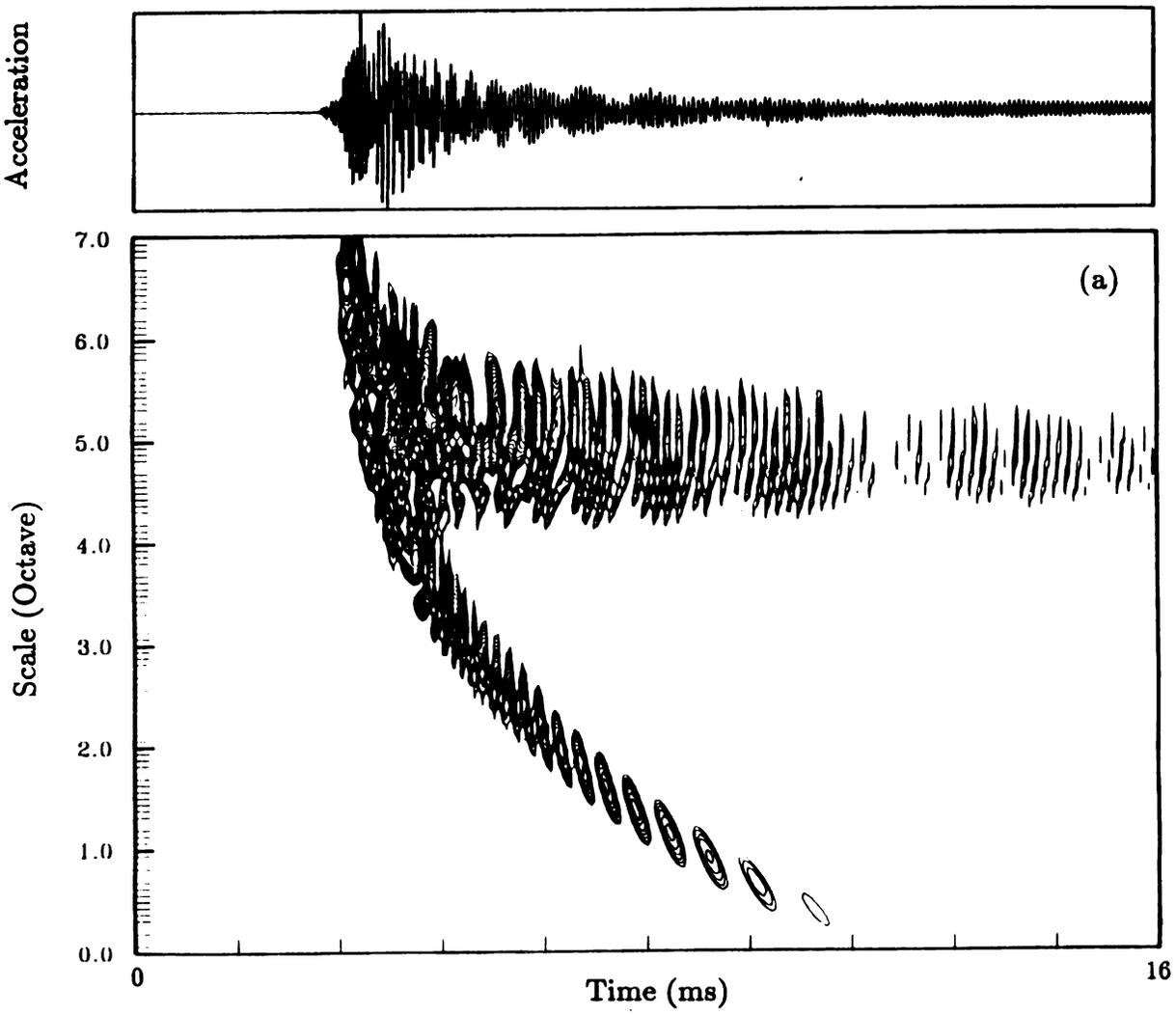

Figure 7.4 The wavelet transform of the reference acceleration signal by using Daubechies's orthonormal wavelet; a) D10 wavelet is employed, and b) time-reversed D10 wavelet is used.

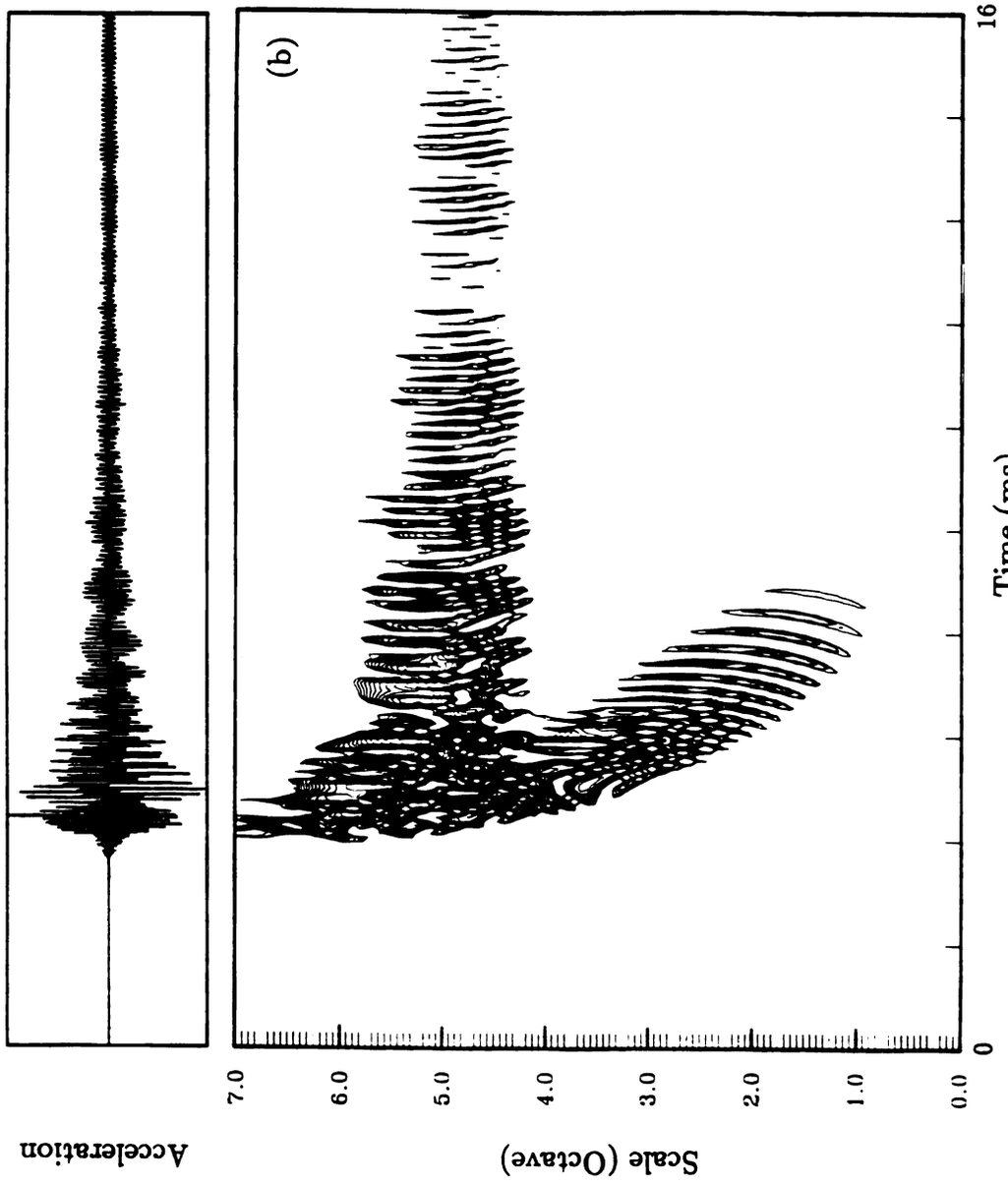

Figure 7.4 (Continued).

7.2 Orthonormal Basis vs. Frames

The preceding discussion on the selection of the wavelet function becomes more important for the wavelet frame reconstruction scheme outlined in the second part of this study. The frame bounds and the redundancy ratio depend on the type of wavelet and the number of voices considered in each construction. As shown in Daubechies's [42,43] study, not all choices of wavelets generate frames that have desirable properties. Certainly, as the number of voices are increased and the translation step size is decreased, the frame becomes tighter. Although, a slightly higher redundancy is favored for signal reconstruction and information recovery purposes, it may sometimes increase the storage space and computations requirements beyond practical limits. Certainly, these practical difficulties can be averted by using an orthonormal wavelet basis, which would give better compression of information and decrease the number of operations. However, the price paid for such advantages is the mathematical complexity involved during the creation of orthonormal basis. In comparison to the wavelet theory, the frame concept is relatively new and there exist exciting possibilities for its future use.

7.3 Other Application of Wavelets in Mechanical Systems

In general, mechanical systems involve a variety of transient phenomena that may be effectively analyzed by using wavelet transform and multiresolution analysis. In such analyses, characterization of the information contained in measured signals is the major task in diagnosing and predicting a particular dynamic phenomenon. For example, a rotating shaft is a natural source of vibrations and involves complex dynamic behaviors. In practical applications, there are many factors, such as clearances in the bearings, mating gears mounted on the shaft and other drive mechanisms, that may all contribute in different ways to the resulting transient vibration response of a rotor-bearing system. As it was demonstrated in this study, the wavelet transform is a powerful tool that can be used to resolve complex transient signals efficiently. The TFRs generated by the wavelet transform can be used to analyze the transient dynamic interactions that occur between

different components of a complex mechanism during its operation. For example in engines, the wavelet transform could be used to detect lifter mulfunctions in the drive-train, valve impacts, piston slap, misaligned bearings and ignition-induced vibrations.

Another specific area that may use wavelets as a powerful analysis tool is that of metal cutting and machining. In general, the metal cutting operations generate substantial vibrations in the workpiece and in the cutting tool. Therefore, the quality of the product depends strongly on the level and nature of these vibrations. Analysis of vibrations in machine tools has been a formidable task due to the time-varying nature of the signals. Since the low-frequency vibrations coming from the drive-train are superimposed on top of the high-frequency vibrations due to the cutting operation, the transient signals can be expected to have a wide spectral range. Therefore, characterization of the transient vibration response can be performed effectively by using the self-adjusting window property of the wavelet transform.

An additional property of wavelets which has not been expoited in this research is that of data (information) compression. The area of telemetry would seem to be an application that could make good use of this property. One more application results from the fact that wavelets are another form of harmonic analysis. It is therefore natural to expect that they will be widely used in the solution of linear and nonlinear PDEs. However, in comparison to the Fourier analysis, where the spectral decomposition of differential operators results in diagonal matrices, the wavelet transform generates near diagonal elements which decay rapidly away from the diagonal. However, the wavelet theory may be of great help in the numerical analysis of some nonlinear equations and analysis of nonlinear phenomena, such as the formation and tracking of shock fronts.

The above list of applications is expected to grow as the potential of wavelets and multiresolution analysis is discovered in mechanical sciences.

7.4 Summary of Properties

In the short-time Fourier transform (STFT), the window size is kept constant during the analysis. Therefore, as implied by the uncertainty principle, $\Delta_t \Delta_\omega \geq \frac{1}{2}$, a compromise between time and frequency resolutions is necessary. The Gaussian window used in the Gabor Transform results in an optimum time-frequency localization. The Gabor transform is found particularly useful in the analysis of finite-energy sinusoidal signals. Shifting the window with smaller steps (or larger overlaps) smooths the transitions during the evolution of the spectra.

In the wavelet transform, the window size is self-adjusted with scale, resulting in an efficient logarithmic "zooming" property. Different analyzing wavelet functions are available to characterize various physical phenomena. The wavelet transform induces a multiple-scale or multi-resolution analysis. It is particularly effective on wide-band nonstationary signals and the time-evolution of high- and low-frequency transient vibration signals are represented efficiently. As an alternative, the wavelet transform can be used to generate space-wavenumber representations (SWR). Wavelet decomposition and reconstruction can be also used as a powerful tool for data compression.

7.5 Conclusions

The analysis and synthesis schemes developed in this study were the result of blending different concepts regarding wavelets, frames, multi-resolution analysis, signal processing and vibrations. In particular, these concepts were utilized to analyze transient wave propagation in dispersive and nondispersive mediums, and to synthesize the transient vibration response of proportional-bandwidth, linear, time-invariant systems. It is believed that this thesis has established a foundation for further advancement of applications of the preceding concepts in mechanical sciences.

In Chapter 1, the antecedents of the present wavelet research were briefly reviewed. Chapter 2 was devoted to the introduction of the basic mathematical

concepts, definitions, properties and algorithms regarding linear time-frequency representations. The advantages, limitations and the conceptual similarities of the wavelet transform were compared to the short-time Fourier (STFT) and Gabor transforms by using a few examples selected from synthetic signals.

In the analysis sections (Chapters 3 and 4), the wavelet transform was used to study transient wave propagation in physical systems. The dispersion of a transient waveform was introduced as an excellent example for the efficient use of the self-adjusting window and the variable resolution properties of the wavelet transform. The evolution of the spectra during the dispersion of an impulsive waveform were displayed clearly by the time-scale representations (TSRs) of measured acceleration signals. In the examples involving a semi-infinite beam (Chapter 3), the distinctive signature of a transient waveform was uncovered and used to identify the wavebearing characteristics of the medium. The arrival times observed from the wavelet transform were shown to be related to the group velocities of the wavelet components. In the analysis of wave-guides, the wavelet transform was confirmed to be an effective tool in seperating the evolution of different wave-modes and in analyzing and clearly demonstrating the transients of the cut-off phenomenon. In a nondispersive medium, time-frequency analysis helped to localize echos from the boundaries. In addition, the dynamic characteristics of the boundaries and the medium were identified by studying the local spectral content of the reflected waves observed in the TSRs.

As an alternative, a space-wavenumber representation (SWR) was introduced in Chapter 3 to analyze a one-dimensional system. The display of SWRs successively in time gave a clear picture of the spatial-evolution of the wave components. The use of SWRs and TSRs together was shown to clearly depict the dispersive characteristics of a medium.

In the analysis of a finite dispersive system (Chapter 4), multiple reflections from the boundaries were identified from the TSRs. The self-adjusting window structure of the wavelet transform was found to provide an adequate resolution over a wide spectral range and, thus, resulted in an efficient localization of the

complex interference patterns in the time-scale domain. During the analysis of an impact excited free-free beam, the TSRs of the acceleration signals were utilized to uncover a symmetric grid pattern and a periodic pulse-reformation phenomenon.

The second part of this study (Chapters 5 and 6) was devoted to the development and testing of a new synthesis scheme which can be used to predict the transient vibration response of linear systems. In Chapter 5, the wavelet frame expansion and multi-resolution concepts were utilized to replace the convolution integral with a more efficient synthesis scheme. It was demonstrated that the response of a system could be accurately constructed by adding together the contributions coming from different resolution levels. The wavelet frame decomposition of the forcing function was employed to partition the spectrum into constant-Q frequency bands (resolution levels). This partitioning of the spectral range by using wavelet frames resulted in an automatic adjustment of the resolution and time-duration at different levels of detail, and therefore avoided possible time-domain aliasing problems. Consequently, the proposed synthesis scheme is particularly effective in situations where proportional damping is present. A common example of this is the bending vibrations of beams and plates, where the duration of a transient vibration (determined by the bandwidth) decreases with increasing frequency.

In Chapter 6, the proposed wavelet frame synthesis scheme was applied to the prediction of the transient response of a beam. The wavelet frame synthesis scheme was shown to generate the short- and long-term vibration response of a beam at different resolution levels. The proposed synthesis scheme provided sufficent detail over a self-adjusting window in time, and therefore prevented time-domain aliasing problems observed in uniformly-sampled FFT synthesis schemes.

In closing, this study exploited the fundamental properties of the wavelet transform and established an effective scheme for the analysis of wide-band transient vibration signals. The wavelet transform was found to be particulary usefull in the study of dispersion and cut-off phenomena. The analysis scheme, demonstrated in this study for the flexural vibrations of a beam, is perfectly applicable to more complex systems that have different dispersive characteristics and

structural configurations. In addition, the concepts regarding frequency response functions, wavelet frame expansions, and multiresolution analysis are combined to generate an efficient synthesis scheme for the prediction of the transient vibration response of linear proportional-bandwith systems. The proposed synthesis scheme is based on a newly defined wavelet response function, which was introduced as an alternative to impulse and frequency response functions and features better time-frequency localization characteristics.

APPENDICES

APPENDIX A

The following properties of the Fourier transform are used frequently during the development and implementation of the wavelet theory.

A.1 Derivatives

The following Fourier transform pairs are related

$$g(x) \quad \overset{\mathcal{F}}{\longleftrightarrow} \quad \widehat{g}(\omega)$$

$$D^n g(x) \quad \overset{\mathcal{F}}{\longleftrightarrow} \quad (i\omega)^n \, \widehat{g}(\omega)$$

where the derivative operator $D^n = d^n/dx^n, \quad (n = 1, 2, ...)$.

A.2 Scaling

Following Fourier transform pairs are used frequently during the dilations of wavelets;

$$h(x) \quad \overset{\mathcal{F}}{\longleftrightarrow} \quad \widehat{h}(\omega)$$

$$h(ax) \quad \overset{\mathcal{F}}{\longleftrightarrow} \quad \frac{1}{|a|} \widehat{h}(\omega/a)$$

$$h(x/a) \quad \overset{\mathcal{F}}{\longleftrightarrow} \quad |a| \, \widehat{h}(a\omega)$$

$$\frac{1}{\sqrt{|a|}} h(x/a) \quad \overset{\mathcal{F}}{\longleftrightarrow} \quad \sqrt{|a|} \, \widehat{h}(a\omega)$$

A.3 Shifting

Shifting in time-domain causes phase change in frequency domain;

$$h(x) \quad \overset{\mathcal{F}}{\longleftrightarrow} \quad \widehat{h}(\omega)$$

$$h(x-b) \quad \overset{\mathcal{F}}{\longleftrightarrow} \quad e^{-ib\omega} \, \widehat{h}(\omega)$$

APPENDIX B

The following window functions, $g(n)$ with $n = 0, ..., M-1$, are commonly used during the implementation of the STFT.

Parzen (Triangular) Window:

$$g(n) = 1 - \left| \frac{2n - (M-1)}{(M+1)} \right|$$

Welch Window:

$$g(n) = 1 - \left[\frac{2n - (M-1)}{(M+1)} \right]^2$$

Hanning (Raised-Cosine) Window:

$$g(n) = \frac{1}{2} \left[1 - \cos\left(\frac{2\pi n}{M-1} \right) \right]$$

Hamming Window:

$$g(n) = 0.54 - 0.46 \cos\left(\frac{2\pi n}{M-1} \right)$$

Blackman Window:

$$g(n) = 0.42 - 0.5 \cos\left(\frac{2\pi n}{M-1} \right) + 0.08 \cos\left(\frac{4\pi n}{M-1} \right)$$

Gaussian Window:

$$g(n) = \exp\left[-0.5 \left(\frac{n - M/2}{(M/2)/\alpha} \right)^2 \right]$$

APPENDIX C

The uncertainty principle is prooved as shown in the following. One of the the fundamental theorems that is needed in the proof is stated as

$$\int \frac{df}{dt}\,\frac{df^*}{dt}\,dt = \int \omega^2\,\hat{f}(\omega)\,\hat{f}^*(\omega)\,d\omega$$

where "$*$" denotes complex conjugation. Also, the Shwartz inequality will be needed;

$$4\int f(t)\,f^*(t)\,dt\;\int g(t)\,g^*(t)dt\;\geq\;\left|\int [f^*(t)\,g(t)+f(t)\,g^*(t)]\,dt\right|^2$$

The centers t_c and ω_c are assumed to be located at the origin. In the following, all integrals are to be taken between infinite limits and the notation $\|\cdot\|$ refers to the L^2 norm defined at the beginning. Then the derivation of the uncertainty principle goes as follows:

$$(\Delta_f)^2(\Delta_{\hat{f}})^2 = \frac{\int t^2|f(t)|^2dt\int \omega^2|\hat{f}(\omega)|^2d\omega}{\|f\|\;\|\hat{f}\|} = \frac{\int t^2 f(t)\,f^*(t)\,dt\int \omega^2\hat{f}(\omega)\,\hat{f}^*(\omega)d\omega}{\int f(t)\,f^*(t)\,dt\;\int \hat{f}(\omega)\,\hat{f}^*(\omega)\,d\omega}$$

$$= \frac{\int [t\,f(t)]\,[t\,f^*(t)]\,dt\;\int \frac{df}{dt}\,\frac{df^*}{dt}\,dt}{\left(\int f(t)\,f^*(t)\,dt\right)^2}$$

$$\geq \frac{\left|\int \left[t\,f^*(t)\,\frac{df}{dt}+t\,f(t)\,\frac{df^*}{dt}\right]\,dt\right|^2}{4\left(\int f(t)\,f^*(t)\,dt\right)^2}$$

$$= \frac{\left|\int t\,\frac{d}{dt}[f(t)f^*(t)]\,dt\right|^2}{4\left(\int f(t)\,f^*(t)\,dt\right)^2} = \frac{\left|\int f(t)f^*(t)\,dt\right|^2}{4\left(\int f(t)\,f^*(t)\,dt\right)^2} = \frac{1}{4}$$

which implies

$$\Delta_f\,\Delta_{\hat{f}} \geq \frac{1}{2}.$$

The definitions of the radia Δ_f and $\Delta_{\hat{f}}$ were given in section 2.2.3.

APPENDIX D

Daubechies's Wavelets

The compactly supported orthonormal wavelet ψ and its companion, the scaling function ϕ, are defined by the dilation equations [43]:

$$\psi(x) = \sqrt{2} \sum_{n=0}^{N-1} g_n \phi(2x - n) \tag{D.1}$$

$$\phi(x) = \sqrt{2} \sum_{n=0}^{N-1} h_n \phi(2x - n) \tag{D.2}$$

where the coefficients are related by $g_n = (-1)^n h_{N-n}$ with $n = 0, \ldots, N-1$. Similar to the admisibility condition used during the definition of a wavelet, the scaling function has to satisfy $\int \phi(x)dx = 1$. The number of coefficients in the preceding summation, N, is twice the the number of vanishing moments, $N = 2M$, such that $\int \psi(x)x^m dx = 0$ for $m = 0, \ldots, M-1$.

In the construction of a mother wavelet, first the Fourier transform of the scaling function, given in equation (D.2), is considered

$$\begin{aligned} \widehat{\phi}(\omega) &= \frac{1}{\sqrt{2}} \sum_{n=0}^{N-1} h_n \, e^{-in\omega/2} \, \widehat{\phi}(\omega/2) \\ &= H(\omega/2) \, \widehat{\phi}(\omega/2) \end{aligned} \tag{D.3}$$

where the low-pass filter H is defined by

$$H(\omega) = \frac{1}{\sqrt{2}} \sum_{n=0}^{N-1} h_n \mathrm{e}^{-in\omega} \, . \tag{D.4}$$

The 2π-periodic function $H(\omega)$ satisfies the equation

$$|H(\omega)|^2 + |H(\omega + \pi)|^2 = 1 \,. \tag{D.5}$$

The trigonometric polynomial solutions of H define the compactly supported wavelets with vanishing moments.

Daubechies [43] gives the trigonometric polynomial solution of $H(\omega)$ in the form

$$H(\omega) = \left(\frac{1 + e^{i\omega}}{2}\right)^M \mathcal{L}(e^{i\omega}) \tag{D.6}$$

where $\mathcal{L}$ is a polynomial given by

$$|\mathcal{L}(e^{i\omega})|^2 = P\left(\sin^2 \frac{\omega}{2}\right) + \sin^{2M}\left(\frac{\omega}{2}\right) \; R\left(\frac{\cos(\omega)}{2}\right). \tag{D.7}$$

The polynomials P and R in this last expression satisfy the following relations:

$$P(y) = \sum_{n=0}^{M-1} \binom{M-1+n}{n} y^n, \tag{D.8}$$

$$0 \leq P(y) + y^M R(\frac{1}{2} - y) \quad \text{for} \quad 0 \leq y \leq 1, \tag{D.9}$$

$$\sup_{0 \leq y \leq 1} \left[P(y) + y^M R(\frac{1}{2} - y)\right] < 2^{2(M-1)}, \quad \text{if} \quad M \geq 2, \tag{D.10}$$

$$-\frac{2}{1-2|x|} \leq R(x) \leq \frac{2}{1+2|x|} \quad \text{for} \quad |x| \leq \frac{1}{2}, \quad \text{if} \quad M = 1.$$

Therefore, once the solution given by equation (D.6) is constructed, then the coefficients h_n can be determined and used in equation (D.1) to define the mother wavelet. The mathematical derivations of the preceding relations for the compactly supported wavelets can be found in more detail in Daubechies's work [38-43].

Haar W

Th
wavelet
structio
subspac

V_m =

These s
induce
is consi
definiti

Then,

where
expec

wher

APPENDIX E

Haar Wavelet Basis and Multi-Resolution Analysis

The Haar function is a classical academic example for an orthonormal wavelet basis which is nicely related to the multiresolution analysis. The construction of the Haar wavelet starts from the box function. Consider a ladder of subspaces $\mathbf{V}_m$ containing piecewise constant box functions

$$\mathbf{V}_m = \{f \in L^2(\mathbf{R}); \quad f(x) = constant, \quad 2^m n \leq x < 2^m(n+1), \quad \forall n \in \mathbf{Z}\} \tag{E.1}$$

These subspaces $\mathbf{V}_m$ satisfy the conditions given in equation (2.32), and therefore induce a multiresolution analysis of $L^2(\mathbf{R})$. In particular, if the subspace $\mathbf{V}_0$ is considered, the constant function corresponding to $n = 0$ yields the following definition of the scaling function

$$\phi(x) = \begin{cases} 1, & 0 \leq x < 1, \\ 0, & \text{otherwise.} \end{cases} \tag{E.2}$$

Then, the corresponding discrete lattice of scaling functions are obtained as

$$\begin{aligned} \phi_{m,n}(x) &= 2^{-m/2}\, \phi(2^{-m}x - n) \\ &= \begin{cases} 2^{-m/2}, & 2^m n \leq x < 2^m(n+1), \\ 0, & \text{otherwise.} \end{cases} \end{aligned} \tag{E.3}$$

where $\phi_{0,0} = \phi \in \mathbf{V}_0$ and for a fixed m the subspace $\mathbf{V}_m = \overline{\text{span}\{\phi_{m,n}\}}$ as expected. Furthermore, at a coarser level $m+1$, the scaling function becomes

$$\phi_{m+1,n} = 2^{-1/2}\,(\phi_{m,2n} + \phi_{m,2n+1}) \tag{E.4}$$

where the translated components of the scaling function at level m are averaged.

The preceding definitions of the multiresolution subspaces $\mathbf{V}_m$ and the corresponding basis functions $\phi_{m,n}$ allow us to find the projection of any arbitrary function $f \in L^2(\mathbf{R})$ onto the subspaces $\mathbf{V}_m$. Therefore, first the following inner product is defined;

$$\langle f, \phi_{m,n} \rangle = 2^{-m/2} \int_{2^m n}^{2^m (n+1)} f(x)\, dx \tag{E.5}$$

In addition, the use of equation (E.4) results in an expression for the inner product at a coarser level $m+1$

$$\langle f, \phi_{m+1,n} \rangle = 2^{-1/2} \Big(\langle f, \phi_{m,2n} \rangle + \langle f, \phi_{m,2n+1} \rangle \Big) \tag{E.6}$$

which will be of use in later derivations. The inner product defined in equation (E.5) yields the following expression for the orthogonal projection of $f \in L^2(\mathbf{R})$ onto a subspace $\mathbf{V}_m$

$$\begin{aligned} P_m f &= \sum_n \langle f, \phi_{m,n} \rangle \, \phi_{m,n} \\ &= \frac{1}{2^m} \sum_n \int_{2^m n}^{2^m (n+1)} f(x)\, dx \end{aligned} \tag{E.7}$$

Note that, as the scale m adopts large negative values, the support $[2^m n, 2^m (n+1)]$ becomes narrower, and in the limit as $m \to -\infty$, $P_m f \to f$, which implies $\mathbf{V}_m \to L^2(\mathbf{R})$.

As stated in equation (E.4), $\phi_{m+1,n}$ can be obtained from $\phi_{m,2n}$ and $\phi_{m,2n+1}$, through an averaging process. Such a relation between basis functions leads us to search for the difference between projections onto $\mathbf{V}_{m+1}$ and $\mathbf{V}_m$. Therefore, we define

$$Q_{m+1} f = P_m f - P_{m+1} f \tag{E.8}$$

Then, using equations (E.4-E.7) in (E.8) gives

$$\begin{aligned} Q_{m+1}f &= \sum_n \langle f, \phi_{m,n}\rangle\, \phi_{m,n} - \sum_n \langle f, \phi_{m+1,n}\rangle\, \phi_{m+1,n} \\ &= \frac{1}{2}\sum_n \Big(\langle f, \phi_{m,2n}\rangle - \langle f, \phi_{m,2n+1}\rangle\Big)\Big(\phi_{m,2n} - \phi_{m,2n+1}\Big) \qquad (E.9) \\ &= \sum_n \langle f, \phi_{m+1,n}\rangle\, \psi_{m+1,n} \end{aligned}$$

where the final equality is based upon the definitions

$$\psi_{m+1,n} = \frac{1}{\sqrt{2}}\left(\phi_{m,2n} - \phi_{m,2n+1}\right)$$

$$\langle f, \phi_{m+1,n}\rangle = \frac{1}{\sqrt{2}}\Big(\langle f, \phi_{m,2n}\rangle - \langle f, \phi_{m,2n+1}\rangle\Big)$$

As a result of the preceding definitions, it is clear that

$$\begin{aligned} \psi_{m,n} &= \frac{1}{\sqrt{2}}\Big(\phi_{m-1,2n} - \phi_{m-1,2n+1}\Big) \\ &= 2^{-m/2}\,\psi(2^{-m}x - n) \end{aligned} \qquad (E.10)$$

Consequently, the mother wavelet, $\psi = \psi_{0,0} = 2^{-1/2}(\phi_{-1,0} - \phi_{-1,1})$, can be defined as

$$\psi(x) = \phi(2x) - \phi(2x-1) = \begin{cases} 1, & 0 \le x < \frac{1}{2}, \\ 1, & \frac{1}{2} \le x < 1, \\ 0, & \text{otherwise.} \end{cases} \qquad (E.11)$$

which has been known as the Haar function since 1910.

For a fixed m, the set of functions $\{\psi_{m,n}\}$ is an othonormal basis for the subspace $\mathbf{W}_m = \mathbf{V}_m^{\perp}$, which is the orthogonal complement of $\mathbf{V}_m$ in $\mathbf{V}_{m-1}$. Since the set of functions $\{\psi_{m,n};\ m,n \in \mathbf{Z}\}$ is an orthonormal wavelet basis for $L^2(\mathbf{R})$, any L^2-function f can be approximated by a linear combination of $\psi_{m,n}$. Since $\mathbf{W}_m \perp \mathbf{V}_m$ and $\mathbf{V}_{m-1} = \mathbf{V}_m \oplus \mathbf{W}_m$, the subspaces $\mathbf{W}_m$ are mutually orthogonal and their direct sum gives $L^2(\mathbf{R})$. The relation given in equation (E.9) defines the orthogonal projection of f onto $\mathbf{W}_{m+1}$.

APPENDIX F

F.1 Bending Vibration Response of a Beam: Transfer Matrices

The flexural vibrations of a uniform isotropic beam is governed by

$$B\frac{\partial^4 y(x,t)}{\partial x^4} + \rho A\frac{\partial^2 y(x,t)}{\partial t^2} = f(x,t) \qquad (F.1)$$

where the effects of the shear deformation and rotatory inertia have been neglected. In equation (F.1), $B = EI[1 - i\,\eta(\omega)]$ is the complex bending stiffness and $\eta(\omega)$ is the structural loss factor. Considering a time-harmonic external disturbance, $f(x,t) = F(x,\omega)\exp(-i\omega t)$, the vibration response of the linear system is anticipated to take the form $y(x,t) = Y(x,\omega)\exp(-i\omega t)$. Therefore, in terms of the velocity response of the beam, $V(x,\omega) = (-i\omega)Y(x,\omega)$, equation (F.1) yields

$$\frac{d^4 V(x,\omega)}{dx^4} - k_p^4 V(x,\omega) = -\left(\frac{i\,\omega}{B}\right) F(x,\omega) \qquad (F.2)$$

where $k_p = \sqrt[4]{\rho A\omega^2/B}$ is the complex propagation constant or the free bending wavenumber of the beam.

The state variable form of the fourth order ODE given in equation (F.2) is obtained as

$$\underbrace{\begin{bmatrix} dv_1/dx \\ dv_2/dx \\ dv_3/dx \\ dv_4/dx \end{bmatrix}}_{dv/dx} = \underbrace{\begin{bmatrix} 0 & 1 & 0 & 0 \\ 0 & 0 & 1 & 0 \\ 0 & 0 & 0 & 1 \\ k_p^4 & 0 & 0 & 0 \end{bmatrix}}_{A} \underbrace{\begin{bmatrix} v_1 \\ v_2 \\ v_3 \\ v_4 \end{bmatrix}}_{v} + \underbrace{\begin{bmatrix} 0 \\ 0 \\ 0 \\ \frac{-i\,\omega}{B}F(x,\omega) \end{bmatrix}}_{f} \qquad (F.3)$$

where the state variables are defined by

$$v_1 = V, \quad v_2 = \frac{dV}{dx} = \frac{dv_1}{dx}, \quad v_3 = \frac{d^2V}{dx^2} = \frac{dv_2}{dx}, \quad v_4 = \frac{d^3V}{dx^3} = \frac{dv_3}{dx} \qquad (F.4)$$

Since

the r

and t

by co

is der

Furth

For a

can b

its el

v_{j_1} =

v_j =

matr

matr

In or

into

wher

Since equation (F.3) is in the general state variable form defined in equation (4.1), the rest of the procedure outlined earlier applies directly to the present system.

The construction of the transformation matrix **M** requires the eigenvectors and the eigenvalues of the system. The eigenvalues of the system are determined by considering the characteristic equation obtained from $\det(\lambda \mathbf{I} - \mathbf{A}) = 0$, which is derived as $\lambda^4 - k_p^4 = 0$. The roots of this characteristic equation are given by

$$\lambda_1 = i\,k_p, \qquad \lambda_2 = -\,k_p, \qquad \lambda_3 = -i\,k_p, \qquad \lambda_4 = k_p \tag{F.5}$$

Furthermore, the eigenvectors of the system are determined by considering

$$(\lambda_j \mathbf{I} - \mathbf{A})\,\mathbf{v}_j = 0\,, \qquad j = 1,2,3,4 \tag{F.6}$$

For a particular eigenvalue, any three of the relations implied by equation (F.6) can be utilized to determine the corresponding eigenvector in terms of one of its elements. The normalized form of the eigenvectors can be defined by setting $\mathbf{v}_{j_1} = 1$. Then, solving other elements of the eigenvectors from equation (F.6) gives $\mathbf{v}_j = [1 \;\; \lambda_j \;\; \lambda_j^2 \;\; \lambda_j^3]^{\mathrm{T}}$, where λ_j are defined in equation (F.5). The transformation matrix is constructed by placing the eigenvectors into the columns of a 4 × 4 matrix;

$$\mathbf{M} = \begin{bmatrix} 1 & 1 & 1 & 1 \\ ik_p & -k_p & -ik_p & k_p \\ -k_p^2 & k_p^2 & -k_p^2 & k_p^2 \\ -ik_p^3 & -k_p^3 & ik_p^3 & k_p^3 \end{bmatrix} \tag{F.7}$$

In order to ease the manipulation of matrices, the modal matrix is decomposed into two sub-matrices; a diagonal and a constant matrix, given as

$$\mathbf{M} = \mathbf{K}\,\mathbf{C} \qquad \text{and} \qquad \mathbf{M}^{-1} = \mathbf{C}^{-1}\,\mathbf{K}^{-1} \tag{F.8}$$

where

$$\mathbf{K} = \begin{bmatrix} 1 & 0 & 0 & 0 \\ 0 & k_p & 0 & 0 \\ 0 & 0 & k_p^2 & 0 \\ 0 & 0 & 0 & k_p^3 \end{bmatrix}, \qquad \mathbf{C} = \begin{bmatrix} 1 & 1 & 1 & 1 \\ i & -1 & -i & 1 \\ -1 & 1 & -1 & 1 \\ -i & -1 & i & 1 \end{bmatrix}$$

K

Note tha

where

matrix
is give

where

and t

T

Furth
x_0 =
$[a^+$

$$\mathbf{K}^{-1} = \begin{bmatrix} 1 & 0 & 0 & 0 \\ 0 & 1/k_p & 0 & 0 \\ 0 & 0 & 1/k_p^2 & 0 \\ 0 & 0 & 0 & 1/k_p^3 \end{bmatrix}, \qquad \mathbf{C}^{-1} = \frac{1}{4}\begin{bmatrix} 1 & -i & -1 & i \\ 1 & -1 & 1 & -1 \\ 1 & i & -1 & -i \\ 1 & 1 & 1 & 1 \end{bmatrix}$$

Note that, for the present system, the similarity transformation becomes

$$\mathbf{\Lambda} = \mathbf{M}^{-1}\,\mathbf{A}\,\mathbf{M} = \mathbf{C}^{-1}\,\mathbf{K}^{-1}\,\mathbf{A}\,\mathbf{K}\,\mathbf{C} \tag{F.9}$$

where $\mathbf{\Lambda} = \mathrm{diag}(\lambda_1, \lambda_2, \lambda_3, \lambda_4)$.

In order to determine the response of the system, the inverse of the modal matrix, given in equation (F.8), is substituted into equation (4.3) and the result is given by

$$\mathbf{z}(x) = \mathbf{T}_{(x-x_0)}\,\mathbf{z}(x_0) + \mathbf{f}_F \tag{F.10}$$

where the force vector $\mathbf{f}_F$ is defined as

$$\mathbf{f}_F = \int_{x_0}^{x} \mathbf{T}_{(x-\xi)}\mathbf{C}^{-1}\mathbf{K}^{-1}\mathbf{f}(\xi)\,d\xi \tag{F.11}$$

and the field transfer matrix is given by

$$\mathbf{T}_{(x-x_0)} = \mathrm{diag}\left[\, e^{ik_p(x-x_0)} \quad e^{-k_p(x-x_0)} \quad e^{-ik_p(x-x_0)} \quad e^{k_p(x-x_0)} \,\right] \tag{F.12}$$

Furthermore, if the origin of the space coordinate is assigned to the first station, $x_0 = 0$, and the corresponding canonical state variables are defined as $\mathbf{z}(0) = \left[a^+ \;\; a_N^+ \;\; a^- \;\; a_N^-\right]^{\mathrm{T}}$, then equation (F.10) can be expressed expilicitly as

$$\begin{bmatrix} z_1(x) \\ z_2(x) \\ z_3(x) \\ z_4(x) \end{bmatrix} = \begin{bmatrix} a^+\, e^{ik_p(x-x_0)} \\ a_N^+\, e^{-k_p(x-x_0)} \\ a^-\, e^{-ik_p(x-x_0)} \\ a_N^-\, e^{k_p(x-x_0)} \end{bmatrix} - \frac{i\omega}{4Bk_p^3}\begin{bmatrix} i\int_{x_0}^{x} e^{ik_p(x-\xi)}\,F(\xi,\omega)\,d\xi \\ -\int_{x_0}^{x} e^{-k_p(x-\xi)}\,F(\xi,\omega)\,d\xi \\ -i\int_{x_0}^{x} e^{-ik_p(x-\xi)}\,F(\xi,\omega)\,d\xi \\ \int_{x_0}^{x} e^{k_p(x-\xi)}\,F(\xi,\omega)\,d\xi \end{bmatrix} \tag{4.18}$$

where

ditribu

the co

transf

partic

tribut

soluti

F.2 I

equat

syste

In th

iden

and

nega

vect

are

hon

the

ope

Th

vec

wh

vel

where $z_j(x)$ are the elements of the vector $\mathbf{z}(x)$ and $F(x,\omega)$ is an external ditributed force. Equation (F.13) implies that, across a distributed external force, the complex wave amplitudes at the later station are determined by adding the transfered wave component to the corresponding contribution coming from the particular integral. In the following, two of the frequently encountered force distributions are considered to obtain the special forms of the preceding general solution.

F.2 Homogenous Solution

In this case, the external force distribution is removed, $F(x,\omega) = 0$. Then, equation (F.13) gives the homogenous solution. The unforced response of the system at the later station x becomes

$$\mathbf{z}(x) = \mathbf{T}_{(x)}\,\mathbf{z}(0) = \left[a^+ e^{ik_p x} \quad a_N^+ e^{-k_p x} \quad a^- e^{-ik_p x} \quad a_N^- e^{k_p x} \right]^{\mathrm{T}} \qquad (F.14)$$

In this phase-variable canonical form of the homogenous solution, it is possible to identify the four flexural wave components as the propagating waves in the positive and negative directions, e^{ikx} and e^{-ikx}, and evanescent waves in the positive and negative directions, e^{kx} and e^{-kx}, [37]. It follows that the elements of this state vector, $\mathbf{z}(0)$, correspond to the amplitudes of the flexural wave components, which are a^+, a_N^+, a^- and a_N^-. Since, in general, k_p is a complex wave number, the homogenous solution, given in equation (F.14), implies that the magnitude and the phase of these complex wave amplitudes will vary along the x-coordinate.

It is useful to define a relationship between the field transfer matrix developed above and the transfer matrices that use the physical variables of a beam. The state variables of a beam in terms of physical parameters are defined by a vector as

$$\mathbf{s} = \left[V(x,\omega) \;\; \varphi(x,\omega) \;\; M(x,\omega) \;\; Q(x,\omega) \right]^{\mathrm{T}} \qquad (F.15)$$

where $V(x,\omega)$, $\varphi(x,\omega)$, $M(x,\omega)$ and $Q(x,\omega)$ are the amplitudes of the transverse velocity, angular velocity, the bending moment, and the shear force, respectively.

The relationship between this state vector **s** and the state vectors used in the present analysis can be given as

$$\mathbf{s} = \mathbf{H}\,\mathbf{v} = \mathbf{H}\,\mathbf{K}\,\mathbf{C}\,\mathbf{z} \tag{F.16}$$

where the diagonal matrix $\mathbf{H} = \mathrm{diag}[1,\ 1,\ B/i\omega,\ -B/i\omega]$. Substitution of the respective matrices and vectors into equation (4.21), gives

$$V(x,\omega) = a^{+}e^{ik_p x} + a_N^{+}e^{-k_p x} + a^{-}e^{-ik_p x} + a_N^{-}e^{k_p x} \tag{F.17}$$

$$\varphi(x,\omega) = k_p\left(i\,a^{+}e^{ik_p x} - a_N^{+}e^{-k_p x} - i\,a^{-}e^{-ik_p x} + a_N^{-}e^{k_p x}\right) \tag{F.18}$$

$$M(x,\omega) = \frac{Bk_p^2}{i\omega}\left(-a^{+}e^{ik_p x} + a_N^{+}e^{-k_p x} - a^{-}e^{-ik_p x} + a_N^{-}e^{k_p x}\right) \tag{F.19}$$

$$Q(x,\omega) = \frac{Bk_p^3}{-i\omega}\left(-i\,a^{+}e^{ik_p x} - a_N^{+}e^{-k_p x} + i\,a^{-}e^{-ik_p x} + a_N^{-}e^{k_p x}\right) \tag{F.20}$$

As expected, the velocity response of the system, $V(x,\omega)$ is composed of contributions coming from each one of the flexural wave components. In an unforced segment of the beam, these contributions coming from the wave components are determined by the field transfer matrix, which depends on the bending wave number, k_p, and the distance between the two stations.

F.3 Point Force

The transfer function between two stations of a beam, with a point source in between, can be found by substituting the mathematical definition of a point force, $\mathbf{f} = \mathbf{f}_0(\omega)\delta(x - x_f)$, into equation (F.10). Then, evaluating the integrals results in

$$\mathbf{z}(x) = \mathbf{T}_{(x-x_0)}\,\mathbf{z}(x_0) + \mathbf{T}_{(x-x_f)}\,\mathbf{C}^{-1}\,\mathbf{K}^{-1}\,\mathbf{f}_0 \tag{F.21}$$

The vector $\mathbf{f}_0(\omega)$ represents a combination of a frequency-dependent external force and moment.

$$\mathbf{f}_0 = \left[\begin{array}{cccc} 0 & 0 & \dfrac{i\omega M_0(\omega)}{B} & \dfrac{-i\omega F_0(\omega)}{B} \end{array}\right]^{\mathrm{T}} \tag{F.22}$$

Then, the transfer of state just across the drive point becomes

$$\mathbf{z}_f^+ = \mathbf{z}_f^- + \mathbf{C}^{-1}\,\mathbf{K}^{-1}\,\mathbf{f}_0 \qquad (F.23)$$

This change in the state of vibrations depends on the type of the excitation, which could be a moment, shear, or a combination of forcing terms.

F.4 Transfer Matrices for the Boundaries

Boundary conditions are treated in a way similar to the point impedances. The transfer matrices governing the boundaries are obtained by using the physical state variables of the beam. For future use, the boundaries are characterized by translational and rotational impedances T and Z, respectively. The subscripts 0 and L are used to indicate the boundaries at $x = 0$ and $x = L$ of the beam.

As in the previous analysis, force and moment relationships for the boundary at $x = 0$ can be given as

$$Z_0\,V = -Q \qquad \text{and} \qquad T_0\varphi = -M \qquad (F.24)$$

Substituting equations (F.17-F.20) into equation (F.24), and then organizing the result in a matrix form gives

$$\begin{bmatrix} \widetilde{Z}+i & \widetilde{Z}+1 \\ 1-i\widetilde{T} & 1-\widetilde{T} \end{bmatrix} \begin{bmatrix} a^+ \\ a_N^+ \end{bmatrix} = \begin{bmatrix} -\widetilde{Z}+i & -1-\widetilde{Z} \\ 1+i\widetilde{T} & -1-\widetilde{T} \end{bmatrix} \begin{bmatrix} a^- \\ a_N^- \end{bmatrix} \qquad (F.25)$$

where $\widetilde{Z}_0 = i\omega\,Z_0/(B\,k_p^3)$ and $\widetilde{T}_0 = i\omega\,T_0/(B\,k_p)$ are the normalized impedances.

The expressions for the incident wave $[a^+ \quad a_N^+]^{\mathrm{T}}$, and the reflected wave $[a^- \quad a_N^-]^{\mathrm{T}}$, can be combined to define a reflection matrix $\mathbf{R}_0$:

$$\mathbf{R}_0 = \begin{bmatrix} \ell_{11} & \ell_{12} \\ \ell_{21} & \ell_{22} \end{bmatrix} \qquad (F.26)$$

where

$$\ell_{11} = [(1-i)(1-\tilde{T}_0\tilde{Z}_0) + 2\tilde{Z}_0 + 2i\tilde{T}_0]/\ell_d$$

$$\ell_{12} = 2(1+\tilde{T}_0\tilde{Z}_0)/\ell_d$$

$$\ell_{21} = -2i(1+\tilde{T}_0\tilde{Z}_0)/\ell_d \qquad (F.27)$$

$$\ell_{22} = [(1-i)(\tilde{T}_0\tilde{Z}_0 - 1) + 2i\tilde{T}_0 + 2\tilde{Z}_0]/\ell_d$$

$$\ell_d = (1+i)(1-\tilde{T}_0\tilde{Z}_0) + 2\tilde{Z}_0 - 2i\tilde{T}_0$$

The boundary conditions at $x = 0$ and $x = L$ are defined in terms of the reflection matrix, in a partitioned matrix form, as

$$\mathbf{A}_0\,\mathbf{z}(0) = 0\,, \qquad \mathbf{A}_L\,\mathbf{z}(L) = 0 \qquad (F.28)$$

where $\mathbf{A}_0 = [\mathbf{I} \mid \mathbf{R}_0]$, $\mathbf{A}_L = [\mathbf{R}_L \mid \mathbf{I}]$ and $\mathbf{I}$ is a 2×2 identity matrix. The reflection matrix $\mathbf{R}_L$ has the same form as the matrix $\mathbf{R}_0$. The elements of the matrix $\mathbf{R}_L$, which are designated by r_{ij}, can be defined by substituting the normalized boundary impedances, $\tilde{Z}_L$ and $\tilde{T}_L$ into the definition of ℓ_{ij}. The size of the coefficient matrices, $\mathbf{A}_0$ and $\mathbf{A}_L$, is 2×4, each defining two boundary conditions, as they should.

APPENDIX G

In the engineering applications, the bandwith of a simple oscillator or a filter is defined in several different ways. Considering the frequency response function $H(\omega)$ of an oscillator, the following definitions apply for its bandwidth:

a) Half-power or 3dB bandwidth

$$B_{3dB} = f_2 - f_1 \tag{G.1}$$

such that the power supplied to the oscillator is drops to half of its maximum at f_1 and f_2; $|H(f_1)|^2 = |H(f_2)|^2 = \frac{1}{2}|H(f_n)|^2$, as shown in Appendix H Figure H.1.

b) Mean square or noise bandwidth

$$B_n = \frac{\int_{-\infty}^{\infty} |H(f)|^2 \, df}{|H_{max}|^2} \tag{G.2}$$

which is the width of a rectangle that has the height as the maximum power and the area equivalent to the total spectral power of the oscillator.

c) Root-Mean-Square (rms) bandwidth:

$$B_{rms} = \frac{1}{\|H(\omega)\|_2} \left[\int_{-\infty}^{\infty} \omega^2 |H(\omega)|^2 \, d\omega \right]^{1/2} \tag{G.3}$$

This definition is mathematically more convenient and conceptually more informative for complex spectra. It is analogous to the radius of gyration of a body about an axis of rotation or to the standard deviation of a statistical distribution.

APPENDIX H

Single-Degree of Freedom System

A mass-spring-dashpot is the elementary model that is frequently used in the vibration analysis of multi-degree-of-freedom systems. Considering an external force $f(t)$, the equation governing the vibrations of the mass is given by

$$m\,\frac{d^2x(t)}{dt^2} + c\,\frac{dx(t)}{dt} + k\,x(t) = f(t)$$

which can be written in an alternate form as

$$\ddot{x}(t) + \omega_n \eta\,\dot{x}(t) + \omega_n^2\,x(t) = f(t)/m \qquad (H.1)$$

In the preceding equation, $\omega_n = \sqrt{k/m}$ is the natural frequency and $\eta = c/\sqrt{km}$ is the loss factor. The loss factor is related to the critical damping ratio $\zeta = \eta/2$ and to the quality factor $Q = 1/\eta$.

The unforced response of the system is given by

$$x(t) = A\,e^{\frac{1}{2}\omega_n \eta t}\,\sin(\omega_d t + \phi) \qquad (H.2)$$

where $\omega_d = \omega_n\sqrt{1-\eta^2/4}$. The constants A and ϕ are determined from the initial conditions.

For a physical sytem, the oscillations will decay in time due to energy disipation. In acoustics, the duration of decay is measured by the reverberation time T_R, which represents a decrease in the vibrational energy by a factor of 10^{-6}. If we consider the time-averaged total energy in the system $E = E_0 e^{-\omega_n \eta t}$, then $e^{-\omega_n \eta T_R} = 10^{-6}$ gives the revebration time as

$$T_R = \frac{2.2}{\eta f_n} \qquad (H.3)$$

where $f_n = \omega_n/2\pi$.

The response of the system to a harmonic excitation is determined by considering $f(t) = Fe^{-i\omega t}$ and $\dot{x}(t) = Ve^{-i\omega t}$. Then, the mobility of the system is defined as

$$H(\omega) = \frac{V}{F} = \frac{1/m}{\omega_n \eta - i(\omega - \omega_n/\omega)} \qquad (H.4)$$

The magnitude of the mobility is plotted in Figure H.1.

The time-averaged power supplied to the system is given by

$$\mathcal{I} = \frac{1}{2}\Re\{F\,V^*\} = \frac{1}{2}|F|^2\,\Re\{H(\omega)\} = \frac{1}{2}\omega_n\,\eta\,m\,|F|^2\,|H(\omega)|^2 \qquad (H.5)$$

The maximum power is supplied when $|H(\omega)|_{max} = 1/(m\omega_n\eta)$, which occurs at $\omega = \omega_n(1-\eta^2/2)$. For small η, the power absorbed by the oscillator drops to half of its peak value at $\omega_1 = \omega_n(1-\eta/2)$ and $\omega_2 = \omega_n(1+\eta/2)$. A commonly used definition of bandwith corresponds to the span between the preceding frequencies and is defined as the "half-power or 3dB bandwidth" of the oscillator

$$B_{3dB} = \eta\, f_n \qquad (H.6)$$

which, for a given loss factor, is linearly proportional to the center frequency, f_n. The definition of the $3dB$-bandwidth is sketched in Figure H.1. In terms of the $3dB$-bandwith, the reveberation time given in equation (H.3) becomes

$$T_R = \frac{2.2}{B_{3dB}} \qquad (H.7)$$

which is a convenient measure for the duration of the time decay for the transient vibration response of a single degree-of-freedom system.

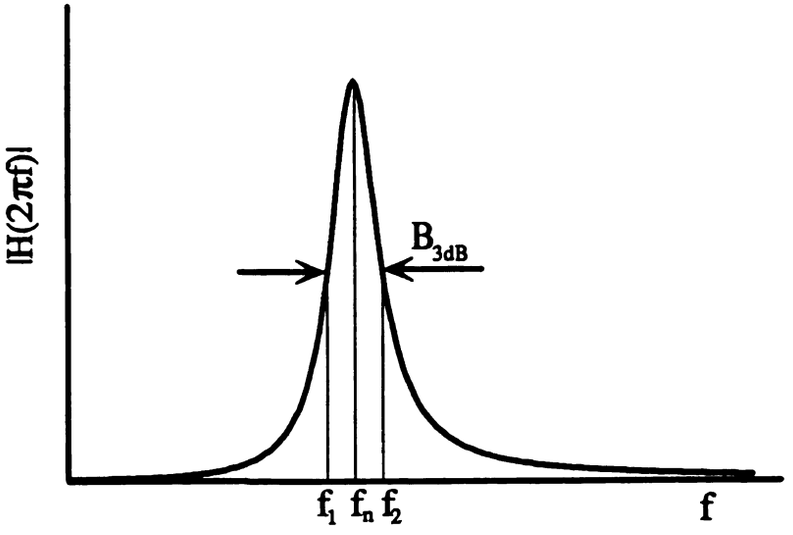

Figure H.1. The 3dB-bandwidth of an oscillator.

APPENDIX I

Color Code for the Display of Wavelet Transforms

The color scale used for the representation of the wavelet transform magnitude is obtained by mixing red, green, and blue colors. A total of 256 different colors were utilized to display the magnitude information. The assignments were made as follows:

dark red	=	maximum transform magnitude
⋮		
bright yellow	=	20 dB below the maximum
⋮		
dark greeen	=	40 dB below the maximum
⋮		
black	=	60 dB below the maximum.

BIBLIOGRAPHY

BIBLIOGRAPHY

1. Achenbach, J.D., 1973, *Wave Propagation in Elastic Solids*, Amsterdam: North-Holland Publishing Company.

2. Allen, J.B. and Rabiner, L.R., 1977, "A Unified Approach to Short-Time Fourier Analysis and Synthesis," *Proceedings of the IEEE*, Vol. 65, No. 11, pp.1558–1564.

3. Alpert, B.K, 1992, "Construction of Simple Multiscale Bases for Fast Matrix Operations," in *Wavelets and Their Applications*, Ruskai, M.B. et al., Eds., Boston: Jones and Bartlett, pp.211–227.

4. Alpert, B. K., 1993, "A Class of Bases in L^2 for the Sparse Representation of Integral Operators," *SIAM Journal of Mathematical Analysis*, Vol. 24, No. 1, pp.246–262.

5. Alpert, B.K., 1992, "Wavelets and Other Bases for Fast Numerical Linear Algebra," in *Wavelets: A Tutorial in Theory and Applications*, Ed.: C.K. Chui, San Diego: Academic press, pp.181–216.

6. Aslaksen, E.W. and Klauder, J.R., 1969, "Continuous Representation Theory Using the Affine Group," *Journal of Mathematical Physics*, Vol. 10, No. 12, pp.2267–2275.

7. Auscher, P., et al., 1992, "Local Sine and Cosine Bases of Coifman and Meyer and the Construction of Smooth Wavelets," in *Wavelets: A Tutorial in Theory and Applications*, Ed.: C.K. Chui, San Diego: Academic press, pp.237–256.

8. Auscher, P., 1994, "Remarks on the Local Fourier Bases," in *Wavelets: Mathematics and Applications*, Eds.: Benedetto, J.J. and Frazier, M.W., Boca Raton: CRC Press, pp.203–218.

9. Bastiaans, M. J., 1980, "Gabor's Expansion of a Signal into Gaussian Elementary Signals," *Proceedings of the IEEE*, Vol. 68, No. 4, pp.538–539.

10. Bastiaans, M. J., 1985, "On the Sliding-Window Representation in Digital Signal Processing," *IEEE Transactions on Acoustics, Speech, and Signal Processing*, Vol. ASSP-33, No. 4, pp.868–873.

11. Battle, G., 1987, "A Block Spin Costruction of Ondelettes. Part I: Lemarie Functions," *Communications in Mathematical Physics*, Vol. 110, pp.601–615.

12. Battle, G., 1988, "Heisenberg Proof of the Balian-Low Theorem," *Letters in Mathematical Physics*, Vol. 15, pp.175–177.

13. Battle, G., 1989, "Phase Space Localization Theorem for Ondelettes," *Journal of Mathematical Physics*, Vol. 30, No. 10, pp.2195–2196.

14. Benedetto, J.J. and Frazier, M.W., (Eds.), 1994, *Wavelets: Mathematics and Applications* , Boca Raton: CRC Press.

15. Benedetto, J.J. and Walnut, D.F., 1994, "Gabor Frames for L^2 and Related Spaces," in *Wavelets: Mathematics and Applications*, Eds.: Benedetto, J.J. and Frazier, M.W., Boca Raton: CRC Press, pp.97–162.

16. Benedetto, J.J, 1994, "Frame Decompositions, Sampling, and Uncertainity Principle Inequalities," in *Wavelets: Mathematics and Applications*, Eds.: Benedetto, J.J. and Frazier, M.W., Boca Raton: CRC Press, pp.247–304.

17. Beylkin, G., Coifman, R. and Rokhlin, V., 1991, "Fast Wavelet Transforms and Numerical Algorithms I," *Communications on Pure and Applied Mathematics*, Vol. 44, pp.141–183.

18. Beylkin, G., "On the Representation of Operators in Bases of Compactly Supported Wavelets," (Preprint from Yale University Mathematics Department)

19. Beylkin, G., Coifman, R. and Rokhlin, V, 1992, "Wavelets in Numerical Analysis," in *Wavelets and Their Applications*, Ruskai, M.B. et al., Eds., Boston: Jones and Bartlett, pp.181–210.

20. Beylkin, G., 1994, "On Wavelet-Based Algorithms for Solving Differential Equations," in *Wavelets: Mathematics and Applications*, Eds.: Benedetto, J.J. and Frazier, M.W., Boca Raton: CRC Press, pp.449–466.

21. Boussinesq, J., 1885, *Application des Potentiels*, Paris: Gauthier-Villars, p.463.

22. Brillouin, L., 1960, *Wave Propagation and Group Velocity*, New York: Academic Press.

23. Chui, C.K., 1992, *An Introduction to Wavelets*, New York: Academic Press.

24. Chui, C.K., (Editor), 1992, *Wavelets: A Tutorial in Theory and Applications*, New York: Academic Press.

25. Chui, C.K., 1992, "On Cardinal Spline-Wavelets," in *Wavelets and Their Applications*, Ruskai, M.B. et al., Eds., Boston: Jones and Bartlett, pp.419–438.

26. Chui, C.K. and Li, C., 1993, "Nonorthogonal Wavelet Packets," *SIAM Journal of Mathematical Analysis*, Vol. 24, No. 3, pp.712–738.

27. Chui, C. K., and Shi, X., 1993, "Inequealities of Littlewood-Paley Type for Frames and Wavelets," *SIAM Journal of Mathematical Analysis*, Vol. 24, No. 1, pp.263–277.

28. Cohen, A., Daubechies, I. and Feauveau, J.C., 1992, "Biorthogonal Bases of Compactly Supported Wavelets," *Communications on Pure and Applied Mathematics*, Vol. 45, No. 5, pp.485–560.

29. Cohen, L., 1989, "Time-Frequency Distributions- A Review," *Proceedings of the IEEE*, Vol. 77, No. 7, pp.941–981.

30. Cohen, L., 1992, "Wavelets and Digital Signal Processing," in *Wavelets and Their Applications*, Ruskai, M.B. et al., Eds., Boston: Jones and Bartlett, pp.105–121.

31. Cohen, A. and Daubechies, I., 1993, "Orthonormal Bases of Compactly Supported Wavelets III. Better Frequency Resolution," *SIAM Journal of Mathematical Analysis*, Vol. 24, No. 2, pp.520–527.

32. Coifman, R.R. and Wickerhauser, M.V., 1992, "Entropy-Based Algorithms for Best Basis Selection," *IEEE Transactions on Information Theory*, Vol. 38, No. 2, pp.713–718.

33. Coifman, R.R., Meyer, Y. and Wickerhauser, V., 1992, "Wavelet Analysis and Signal Processing," in *Wavelets and Their Applications*, Ruskai, M.B. et al., Eds., Boston: Jones and Bartlett, pp.153–178.

34. Coifman, R.R. and Wickerhauser, M.V., 1994, "Wavelets and Adapted Waveform Analysis," in *Wavelets: Mathematics and Applications*, Eds.: Benedetto, J.J. and Frazier, M.W., Boca Raton: CRC Press, pp.399–423.

35. Collacott, R. A., 1979, *Vibration Monitoring and Diagnosis*, London: George Godwin Limited.

36. Combes, J.M., Grossman, A. and Tchamitchian, Ph., (Eds.), 1987, "Wavelets: Time-Frequency Methods and Phase Space," Berlin: Springer-Verlag.

37. Cremer, L., Heckl, M. and Ungar, E. E., 1973, *Structure-Borne Sound*, New York: Springer-Verlag.

38. Daubechies, I., Grossmann, A. and Meyer, Y., 1986, "Painless Nonorthogonal Expansions," *Journal of Mathematical Physics*, Vol. 27, No. 5, pp.1271–1283.

39. Daubechies, I., 1988, "Orthonormal Bases of Compactly Supported Wavelets," *Communications on Pure and Applied Mathematics*, Vol. 41, No. 7, pp.909–996.

40. Daubechies, I., 1988, "Time-Frequency Localization Operators: a Geometric Phase Space Approach" *IEEE Transactions on Information Theory*, Vol. 34, No. 4, pp.605–612.

41. Daubechies, I. and Grossmann, A., 1988, "Frames in the Bargman Space of Entire Functions," *Communications on Pure and Applied Mathematics*, Vol. 41, No. 2, pp.152–164.

42. Daubechies, I., 1990, "The Wavelet Transform, Time-Frequency Localization and Signal Analysis" *IEEE Transactions on Information Theory*, Vol. 36, No. 15, pp.961–1005.

43. Daubechies, I., 1992, *Ten Lectures on Wavelets*, Philadelphia: Society for Industrial and Applied Mathematics.

44. David, G., 1991, "Wavelets and Singular Integrals on Curves and Surfaces," *Lecture Notes in Mathematics-No.1465*, Berlin: Springer-Verlag.

45. Davies, R. M., 1948, "A critical study of the Hopkinson pressure bar," *Philosophical Transactions of the Royal Society of London* , Vol. 240, pp.375-457.

46. Delprat, N., *et al.*, 1992, "Asymptotic Wavelet and Gabor Analysis: Extraction of Instantaneous Frequencies," *IEEE Transactions on Information Theory*, Vol. 38, No. 2, pp.644–664.

47. DeVore, R.A., Jawerth, B., and Lucier, B.J., 1992, "Image Compression Through Wavelet Transform Coding," *IEEE Transactions on Information Theory*, Vol. 38, No. 2, pp.719–746.

48. Duffin, R. J. and Schaeffer, A. C., 1952, "A Class of Nonharmonic Fourier Series," *Transactions of the American Mathematical Society*, Vol. 72, pp.341–366.

49. Duval-Destin, M., Muschietti, M. A. and Torresani, B., 1993, "Continuous Wavelet Decompositions, Multiresolution, and Contrast Analysis," *SIAM Journal of Mathematical Analysis*, Vol. 24, No. 3, pp.739–755.

50. Dutilleux, P., 1989, "An Implemantation of the 'Algorithme á Trous' to Compute the Wavelet Transform," in *Wavelets: Time-Frequency Methods and Phase Space*, Proceedings of Int. Conf., Marseille, France, 1987. Eds.: J.M.Combes, et al., Berlin: Springer-Verlag, pp.298–304.

51. Farge, M., 1992, "The Continuous Wavelet Tansform of Two-Dimensional Turbulent Flows," in *Wavelets and Their Applications*, Ruskai, M.B. et al., Eds., Boston: Jones and Bartlett, pp.275–302.

52. Feauveau, J. -C., 1992, "Nonorthogonal Multiresolution Analysis Using Wavelets," in *Wavelets: A Tutorial in Theory and Applications*, Ed.: C.K. Chui, San Diego: Academic press, pp.153–178.

53. Flandrin, P., 1989, "Some Aspects of Non-Stationary Signal Processing with Emphasis on Time-Frequency and Time-Scale methods," in *Wavelets: Time-Frequency Methods and Phase Space*, Proceedings of Int. Conf., Marseille, France, 1987. Eds.: J.M.Combes, et al., Berlin: Springer-Verlag, pp.68–98.

54. Frazier, M. and Jawerth, B., 1985, "Decomposition of Besov Spaces," *Indiana University Mathematical Journal*, Vol. 34, No. 4, pp.776–799.

55. Frazier, M. and Jawerth, B., 1988, "The φ-Transform and Application to Distribution Spaces," M. Cwikel, *et al.* (Eds.), *Lecture Notes in Mathematics*, Berlin: Springer-Verlag, pp.233–246.

56. Frazier, M., Jawerth, B. and Weiss, G., 1989, "Littlewood-Paley Theory and the Study of Function Spaces" Conference Board of Mathematical Sciences, American Mathematical Society, No.79.

57. Frazier, M. and Jawerth, B., 1992, "Applications of the φ and Wavelet Transforms to the Theory of Function Spaces," in *Wavelets and Their Applications*, Ruskai, M.B. et al., Eds., Boston: Jones and Bartlett, pp.377–417.

58. Frazier, M.W. and Kumar, A., 1994, "An Introduction to the Orthonormal Wavelet Transform on Discrete Sets," in *Wavelets: Mathematics and Applications*, Eds.: Benedetto, J.J. and Frazier, M.W., Boca Raton: CRC Press, pp.51–96.

59. Frazier, M.W. and Torres, R., 1994, "The Sampling Theorem, φ-Transform, and Shannon Wavelets for $\mathbf{R}$, $\mathbf{Z}$, $\mathbf{T}$ and $\mathbf{Z}_N$," in *Wavelets: Mathematics and Applications*, Eds.: Benedetto, J.J. and Frazier, M.W., Boca Raton: CRC Press, pp.221–245.

60. Gabor, D., 1946, "Theory of communications," *Journal of the Institution of Electrical Engineers*, Vol. 93, No. 3, pp.429–457.

61. Genossar, T. and Porat, M., 1992, "Can One Evaluate the Gabor Expansion Using Gabor's Iterative Algorithm," *IEEE Transactions on Signal Processing*, Vol. 40, No. 8, pp.1852–1861.

62. Goupillaud, P., Grossmann, A. and Morlet, J., 1984, "Cycle-Octave and Related Transforms in Seismic Signal Analysis," *Geoexploration*, Vol. 23, pp. 85–102.

63. Gröchenig, K. and Madych, W.R., 1992, "Multiresolution Analysis, Haar Bases, and Self-Similar Tilings of R^n," *IEEE Transactions on Information Theory*, Vol. 38, No. 2, pp.556–568.

64. Grossmann, A. and Morlet, J., 1984, "Decomposition of Hardy Functions into Square Integrable Wavelets of Constant Shape," *SIAM Journal on Mathematical Analysis*, Vol. 15, No. 4, pp.723–737.

65. Grossmann, A., Morlet, J. and Paul, T., 1985, "Transforms Associated to Square Integrable Group Representations. I. General Results," *Journal of Mathematical Physics*, Vol. 26, No. 10, pp.2473–2479.

66. Grossmann, A., Kronland-Martinet, R. and Morlet, J., 1989, "Reading and Understanding Continous Wavelet Transforms," in *Wavelets: Time-Frequency Methods and Phase Space*, Proceedings of Int. Conf., Marseille, France, 1987. Eds.: J.M.Combes, et al., Berlin: Springer-Verlag, pp.2–20.

67. Havelock, T. H., 1964, *The propagation of disturbances in dispersive media* in Cambridge Tracts in Mathematics and Mathematical Physics, No.17, New York: Stechert-Hafner Service Agency, 1964.

68. Heil, C. E. and Walnut, D. F., 1989, "Continuous and Discrete Wavelet Transform," *SIAM Review*, Vol. 31, No. 4, pp.628–666.

69. Hlawatsch, F. and Boudreaux-Bartels, G.F., 1992, "Linear and Quadratic Time-Frequency Signal Representations," *IEEE Signal Processing Magazine*, Vol. 9, No. 2, pp.21–67.

70. Hodges, C. H., Power, J., and Woodhouse, J., 1985, "The use of the sonogram in structural acoustics and an application to the vibrations of cylindrical shells," *J. Sound and Vibration* , Vol. 101, pp.203-218.

71. Holschneider, M., et al., 1989, " A Real-Time Algorithm for Signal Analysis with the Help of the Wavelet Transform," in *Wavelets: Time-Frequency Methods and Phase Space*, Proceedings of Int. Conf., Marseille, France, 1987. Eds.: J.M.Combes, et al., Berlin: Springer-Verlag, pp.286–297.

72. Jaffard, S. and Laurencot, P., 1992, "Orthonormal Wavlets, Analysis of Operators, and Applications to Numerical Analysis," in *Wavelets: A Tutorial in Theory and Applications*, Ed.: C.K. Chui, San Diego: Academic press, pp.543–601.

73. Janssen, A.J.E.M., 1982, "Bargmann Transform, Zak Transform, and Coherent States," *Journal of Mathematical Physics*, Vol. 23, No. 5, pp.720–731.

74. Kadambe, S., and Boudreaux-Bartels, G.F., 1992, "A Comparison of the Existence of 'Cross Terms' in the Wigner Ditribution and the Squared Magnitude of the Wavelet Transform and the Short Time Fourier Transform," *IEEE Transactions on Signal Processing*, Vol. 40, No. 10, pp.2498–2517.

75. Kreyszig, E., 1978, *Introductory Functional Analysis with Applications*, New York: John Wiley and Sons.

76. Kootsookos, P.J., Lovell, B.C. and Boashash, B., 1992, "A Unified Approach to the STFT, TFD's and Instantaneous Frequency," *IEEE Transactions on Signal Processing*, Vol. 40, No. 8, pp.1971–1982.

77. Kumar, A., et al., 1992, "A New Transform for Time-Frequency Analysis," *IEEE Transactions on Signal Processing*, Vol. 40, No. 7, pp.1697–1707.

78. Leckie, F. A. and Pestel, E., 1960, "Tranfer-Matrix Fundamentals", *International Journal of Mechanical Science*, Vol. 2, pp.137–167.

79. Lim, J. S. and Oppenheim, A.V., 1988, *Advanced Topics in Signal Processing*, Englewood Cliffs: Prentice Hall.

80. Lin, Y. K. and Donaldson, B. K., 1969, "A Brief Survey of Transfer Matrix Techniques With Special Reference To The Analysis of Aircraft Panels", *Journal of Sound and Vibration*, Vol. 10(1), pp.103–143.

81. Mace, B. R., 1984, "Wave Reflection and Transmission in Beams", *Journal of Sound and Vibration*, Vol. 97(2), pp.237–246.

82. Mallat, S.G., 1989, "A Theory for Multiresolution Signal Decomposition: The Wavelet Representation," *IEEE Transactions on Pattern Analysis and Machine Intelegence*, Vol. 11, No. 7, pp.674–693.

83. Mallat, S.G., 1989, " Multifrequency Channel Decompositions of Images and Wavelet Models," *IEEE Transactions on Acoustics, Speech, and Signal Processing*, Vol. 37, No. 12, pp.2091–2110.

84. Mallat, S.G., 1989, "Multiresolution Approximations and Wavelet Orthonormal Bases of $L^2(R)$," *Transactions of the Mathematical Society of America*, Vol. 315, No. 1, pp.69–87.

85. Mallat, S.G. and Hwang, W.L., 1992, "Singularity Detection and Processing with Wavelets," *IEEE Transactions on Information Theory*, Vol. 38, No. 2, pp.617–643.

86. Mead, D. J., 1986, "A New Method of Analyzing Wave Propagation in Periodic Structures; Applications to Periodic Timoshenko Beams and Stiffened Plates", *Journal of Sound and Vibration*, 104(1), pp.9–27.

87. Mead, D. J., 1975, "Wave Propagation and Natural Modes in Periodic Systems: I. Mono-Coupled Systems", *Journal of Sound and Vibration*, 40(1), pp.1–18.

88. Mead, D. J., 1975, "Wave Propagation and Natural Modes in Periodic Systems: II. Multi-Coupled Systems, With and Without Damping", *Journal of Sound and Vibration*, 40(1), pp.19–39.

89. Mead, D. J., 1970, "Free Wave Propagation in Periodically Supported Infinite Beams", *Journal of Sound and Vibration*, 11(2), pp.181–197.

90. Mead, D. J., 1973, "A General Theory of Harmonic Wave Propagation in Linear Periodic Systems With Multiple Coupling", *Journal of Sound and Vibration*, 27(2), pp.235–260.

91. Mead, D. J., 1971, "Vibration Response and Wave Propagation in Periodic Structures", *Journal of Engineering for Industry*, pp.783–792.

92. Meirovitch, L., 1967, *Analytical Methods in Vibrations*, New York: MacMillan Company.

93. Meyer, Y., 1989, "Orthonormal Wavelets," in *Wavelets: Time-Frequency Methods and Phase Space*, Proceedings of Int. Conf., Marseille, France, 1987. Eds.: J.M.Combes, et al., Berlin: Springer-Verlag, pp.20–37.

94. Meyer, Y., 1990, *Ondelettes et Opérateurs*, Vol. I, II, Paris: Hermann Éditeurs des Sciences et des Arts.

95. Meyer, Y., (Editor), 1992, *Wavelets and Applications*, Proceedings of the International Conference, Marseille, 1989, Paris: Masson.

96. Meyer, Y., 1993, *Wavelets Algorithms and Applications*, Philadelphia: Society for Industrial and Applied Mathematics.

97. Miklowitz, J., 1978, *Elastic waves and waveguides* , New York: North-Holland Publishing Company.

98. Miller, J.H. and Chiu, C.S., 1992, "Localization of the Sources of Short Duration Acoustic Signals," *Journal of the Acoustical Society of America*, Vol. 92, No. 5, pp.2997–2999.

99. Milne, H. K., 1989, "The Receptance Functions of Uniform Beams", *Journal of Sound and Vibration*, Vol. 131(3), pp.353–365.

100. Morlet, J., et al., 1982, "Wave Propagation and Sampling Theory—Part I: Complex Signal and Scattering in Multilayered media," *Geophysics*, Vol. 47, No. 2, pp.203–221.

101. Morlet, J., et al., 1982, "Wave Propagation and Sampling Theory—Part II: Sampling Theory and Complex Waves," *Geophysics*, Vol. 47, No. 2, pp.222–236.

102. Morse, P. M. and Ingard, K. U., 1968, *Theoretical Acoustics*, Princeton: Princeton University Press.

103. Nawab, S. H. and Quatieri, T. F., 1988, "Short-Time Fourier Transform," in *Advanced Topics in Signal Processing*, Eds.: Lim, J. S. and Oppenheim, A.V., Englewood Cliffs: Prentice Hall.

104. Önsay, T. and Haddow, A. G., 1994, "Wavelet Transform Anlysis of Transient Wave Propagation in a Dispersive Medium," *Journal of the Acoustical Society of America*, Vol.95(3), pp.1441–1449.

105. Önsay, T. and Haddow, A. G., 1993, "Comparison of STFT, Gabor and Wavelet Transforms in Transient Vibration Analysis of Mechanical Systems," *Journal of the Acoustical Society of America*, Vol.93, 2290(A).

106. Önsay, T., 1993, "Effects of Layer Thickness on the Vibration Response of a Plate-Fluid Layer System," *Journal of Sound and Vibration*, Vol.163(2), pp.231–259.

107. Önsay, T., 1991, "Flexural Vibration Response of Beams with General Boundary Conditions: A Transfer Matrix Approach," ASME DE-38, *Proceedings of the 13th Biennial Conference on Mechanical Vibration and Noise*, Miami, Florida, pp.283–290.

108. Oppenheim, A. V. and Schafer, R. W., 1989, *Discrete-Time Signal Processing*, Englewood Cliffs: Prentice Hall.

109. Paul, T. and Seip, K., 1992, "Wavelets and Quantum Mechanics," in *Wavelets and Their Applications*, Eds.: Ruskai, M.B. et al., Boston: Jones and Bartlett, pp.303–321.

110. Pestel, E. and Leckie, F. A., 1963, *Matrix Methods in Elastomechanics*, McGraw-Hill Book Company, Inc., New York.

111. Proakis, J. G. and Manolakis, D. G., 1988, *Introduction to Digital Signal Processing*, New York: Macmillan Publishing Company.

112. Rabiner, L.R. Allen, J.B., 1980, "On the Implementation of a Short-Time Spectral Analysis Method for System Identification," *IEEE Transactions on Acoustics, Speech, and Signal Processing.* Vol. 28, No. 1, pp.69–78.

113. Rayleigh, J. W. S., 1945, *The Theory of Sound*, New York: Dover Publications, Vol. 2.

114. Resnicoff, H.L. and Burrus, C.S., July 1990, "Relationship Between the Fourier Transform and the Wavelet Transform," *Advanced Signal-Processing Algorithms, Architectures, and Implementation*, San Diego: Proceedings of the Society of Photo-Optical Instrumentation Engineers, Vol. 1348.

115. Resnicoff, H.L., June 1992, "Wavelets and Adaptive Signal Processing," *Optical Engineering*, pp. 1229-1233.

116. Rioul, O. and Vetterli, M., Oct.1991, "Wavelets and Signal Processing," *IEEE Signal Processing Magazine*, pp. 14–38.

117. Rioul, O. and Flandrin, P., 1992, "Time-Scale Energy Distributions: A General Class Extending Wavelet Transforms," *IEEE Transactions on Signal Processing*, Vol. 40, No. 7, pp.1746–1757.

118. Rioul, O. and Duhamel, P., 1992, "Fast Algorithms for Discrete and Continuous Wavelet Transforms," *IEEE Transactions on Information Theory*, Vol. 38, No. 2, pp.569–586.

119. Royden, H. L., 1988, *Real Analysis*, New York: Macmillan Publishing Company.

120. Rubin, S., 1967, "Mechanical Immittance and Transmission Matrix Concepts", *Journal of the Acoustical Society of America*, Vol. 41(5), pp.1171–1179.

121. Rudin, W., 1987, *Real and Complex Analysis*, New York: McGraw-Hill Book Company.

122. Ruskai, M.B. et al., (Eds.), 1992, *Wavelets and Their Applications*, Boston: Jones and Bartlett.

123. Shensa, M., 1992, "The Discrete Wavelet Transform: Wedding the Á trous and Mallat Algorithms," *IEEE Transactions on Signal Processing*, Vol. 40, No. 10, pp.2464–2482.

124. Strang, G., 1989, "Wavelets and Dilation Equations: A Brief Introduction," *SIAM Review*, Vol. 31, No. 4, pp.614–627.

125. Tchamitchian, PH. and Torresani, B., 1992, "Ridge and Skeleton Extraction from the Wavelet Transform," in *Wavelets and Their Applications*, Ruskai, M.B. et al., Eds., Boston: Jones and Bartlett, pp.123–151.

126. Tewfik, A.H., Sinha, D. and Jorgensen, P., 1992, "On the Optimal Choise of a Wavelet for Signal Representation," *IEEE Transactions on Information Theory*, Vol. 38, No. 2, pp.747–765.

127. Torresani, B., 1992, "Wavelet Analysis of Asymptotic Signals, I: Ridge and Skeleton of the Transform," in *Wavelets and Applications* edited by Y. Meyer, Paris: Masson and Springer-Verlag, pp.13–27.

128. Unser, M., 1992, "On the Asymptotic Convergence of B-Spline Wavelets to Gabor Functions," *IEEE Transactions on Information Theory*, Vol. 38, No. 2, pp.864–872.

129. Vetterli, M. and Herley, C., 1992, "Wavelets and Filter Banks: Theory and Design," *IEEE Transactions on Signal Processing.* Vol. 40, No. 9, pp.2207–2232

130. Villemoes, L. F., 1992, "Energy Moments in Time and Frequency for Two-scale Difference Equation Solutions and Wavelets" *SIAM Journal of Mathematical Analysis*, Vol. 23, No. 6, pp.1519-1543.

131. Wahl, T. J. and Bolton, J. S., 1993, "The application of the Wigner distribution to the identification of structure-borne noise components," *J. Sound and Vibration* , Vol. 163, pp.101-122.

132. Wickerhauser, M.V., 1992, "Acoustic Signal Compression with Wavelet Packets," in *Wavelets: A Tutorial in Theory and Applications*, Ed.: C.K. Chui, San Diego: Academic press, pp.679–700.

133. Wong, P.W., 1993, "Wavelet Decomposition of Harmonizable Random Processes," *IEEE Transaction on Information Theory*, Vol. 39, No. 1, pp.7–18.

134. Von Flotow, A. H., 1986, "Disturbance Propagation in Structural Networks", *Journal of Sound and Vibration*, Vol. 106(3), pp.433–450.

135. Young, R. M., 1980, *An Introduction to Nonharmonic Fourier Series*, New York: Academic Press.